Formation, Structure and Habitability of Super-Earth and Sub-Neptune Exoplanets

by

Leslie Anne Rogers

B.Sc., Honours Physics-Mathematics, University of Ottawa (2006)

Submitted to the Department of Physics
in partial fulfillment of the requirements for the degree of

Doctor of Philosophy

at the

MASSACHUSETTS INSTITUTE OF TECHNOLOGY

June 2012

Author ....
Department of Physics
May 22, 2012

Certified by...
Sara Seager
Professor of Planetary Science
Professor of Physics
Class of 1941 Professor
Thesis Supervisor

Accepted by ....
Krishna Rajagopal
Professor of Physics
Associate Department Head for Education

Formation, Structure and Habitability of Super-Earth and Sub-Neptune Exoplanets

by

Leslie Anne Rogers

Submitted to the Department of Physics
on May 22, 2012, in partial fulfillment of the
requirements for the degree of
Doctor of Philosophy

Abstract

Insights into a distant exoplanet's interior are possible given a synergy between models and observations. Spectral observations of a star's radial velocity wobble induced by an orbiting planet's gravitational pull measure the planet mass. Photometric transit observations of a planet crossing the disk of its star measure the planet radius. This thesis interprets the measured masses and radii of super-Earth and sub-Neptune exoplanets, employing models to constrain the planets' bulk compositions, formation histories, and habitability.

We develop a model for the internal structure of low-mass exoplanets consisting of up to four layers: an iron core, silicate mantle, ice layer, and gas layer. We quantify the span of plausible bulk compositions for low-mass transiting planets CoRoT-7b, GJ 436b, and HAT-P-11b, and describe how Bayesian analysis can be applied to rigorously account for observational, model, and inherent uncertainties.

We present a detailed case study of GJ 1214b, the first exemplar of a new class of volatile-rich super-Earth exoplanets. At 6.5 $M_\oplus$ and 2.7 $R_\oplus$, GJ 1214b must have a gas layer to account for its low mean density. We present three possible scenarios for the origin of the gas layer on GJ 1214b: direct accretion of H/He gas from the protoplanetary nebula, sublimation of ices, and outgassing of volatiles from a rocky interior.

We next explore the low-density extreme of the mass-radius relations for volatile-rich super-Earth exoplanets. Using models of planet formation, structure, and survival, we constrain the minimum plausible planet mass for a measured planet radius and equilibrium temperature. We explore both core-nucleated accretion and outgassing as two separate formation pathways for Neptune-size planets with voluminous atmospheres of light gases.

Finally, we present a practical method to assess whether a hydrogen-rich sub-Neptune planet with measured mass and radius could potentially harbor a liquid water ocean. Using a one-dimensional radiative-convective model of energy transport through water-saturated hydrogen-rich envelopes, we constrain the combinations of planet properties (mass, radius, equilibrium temperature, intrinsic luminosity) that are conducive to liquid water oceans.

The pace of low-mass exoplanet discoveries is poised to accelerate, and this thesis will contribute to constraining the interior properties of newfound planets.

Thesis Supervisor: Sara Seager
Title: Professor of Planetary Science
Professor of Physics
Class of 1941 Professor

Acknowledgments

My doctoral study at MIT has been a formative experience for me as a scientist and as a person. Before arriving in Cambridge MA, I knew MIT would be an amazing place to push my academic development, but I had no idea about the other experiences and challenges that awaited me. Who would have guessed (not me) that I would discover my dream job (pondering the nature of distant planets), find a second home (outside my beloved Nova Scotia), earn a black belt in karate, battle a flying squirrel, start drinking coffee, fall in love, dance on stage again, learn to mediate, and be part of the executive leadership of a 700-person graduate student community. So many people have helped me along the way. The words on the following pages do not live up to the depth of gratitude that I feel.

First, I want to thank my PhD advisor, Sara Seager, for her mentorship, guidance, and friendship. She has offered me both intense hands-on collaboration and research freedom when I needed them most. I am especially grateful for how she coached me to develop more confidence in myself. I continue to be inspired by her ambitious vision, dedicated efficiency, keen intuition and strong scientific voice.

I would also like to thank the members of my thesis committee, Paul Schechter and Josh Winn, for their sage scientific and career advice. I will always remember (and do my very best to follow) Paul Schechter's maxims (e.g., *Don't let better be the enemy of the good*, *Own your mistakes*). Josh Winn's perspective as an exoplanet observer and interested skeptic has been tremendously valuable in anchoring my theoretical pursuits.

I am very grateful to have had the honor to collaborate with Peter Bodenheimer, Jack Lissauer, Geoff Marcy, Philipp Podsiadlowski, Saul Rappaport, Max Tegmark, and the *Kepler* Science Team during my graduate studies. They have each left a positive mark on my scientific development. I also want to send heartfelt acknowledgements to Robin McKenzie and Robert Hawkes, who prepared me for MIT by nurturing my love of physics and by introducing me to scientific research.

Thank you to the Seager Exoplanet Theory and Computation Group, the MIT

Exoplanets Discussion Group, and the faculty, postdocs, and students at the MIT Kavli Institute for all the camaraderie and invigorating scientific discussions over the years. I also want to thank Paul Hsi, Brian Surette, Arlyn Hertz, Jean Papagianopoulos, Cathy Modica, Crystal Nurazura Hall and the rest of the staff at MKI and the physics department for helping me so much over my time as a graduate student.

I am very grateful to George Elbaum for his financial support, which played a pivotal role in making my graduate career such a positive experience. The Whiteman Fellowship during my first year at MIT allowed me the time and flexibility to find my bearings and to start my PhD research on the right foot. I also acknowledge the financial support of the National Science and Engineering Research Council of Canada.

My friends deserve special recognition for filling my non-academic life with smiles, laughter, dancing, and fun. I especially want to thank Hannah Chang, Eveline Steine, and Sarah Vigeland for all the meals, conversations, and memories that we've shared. I feel tremendously blessed to have found such kindred spirits. I am also very grateful to my dance teacher Robin Offley, to my karate teacher Johnson Chung, and to the Sidney-Pacific Housemasters Roger and Dottie Mark for supporting me, for pushing me beyond my self-imposed limits, and for helping me to develop my leadership skills. Thank you to everyone in Statmechsocial, Movements in Time, the MIT Karate Club, Sidney-Pacific, the MIT Women in Physics, and the Physics REFS for keeping me happy, productive, and balanced. You have made my time at MIT the best years of my life.

Deep heartfelt gratitude goes to my boyfriend, Ben Mares, whose love, patience, kindness and support (of both the IT and emotional varieties) were instrumental in the preparation of this thesis.

Finally, I want to thank my family for always being there for me. Their unwavering love and support have carried me through the most challenging patches at MIT. I dedicate this thesis to them.

Contents

List of Figures

List of Tables

Chapter 1

Introduction

The discovery of planets outside our Solar System (exoplanets) has led to a dramatic increase in the number of known planets of more than two orders of magnitude within the past two decades. The Solar System planets have been a favored target for backyard astronomers for centuries. Children grow up with photographs of Venus, Saturn, and Neptune, returned by *Mariner 10*, *Cassini* and *Voyager* lining the pages of their school textbooks. Glossy pictures of exoplanets cannot immediately be added to the planet family album however; exoplanets (if they can be imaged at all) are not spatially resolved. The exoplanet community relies on artists conceptions to communicate their findings to the public.

How does one draw a planet that is light years away? What can be inferred about the surface and interior of distant exoplanets from their observationally measured properties? These questions do not have an easy answer. In general, the inversion from measured planet properties to interior composition is non-unique and relies on several assumptions. Super-Earth ($R_p \geq 1\ R_\oplus$ and/or $M_p \geq 1\ M_\oplus$) and Sub-Neptune ($R_p \leq 4\ R_\oplus$ and/or $M_p \leq 17\ M_\oplus$) exoplanets offer an especially intriguing puzzle because they have no Solar System analogs. This thesis focusses on modeling the interior structure and formation of volatile-rich super-Earth exoplanets to constrain the planets' bulk compositions, formation histories, and habitability.

1.1 Definition of a Planet

What defines a planet? How does a planet differ from a rubble pile of rocks or from a star? To gain physical intuition, we turn to order of magnitude calculations (adapted from Basri & Brown, 2006) that illustrate the competition between pressure support and gravity for successively more massive bodies.

At the low mass extreme, rocks are supported entirely by coulomb forces (bound-electron degeneracy in atoms and molecules). Once a pile of rocks is sufficiently massive for its sphere of gravitational influence to exceed its physical size, self-gravity can hold the rubble pile together (e.g., the near-Earth asteroid 25143 Itokawa Fujiwara et al., 2006). At still higher mass, the force of gravity will exceed the material forces, and the body will assume the shape of a (near spherical) equipotential surface. This transition occurs at a radius of approximately ~ 400 km for rocky bodies, and at smaller radii for icy bodies due to their lower rigidity. Continuing up the mass scale, once the gravitational potential energy per atom approaches the typical energy scale of chemical reactions (i.e., $GM_p\bar{\mu}/R_p \sim 1$ eV, where $\bar{\mu}$ is the mean molecular weight) the composition of the material forming the body can be substantially modified from its original form. For Earth-like densities, this is achieved at a radius of ~ 1500 km. Compression effects also gain in importance at this mass scale, as the central pressure of the body exceeds the bulk modulus of the material (on order 100 GPa for rock, and 1 GPa for ices). An important transition in the dominant source of central pressure support (from electrostatic to electron degeneracy) occurs at around 2 Jupiter masses. At masses larger than this, the planet radius decreases with increasing mass. Finally, the onset of nuclear burning demarcates the transition to a brown dwarf (D-burning, $\sim 13\ M_J$) and star (H-burning $\sim 0.08\ M_\odot$).

The formal definition of a planet is a topic of ongoing debate. In August 2006, the International Astronomical Union (IAU) resolved that, for bodies within the Solar System,

> A "planet" is a celestial body that: (a) is in orbit around the Sun, (b) has sufficient mass for its self-gravity to overcome rigid body forces so that

it assumes a hydrostatic equilibrium (nearly round) shape, and (c) has cleared the neighborhood around its orbit.

This IAU definition of a planet deals only with the lower bound on a planet's mass. The resulting demotion of Pluto from planet status (on account of its failure to satisfy condition *c* of the definition) caused quite a stir within our Solar System. However, for planetary systems around distant stars, the upper bound on a planet's mass is more pertinent; current observations simply cannot yet detect exo-dwarf-planets. The threshold between the planetary and sub-stellar (brown dwarf) regimes is conventionally defined by the onset of deuterium burning at $\sim 13\ M_J$ (Spiegel et al., 2011).

1.2 Planet Interior Structure Observations

Our knowledge of Solar System planet interiors is informed by cosmic abundances of the elements, by laboratory measurements of materials under extreme conditions, and by observations of the planets themselves (both ground-based and space missions). We briefly summarize each of these areas below.

1.2.1 Cosmological Abundances

What are the basic ingredients from which planets are formed? For this we look to the cosmic abundances of the elements, which are largely set by nuclear reactions in the moments after the Big Bang and later within stars. Cosmic abundances are determined empirically from observations of stars and the interstellar medium (ISM). On a more local scale, the solar photosphere and primitive meteorites (CI carbonaceous chondrites) yield insights into abundances within the Solar System (e.g., Lodders, 2003). Hydrogen and Helium are the most abundant elements by far; accounting for nearly 98% of the baryonic mass in the universe and in the Solar System. Including the twelve next most abundant elements (O, C, Ne, N, Mg, Si, Fe, Al, S, Ca, Na, Ni) in the census, takes us up to 99.865% of the baryonic mass. Cosmochemical arguments shape our perspective on what planetary materials are most plausible. For instance, there is no direct observational evidence to rule out a niobium-alloy for the composition of the Earth's core, but an iron-alloy (with similar density and bulk modulus) is a more highly favored scenario because Fe is more than 10^6 times more plentiful than Nb.

Mean elemental abundances are not the end of the story, however, as evidenced by the Solar System planets' enhanced metalicity relative to the universe (and Solar System) as a whole. The sequence in which major minerals and molecules condense from the cooling protoplanetary nebula has an important effect in concentrating heavy elements into solids and eventually into planets. In a coarse sense, planet forming material can be divided into three broad condensation temperature-based categories.

1. "Rock", or refractory materials with high condensation temperatures, condense first as the nebula cools, and persist closest to the star in condensed formed. This category comprises metals, sulfites, silicates, and oxides with condensation temperatures ranging from approximately 350 K to 1700 K.[1]

2. "Ices" (consisting of H_2O, CH_4, NH_3, N_2, CO, CO_2, HCN) have condensation temperatures ranging from $\sim$ 50 K to $\sim$ 200 K. Far from the star, in the outer reaches of planetary systems, ices will be found in solid form, while closer to the star (at temperatures above their condensation point) they will be in the gas phase. The transition region is commonly called the "ice line".

3. "Gases" (H, He, Ne, Ar), the most volatile constituents, are not expected to condense in the protoplanetary disk ($T_c \lesssim 20$ K).

The relative abundance of rock, ices, and gas comprising a planet may offer important clues to a planet's formation history and subsequent evolution.

The cosmic abundance of the elements and the condensation sequence help to motivate several simplifications in the materials considered in planetary interior modeling. Water – the least volatile and most abundant of the ices – is often used

---

[1] All condensation temperatures listed are for pressures of 10 Pa.

as a proxy for all ices in planet interior structure models. Models of giant planets often treat refractory materials as isothermal, neglecting thermal effects for high atomic number species in their degenerate interiors (e.g. Hubbard & Macfarlane, 1980; Fortney et al., 2007). For terrestrial planets, little error is introduced ($\lesssim 1$ % in the mass-radius relations) by simplifying the model rheology considered to the dominant silicate mineral phases of Si, Mg, Fe, and O and neglecting trace elements (Sotin et al., 2007). The planet interior models presented in this thesis proceed in a similar spirit. By distilling the materials considered, we minimize the number of model parameters while still conserving sufficient fidelity to constrain relative abundances of gas, ice, and rock. We emphasize, however, that these cosmochemical arguments are based on plausibility rather than rigor. A wide range of exotica can be imagined that are not encompassed by these approximations (e.g., carbon planets, Kuchner & Seager, 2005).

1.2.2 Material Properties

A description of material properties at extreme densities is a critical ingredient for understanding planet interiors. Much of the relevant physics is encapsulated in the equation of state (EOS), a function relating the density of a material to its pressure, temperature, and composition. The conditions of planetary interest run the gamut from 100 Pa to ~ 3000 GPa, and from ~ 100 K to $\gtrsim 10^4$ K. Consequently, a patch-work approach is needed to constrain the EOS with a combination experiments, theory and simulations. For a recent review, see e.g., Fortney et al. (2009).

Laboratory experiments probe the low-pressure regime. Diamond anvil static compression and shock wave techniques have achieved maximum pressures of ~ 200 GPa (e.g., Eggert et al., 2008). A common approach is to fit experimental data to standard EOS formulae from Vinet (Vinet et al., 1987, 1989) or Birch-Murnagham (Birch, 1947) for interpolation.

At extreme high pressures ($\gtrsim 10^4$ GPa), analytic theory is applied to describe the EOS of pressure ionized material. As pressure increases, the importance of chemical bonds and crystal structure fades in comparison to the kinetic energy of the degenerate electron gas. This drastically simplifies the material behavior. By approximating the electrons as a non-interacting gas of fermions moving in the slowly-varying potential field of the nuclei, the Thomas-Fermi-Dirac (TFD) theory yields an analytic EOS in this high pressure regime (Salpeter & Zapolsky, 1967).

There remains a significant range of intermediate pressures that are neither accessible to experiments nor to TFD theory. For material under these conditions, computationally intensive numerical solutions to Schrodinger's equation (ab initio calculations and density functional theory) provide important insights into the EOS. First-principles EOS models have been developed for hydrogen, helium, water, and carbon (Militzer et al., 2008; Nettelmann et al., 2008; Driver & Militzer, 2012).

1.2.3 Solar System Planet Observations

Ultimately we must rely on external observations of planets to tell us about what is on the inside. Earth-based astronomy, orbiters, fly-bys, landers, sample returns and meteorites all contribute to shaping our understanding of the Solar System planets. Table 1.1 summarizes broad classes of measurement that are available for Solar System bodies.

The process of inferring interior composition and interior structure from observable properties is a challenging inversion problem. The inferred properties can be very non-unique, and a wide range of planet compositions can agree with the observed data. For instance, whether or not Jupiter has a rock core is still unknown. Models using a state of the art hydrogen EOS constrain Jupiter's rock core mass to 0–8 $M_\oplus$ and Jupiter's total mass of heavy elements to $M_Z = 28$–32 $M_\oplus$ (Nettelmann et al., 2012). Constraints on the compositions of all the Solar System planets are summarized in Figure 1-1.

Composition trends are apparent in Figure 1-1, despite the non-uniqueness of the composition interpretation. In the Solar System, the terrestrial planets, gas-giants, and ice giants are neatly segregated in regions with increasing distance from the sun. Planet formation theories were developed to retrodict these Solar System composition trends (e.g., Safronov, 1969; Chambers, 2010). Exoplanetary systems now offer fertile testing ground for these formation theories.

Table 1.1: Solar System Planet Observations

Property	Measurement Technique	Interior Inferences
Gravity	Orbits of satellites (natural and artificial)	Mass (0th Moment); k_2, degree of central concentration (2nd moment); Dynamic structure, convection and zonal flows (high order moments)
Orbit	Astrometry	Distance; Energy budget (level of irradiation and tidal effects)
Size and Shape	Spatially resolved imaging; Stellar occultations; Radar echos; Altimetry; Reflectivity dependence on phase angle	Mean density (with mass); Lithosphere rigidity (rocky bodies); Test hydrostatic equilibrium (giant planets)
Rotation	Motion of spatially resolved surface features (rocky bodies); Periodicity of light curve (unresolved body); Radio signal periodicity (gas giants)	Moment of inertia; Fluidity of interior
Seismology	In-situ networked seismographs (Earth); Spectro-imaging (Jupiter)	Seismic velocity profile (density, temperature, and phase transitions); Planet dynamics (plate tectonics, volcanic events, turbulent excitation in giant planets)
Heat Flow	In situ measurements of surface conductive heat flow (Earth and moon); Direct measurement of excess luminosity (giant planets)	Internal thermal structure and evolution
Tidal Response	Tide phase lag; Amplitude of tides; Orbital evolution	Anelasticity
Surface Temperature	In situ measurement; Emission spectrum	Surface boundary condition; Greenhouse heating
Surface Composition	Spectra (reflectance, thermal IR, radio); Radar reflectivity; Xray and gamma-ray fluorescence; Chemical analysis (in situ, sample returns, meteorites)	Surface boundary condition
Intrinsic Magnetic Field	In situ magnetometer; Rock sample returns; Cyclotron radio emissions	Core composition, fluidity and dynamical state (core field); Past dynamo action and geologic history (crustal field)
Electromagnetic Response	Long-wavelength radio	Electrical conductivity of interior
Petrology	Xenoliths; Noble gases; Basalts	Interior composition and processes

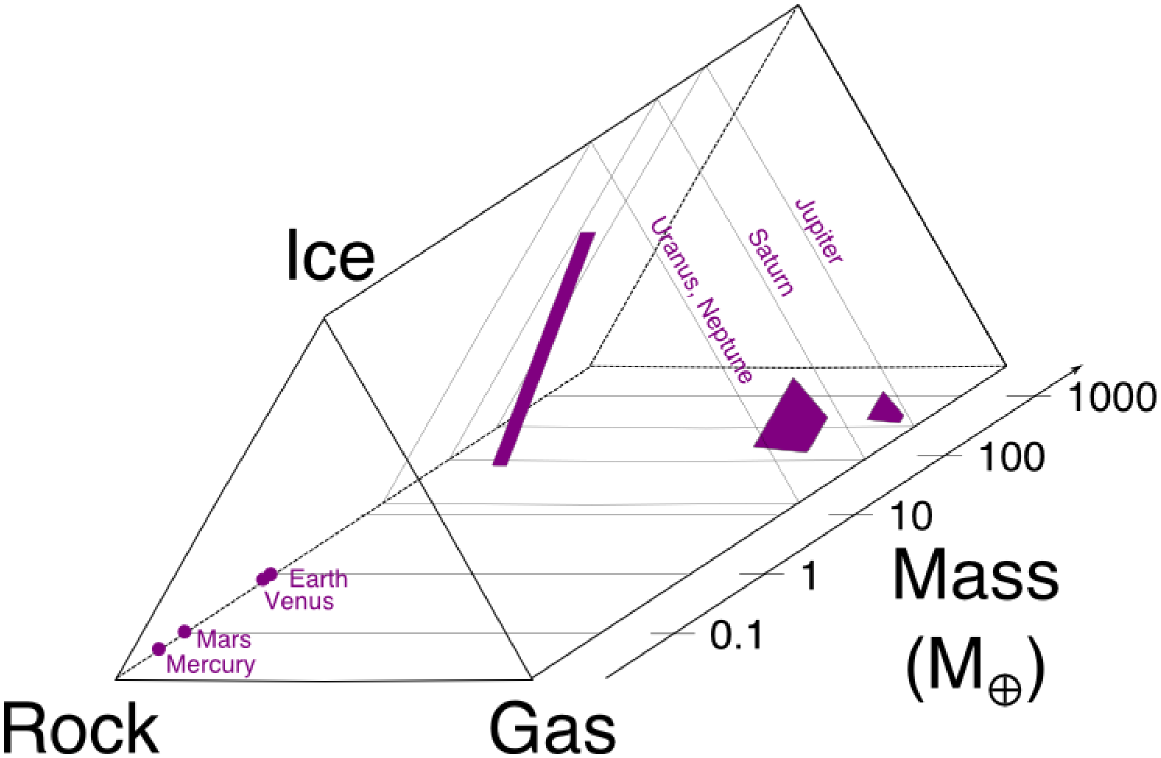

Figure 1-1: Schematic diagram illustrating the range of possible planet bulk compositions. In this figure "gas" refers to H and He accreted from the nebula, "ice" refers to ice-forming materials, and "rock" refers to refractory materials (e.g., iron and silicates). Constraints on the Solar System planet compositions (adapted from Guillot, 2005) are plotted in purple. This diagram was inspired by Chambers (2010) and Stevenson (2004).

1.2.4 Exoplanet Observations

Our exploration of Solar System planets has visited planet surfaces, plunged through planet atmospheres, monitored the planet from orbit, and observed the planet at a distance of several AU from our vantage point here on Earth. For planets outside our Solar System, we are currently (but hopefully not perpetually) limited to characterization from afar — the nearest known exoplanet to the Earth (epsilon Eridani b) is 3.2 pc away. At these distances, planets within tens of AU from their star are lost in the glare from their host star — only long-period hot young planets orbiting nearby stars are amenable to direct detection. A medley of indirect methods for exoplanet detection and characterization have been developed to overcome the observational challenges presented by the large contrasts in mass, radius, and luminosity between planets and their stars. These techniques include pulsar timing, periodic radial velocity variations, gravitational microlensing (Figure 1-2), astrometry, transit photometry, radio auroral emissions, polarimetry, and circumstellar disk features. In this thesis, we focus on small planets discovered through the radial velocity and transit methods (the two most prolific exoplanet detection techniques to date). We review the radial velocity and transit methods in more detail below.

Radial Velocity

The radial velocity (RV) detection technique played a pivotal role pioneering the study of exoplanets. The RV-discovery of the first confirmed exoplanet orbiting a main sequence star, 51 Peg (Mayor & Queloz, 1995), opened the flood gates; today, more than 700 exoplanets have been characterized with RV measurements.

The RV detection method centers on inferring the presence of a planet from the effect its gravitational pull has on its host star. Known as the "Kepler Problem", the motion of a planet orbiting a star has a prominent place in world history and in every introductory astrophysics textbook. Newtonian mechanics reveals that two bodies moving in the r^{-1} gravitational potential orbit their common center of mass on elliptical orbits. Thus as the planet orbits around the star, the star also wobbles back

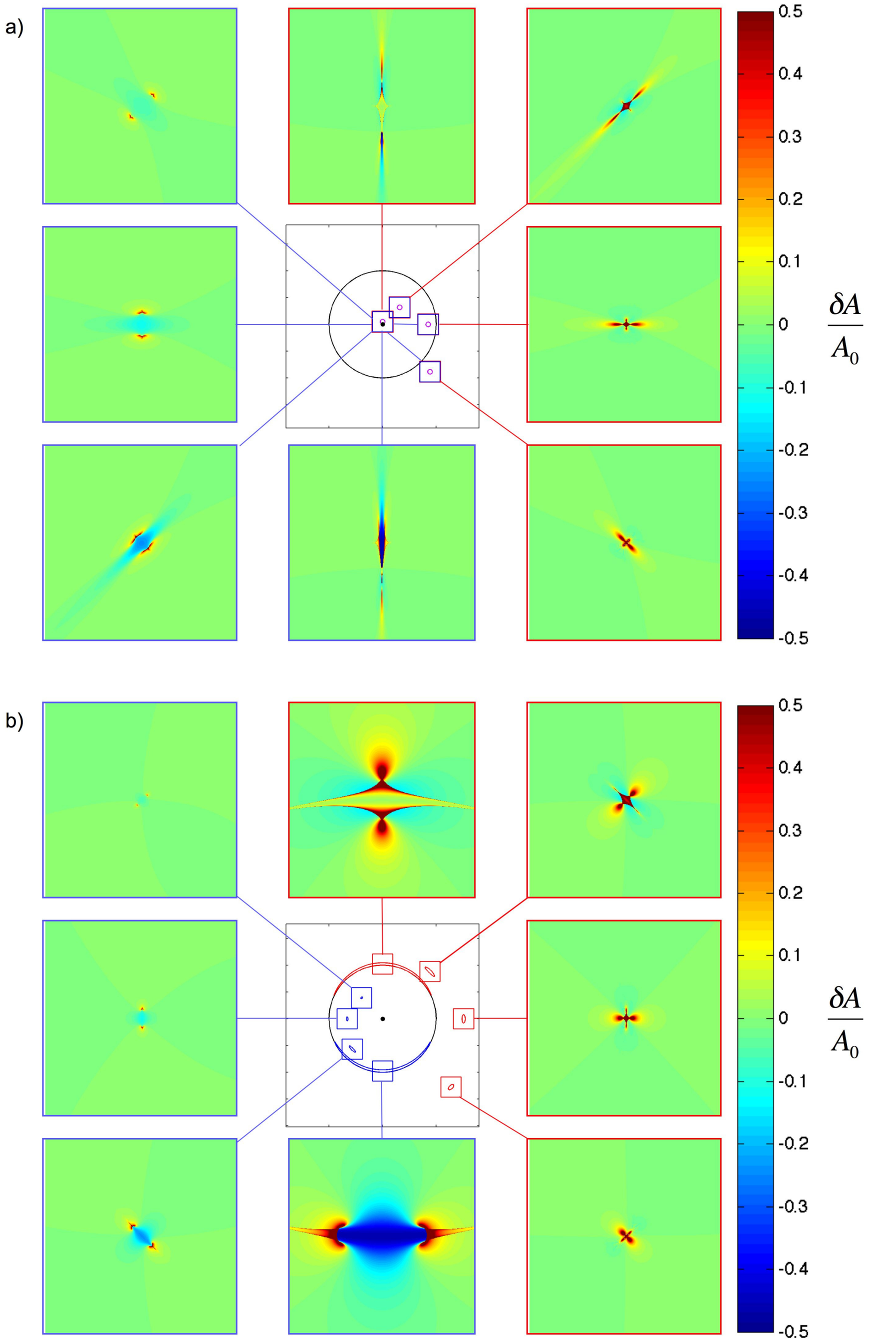

Figure 1-2: A Visual Guide to Planetary Microlensing plotting the fractional change in magnification of a point source induced by a planet around the lens star ($M_p = 10^{-4} M_\star$) relative to the point mass lens (no planet) case. In the magnification map color scale, red and yellow denote magnification increases, shades of blue denote magnification decreases, and green denotes magnifications relatively unchanged by the presence of the planet. In a) we plot how the magnification varies with the position of the source star for a fixed planet position, while in b) we show how the magnification depends on the planet position in the lens plane for fixed source position. Adapted from Rogers & Schechter (2011).

and forth due to the gravitational tug of the planet. The "radial" component, v_r, of the star's motion along the line of sight imprints the stellar spectrum received here on Earth with a periodic doppler shift $\left(\frac{\Delta\lambda(t)}{\lambda} = \frac{v_r(t)}{c}\right)$. The semi-amplitude of the star's motion along the line of sight to Earth, K, determines the magnitude of this effect, and is related to the planet mass, M_p, stellar mass, $M_\star$, orbital eccentricity, e, and orbital period P,

$$K = \left(\frac{2\pi G}{P}\right)^{1/3} \frac{M_p \sin i}{(M_\star + M_p)^{2/3}\sqrt{1-e^2}}. \tag{1.1}$$

For Jupiter and Earth viewed edge-on ($i = 90°$), $K \approx 12\ \mathrm{m\,s^{-1}}$ and $K \approx 10\ \mathrm{cm\,s^{-1}}$ respectively. Current state of the art spectrometers currently achieve precisions of $\sim 1\ \mathrm{m\,s^{-1}}$ on favorable targets.

The radial velocity detection technique is most sensitive to short-period orbits. Two factors contribute to this bias. First, the radial velocity amplitude is high when planets are closer to their star and exert a stronger gravitational force ($K \propto P^{-1/3}$). Second, since the full orbital period of the planet should be sampled with radial velocity measurements, shorter period planets necessitate shorter time-baselines to achieve a conclusive detection and to pin down the planet orbital properties. As a result, most planets discovered by this technique have short periods ($\lesssim 50$ days), and the current record holder (as of 05/01/12) with the longest orbital period is 55 Cnc d at 5400 ± 230 days (Fischer et al., 2008).

The radial velocity semi-amplitude scales with $M_p \sin i$. Assuming the stellar mass is constrained (e.g. from stellar isochron fitting or asteroseismology spectral observations of a star's radial velocity wobble provide a lower bound on the orbiting planet's mass.

Transits

While ancient civilizations venerated solar eclipses as the work of a heavenly being, modern day astronomers also revere the eclipses of distant stars by planets as a valuable tool for exoplanet detection and characterization. The first transiting exoplanet was discovered near the turn of the millenium (Charbonneau et al., 2000; Henry et al., 2000). To date, more than 200 transiting exoplanets have been confirmed, and the *Kepler* mission has discovered more than 2000 transiting planet candidates (Borucki et al., 2011a,b; Batalha et al., 2012).

When a planet transits in front of its host star, it blocks a fraction δ of the star's light headed to Earth. In the approximation of a uniform surface brightness across the stellar disk,

$$\delta = \left(\frac{R_p}{R_\star}\right)^2. \tag{1.2}$$

Variations in the surface brightness of the star (e.g. from limb darkening, gravity darkening, or star spots) can perturb the transit depth. For a Jupiter transiting a sun-like star (or a super-Earth transiting an M-dwarf), the transit depth is on the order of $\delta \sim 1\%$, while for an Earth orbiting a G type star, $\delta \sim 0.01\%$. Photometric transit observations of a planet crossing the disk of its star reveal the planet radius relative to the stellar radius.

A planet's orbit must be serendipitously aligned relative to our line of sight to the star for Earth-bound astronomers to see the planet transit. The condition for a planet on a circular orbit to transit is,

$$\cos i \leq \frac{R_\star + R_p}{a}. \tag{1.3}$$

This constraint on the planet orbital inclination becomes more and more stringent for larger planet–star orbital separations. For an isotropic distribution of planet orbital angular momentum directions, the transit probability $P_{\rm trans}$, is given by

$$P_{\rm trans} = \frac{R_\star + R_p}{a}. \tag{1.4}$$

$P_{\rm trans}$ decreases for planets that are further from their stars. Transit detections — like radial velocity discoveries — are biased toward short orbital periods.

The precious sub-sample of planets that transit their star offer tremendous potential for characterization. The transit shape, duration, timing, wavelength dependence, and RV-signal may offer insights into the planet atmosphere composition, rings, moons, orbital obliquity, planet spin, and unseen non-transiting planets. For transiting planets that are also detected by a second dynamical method (radial velocity or transit timing variations), both their mass and radius are known and the resulting average density restricts the planet's bulk composition. Figure 1-3 presents the known transiting planets (as of May 1, 2012) on a mass radius diagram.

1.3 Sub-Neptune and Super-Earth Exoplanets

Over the half-decade in which this thesis was written, transiting super-Earths have gone from a purely theoretical construct, to a handful of discoveries, to a planet category with more planet candidates than can be remembered by name. Super-Earth's are near the detection sensitivity threshold of current radial velocity and transiting planet surveys. As detection techniques continue to improve, the pace of transiting super-Earth discoveries is poised to accelerate.

Exoplanet surveys are revealing that planets Neptune-size (and smaller) are common. Microlensing surveys were the first to intimate that Neptune mass planets are far more abundant than their Jovian-mass brethren. A statistical analysis of 10 microlensing-discovered planets (comprised of four cold Neptune/super-Earths, one sub-Saturn mass planet, and five gas giant planets) revealed that, on orbits beyond the snow line ($\gtrsim$ 2.5 AU), Neptune-mass planets are at least three times more common than Jupiters at the 95% confidence level (Sumi et al., 2010). Based on radial velocity surveys, the trend of increasing planet abundance with decreasing planet mass also holds true for planets closer to their star. The HARPS survey measured that $11.8^{+4.3}_{-3.5}\%$ of sun-like stars have a planet in the mass range of 3–10 $M_\oplus$ with orbital periods less than 50 days, compared to $1.6^{+1.2}_{-0.8}\%$ of stars with with short period planets between 300–1000 $M_\oplus$ (Howard et al., 2010). Finally, nearly three quarters (74%) of the transiting planet candidates released by *Kepler* in their February 2011 data release have radii smaller than Neptune (Borucki et al., 2011b). A detailed statistical analysis of this same suite of *Kepler* candidates by Howard et al. (2011) found an occurrence rate of $13.0 \pm 0.8\%$ for planets with 2–4 $R_\oplus$ and orbital periods less than 50 days.

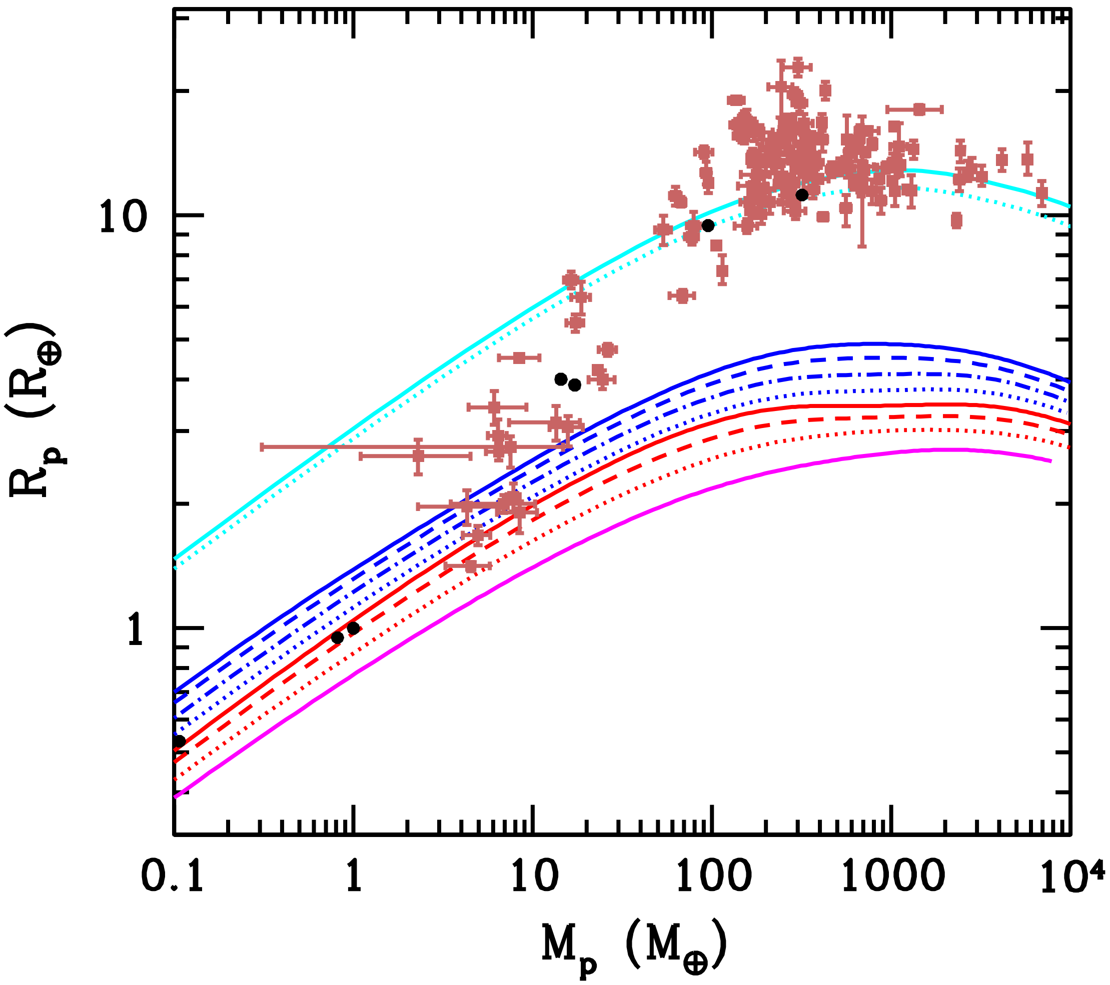

Figure 1-3: Mass-radius relationships of transiting planets. Solar System planets are denoted by black dots, while exoplanets are shown by pink squares. The curves are illustrative constant-temperature (300 K) mass-radius relations for cold isothermal bodies from Seager et al. (2007). The solid lines are homogeneous-composition planets: hydrogen (cyan solid), hydrogen–helium mixture with 25% He by mass (cyan dotted), water ice (blue solid), $MgSiO_3$ perovskite (red solid), and iron (magenta solid). The non-solid lines are mass-radius relations for differentiated planets: 75% water ice, 22% silicate shell, and 3% iron core (blue dashed); Ganymede-like with 45% water ice, 48.5% silicate shell, and 6.5% iron core (blue dot-dashed); 25% water ice, 52.5% silicate shell, and 22.5% iron core (blue dotted); Earth-like with 67.5% silicate mantle and 32.5% iron core (red dashed); and Mercury-like with 30% silicate mantle and 70% iron core (red dotted).

Though Neptunes are abundant, their nature and formation are still mysteries.

Core nucleated accretion – one of the most popular and successful theories for explaining Jupiter's formation – has trouble explaining the origins of Neptune-size planets. In the core-nucleated paradigm, solids in the protoplanetary nebula collide and coalesce to form protoplanet cores that then disrupt and accrete nebular gas (Harris, 1978; Mizuno, 1980). Once the mass of the gaseous envelope becomes comparable to the mass of the core, instability sets in and rapid runaway gas accretion feeds an incredible planet growth spurt (from $M_p \sim 10\ M_\oplus$ to $M_p \sim\ M_{\rm Jupiter}$ on the order of 0.1 Myr). In our Solar System, the formation of Uranus and Neptune is a long-standing puzzle, seemingly requiring a sudden gas accretion cut-off (disk dispersal) just as the ice-giants' cores reached critical mass. Extra patches can be added to the core nucleation theory to mitigate the fine-tuning problem (for instance, if Uranus and Neptune formed in a solid-rich feeding zone before experiencing by outward migration, Dodson-Robinson & Bodenheimer, 2010). Nonetheless, on a population-wide scale, statistical planet synthesis calculations predict a planet desert in the Neptune mass range due to the thresholding behaviour at the onset of runaway gas accretion (Ida & Lin, 2004). The observed abundance of Neptune-mass and Neptune-size planets runs counter to this prediction. Neptune-size and super-Earth exoplanets are important diagnostics of planet formation processes.

Super-Earth and sub-Neptune exoplanets are very interesting from the interior structure stand point. They populate a mass range that is notably absent from the Solar System between the terrestrial planets ($\leq 1\ M_\oplus$) and the ice giants ($\geq 14.5\ M_\oplus$). To understand their interior structure, it is necessary to develop models that bridge the gap and borrow physical insights from both the terrestrial planet and ice-giant planet communities. For super-Earths, the heavy element interior and volatile envelope can make comparable contributions to the planet mass, radius, and energy budget. The nature of planets in this regime is not yet known; terrestrial super-Earths, mini-Neptunes with hydrogen gas layers, and ocean-worlds with vast quantities of water are all plausible scenarios. A wide range of compositions a priori possible, and significant degeneracies exist in the interpretation (see e.g., Chapters 2 and 3, Adams et al., 2008;

Valencia et al., 2007a).

1.4 Thesis Overview

Models of planet interior structure, formation and evolution are needed to make the leap from observed planet properties to compositional inferences. The main objective of this thesis is to interpret the measured masses and radii of sub-Neptune exoplanets, employing models to constrain the planets' bulk compositions, formation histories, and habitability.

In Chapter 2 we develop a model for the internal structure of low-mass exoplanets. We consider differentiated planets consisting of up to four layers: an iron core, silicate mantle, ice layer, and gas layer. For a given planet mass and radius, we explore with the model all possible ways that the planet's mass can be distributed among the four layers. Although it is impossible to pinpoint the unique true composition of a planet from radial velocity and transit observations alone, we quantify the span of plausible compositions, and describe how Bayesian analysis can be applied to rigorously account for observational, model, and inherent uncertainties. We apply this approach to constrain bulk compositions of low-mass transiting planets CoRoT-7b, GJ 436b, and HAT-P-11b.

In Chapter 3 we present a case study of GJ 1214b, a transiting super-Earth orbiting a nearby M-dwarf. GJ 1214b is the first exemplar of a new class of volatile-rich super-Earth exoplanets; at 6.5 $M_\oplus$ and 2.7 $R_\oplus$, the planet must have a gas layer to account for its low mean density. In contrast to jovian-size planets for which only primordial H/He from the protoplanetary disk is sufficiently abundant to account for the planet envelope, gas layers on super-Earths may originate from a wider variety of sources. We present three possible scenarios for the gas layer on GJ 1214b: direct accretion of H/He gas from the protoplanetary nebula, sublimation of ices, and outgassing of volatiles from a rocky interior. This case study serves to motivate follow-up observations of GJ 1214b with the *Spitzer Space Telescope*, *Hubble Space Telescope*, and ground based observatories to discriminate between the composition scenarios presented.

We investigate the low-density extreme of planet mass-radius relationships in Chapter 4. Most *Kepler* transiting planet candidates orbit stars that are too faint for radial velocity measurements of the planet mass. Using theoretical models of planet formation, structure and survival, we constrain the minimum plausible planet mass as a function of planet radius and equilibrium temperature. We explore both core-nucleated accretion and outgassing as two separate formation pathways for Neptune-size planets with voluminous atmospheres of light gases. We show that Neptune-size (2–6 $R_\oplus$) planets at equilibrium temperatures $T_{\rm eq} = 500$–1000 K can potentially have masses less than 4 $M_\oplus$ (many times smaller than Neptune's mass of 17 $M_\oplus$). The possibility for low-mass low-density planets has important implications for the interpretation of the *Kepler* planet radius distribution, and for the radial velocity precision required to confirm planet candidates from transit surveys such as *Kepler*, HAT, WASP, and MEarth.

In Chapter 5, we constrain the scenarios in which a super-Earth with a hydrogen dominated envelope could harbor a surface liquid water ocean. Whereas the classical studies of the habitable zone for Earth-like planets have assumed H_2O-CO_2 dominated atmospheres, planet energy budgets dominated by incoming starlight, and gas layers with negligible contributions to the planet radius, these assumptions can break-down for sub-Neptune planets. In our more general treatment of the habitable zone, we consider the possibility of hydrogen-rich atmosphere compositions, take into account the intrinsic planet luminosity (from radioactive heating or release of left-over heat from accretion), and compute the radial extent of the gas envelope. By combining planet interior structure models with a one-dimensional radiative-convective semi-grey climate model, we constrain the combinations of observable planet properties (mass, radius, and orbital period) that are conducive to liquid water oceans.

Chapters 2, 3, and 4 are published in Rogers & Seager (2010a,b) and Rogers et al. (2011), respectively. In Chapter 4, I performed all the outgassing and equilibrium model calculations, and wrote the majority of the paper. Peter Bodenheimer ran the core-nucleated accretion planet formation simulations and wrote the section of the paper describing his calculations. Chapter 5 is in preparation for submission to the

Astrophysical Journal.

Chapter 2

A Framework for Quantifying the Degeneracies of Exoplanet Interior Compositions

Abstract

Several transiting super-Earths are expected to be discovered in the coming few years. While tools to model the interior structure of transiting planets exist, inferences about the composition are fraught with ambiguities. We present a framework to quantify how much we can robustly infer about super-Earth and Neptune-size exoplanet interiors from radius and mass measurements. We introduce quaternary diagrams to illustrate the range of possible interior compositions for planets with four layers (iron core, silicate mantles, water layers, and H/He envelopes). We apply our model to CoRoT-7b, GJ 436b, and HAT-P-11b. Interpretation of planets with H/He envelopes is limited by the model uncertainty in the interior temperature, while for CoRoT-7b observational uncertainties dominate. We further find that our planet interior model sharpens the observational constraints on CoRoT-7b's mass and radius, assuming the planet does not contain significant amounts of water or gas. We show that the strength of the limits that can be placed on a super-Earth's composition depends on the planet's density; for similar observational uncertainties, high-density super-Mercuries allow the tightest composition constraints. Finally, we describe how techniques from Bayesian statistics can be used to take into account in a formal way the combined contributions of both theoretical and observational uncertainties to ambiguities in a planet's interior composition. On the whole, with only a mass and radius measurement an exact interior composition cannot be inferred for an exoplanet because the problem is highly underconstrained. Detailed quantitative ranges of plausible compositions, however, can be found.

The contents of this chapter are also published in *Rogers, L. A., & Seager, S. 2010a, ApJ, 712, 974.*

2.1 Introduction

Over two dozen low-mass exoplanets with masses less than 30 Earth masses are known[1]. As their numbers increase, so does the probability to uncover a population of transiting low-mass exoplanets. The first transiting super-Earth exoplanet has been discovered (Léger et al., 2009)-based on the young history of exoplanets once one example of new type of object is discovered many more soon follow. Now that we are on the verge of discovering a good number of low-mass transiting planets (Baglin et al., 2009; Borucki et al., 2008; Irwin et al., 2009; Mayor et al., 2009a; Lovis et al., 2009), methods to constrain their interior composition from observations are required.

A good example of why quantitative methods to constrain planetary interior compositions are needed is GJ 436b (Butler et al., 2004; Gillon et al., 2007b), a Neptune-mass ($M_p = 23.17 \pm 0.79 M_{\oplus}$,; Torres et al. (2008)), Neptune-size ($R_p = 4.22^{+0.09}_{-0.10} R_{\oplus}$; Torres et al. (2008)) planet in a 2.6-day period around an M2.5 star. Initially, because of its similarity to the physical proportions of Neptune, Gillon et al. (2007b) assumed that GJ 436b was composed mostly of ices. Others showed that it could instead be composed of a rocky interior with a more massive H/He envelope (Adams et al., 2008).

Previously, Valencia et al. (2007a) introduced ternary diagrams to constrain the interior composition of super-Earths without gas envelopes. Zeng & Seager (2008) presented a detailed description of the functional form of the ternary diagram interior composition curves. Super-Earths are loosely defined as planets with masses between 1 and 10 Earth masses that are composed of rocky or iron material. While the terms "mini-Neptune" or "Neptune-like" are not in common usage, they refer to planets with significant gas envelopes. Others have modeled evolution of Neptune-mass planets to predict radii (e.g. Fortney et al., 2007; Baraffe et al., 2006). Figueira et al. (2009) used planet formation and migration models to suggest interior compositions for GJ 436b.

---

[1] See `exoplanet.eu` and references therein.

In this paper, we aim to quantify the constraints placed on a low-mass exoplanet's interior structure by transit and radial velocity observations. We use a planetary structure model to explore the range of plausible interior compositions that are consistent with a given pair of mass and radius measurements, independent of planet formation arguments. We extend previous work by including the possibility of a gas envelope and by considering a range of mantle iron enrichments. Our model of low-mass planet interiors includes an iron core, silicate mantle, water ice layer, and H/He layer. To plot four-layer interior compositions we introduce quaternary diagrams, an expansion of ternary diagrams into three dimensions. Finally, we present a new framework to combine both model and observational uncertainties in a rigorous way using Bayesian techniques when interpreting the interior composition of a transiting exoplanet. Our overall goal is to be able to interpret planetary mass and radius observations with a quantitative understanding of the effects of model uncertainties, observational uncertainties, and the inherent degeneracy originating from the fact that planets of differing compositions can have identical masses and radii.

We describe our planetary interior structure model in Section 2.2. We introduce quaternary diagrams in Section 2.3. In Section 2.4, we apply our model to constrain the compositions of low-mass exoplanets. In Section 2.5, we describe how Bayesian techniques may be applied to the problem of drawing inferences about an exoplanet's interior from measurements of the planet's mass and radius. Discussion and conclusions follow in Section 2.6 and 2.7.

2.2 Model

2.2.1 Model Overview

We consider a spherically symmetric differentiated planet in hydrostatic equilibrium. With these assumptions, the radius $r\left(m\right)$ and pressure $P\left(m\right)$, viewed as functions of the interior mass m, obey the coupled differential equations

$$\begin{aligned} \frac{dr}{dm} &= \frac{1}{4\pi r^2 \rho}, && (2.1) \\ \frac{dP}{dm} &= -\frac{Gm}{4\pi r^4}, && (2.2) \end{aligned}$$

where ρ is the density and G is the gravitational constant. Equation (2.1) is derived from the mass of a spherical shell, while Equation (2.2) describes the condition for hydrostatic equilibrium. The equation of state (EOS) of the material

$$\rho = f\,(P, T) \tag{2.3}$$

relates the density $\rho\,(m)$ to the pressure $P\,(m)$ and temperature $T\,(m)$ within a layer. We allow our model planets to have several distinct chemical layers ordered such that the density $\rho\,(m)$ is monotonically decreasing as m increases toward the planet surface. Throughout the rest of this work, we shall use $x_i = M_i/M_p$ to denote the fraction of a planet's total mass M_p in the ith layer from the planet center ($i = 1$ denotes the innermost layer).

To model a planet having mass M_p, radius R_p, and a specified composition $\{x_i\}$, we employ a fourth-order Runge-Kutta routine to numerically integrate Equations (2.1) and (2.2) for $r\,(m)$ and $P\,(m)$ from the outer boundary of the planet ($m = M_p$) toward the planet center ($m = 0$). We describe our scheme for setting the exterior boundary conditions in Section 2.2.3. We impose that both P and r are continuous across layer boundaries. At each step in the integration, the EOSs and temperature profiles described in Section 2.2.2 are used to evaluate $\rho\,(m)$.

The planet parameters $\{M_p,\ R_p,\ \{x_i\}\}$ in fact form an overdetermined system; there is a single radius R_p that is consistent with M_p and $\{x_i\}$. For a given mass and composition, we use a bisection root-finding algorithm to iteratively solve for the planet radius R_p that yields $r\,(m = 0) = 0$ upon integrating Equations (2.1) and (2.2) to the planet center. We stop the iteration once we have found R_p to within 100 m. Alternatively, in some applications it is convenient to be able to stipulate the planet radius (for instance when exploring the range of compositions $\{x_i\}$ allowed for a confirmed transiting exoplanet of measured mass and radius). In these cases, we use a bisection root-finding algorithm to iteratively solve for the mass ratio of the inner two material layers (x_2/x_1) of the planet given M_p, R_p, and valid mass distribution in the outer layers of the planet $\{x_i \,|\, i > 2\}$. We stop this iteration once we have found x_1 and x_2 to within 10^{-10}.

We increase the achievable accuracy in the composition of our modeled planets and the stability of this iterative process by employing the Lagrangian form of the equations of structure. With mass m as the independent integration parameter, we can take a partial mass step at the conclusion of each layer i to ensure that the specified value of x_i is precisely obtained. Within each layer, we employ an adaptive mass step-size such that each integration step corresponds to a radius increment of approximately 100 m. An adaptive step-size is necessary because both Equations (2.1) and (2.2) diverge as $r \to 0$ and $m \to 0$.

2.2.2 Material EOS and Thermal Profiles

In this section, we describe the EOS and thermal profile $T(m)$ assumed for each material layer.

We allow for the presence of an outer gas envelope in our modeled planets. We use the H/He EOS with helium mass fraction $Y = 0.28$ from Saumon et al. (1995). As mentioned in Adams et al. (2008), we ignore the "plasma phase transition" in the H/He EOS. To set the thermal profile we divide the H/He layer into two regimes: a thin outer radiative layer and an inner convective layer.

In the radiative regime of the gas envelope, we employ the analytic work of Hansen (2008) to approximate the temperature profile. Hansen (2008) considered a plane-parallel atmosphere in radiative equilibrium that is releasing heat flux generated in the planet interior while also being irradiated by a mono-directional beam of starlight. He solved the gray equations of radiative transfer with a 'two-stream' approach, allowing the incoming optical stellar photons to have a different opacity and optical depth than the infrared photons reradiated by the planet, and obtained a temperature profile

$$\begin{aligned} T^4 &= \frac{3}{4}{T_{\mathrm{eff}}}^4\left[\tau+\frac{2}{3}\right] \\ &+\mu_0{T_0}^4\left[1+\frac{3}{2}\left(\frac{\mu_0}{\gamma}\right)^2-\frac{3}{2}\left(\frac{\mu_0}{\gamma}\right)^3\ln\left(1+\frac{\gamma}{\mu_0}\right)-\frac{3}{4}\frac{\mu_0}{\gamma}e^{-\gamma\tau/\mu_0}\right]. \end{aligned} \quad (2.4)$$

In the above equation, T is the atmospheric temperature, τ is the infrared optical depth, γ is the ratio between the optical and infrared optical depths, μ_0 is angle cosine of the incoming beam of starlight relative to the local surface normal, T_{eff} is the effective temperature of the planet in the absence of stellar irradiation, and T_0 characterizes the magnitude of the stellar flux at the orbital distance of the planet $\left(F_*\left(R_*/a\right)^2=\sigma{T_0}^4\right)$. While μ_0 varies over the surface of the planet, our planet model is one-dimensional spherically symmetric model. We adopt a single fiducial value of $\mu_0=1/2$ (the average of μ_0 over the day hemisphere) when calculating the temperature profile of the radiative gas layer. Equation (2.4) yields the temperature in the radiative gas layer as a function of the (infrared) optical depth. The variation of optical depth τ, with interior mass m obeys

$$\frac{d\tau}{dm}=-\frac{\kappa}{4\pi r^2}, \quad (2.5)$$

where κ is the opacity. In the radiative regime of the gas layer, we integrate Equation (2.5) along with Equations (2.1) and (2.2). For κ, we use tabulated Rosseland mean opacities of H/He at solar abundance metallicity ($[M/H]=0.0$) from Freedman et al. (2008).

In our model gas layer, we allow for the presence of an inner adiabatic regime within which energy transport is dominated by convection. Neglecting the effects of conduction and diffusion, we take the temperature profile in the convective layer to follow the adiabat fixed to the specific entropy at the base of the radiative regime. The transition between the radiative and convective regimes is determined by the onset of convective instabilities. An adiabatically displaced fluid element in the gas layer will experience a buoyancy force tending to increase its displacement if

$$0 < \left(\frac{\partial \rho}{\partial s}\right)_P \frac{ds}{dm} = -\frac{\rho}{V}\left(\frac{\partial T}{\partial P}\right)_s \frac{ds}{dm}, \tag{2.6}$$

where the density $\rho \equiv \rho(P, s)$ is viewed as a function of the pressure P and specific entropy per unit mass s. Whenever Equation (2.6) is satisfied, the gas layer is unstable to convection. In the H/He EOS from Saumon et al. (1995), the adiabatic gradient $(\partial T/\partial P)_s$ is positive for all values of P, T, and He mass fraction Y. It thus suffices to test for $ds/dm < 0$ to define the outer boundary of the convection regime. As we integrate Equations (2.1), (2.2), and (2.5) from the planet exterior inward, we transition from the radiative regime to the convective regime once $ds/dm < 0$.

In the interior solid layers of the planet, we neglect the temperature dependence of the EOS. Thermal effects in the solid layers of a planet have a small effect on the planet radius (Seager et al., 2007) justifying the assumption of a simplified isothermal temperature profile. For every solid material considered in this study (Fe, FeS, $Mg_{1-\chi}Fe_{\chi}SiO_3$, and H_2O) we use the EOS data sets from Seager et al. (2007) derived by combining experimental data at $P \lesssim 200$ GPa with the theoretical Thomas-Fermi-Dirac EOS at high pressures, $P \gtrsim 10^4$ GPa.

2.2.3 Exterior Boundary Condition

In our model (described in Section 2.2.1), the exterior boundary of the planet sets the initial conditions for integrating the equations of structure. In the absence of a gas layer, we take the pressure to be 0 at the solid surface of the planet ($m = M_p$, $r = R_p$, $P = 0$). For planets having gas layers, we use a simplified constant scale height atmospheric model to choose appropriate exterior boundary conditions on the pressure P and optical depth τ at $r(M_p) = R_p$ as elaborated below.

To physically motivate our choice of exterior boundary conditions for planets with gas layers, we make several simplifying approximations about the properties of the planet gas layer in the neighborhood of the measured planet radius R_p. We assume that in this region the gas layer can be approximated as an ideal gas, so that

$$P = \frac{\rho k_B T}{\mu_{\rm eff}}, \tag{2.7}$$

where $\mu_{\rm eff}$ is the effective molecular mass of the gas. We further assume that the outer atmosphere of the planet is isothermal. This is consistent with the radiative temperature profile from Hansen (2008) (Equation (2.4)), which is largely isothermal for $\tau \ll 1$. We also neglect variations in the surface gravity $g = GM/R^2$ over the range of radii being considered. Finally, to account for the pressure dependence of the opacity, we assume a power-law dependence

$$\kappa = CP^{\alpha}T^{\beta}, \tag{2.8}$$

where $\log C = -7.32$, $\alpha = 0.68$, and $\beta = 0.45$ are determined by fitting to the Freedman et al. (2008) tabulated opacities (with all quantities in SI units). These assumptions, when coupled with the equation of hydrostatic equilibrium ($dP/dr = -\rho g$) and the definition of the radial optical depth ($d\tau/dr = -\kappa\rho$), yield an exponential dependence of both P and τ on r,

$$\begin{aligned} P\left(r\right) &= P_R e^{-(r-R_p)/H_P}, & (2.9) \\ \tau\left(r\right) &= \tau_R e^{-(\alpha+1)(r-R_p)/H_P}, & (2.10) \end{aligned}$$

with the pressure scale height H_P given by

$$H_P = \frac{R_p^2 k_B T}{G M_p \mu_{\rm eff}}, \tag{2.11}$$

and the pressure and optical depth at R_p (P_R and τ_R, respectively) related by

$$P_R = \left(\frac{G M_p \left(\alpha+1\right) \tau_R}{R_p^2 C T^{\beta}}\right)^{1/(\alpha+1)}. \tag{2.12}$$

It is important to maintain a direct correspondence to observations when defining the radius of a gas-laden planet in our model. Planet radii are measured observationally from transit depths and thus reflect the effective occulting area of the planet disk. We denote the optical depth for absorption of starlight through the limb of the planet $\tau_t\left(y\right)$, where y is the cylindrical radius from the line of sight to the planet center. In our models we define the transit radius R_p to occur at

$$\tau_t\left(R_p\right) = 1. \tag{2.13}$$

We use a development similar to that in Hansen (2008) to relate the transverse optical depth through the limb to the radial optical depth τ. Integrating along the line of sight through the planet limb, the transverse optical depth for starlight is given by:

$$\begin{aligned} \tau_t\left(y\right) &= 2\gamma\int_y^\infty \frac{\kappa\left(r\right)\rho\left(r\right)}{\sqrt{1-\left(y/r\right)^2}}dr \\ &\approx \gamma\tau_R\sqrt{\frac{2\pi\left(\alpha+1\right)y}{H_P}}e^{-(\alpha+1)(y-R_p)/H_P}. \end{aligned} \tag{2.14}$$

The right-hand side of Equation (2.14) is obtained by recognizing that for $y\sim R_p \gg H_P/\left(\alpha+1\right)$ only values of r with $\left(r-y\right)\ll y$ contribute significantly to the integral due to the exponential decay of the integrand. We obtain exterior boundary condition on τ by combining our model definition of the transit radius (Equation. (2.13)) with Equation (2.14):

$$\tau_R = \frac{1}{\gamma}\sqrt{\frac{H_P}{2\pi\left(\alpha+1\right)R_p}}. \tag{2.15}$$

The boundary condition for pressure follows from τ_R using Equation (2.12).

2.2.4 Model Parameter Space

In this section, we describe our procedure for choosing value ranges for γ, T_0, and T_{eff} that describe the atmospheric absorption, stellar insolation, and the intrinsic luminosity of exoplanets simulated with our model.

The parameter γ in Equation (2.4) denotes the ratio of the gas layer's optical depth to incident starlight over its optical depth to thermal radiation. At large values of γ the starlight is absorbed high in the atmosphere, while at small values of γ the stellar energy penetrates deeper into the atmosphere. We adopt a fiducial value of $\gamma = 1$, but also consider values spanning from 0.1 to 10. In this way, we encompass a wide range of possible absorptive properties in our model H/He envelopes.

In Equation (2.4), $\mu_0 \sigma {T_0}^4$ represents the stellar energy flux absorbed (and reradiated) locally at a given point on the planet's irradiated hemisphere. The stellar insolation impinging on a planet can be calculated with knowledge of the host star's luminosity L_* or spectral class, and of the semimajor axis a of the planet's orbit. The fraction of this energy that is reflected by the planet and how the energy that does get absorbed is distributed around the planet's surface area, however, remain unknown for the super-Earth and hot Neptune planets considered in this paper. Our parameterization of the energy received at the planet from the star is further complicated by the fact that we are using a spherically symmetric planetary model, whereas the effect of stellar insolation varies over the planet surface. We take these uncertainties into account by considering a range of plausible T_0 values for each planet. For our fiducial value, we use the equilibrium temperature of the planet assuming full redistribution and neglecting reflection

$$T_0 = \left(\frac{L_*}{16 \pi \sigma a^2} \right)^{1/4} . \tag{2.16}$$

Similar fiducial choices of T_0 have been made in other studies that used Equation (2.4) to describe the gas layer temperature profiles of low-mass exoplanets (Adams et al., 2008; Miller-Ricci et al., 2009). By considering reflection of starlight by the planet in addition to full redistribution, we set a lower bound on T_0:

$$T_0 = \left(\frac{L_* \left(1 - A\right)}{16 \pi \sigma a^2} \right)^{1/4} , \tag{2.17}$$

where A is the planet's Bond albedo. A plausible upper limit of $A = 0.35$ is chosen; all the solar system planets except Venus have Bond albedos below this value. Finally, to establish an upper limit on T_0 we neglect both redistribution and reflection and take

$$T_0 = \left(\frac{L_*}{4\pi\sigma a^2} \right)^{1/4} . \tag{2.18}$$

This upper bound corresponds to the formal definition of T_0 used by Hansen (2008) to derive Equation (2.4).

A planet's intrinsic luminosity (produced by radiogenic heating and by contraction and cooling after formation) is another important component of the planetary energy budgets. In Equation (2.4), $T_{\rm eff}$ parameterizes the heat flux from the planet interior entering the planet gas layer from below, $F_{int} = \sigma {T_{\rm eff}}^4$. Within the plane-parallel gas layer assumption, we can relate $T_{\rm eff}$ to the intrinsic luminosity, L_{int}, of the planet

$$T_{\rm eff} = \left(\frac{L_{int}}{4\pi\sigma R^2} \right)^{1/4} . \tag{2.19}$$

We require a scheme to constrain the intrinsic luminosities of low-mass exoplanets.

A full evolution calculation, modeling the energy output of a planet as it ages after formation, is outside of the scope of this work. There are many physical effects (including phase separation, chemical differentiation, chemical inhomogeneities, irradiation, radiogenic heating, impacts, geological activity, tidal heating, and evaporation) that can influence the thermal evolution of a planet and flummox attempts to predict a planet's intrinsic luminosity (see Section 2.6.3 for a full discussion). Additionally, the ages of the planet-hosting stars considered here (and of the planets that surround them) are very poorly constrained. This severely limits the insights that a cooling simulation could yield into the planets' intrinsic luminosities. Instead of directly simulating planetary evolution, we take an approximate scaling approach to bracket plausible values for the intrinsic luminosities of low-mass exoplanets.

We use planet evolution tracks modeled by Baraffe et al. (2008) to constrain the intrinsic luminosities of the gas-laden planets considered in this work. Baraffe et al. (2008) modeled the evolution of planets ranging from 10 $M_\oplus$ to 10 $M_{\jupiter}$, having heavy metal enrichments of $Z = 2\%$, 10%, 50%, and 90%, and that were either receiving negligible stellar irradiation or suffering insolation equivalent to that from a sun at 0.045 AU. We limit our consideration to the simulated irradiated planets that are at least 1 Gyr old and that are no more than 1 $M_{♃}$. We then fit the intrinsic luminosities of this sub-sample of Baraffe et al. (2008) models to a simple power law in planetary mass, radius, and age (t_p):

$$\log\left(\frac{L_{int}}{L_{\odot}}\right) = a_1 + a_{M_p}\log\left(\frac{M_p}{M_{\oplus}}\right) + a_{R_p}\log\left(\frac{R_p}{R_{♃}}\right) + a_{t_p}\log\left(\frac{t_p}{1\text{ Gyr}}\right). \quad (2.20)$$

The values obtained for the coefficients and their 95% confidence intervals are $a_1 = -12.46 \pm 0.05$, $a_{M_p} = 1.74 \pm 0.03$, $a_{R_p} = -0.94 \pm 0.09$, and $a_{t_p} = -1.04 \pm 0.04$. The fit had $R^2 = 0.978$ and rms residuals of 0.14 in $\log(L_{int}/L_{\odot})$. For a given planet, we use the measured planetary mass, planetary radius, and host star age (a proxy for the planet age) with the best-fit coefficients in Equation (2.20) to calculate a fiducial value for L_{int}. We then employ the uncertainties in the fit coefficients, the rms residuals, and the range of possible planet ages to establish a nominal range of intrinsic luminosities L_{int} to consider when constraining the interior compositions of planets with gas layers. The poorly constrained planet age dominates the other sources of uncertainties in its contribution to the range of L_{int} for all the planets we consider.

Additional limitations on T_{eff} can be required if the nominal range of L_{int} determined by the procedure above is too broad. At very low values of T_{eff} (low intrinsic luminosities) the gas layer P-T profile can enter an unphysical high-pressure low-temperature regime ($P \gtrsim 2.5 \times 10^{10}$ Pa, $\mathrm{T} \lesssim 3500$ K). These conditions, under which hydrogen may form a Coulomb lattice or a molecular solid, are not included in the coverage of the Saumon et al. (1995) hydrogen EOS. If necessary, we truncate the lower range of T_{eff} values that we consider to avoid exceeding the range of applicability of the Saumon et al. (1995) EOS. Out of all the planets considered in the work, such a reduction in the range of T_{eff} was only required for HAT-P-11b (Section 2.4.4).

Adopting a simple scaling approach to estimate T_{eff} allows us to consider a wider variety of possible interior compositions than we could by simulating full evolution tracks. Nonetheless, our procedure to constrain T_{eff} is very approximate. It estimates the intrinsic luminosity of a planet from its mass, radius, and age alone. The effects of interior composition and stellar irradiation on a planet's evolution are not addressed. For instance, because solar system planets are less strongly irradiated than the transiting planets considered in this work, the scaling relation systematically overestimates their intrinsic luminosities. Further, the extrapolation of the Baraffe et al. (2008) models to super-Earth-sized planets is very uncertain. Although phenomenological, the procedure described above provides a consistent way to estimate a plausible range of intrinsic luminosities in which the span of the range reflects the uncertainties in the planet age and thermal history.

2.2.5 Model validation

We have validated our planet interior model by comparing our results with Earth and other models. Our fiducial Earth-planet composition is one with a 32.6% by mass core consisting of FeS (90% iron and 10% sulfur by mass) and a 67.4% by mass mantle consisting of $Mg_{0.9}Fe_{0.1}SiO_3$. For this composition, our model gives a radius of 6241 km for a 1 $M_\oplus$ planet. This radius value is within 2.2% of Earth's true radius, well within expected observational uncertainties for future discovered Earth-mass, Earth-sized exoplanets. More importantly, our solid planet models are not intended to be accurate for such low masses (Seager et al., 2007), because we ignore thermal pressure. This approximation is much more appropriate for more massive planets, where a larger fraction of the planet's material is at high pressure where thermal effects are small.

We further compared our model output with the results presented in Valencia et al. (2007b). Specifically, we reproduced the values in their Table 3 for GJ 876d's radius under various assumed bulk compositions . We found that for solid planets composed of iron and silicates our radii matched those from Valencia et al. (2007b) to 0.2%. For planets that also included a water layer, our radii were within 1%. This is a very reasonable agreement. The larger discrepancy in the water planet radii as compared to the dry-planet radii stems from differences in the EOS for water. See Seager et al. (2007) for our calculations on the water EOS, and a detailed description of our EOS choices.

We tested our model of planets with significant gas envelopes by comparing to Baraffe et al. (2008) models of hot Neptunes. For planets of 10 and 20 $M_\oplus$ with 10% by mass layer of H_2 and He, we found very good agreement between the model radii. The Baraffe et al. (2008) radii fall within the range of planetary radii derived from our model when uncertainties on the atmospheric thermal profile and energy budget in our model are taken into account. In other words, it is possible to choose values of $T_{\rm eff}$, γ, and T_0 within the ranges described in Section 2.2.4 such that our model radii agree precisely with those from Baraffe et al. (2008). Further, over the full range of atmospheric parameters considered our model radii deviate by no more than 27% from those of Baraffe et al. (2008).

2.3 Ternary and Quaternary Diagrams

In this work, we use ternary and quaternary diagrams to plot the relative contributions of the core, mantle, ice layer, and gas layer to the structure of a differentiated exoplanet. Valencia et al. (2007a) and Zeng & Seager (2008) also employed ternary diagrams to present the interior composition of terrestrial exoplanets, and provide detailed discussions of these three-axis equilateral triangle diagrams. While both Valencia et al. (2007a) and Zeng & Seager (2008) considered three-component planets comprised of a core, a mantle, and water ices, our fiducial model also allows for a gas layer. Three-dimensional tetrahedron quaternary diagrams provide a natural extension of ternary diagrams to four-component systems.

Quaternary diagrams are useful for plotting four-component data (w, x, y, z) that are constrained to have a constant sum ($w + x + y + z = A =$ constant). The axes of a quaternary diagram form a tetrahedron of height A. The four vertices of the diagram represent $w = A$, $x = A$, $y = A$, and $z = A$, while the opposing faces are surfaces on which $w = 0$, $x = 0$, $y = 0$, and $z = 0$, respectively. At each point inside the tetrahedron, the value of w is given by perpendicular distance to the $w = 0$ face, and the values of the other components are defined analogously. Equilateral tetrahedrons have the property that the sum of the distances from any interior point to each of the four faces equals the height of the tetrahedron A. We are thus assured that $w + x + y + z = A$ is satisfied at every point within the quaternary diagram.

We use quaternary diagrams to plot all the possible ways a planet of mass M_p and radius R_p can be partitioned into the four layers of our fiducial model described in Section 2.2. In this case, the four-component data that we are plotting in the diagram are the fractions of the mass of the planet in each of the four interior layers $\left(x_{core}, x_{mantle}, x_{\mathrm{H_2O}}, x_{\mathrm{H/He}}\right)$, which are constrained to sum to unity. The summits of the tetrahedron represent extreme cases in which the planet is 100% iron, 100% silicates, 100% water ices, or 100% H/He. The face opposite the H/He summit turns out to be a ternary diagram for the gas-less interior compositions of the planet.

2.4 Results

Our eventual aim is to draw robust conclusions about the composition of a low-mass exoplanet by fully exploring and quantifying the associated uncertainties. There is an inherent degeneracy in the planetary compositions that can be inferred from planet mass and radius measurements alone; for a specified planet mass, many different distributions of matter within the planet interior layers can produce identical radii. In planet interior models incorporating N distinct chemical layers, specifying a planet mass and radius each impose a constraint on the layer masses, leaving $(N - 2)$ degrees of freedom in the allowed compositions $\{x_i\}$. Further compositional uncertainties may be introduced if the planetary energy budget or chemical makeup are not well known and if significant measurement uncertainties are present in observationally derived parameters.

In this work, we examine the constraints that can be placed on a transiting exoplanet's interior using only structural models for the planet. By not employing planet formation arguments to impose further constrain the planetary compositions, our results remain largely independent of planet formation theories. In this section, we apply our interior structure model to examine the possible compositions of several example planets: CoRoT-7b, GJ 581d, GJ 436b, and HAT-P-11b.

2.4.1 CoRoT-7b

The recent discovery of the first transiting super-Earth, CoRoT-7b, has ushered in a new era of exoplanet science (Léger et al., 2009). CoRoT-7b is on a 0.85359 ± 0.00005 day period around a bright $V = 11.7$ G9V star. The host star is very active which complicates measurement of the transiting planet's mass and radius. By forcing the stellar radius to be $R_* = (0.87 \pm 0.04)\ R_\odot$, a planetary radius of $R_p = (1.68 \pm 0.09)\ R_\oplus$ is derived from the transit depth (Léger et al., 2009). The planetary nature of CoRoT-7b has recently been confirmed by Doppler measurements revealing a planetary mass of $M_p = (4.8 \pm 0.8)\ M_\oplus$ (Queloz et al., 2009). For the very first time, both the mass and radius of a super-Earth sized exoplanet have been measured, thereby offering the first hints about the interior composition of a planet in the mass range between Earth and Neptune.

In this section we do not consider the possibility that CoRoT-7b could harbor a gas layer or a significant water ocean. With an orbital semimajor axis of $a = (0.0172 \pm 0.00029)$ AU (about four stellar radii), CoRoT-7b is receiving an extreme amount of stellar irradiation. CoRoT-7b is most likely tidally locked, with a temperature of up to 2560 ± 125 K at the sub-stellar point assuming an albedo of $A = 0$ and no energy redistribution (Léger et al., 2009). Limits on the lifetime of a gas layer or a water ocean under such extreme radiation are discussed in Section 2.6. We focus here on what we can learn about the composition of CoRoT-7b if it is a purely dry, gas-less telluric planet. Valencia et al. (2010) offer another point of view, considering the possibility of an H/He or vapor atmosphere on CoRoT-7b.

We first examine the interior composition of COROT-7b under the assumption of an iron core and a mantle composed of silicate perovskite ($Mg_{0.9}Fe_{0.1}SiO_3$, approximately similar to Earth's mantle). When considering only two compositional layers, the measured mass and radius uniquely determine the two layer masses. The core mass fraction as a function of planet radius for CoRoT-7b is displayed in Figure 2-1. The solid black line denotes the fraction of CoRoT-7b's mass in its iron core assuming the fiducial planetary mass $M_p = 4.8\ M_\oplus$, while the red, yellow and blue shaded regions delimit the 1 σ, 2 σ, and 3 σ error bars on M_p respectively. The measured planet radius and its 1 σ error bars are denoted by the dashed and dotted black vertical lines, respectively. An Earth-like composition, having 30% of its mass in an iron core and the remaining 70% of its mass in a silicate mantle, is consistent with the measured mass and radius for CoRoT-7b within 1 σ. If the CoRoT-7b core is not pure iron but also contains a light element, the core mass fraction at a specified planetary radius will be larger. Including 10% sulfur by mass in the iron core EOS increases the CoRoT-7b radius by 0.08 $R_\oplus$ at a core mass fraction of 1 (at the top of Figure 2-1), while having no effect on the radius at a core mass fraction of 0 (at the bottom of Figure 2-1).

Our interior structure model can strengthen the observational constraints on CoRoT-7b's mass and radius. With the assumption that CoRoT-7b does not have a significant water or gas layer, some of the mass-radius pairs within $M_p \pm 1\sigma_M$ and $R_p \pm 1\sigma_R$ (including the fiducial 0 σ mass-radius pair) can be ruled out because they correspond to bulk densities lower than a pure silicate planet. These excluded mass-radius pairs would necessitate water (or some other component lighter than perovskite) in their composition. The fact that some 1σ CoRoT-7b mass-radius pairs are excluded can be seen from Figure 2-1, where the red band denoting planetary masses within 1 σ of the measured value never fully crosses the $R_p + 1\sigma_R$ dotted line even at a 100% perovskite composition. While most of this work is devoted to constraining a planet's interior structure from mass and radius measurements, this is an example of how limits on a planet's interior structure could be used to improve our constraints on a planet's mass and radius.

The amount of iron in a exoplanetary mantle is not known. Earth's mantle has about 10% iron and 90% Mg by number fraction ($Mg_{0.9}Fe_{0.1}SiO_3$), but exoplanets may have varying amounts. Elkins-Tanton & Seager (2008a) describe an extreme example of a coreless terrestrial planet in which all of the planet's iron is mixed in the mantle instead of sequestered in the core. To explore the effect of varying the mantle iron fraction we present a ternary diagram in Figure 2-2 that shows the tradeoff between the mass of iron in the mantle compared to the mass of iron in the core. The fractions of the planet's mass in the Fe core, in $MgSiO_3$ and in $FeSiO_3$ are plotted on the three

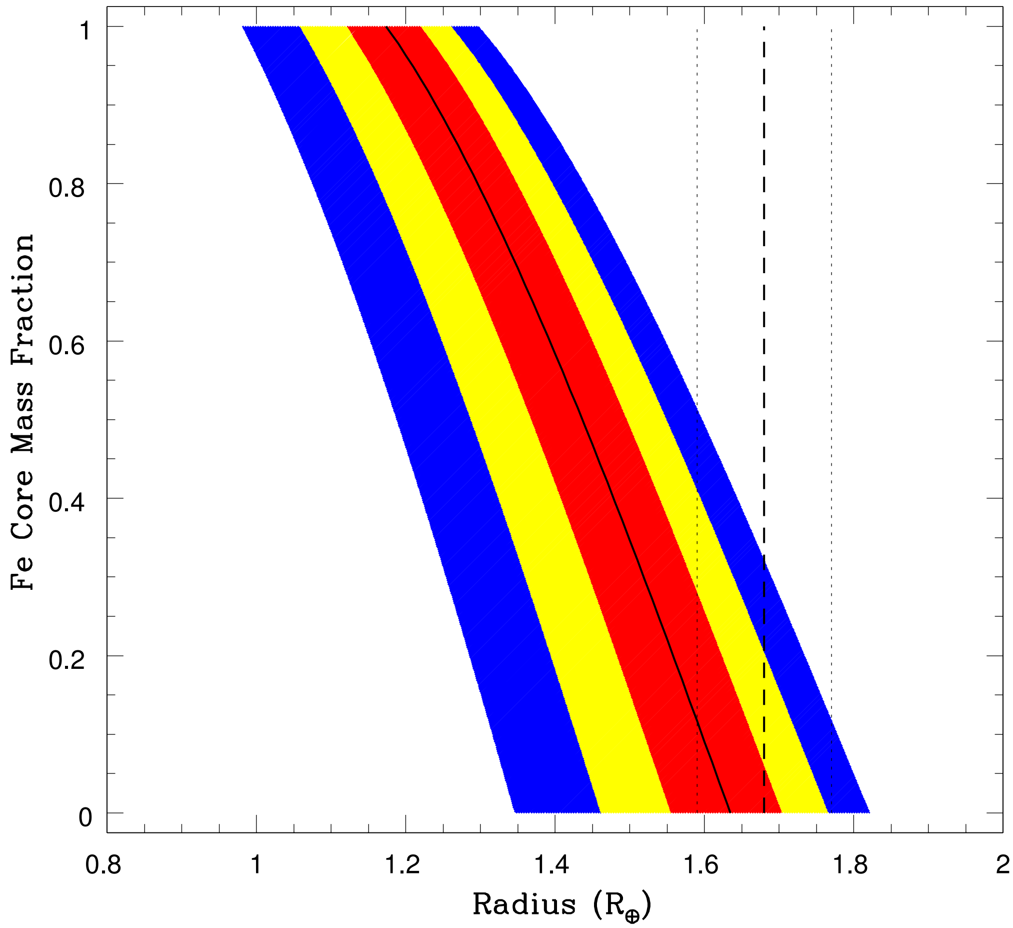

Figure 2-1: CoRoT-7b core mass fraction as a function of planetary radius. The planetary mass is $(4.8 \pm 0.8)\ M_\oplus$. We neglect the possible presence of water or a gas layer and consider a two-layer planet comprised of a pure iron core surrounded by a $Mg_{0.9}Fe_{0.1}SiO_3$ mantle. The red, yellow and blue shaded regions denote the core mass fractions obtained when varying the CoRoT-7b mass within its 1 σ, 2 σ, and 3 σ error bars, respectively. The black vertical lines delimit the measured radius $R = (1.68 \pm 0.09)\ R_\oplus$ (dashed) and its 1 σ error bar (dotted).

axes. $MgSiO_3$ and $FeSiO_3$ are mixed together in the mantle as $Mg_{1-\chi}Fe_{\chi}SiO_3$, where χ is the number fraction of $FeSiO_3$. The red, yellow and blue shaded regions denote interior compositions that are consistent with the measured planetary mass and radius to within 1 σ, 2 σ, and 3 σ of the observational uncertainties respectively. All the ternary diagram except the high Fe corner ($x_{\mathrm{Fe}} \gtrsim 0.76 - 0.86$) is shaded to within 3 σ. Because $FeSiO_3$ and $MgSiO_3$ have similar densities (compared to the density contrast between pure Fe and perovskite), we have very little ability to discriminate the iron content of the mantle from a mass and radius measurement alone. Nonetheless, χ contributes to the uncertainty in the core mass fraction of CoRoT-7b.

2.4.2 GJ 581d

We now consider the super-Earth exoplanets that are large and cool enough that they might retain a small hydrogen-helium gas layer. As an example we use GJ 581d, a $M_p \sin i = 7.09\ M_{\oplus}$ super-Earth with a semimajor axis $a = 0.22$ AU that is part of a multi-planet system around an $L = 0.013\ L_{\odot}$ M3 dwarf star (Udry et al., 2007; Mayor et al., 2009b). GJ 581 is estimated to be 8^{+3}_{-1} Gyr old[2]. The radius of GJ 581d has not yet been measured. In this section, we adopt the minimum mass for GJ 581d and consider two different possible planetary radii: $R_p = 1.5$ and 2.0 $R_{\oplus}$. While these values may not represent the properties of the true GJ 581d planet, we use them to illustrate how the possible presence of a gas layer and observational uncertainties will affect our ability to make inferences about the interior composition of transiting super-Earths.

The two putative planetary radii considered for GJ 581d lead to interior compositions having very different characteristics. Ternary diagrams assuming a radius of $R_p = 1.5$ and 2.0 $R_{\oplus}$ for GJ 581d are displayed in Figures 2-3(a) and (b), respectively. The leftmost black curve in each diagram represents the locus of possible gas-less compositions for the stipulated mass and radius. The $R_p = 1.5\ R_{\oplus}$ planet is very dense and iron-rich; it could have a Mercury-like composition with 68% of its mass in an iron core enveloped by a silicate mantle accounting for the remaining 32% of the

---

[2] `exoplanet.eu`

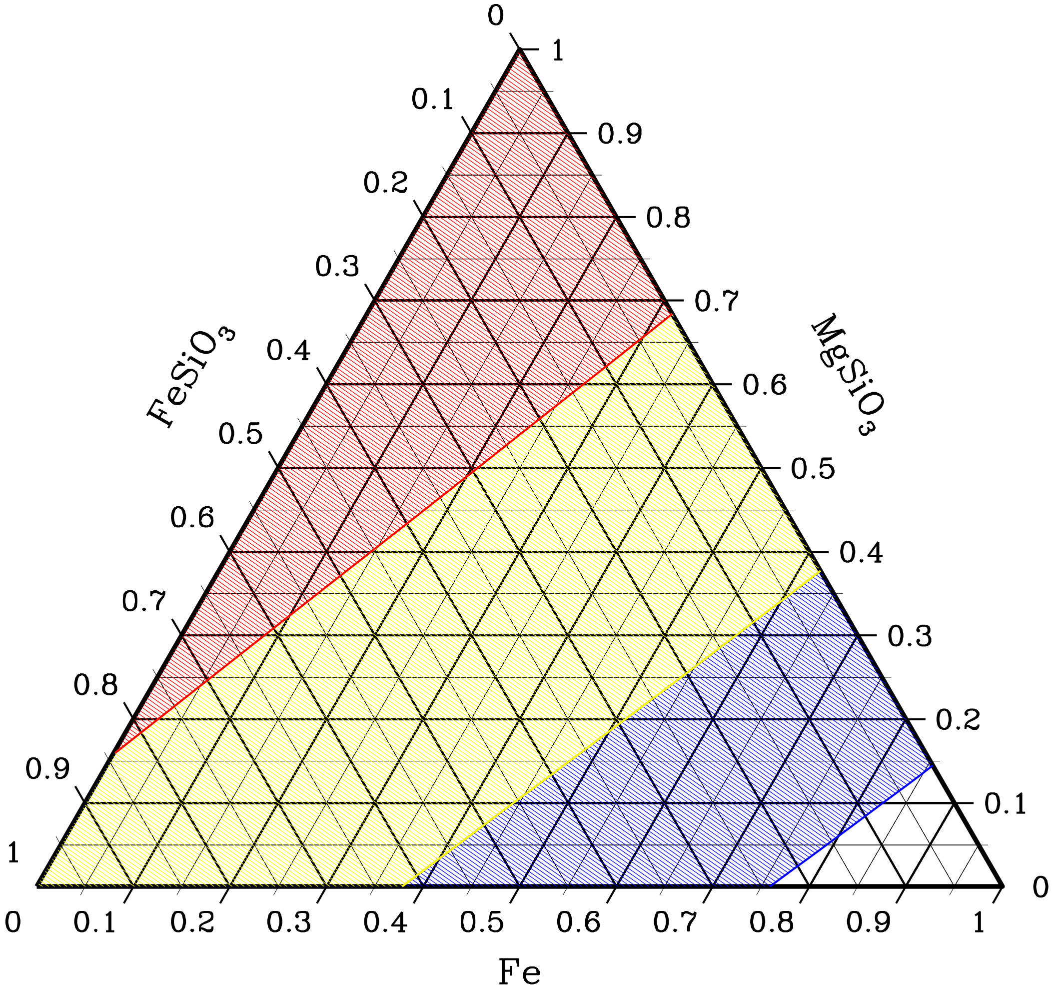

Figure 2-2: CoRoT-7b ternary diagram. Plausible compositions for CoRoT-7b are shown, provided the planet has no interior water and no H/He layer. The fractions of the planet's mass in the Fe core, in $MgSiO_3$, and in $FeSiO_3$ are plotted on the three axes. $MgSiO_3$ and $FeSiO_3$ are mixed together in the mantle as $Mg_{1-\chi}Fe_{\chi}SiO_3$.

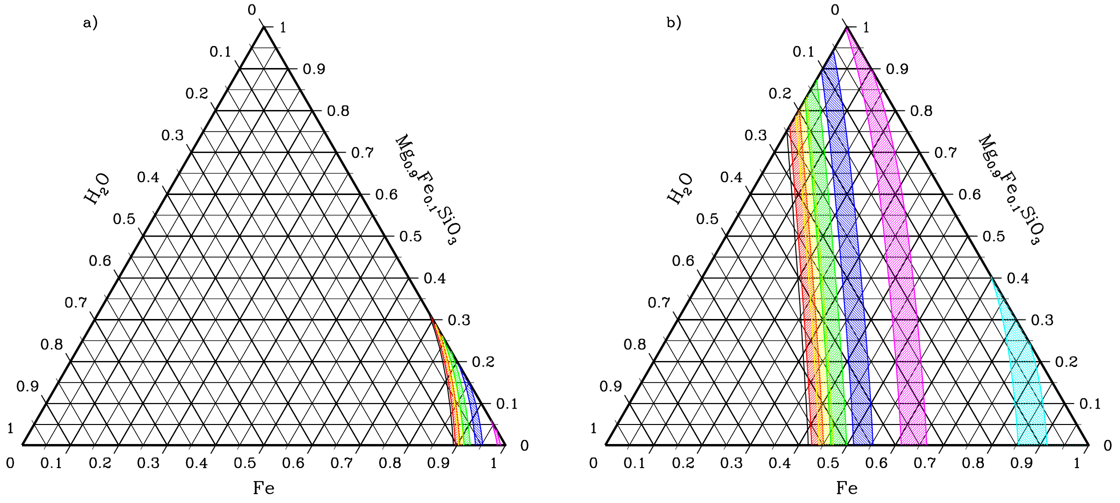

Figure 2-3: Ternary diagram for the solid core of GJ 581d. The GJ 581d minimum mass $M_p = 7.09\ M_\oplus$ is assumed. Each diagram represents a different possible planetary radius: (a) $R_p = 1.5R_\oplus$, and (b) $R_p = 2.0R_\oplus$. The relative contributions of the iron core, $Mg_{0.9}Fe_{0.1}SiO_3$ mantle, and H_2O ices to the mass of the solid planet bulk are plotted. The leftmost black curve represents the locus of gas-less compositions, and gas mass fraction increases to the right toward the Fe vertex. The different colored bands designate various gas mass fractions $\left(x_{H/He}\right)$: 10^{-7} (red), 10^{-6} (yellow), 10^{-5} (green), 10^{-4} (blue), 10^{-3} (magenta), and 10^{-2} (cyan). For reference, the Earth's gas mass fraction is about 10^{-6} and Venus' is about 10^{-4}. The width of each of the colored bands is produced by varying the atmospheric parameters within the ranges $\gamma = 0.1 - 10$, $T_0 = 181 - 285$, and $T_{\rm eff} = 73 - 93$ ($R_p = 1.5R_\oplus$) or $T_{\rm eff} = 59 - 75$ ($R_p = 2.0R_\oplus$) .

mass. In contrast, possible gas-less compositions for $R_p = 2.0\ R_\oplus$ are all icy planets with 25%-58% H_2O by mass.

In Figure 2-3, each colored band designates a different gas mass fraction. For non-zero gas mass fractions (x_{gas}), the relative contributions of the iron core, $Mg_{0.9}Fe_{0.1}SiO_3$ mantle, and H_2O ices to the solid interior (inner three layers) of GJ 581d are plotted; effectively, the fraction of the planet mass in each of the solid layers is re-normalized by $\left(1 - x_{\mathrm{H/He}}\right)$. The non-zero width of the gas mass fraction bands in the ternary diagrams is due to the uncertainty in the atmospheric P-T profile. Following the scheme described in Section 2.2.4, we consider $\gamma = 0.1 - 10$, $T_0 = 181 - 285$, $T_{\mathrm{eff}} = 73 - 93$ for $R_p = 1.5 R_\oplus$, and $T_{\mathrm{eff}} = 59 - 75$ for $R_p = 2.0 R_\oplus$.

Allowing for the presence of a gas layer on GJ 581d significantly increases the range of interior compositions that can produce the stipulated mass and radius. The more gas GJ 581d contains, the higher the average density of the inner three layers must be to still satisfy the planetary mass and radius constraints. More gas results in an increase in the proportion of iron, as manifested in the ternary diagram (Figure 2-3) by the fact that the gas mass fraction increases to the right toward the Fe vertex. An upper limit on the mass of gas that GJ 581d can support is reached if the planet has no H_2O or silicates but consists solely of H/He enveloping an iron core (a composition corresponding to the iron vertex, Figure 2-3). This H/He mass upper limit occurs at $0.12\% - 0.19\%$ for $R_p = 1.5\ R_\oplus$ and at $1.7\% - 2.2\%$ for $R_p = 2.0\ R_\oplus$. These limits consider only the constraints imposed by the planetary mass and radius and not the lifetime of the gas layer to atmospheric escape. Having a gas layer contribute 10^{-5} of the mass of GJ 581d (for comparison the Earth's atmosphere is about 10^{-6} of an Earth mass) increases the minimum iron core mass fraction for a $R_p = 1.5\ R_\oplus$ planet from the 68% gas-less value to $74\% - 78\%$ and decreases the minimum H_2O mass fraction for a $R_p = 2.0\ R_\oplus$ planet from the 25% gas-less value to $13\% - 17\%$. Although a gas layer on GJ 581d can make at most a small contribution to the planetary mass, it can nonetheless have a very important effect on the allowed proportions of the inner three layers and on our ability to infer the planet's interior composition.

So far we have only considered the inherent uncertainty in the composition of

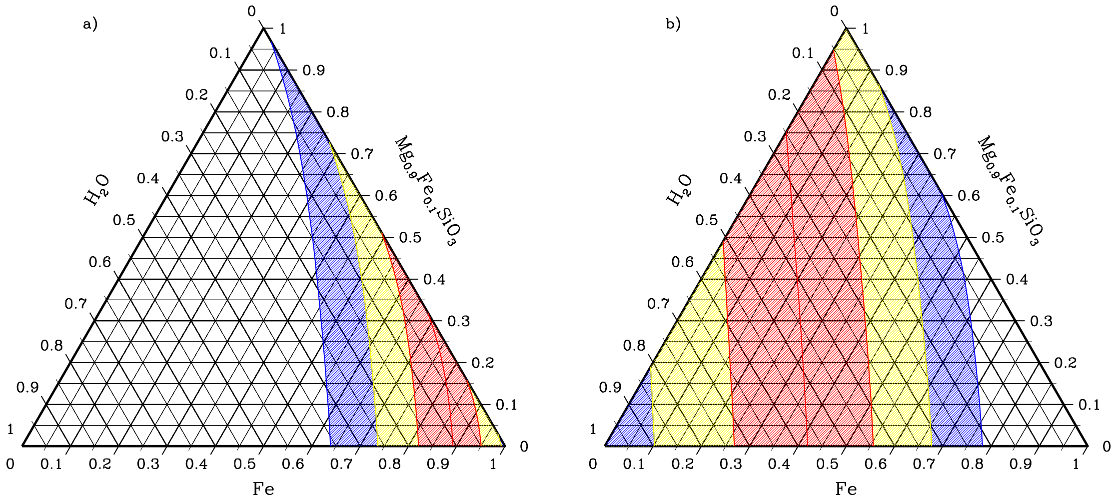

Figure 2-4: Ternary diagram displaying plausible gas-less compositions for GJ 581d. An observational uncertainty of 5% is included on both the assumed mass ($M_p = 7.09\ M_\oplus$) and the assumed radii. Each diagram represents a different possible planetary radius: (a) $R_p = 1.5 R_\oplus$, and (b) $R_p = 2.0 R_\oplus$. The red, yellow, and blue shaded regions denote compositions that are consistent with M_p and R_p to within 1 σ, 2 σ, and 3 σ, respectively.

GJ 581d that could be inferred from a planetary mass and radius. In practice, observational uncertainties also impact our ability to constrain the interior composition of a transiting super-Earth. For illustration purposes, we consider the same two putative GJ 581d mass-radius pairs, and assume an optimistic but plausible uncertainty of 5% on both the planetary mass and radius. Ternary diagrams plotting gas-less compositions consistent with the planet mass and radius to within 1 σ, 2 σ, and 3 σ are shown in Figure 2-4(a) for $R_p = 1.5 R_\oplus$ and Figure 2-4(b) for $R_p = 2.0 R_\oplus$. If compositions including gas layers were included in Figure 2-4, the shaded $n\ \sigma$ regions would all be smeared out to the right and extended to the Fe vertex.

Even neglecting the effect of a possible gas layer, the interior composition of GJ 581d is far better constrained for a radius of $R_p = (1.5 \pm 5\%)\, R_\oplus$ (Figure 2-4(a)) than it is for $R_p = (2.0 \pm 5\%)\, R_\oplus$ (Figure 2-4(b)). The superior compositional constraints attained at the smaller planetary radius are a consequence of two effects. First, the $R_p = 1.5 R_\oplus$ planet has a lower inherent compositional degeneracy for its fiducial (0 σ) mass and radius. The $R_p = 1.5\ R_\oplus$ planet is dense enough that it must contain a large amount of iron, while the $R_p = 2.0\ R_\oplus$ has a more intermediate density and could be assembled from a wider range of combinations of iron, silicates, and water. This can be seen from the ternary diagrams (Figure 2-4) in which the line representing the gas-less compositions for ($M_p = 7.09\ M_\oplus$, $R_p = 1.5R_\oplus$) is much shorter than the line representing the possible gas-less compositions for ($M_p = 7.09\ M_\oplus$, $R_p = 2.0R_\oplus$). Second, the separation in the 1 σ, 2 σ, and 3 σ contours of the ternary diagram are much wider in the case of $R_p = 2.0R_\oplus$ in Figure 2-4(b) than they are for $R_p = 1.5R_\oplus$ in Figure 2-4(a). The relative uncertainty on the average planet density $\bar{\rho}$ is identical (to first order) for both GJ 581d radii considered $\left(\Delta\bar{\rho}/\bar{\rho} \approx \sqrt{(\Delta M/M)^2 + (3\Delta R/R)^2} = 16\%\right)$, while the spacings between iso-mass and radius curves on the ternary diagram are roughly proportional to $\propto \Delta\bar{\rho}/\bar{\rho}^2$ (Zeng & Seager, 2008). Thus, the separation in the 1 σ, 2 σ, and 3 σ contours of the ternary diagram increases with decreasing planetary density. This example illustrates how our ability to constrain the interior composition of a transiting super-Earth depends not only on the precision of our measurements, but also on the true mass and radius of the planet. For a given relative uncertainty on the average planet density, the composition can be best constrained for very dense planets (near the Fe vertex).

2.4.3 GJ 436b

GJ 436b, a hot Neptune orbiting a nearby M star (Butler et al., 2004; Maness et al., 2007), was the first known transiting intermediate-mass planet. Since GJ 436b was found to transit its star by Gillon et al. (2007b), substantial efforts have been made to measure its mass and radius using photometric data from *the Spitzer Space Telescope* (Deming et al., 2007; Gillon et al., 2007a), from *the Hubble Space Telescope* (Bean et al., 2008), and from further ground-based observations (e.g. Shporer et al., 2009). Here, we adopt values for the properties of GJ 436b and its host star given by Torres (2007) and Torres et al. (2008), who employed a weighted average of light-curve parameters from ground-based (Gillon et al., 2007b) and *Spitzer* studies (Deming et al., 2007; Gillon et al., 2007a): $L_* = 0.0260^{+0.0014}_{-0.0017}\ L_\odot$, $M_p = 23.17 \pm 0.79 M_\oplus$, $R_p = 4.22^{+0.09}_{-0.10} R_\oplus$,

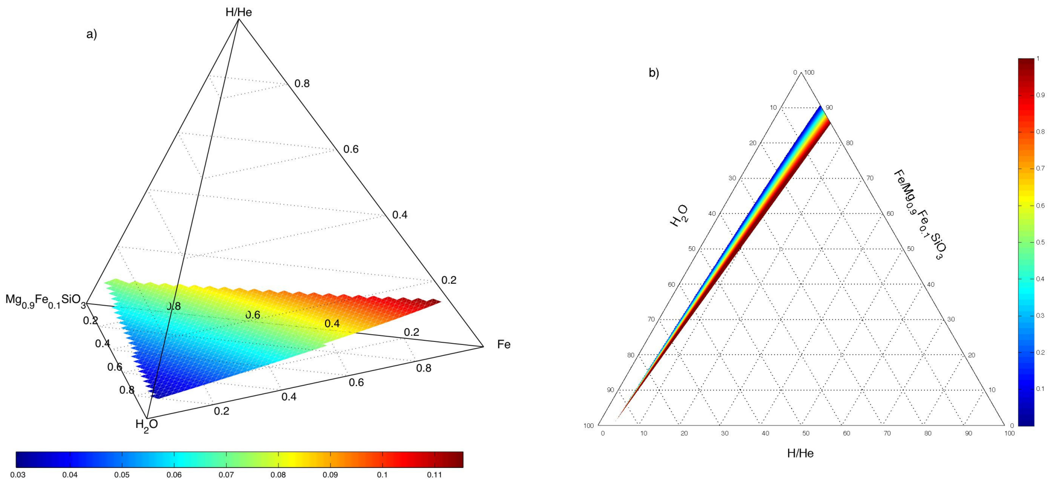

Figure 2-5: Fiducial GJ 436b quaternary and ternary diagrams. The allowed compositions of GJ 436b for our fiducial choice of structural and atmospheric parameters ($M_p = 23.17 M_\oplus$, $R_p = 4.22 R_\oplus$, $T_0 = 663$ K, $T_{\rm eff} = 70$ K, $\gamma = 1$) are shown. In panel (a) we show a three-dimensional quaternary diagram plotting the fraction of the planet's mass in the iron core, $Mg_{0.9}Fe_{0.1}SiO_3$ mantle, water ices, and H/He gas layer. The surface is colored according to the fraction of the mass of the planet found in the gas layer. Panel (b) displays the same data as (a) in a two-dimensional ternary diagram. In panel (b) the core and mantle are combined together on a single axis, with the vertical distance from the upper vertex determined by the fraction of the planet's mass in the two innermost planet layers. The color shading denotes the relative contribution of the core to the total mass in the inner two layers. The width of the shaded wedge of allowed compositions is due to varying the ratio of Fe to $Mg_{0.9}Fe_{0.1}SiO_3$: the blue edge of the allowed compositions represents planets having no Fe, while the red edge represents planets lacking $Mg_{0.9}Fe_{0.1}SiO_3$.

and $a = 0.02872^{+0.00029}_{-0.00026}$ AU.

The measured mass and radius of GJ 436b constrain its bulk interior composition. Allowed compositions for our fiducial planetary parameters ($M_p = 23.17 M_\oplus$, $R_p = 4.22 R_\oplus$, $T_0 = 663$ K, $T_{\rm eff} = 70$ K, $\gamma = 1$) are displayed in Figure 2-5. For our fiducial set of GJ 436b model parameters, the allowed compositions form a two-dimensional surface in the quaternary diagram (Figure 2-5(a)). This illustrates the inherent compositional degeneracy originating from an underconstrained interior model; the measured mass and radius place only two constraints on the masses in each of the four interior layers. When uncertainties in the model parameters are considered, the surface of allowed compositions gains some thickness and spreads into a volume, weakening the constraints that can be placed on GJ 436b's composition (Figure 2-6). Not all of the quaternary diagram is filled, however, even when both observational and model uncertainties are taken into account. Some interior compositions (specifically those outside the red surfaces in Figure 2-6) can thus be ruled out for GJ 436b.

GJ 436b can support a range of gas mass fractions, but must have some gas. For our fiducial parameter choices, GJ 436b could be between 3.6% and 14.5% gas by mass. The gas mass fraction needed to produce the observed transit depth depends on the composition of the planet's solid core: water worlds with large ice layers fall near the minimum gas mass fraction (3.6%), while dry planets with iron-rich cores require up to 14.5% gas. The tradeoff between H/He and water contents is illustrated in Figure 2-5(b), in which the iron core and perovskite mantle are combined together on one axis to form a ternary diagram from the data presented in Figure 2-5(a). In Figure 2-5(b), the shaded wedge of allowed compositions slopes from near the pure H_2O vertex toward increasing H/He and the opposite 0% water edge. Because the allowed compositions span almost the entire H_2O axis (from 0% to 96.4%), the mass fraction of water on GJ 436b is poorly constrained by the measured mass and radius alone.

The range of gas mass fractions that can be supported by GJ 436b strongly depends on the internal heat flux as parameterized by T_{eff}. At higher temperatures, the gas layer is less dense and both the minimum and maximum gas mass fractions decrease, while at lower temperatures the gas layer is more dense and the gas mass fraction extremes both increase. For instance, at $T_{\mathrm{eff}} = 113$ K allowed gas mass fractions range from 2.3% to 11.7%, while at $T_{\mathrm{eff}} = 58$ K GJ 436b must be between 4.2% and 15.5% gas by mass. Figure 2-7 plots the gas mass fraction of GJ 436b as a function of T_{eff} for various interior compositions (with all parameters other than T_{eff} fixed at their fiducial values). Using the formalism described in Section2.2.4, we estimate $T_{\mathrm{eff}} = 70^{+43}_{-12}$ K for a planet age of 6^{+4}_{-5} Gyr; the age of the GJ 436 solar system is essentially unconstrained by observations since GJ 436 is unevolved on the main sequence (Torres, 2007). Any constraints placed on the interior composition of

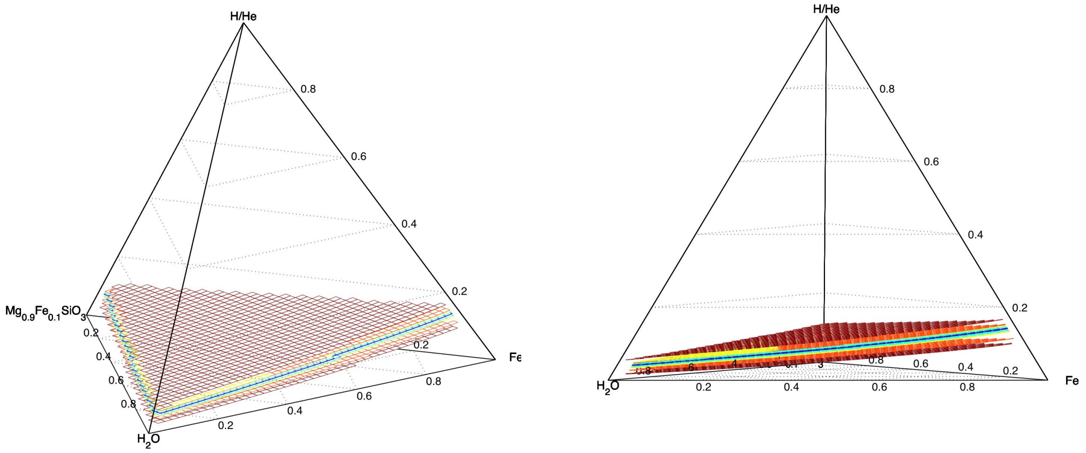

Figure 2-6: GJ 436b quaternary diagram. Both model and observational uncertainties are taken into account to determine the plausible interior compositions of GJ 436b in this diagram. Two different views of the same quaternary diagram are shown. The surface of allowed compositions for our fiducial choice of model parameters ($M_p = 23.17M_\oplus$, $R_p = 4.22R_\oplus$, $T_0 = 663$ K, $T_{\rm eff} = 70$ K, $\gamma = 1$) is displayed in navy blue; this surface is the same as displayed in the quaternary diagram in Figure 2-5(a). To explore how uncertainties in model parameters weaken the constraints that can be placed on GJ 436b's interior composition, we vary each model parameter in turn while keeping all others fixed at their fiducial values. Two surfaces of the same color delimit the volume of composition space that is consistent with the range of values examined for each parameter. We consider $\gamma = 0.1 - 10$ (cyan), $T_0 = 937 - 595$ K (green), and $T_{\rm eff} = 58 - 113$ K (orange). The yellow surfaces denote the effect of varying the planet mass and radius within their 1σ observational uncertainties while maintaining all other model parameters at their fiducial values. Finally, the red surfaces delimit the full volume of possible compositions obtained by varying all parameters within the ranges described above.

GJ 436b will be sensitive to assumptions made about the intrinsic luminosity of the planet.

Out of all the atmospheric parameters in our model, uncertainties in T_{eff} have the most important effect on limiting the compositional constraints that can be placed on GJ 436b. In Figure 2-6, we explore the effect each model parameter has on the volume of allowed compositions while keeping all other parameters fixed at their fiducial values. Varying T_{eff} from 58 to 113 K expands the space of allowed GJ 436b compositions far more than varying $T_0 = 595 - 937$ K or $\gamma = 0.1 - 10$. The relative importance of the T_{eff} parameter was not unexpected. The intrinsic luminosity determines the asymptotic behavior of the Hansen (2008) temperature profile in the radiative regime at larger optical depths ($\tau \gtrsim (T_0/T_{\text{eff}})^4$). While γ and T_0 affect the temperature profile in the outer low-density low-optical-depth region of the gas layer, the intrinsic luminosity T_{eff} dominates in the higher density inner regions of the radiative gas layer. As a result, T_{eff} affects a larger component of the gas layer mass and exerts a larger influence on the transition to a convective gas layer and the entropy of the interior adiabat. Adams et al. (2008) also used the temperature profile from Hansen (2008) and similarly found that T_{eff} had the largest effect on their simulated planet radii.

Observational uncertainties dominate most of the model uncertainties discussed above. The 1σ observational uncertainties on mass and radius are second only to the uncertainty in the planetary internal heat flux T_{eff} in their effect on our ability to constrain the interior composition of GJ 436b. This is evident from Figure 2-6 by comparing the yellow surfaces delimiting the volume of compositions obtained by varying the GJ 436b mass and radius within their 1σ error bars and the orange surfaces denoting the effect of uncertainties in T_{eff}. In this case, he range of plausible T_{eff} would have to be constrained to better than about 20% of its fiducial value before the observational uncertainties in the planet radius would dominate the thickness of the volume of allowed compositions. More theoretical work is required to model the cooling and internal heat flux of hot Neptunes and super-Earths harboring significant gas layers. Until progress is made in constraining T_{eff}, improvements in the observational uncertainties on the GJ 436b mass and radius will not translate into substantial

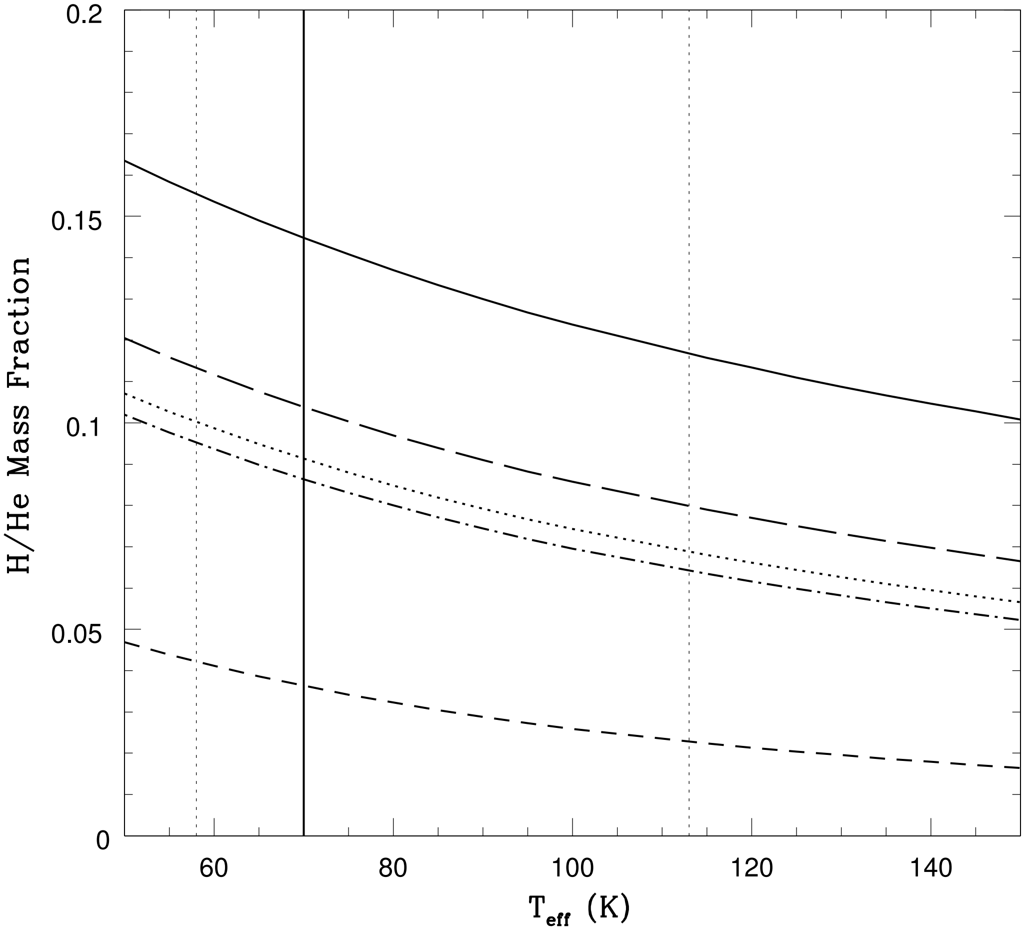

Figure 2-7: Gas mass fraction of GJ 436b as a function of $T_{\rm eff}$. All parameters other than $T_{\rm eff}$ (including M_p, R_p, T_0, and γ) are fixed at their fiducial values. Curves for different end member compositions of the solid bulk of GJ 436b below the H/He layer are displayed: pure iron (solid), pure perovskite $\rm Mg_{0.9}Fe_{0.1}SiO_3$ (dotted), pure water (short dashed), 25% iron 75% perovskite (long dashed), and 25% iron 50% perovskite 25% water (dot-dashed). The solid vertical line denotes the fiducial value of $T_{\rm eff} = 70$ K, while the vertical dotted lines delimit the range of $T_{\rm eff}$ values considered (58-1130 K).

improvements in our ability to constrain the GJ 436b interior composition.

2.4.4 HAT-P-11b

HAT-P-11b is the first hot Neptune to be discovered by transit searches (Bakos et al., 2010). HAT-P-11b existence has since been confirmed by Dittmann et al. (2009). Orbiting at $a = 0.0530^{+0.0002}_{-0.0008}$ AU from a K4 dwarf start with $T_{\mathrm{eff}*} = 4780 \pm 50$ K, HAT-P-11b is similar to GJ 436b in mass and radius: $M_p = 25.8 \pm 2.9 M_\oplus$ and $R_p = 4.73 \pm 0.16 R_\oplus$ (Bakos et al., 2010). Its host star is HAT-P-11 is $6.5^{+5.9}_{-4.1}$ Gyr old (Bakos et al., 2010), as determined from Yale-Yonsei isochrones (Yi et al., 2001). To date, HAT-P-11b and GJ 436b are the only known transiting hot Neptunes.

Plausible interior compositions of HAT-P-11b are plotted in Figure 2-8. Figure 2-8 displays the surface of allowed HAT-P-11b compositions for the fiducial parameter set ($M_p = 25.8 M_\oplus$, $R_p = 4.73 R_\oplus$, $T_0 = 867$ K, $T_{\mathrm{eff}} = 66$ K, $\gamma = 1$), and also shows the effect of considering a range of values for each model parameter. The range of values employed for each parameter ($\gamma = 0.1 - 10$, $T_0 = 778 - 1227$ K, $T_{\mathrm{eff}} = 58 - 86$ K) was determined following the procedure described in Section 2.2.4. The lower limit on the range of T_{eff} values considered had to be truncated at 58 K to avoid having the gas-layer P-T profile enter an unphysical regime at high pressure and low temperatures (see Section 2.2.4). As for GJ 436b, uncertainties in the intrinsic luminosity of HAT-P-11b have an effect comparable to the 1 σ observational uncertainties, and significantly weaken the constraints we can place on the planet's interior composition.

We now attempt to compare the allowed compositions of HAT P-11 (Figure 2-8) and GJ 436b (Figure 2-6). At $\rho_p = 1.33 \pm 0.20$ g cm^{-3} (Bakos et al., 2010), HAT P-11b is less dense than GJ 436b ($\rho_p = 1.69^{+0.14}_{-0.12}$ g cm^{-3} Torres et al., 2008). HAT P-11 could thus support a more massive gas layer (up to 19.0%), and has a larger minimum gas mass fraction (7.1%) for our fiducial choice of parameters. The effect of the average planet density on the gas layer constraints is partially mitigated by the higher level of stellar insolation received by HAT P-11b. When both 1 σ observational and model uncertainties are taken into account, the allowed compositions for HAT-P-11b and GJ 436b overlap; it is plausible that HAT-P-11b and GJ 436b could both have the

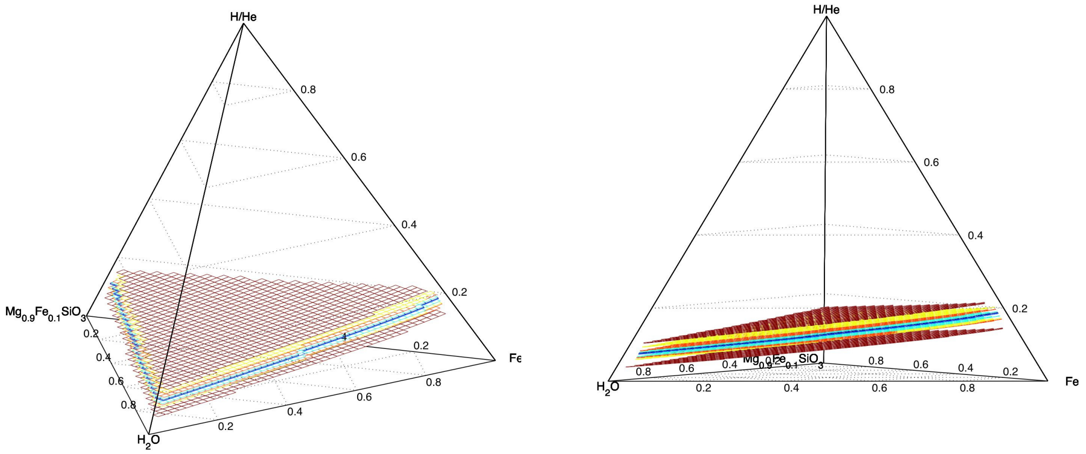

Figure 2-8: Quaternary diagram for HAT-P-11b. Both model and observational uncertainties are taken into account to determine the plausible interior compositions of HAT-P-11b in this diagram. Two different views of the same quaternary diagram are shown. The surface of allowed compositions for our fiducial choice of model parameters ($M_p = 25.8 M_\oplus$, $R_p = 4.73 R_\oplus$, $T_0 = 867$ K, $T_{\text{eff}} = 66$ K, $\gamma = 1$) is displayed in navy blue. To explore how uncertainties in model parameters weaken the constraints that can be placed on GJ 436b's interior composition, we vary each model parameter in turn while keeping all others fixed at their fiducial values. Two surfaces of the same color delimit the volume of composition space that is consistent with the range of values examined for each parameter. We consider $\gamma = 0.1 - 10$ (cyan), $T_0 = 778 - 1227$ K (green), and $T_{\text{eff}} = 58 - 86$ K (orange). The yellow surfaces denote the effect of varying the planet mass and radius within their 1σ observational uncertainties while maintaining all other model parameters at their fiducial values. Finally, the red surfaces delimit the full volume of possible compositions obtained by varying all parameters within the ranges described above. This figure is the HAT-P-11b analog to Figure 2-6 for GJ 436b.

same proportion of core, mantle, water ices, and H/He gas layer.

Our comparison between the possible interior compositions of GJ 436b and HAT-P-11b is fraught with complications and should be interpreted with caution. Our conclusions contrasting the possible interior compositions of GJ 436b and HAT-P-11b are dependent on the method used to constrain the intrinsic luminosity of the hot Neptunes (see Section 2.2.4). Our constraints on the planets' internal heat flux are admittedly rough and do not take into account the influence that two different levels of stellar irradiation could have on the luminosity evolution of these two planets. In addition, significant scatter in the observationally determined planetary masses and radii further hampers a comparative study of the transiting hot Neptunes' possible interior compositions. The GJ 436b radius obtained by Bean et al. (2008) using *HST* observations is larger than that found from the infrared *Spitzer* light curves with a 92% formal significance, and would make GJ 436b less dense than HAT-P-11b. Improvements in the observational uncertainties on the mass and radii and in the constraints on the intrinsic luminosities of these two hot Neptunes are needed before we can truly make a robust comparison of their possible compositions.

2.5 Bayesian Inference Applied to Exoplanet Interior Structure Models

There are many model uncertainties that go into the interpretation of a measured mass and radius, and a major question is can we improve our deductions of interior composition from M_p and R_p by taking a more careful consideration of the uncertainties. So far we have presented our planet interior composition constraints by delimiting a range of compositions on a ternary or quaternary diagram. In our presentation (Figures 2-2, 2-4, 2-6, and 2-8), we know that it is more likely that the exoplanet's true composition falls within the n σ contours (surfaces) on the ternary (quaternary) diagram than outside the contours (surfaces). We do not know quantitatively, however, how likely it is that the exoplanet's true composition falls within the n σ bounds. In this section, we present an approach that yields a more detailed map of the relative likelihoods of the interior compositions on the ternary (quaternary) diagram and that takes all the contributing sources of uncertainty into account in a formal way.

We turn to a more technical description of precisely what the contours in Figures 2-2, 2-4, 2-6, and 2-8 represent, and why there is a more thorough approach. The $n\ \sigma$ contours (or surfaces in the case of quaternary diagrams) delimit the range of compositions that are consistent with the measured planetary mass $\widehat{M_p}$ and radius $\widehat{R_p}$ (where the hats are used to distinguish measured values) to within their $n\ \sigma$ error bars for some choice of γ, T_0, and $T_{\rm eff}$ within the ranges described in Section 2.2.4. In other words, for every composition within the $n\ \sigma$ shadings on the ternary or quaternary diagram, there is at least one choice of the model parameters within the parameter space cube $\left(\widehat{M_p} - n\sigma_{M_p}, \widehat{M_p} + n\sigma_{M_p}\right) \times \left(\widehat{R_p} - n\sigma_{R_p}, \widehat{R_p} + n\sigma_{R_p}\right) \times (\gamma_{min}, \gamma_{max}) \times (T_{{\rm eff}\,min}, T_{{\rm eff}\,max}) \times (T_{0min}, T_{0max})$ that yields a consistent solution. It is important to realize that the $n\ \sigma$ contours in our ternary and quaternary diagrams do not represent confidence intervals. While one may make statements about the likelihood that the true planet mass and radius fall within $n\ \sigma$ of their measured values, our $n\ \sigma$ contours on the interior composition do not have a similar interpretation. This would be possible if only one model parameter were uncertain (for instance, if R_p had an observational uncertainty, while M_p and all other model inputs were known exactly). In reality, however, there is more than one uncertainty (e.g., mass, radius, model inputs), and a more sophisticated technique is needed to draw accurate composition contours that can be associated with a likelihood.

Bayesian statistics provide a more rigorous approach to calculate how different sources of uncertainty combine and translate into ambiguities on the interior composition of a planet. There are three categories of uncertainties. The first is observational uncertainties. The second is model uncertainties, in terms of the usually unconstrained range of input parameters (see Section 2.2.4). The third is the inherent degeneracy in interior compositions that yield a given mass and radius; in other words, the mapping from composition to mass and radius is not one-to-one. Using Bayesian statistics, we can associate every interior composition with a "posterior likelihood", a number quantifying our degree of belief that the particular interior composition is the true interior composition of the planet (given our limited knowledge of the planet, and our assumptions). The "posterior likelihood" function defined over the domain of possible interior mass distributions can then be used to draw well-defined contours (surfaces) in the ternary (quaternary) diagram for which the likelihood of the true composition falling within the contour can be stated. In Section 2.4, we are already drawing contours (surfaces) on ternary (quaternary) diagrams constraining the interior compositions of planets; Bayesian statistics provides an alternative way to accomplish this.

The foundation of Bayesian statistics is Bayes' Theorem, stated below in terms of the problem at hand (of inferring an exoplanets interior composition):

$$p\left(C|D,\,A\right) \propto \theta\left(C|A\right)\mathcal{L}\left(D|C,\,A\right). \tag{2.21}$$

In the above expression, C represents the set of all model parameters (including interior layer mass fractions, planet mass, planet radius, γ, etc.), D represents all the measured data we have (measure planetary mass, planetary radius, stellar mass, stellar age, semimajor axis etc.), and A denotes all of our assumptions (spherical symmetry, differentiated planet, negligible thermal corrections in the interior three layers, etc.). The function $\theta\left(C|A\right)$ is the prior probability of composition/parameters C in the absence of measured data, given the assumptions. The priors θ incorporate assumptions about the range of model parameters to consider. They may also include detailed physics; for instance, one could assume a planet formation theory and use it to dictate a priori which interior compositions are more likely than others. Next, $\mathcal{L}\left(D|C,\,A\right)$ denotes the likelihood of the measured data D for a given set of model parameters. Measurement uncertainties and correlations can be used to define the likelihood. Finally, $p\left(C|D,\,A\right)$ is the posterior likelihood of composition/model parameters C given the measured data D and the assumptions A. This is what we hope to calculate. The proportionality constant in Equation (2.21) is set so as to ensure that the posterior likelihood $p\left(C|D,\,A\right)$ is properly normalized. To make ternary diagram contour plots, one must marginalize (integrate) the posterior likelihood $p\left(C|D,\, A\right)$ over all model parameters (in the set C) other than the compositional layer mass fractions. The resulting marginalized posterior likelihood then represents the likelihood of a composition when the full range of nuisance parameter values is taken into account.

We now provide two examples to illustrate how the Bayesian approach described in the previous paragraph can be applied when drawing inferences about an exoplanet's interior. To begin, we apply Bayesian techniques to the case of a solid gas-less planet having measured mass and radius. We consider GJ 581d, adopting (as mentioned in Section 2.4.2) the GJ 581d minimum mass $M_p = 7.09\ M_\oplus$ and two putative transit radii $R_p = 1.5 R_\oplus$, and $R_p = 2.0 R_\oplus$. We further assume that the measured planet mass and radius each have associated 5% observational uncertainties. In what follows, we reproduce the GJ 581d composition constraints displayed in the Figure 2-4 ternary diagrams, demonstrating how Bayesian statistics can be used to derive more informative and quantitative constraints on a transiting planet's interior composition.

In this example, our assumptions A include the following.

1. Our model described in Section 2.2 is appropriate to characterize the interior structure of GJ 581d.
2. GJ 581d does not have a significant gas layer.
3. GJ 581d has a pure iron core.
4. The Fe number fraction in the planet mantle is similar to that of the Earth ($\chi \approx 0.1$).
5. The measurement uncertainties on the planetary mass and radius are Gaussian and uncorrelated.

Our model parameters in this case are $C \equiv (M_p, x_{core}, x_{mantle})$, where M_p is the planetary mass, and x_i is the mass fraction in the ith component. We do not explicitly include $x_{\mathrm{H_2O}}$ in the parameters since it is determined by the constraint $1 = x_{core} + x_{mantle} + x_{\mathrm{H_2O}}$. For a specified set of parameter values, our interior structure model will calculate a planetary radius $R_p\left(M_p, x_{core}, x_{mantle}\right)$. The data are the (putative) measured planetary mass and radius $D \equiv \left(\widehat{M_p} \pm \sigma_{M_p}, \widehat{R_p} \pm \sigma_{R_p}\right)$. We use the measured planetary mass and radius with their observational uncertainties to define the likelihood in terms of a Gaussian joint distribution for the planetary mass and radius

$$\mathcal{L}\left(M_p, x_{core}, x_{mantle}|D, A\right) = \frac{1}{2\pi\sigma_{M_p}\sigma_{R_p}} e^{-\left(M_p-\widehat{M_p}\right)^2/2{\sigma_{M_p}}^2-\left(R_p-\widehat{R_p}\right)^2/2{\sigma_{R_p}}^2}, \qquad (2.22)$$

where $R_p \equiv R_p\left(M_p, x_{core}, x_{mantle}\right)$. In this example, we take a flat prior,

$$\theta\left(M_p, x_{core}, x_{mantle}|A\right) \propto 1,$$

for which regions of composition space having equal area on the ternary diagram are equally likely. This prior is analogous to what we implicitly assumed when plotting the $n\sigma$ contours in Figure 2-4. Given the assumed prior $\theta\left(M_p, x_{core}, x_{mantle}|A\right)$, we multiply θ and $\mathcal{L}$ to obtain the posterior likelihood $p\left(M_p, x_{core}, x_{mantle}|D, A\right)$ following Equation (2.21). We then marginalize over the planetary mass M_p, obtaining a posterior likelihood depending only on the interior composition,

$$p\left(x_{core}, x_{mantle}|D, A\right) = \int_0^\infty p\left(M_p, x_{core}, x_{mantle}|D, A\right) \mathrm{dM_p}, \qquad (2.23)$$

for plotting on a ternary diagram (Figure 2-9). In Figure 2-9 we show contours of constant posterior likelihood, and label each contour with the posterior likelihood that the true composition lies inside the contour (calculated by integrating the posterior likelihood function over the area within the contour). When drawn in this way, the composition contours in the ternary diagrams are Bayesian confidence regions with confidence values that should be interpreted as the "degree of our belief" that the true composition of a planet falls within the contour given our assumptions and our observations of the planet.

Applying a Bayesian analysis to the putative mass and radius measurements of

GJ 581d, we extract more informative and quantitative composition constraints than those obtained from the non-Bayesian analysis in Section 2.4.2. The non-Bayesian $n\sigma$ contours in Figure 2-4 effectively denote the loci of interior compositions for the discrete mass-radius pairs $\left(\widehat{M_p} \pm n\sigma_{M_p}, \widehat{R_p} \mp n\sigma_{R_p}\right)$. By contrast, the results of our Bayesian analysis (shown in Figure 2-4) take into account the full mass-radius relationship for each possible interior composition. While Figure 2-4 does not give any indication of the relative plausibility of two different compositions within the same $n\sigma$ contour, the Bayesian framework yields a posterior likelihood map $p\left(x_{core}, x_{mantle}|D, A\right)$ over the entire ternary diagram (shown by the color shading in Figure 2-9). Finally, on its own, Figure 2-4 does not reveal an estimate of how likely it is that the true composition of the GJ 581d falls within its $n\sigma$ bounds. The contours in Figure 2-9 are, however, associated with Bayesian confidence values. Comparing Figures 2-4 to 2-9 we see that in this case, given our assumptions, the true composition of the GJ 581d should fall within the 1σ contours in Figure 2-4 with a Bayesian confidence of roughly 75%. For the price of having to assume a prior $\theta\left(C|A\right)$, Bayesian inference yields more detailed and quantitative constraints on a transiting exoplanet's composition than other analysis approaches.

We now present a second example to demonstrate the effect of priors. We consider CoRoT-7b, and for illustration we make several different assumptions about the iron concentration in its mantle. As mentioned in Section 2.4.1, we assume that CoRoT-7b has a pure iron core and does not have a significant water or gas layer. With these restrictions, our model parameters are $C \equiv (M_p, x_{core}, x_{\mathrm{FeSiO_3}})$, where $x_{\mathrm{FeSiO_3}}$ and $x_{\mathrm{MgSiO_3}}$ denote the fraction of the planet's mass consisting of mantle $\mathrm{FeSiO_3}$ and mantle $\mathrm{MgSiO_3}$ respectively ($x_{\mathrm{MgSiO_3}} = 1 - x_{core} - x_{\mathrm{FeSiO_3}}$). We proceed to calculate the interior composition posterior likelihood function $p\left(x_{core}, x_{\mathrm{FeSiO_3}}|D, A\right)$ following an analogous procedure to that outlined in detail in the GJ 581d example above. Again assuming that the measurement uncertainties on the planetary mass and radius are Gaussian and uncorrelated, we define the likelihood in terms of a Gaussian joint distribution for the planetary mass and radius, as given in Equation (2.22). Our choices for the priors $\theta\left(M_p, x_{core}, x_{\mathrm{FeSiO_3}}|A\right)$ are described below.

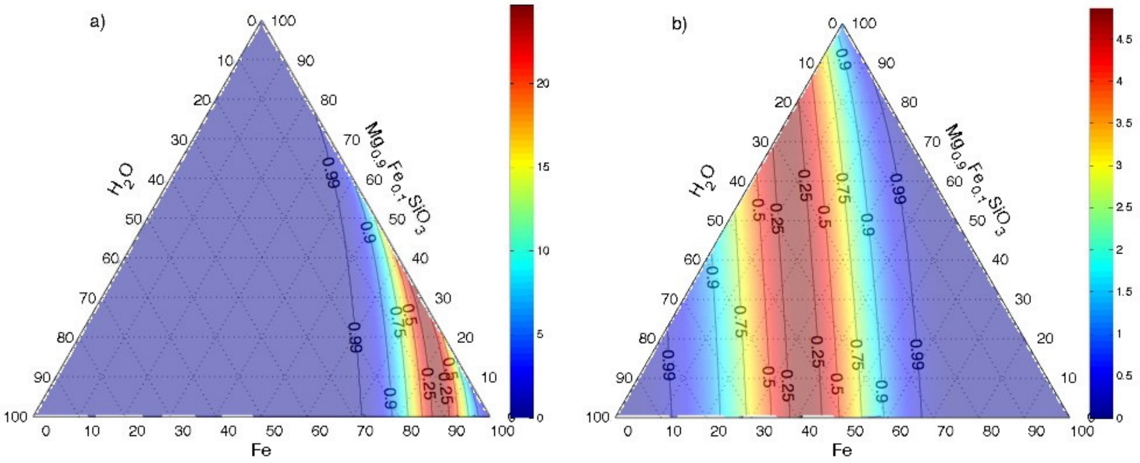

Figure 2-9: GJ 581d interior composition posterior likelihood distribution. Only compositions without an H/He layer are considered. An observational uncertainty of 5% is included on both the assumed mass ($M_p = 7.09\ M_\oplus$) and the assumed radii. Each diagram represents a different possible planetary radius: (a) $R_p = 1.5R_\oplus$ and (b) $R_p = 2.0R_\oplus$. The color shading in the ternary diagrams corresponds to the posterior likelihood distribution $p\left(x_{core}, x_{mantle}|D, A\right)$. Note that, for clarity, the two diagrams have different color scales. The contours are lines of constant posterior likelihood labeled with a Bayesian confidence value indicating the "degree of belief" given the prior assumptions that the true composition of the planet falls within the contour. The confidence value is the integral of the posterior likelihood function over the surface within the contour. Compare these diagrams to Figures 2-4(a) and (b), which show composition constraints obtained from the non-Bayesian approach employed in Section 2.4 under assumptions identical to those used here.

For illustration, we consider three different choices for the prior $\theta\left(M_p, x_{core}, x_{\mathrm{FeSiO_3}}|A\right)$ in Figure 2-10. In all three cases, we take θ to be independent of M_p so that mass intervals of equal size dM_p are equally likely (before taking into account radial velocity observations measuring CoRoT-7b's mass).

For our first prior (Figure 2-10(a)), we take a flat prior in which each division of mass between the Fe core, $\mathrm{MgSiO_3}$, and $\mathrm{FeSiO_3}$ is equally likely: $\theta_1\left(M_p, x_{core}, x_{\mathrm{FeSiO_3}}|A\right) \propto 1$. This prior is most similar to what we have implicitly assumed in plotting Figure 2-2 and corresponds to the case in which regions of equal area on the ternary diagram are, a priori, equally likely.

Second, in Figure 2-10(b) we choose a prior where the mantle iron number fraction, χ, is uniformly distributed between 0 and 1 (with all possible values x_{core} also equally likely). The Fe number fraction χ of a silicate material is defined as the ratio of $\mathrm{Fe}/(\mathrm{Mg}+\mathrm{Fe})$ by number. For perovskite $\mathrm{Mg}_{1-\chi}\mathrm{Fe}_{\chi}\mathrm{SiO_3}$, χ is related to the mass fractions $x_{\mathrm{MgSiO_3}}$ and $x_{\mathrm{FeSiO_3}}$ through

$$\chi\left(x_{core}, x_{\mathrm{FeSiO_3}}\right) = \frac{x_{\mathrm{FeSiO_3}}}{x_{\mathrm{FeSiO_3}} + \left(1 - x_{core} - x_{\mathrm{FeSiO_3}}\right)\left(\mu_{\mathrm{FeSiO_3}}/\mu_{\mathrm{MgSiO_3}}\right)}, \tag{2.24}$$

where $\mu_{\mathrm{MgSiO_3}}$ and $\mu_{\mathrm{FeSiO_3}}$ are the molar weights of $\mathrm{MgSiO_3}$ and $\mathrm{FeSiO_3}$ respectively. Transforming from a uniform prior in x_{core} and χ to the variables x_{core} and $x_{\mathrm{FeSiO_3}}$ we find

$$\begin{aligned}\theta_2\left(M_p, x_{core}, x_{\mathrm{FeSiO_3}}|A\right) &\propto \left|\frac{\partial\chi}{\partial x_{\mathrm{FeSiO_3}}}\right| \\ &= \frac{\left(1 - x_{core}\right)\left(\mu_{\mathrm{FeSiO_3}}/\mu_{\mathrm{MgSiO_3}}\right)}{\left(x_{\mathrm{FeSiO_3}} + \left(1 - x_{core} - x_{\mathrm{FeSiO_3}}\right)\left(\mu_{\mathrm{FeSiO_3}}/\mu_{\mathrm{MgSiO_3}}\right)\right)^2},\end{aligned} \tag{2.25}$$

where the right-hand side of Equation (2.25) is the Jacobian determinant of the transformation. It is important to note that assuming a uniform prior probability on $x_{\mathrm{FeSiO_3}}$ is not the same thing as assuming a uniform prior probability on χ (or in other words $\theta_1 \neq \theta_2$). A uniform prior probability on χ effectively weights compositions having small mantle mass fractions more heavily those having large mantle mass fractions. This is because when $x_{\mathrm{FeSiO_3}} + x_{\mathrm{MgSiO_3}} = 1 - x_{core}$ is small, small increments

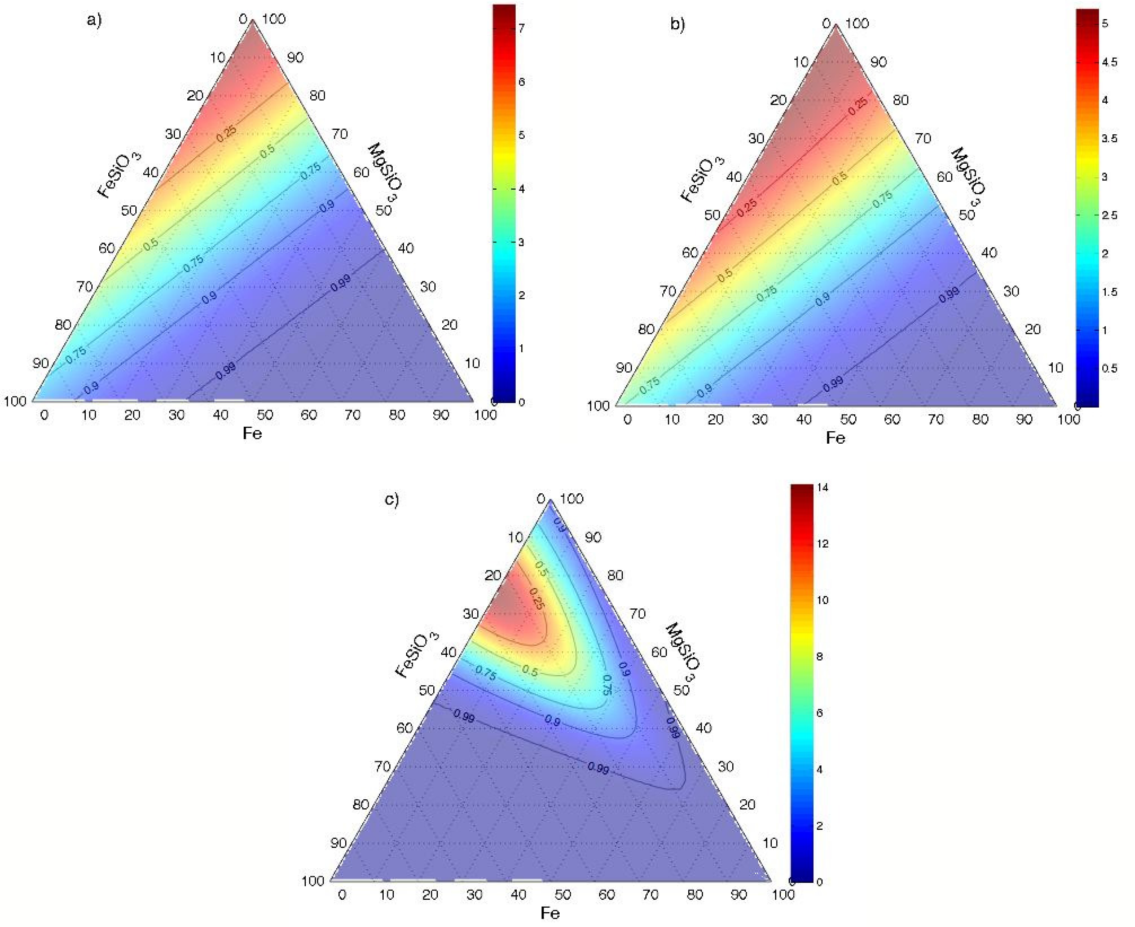

Figure 2-10: CoRoT-7b interior composition posterior likelihood distribution. Three different choices of prior are shown. In panel (a) we take a flat prior on the core and $FeSiO_3$ mass fractions, $\theta_1\left(M_p, x_{core}, x_{\mathrm{FeSiO_3}}|A\right) \propto 1$. In panel (b) we adopt a uniform prior on the mantle iron number fraction, χ (Equation (2.25)). Finally, in panel (c) we take a strong prior on the mantle iron number fraction, in which χ is assumed to have a Gaussian distribution with mean $\bar{\chi} = 0.1$ and standard deviation $\sigma_\chi = 0.1$ (Equation (2.26)). The color shading in the ternary diagrams corresponds to the posterior likelihood distribution $p\left(x_{core}, x_{\mathrm{FeSiO_3}}|D, A\right)$. Note that, for clarity, each diagram has a different color scale. The contours are lines of constant posterior likelihood labeled with a Bayesian confidence value indicating the "degree of belief" given the prior assumptions that the true composition of the planet falls within the contour. The confidence value is the integral of the posterior likelihood function over the surface within the contour.

in $x_{\mathrm{FeSiO_3}}$ can correspond to large changes in χ.

For our final prior (Figure 2-10*c*), we take an extreme case for illustration, adopting a strong prior. We assume that CoRoT-7b's mantle has an iron fraction similar to that of the Earth. Specifically, we take χ to have a Gaussian distribution with mean $\bar{\chi} = 0.1$ and standard deviation $\sigma_\chi = 0.1$:

$$\theta_3 \left(M_p, x_{core}, x_{\mathrm{FeSiO_3}} | A\right) \propto \frac{\left(1 - x_{core}\right) \left(\mu_{\mathrm{FeSiO_3}} / \mu_{\mathrm{MgSiO_3}}\right) e^{-(\chi - \bar{\chi})^2 / 2\sigma_\chi^2}}{\left(x_{\mathrm{FeSiO_3}} + \left(1 - x_{core} - x_{\mathrm{FeSiO_3}}\right) \left(\mu_{\mathrm{FeSiO_3}} / \mu_{\mathrm{MgSiO_3}}\right)\right)^2}. \quad (2.26)$$

In Equation (2.26), $\chi \equiv \chi \left(x_{core}, x_{\mathrm{FeSiO_3}}\right)$. Our third choice of prior has a strong effect on the posterior likelihood distribution in Figure 2-10*c*, favoring compositions near the $\chi = 0.1$ line in the ternary diagram.

The danger in the Bayesian approach described in this section is that one's prior assumptions will affect the compositional likelihoods, as illustrated by the CoRoT-7b example above. While modelers have not formally been using the Bayesian approach, they have been making critical assumptions that affect their interior composition interpretation of the mass and radius. For example, Zeng & Seager (2008) assumed a uniform distribution of allowed compositions; Valencia et al. (2007a) excluded certain regions of the ternary diagram having low mantle mass fractions, but effectively presented all remaining compositions as equally likely; and Figueira et al. (2009) used a planet formation and migration model to predict which bulk compositions of GJ 436b may be more likely. The Bayesian approach above provides a framework in which the priors are explicitly stated, whether they are flat or not. In this way, the effect on the results of choosing different prior assumptions can be quantified.

Bayesian inference may or may not be the best approach to interpret an exoplanet's measured mass and radius. Our goal was to take into account, in a formal way, all the sources of uncertainty contributing to ambiguities in a planet's interior composition. We have shown that the Bayesian approach is a way to meet this goal. Less formal approaches (such as that in Section 2.4) for constraining a planet's interior composition can also be insightful, but one should be heedful of how multiple sources of uncertainty are combined together when interpreting their composition bounds. A problem with the Bayesian approach is that, since the data available on any given transiting planet are limited, the priors assumed can have an important effect on the results. As long as the effect of the priors is explored and acknowledged, Bayesian statistics can help to maximize the compositional inferences we can draw from the limited data that we have on distant exoplanets. Regardless of any statistical approach taken, modelers must be explicit about their prior assumptions and about the precise significance of their compositional constraints.

2.6 Discussion

2.6.1 External Constraints on Planetary Composition

So far, we have only considered the constraints placed on an exoplanet's interior composition by mass and radius measurements alone. In this section, we discuss how planetary formation theories, compositional stability, and cosmic elemental abundances can be used to place additional constraints on a planet's interior composition.

Planet formation models predict that some interior compositions are more likely to form than others. Valencia et al. (2007a) considered the constraints imposed by protoplanetary disk abundances, adopting the point that planets with large iron cores or large water ice layers but small silicate mantles are very unlikely. From the relative abundance of Si and Fe in the solar nebula (Si/Fe ~ 0.6), Valencia et al. (2007a) propose a minimum ratio of mantle to core mass. Further, Valencia et al. (2007a) put forward that, since comets are dirty snowballs comprised of both volatiles (water) and dust, cometary delivery of water to a planet will simultaneously deliver silicates to build up the planet's mantle at the rate of at least $Si/H_2O \sim 0.23$ by mass. Grasset et al. (2009) choose a distribution of Mg/Si and Fe/Si molar ratios in the bulk compositions of their modeled planets based on the measured abundances in a collection of planet-hosting stars. Our approach is to consider the full ternary diagram and to avoid imposing strong priors on the a priori relative likelihood of various interior compositions. In this way, we limit the effect of planet formation assumptions on the composition constraints we derive.

Planet formation models also constrain the mass and composition of hydrogen and helium gas layers. In this paper, we have only considered a fixed ratio of H/He. Planet atmospheres may have a range different from solar, based on the atmosphere formation process. Planet atmospheres can originate from capture of nebular gases, degassing during accretion, and degassing during subsequent tectonic activity. Outgassing would produce a hydrogen atmosphere with negligible helium, because helium is not trapped in rocks (Heber et al., 2007). The mass of the atmosphere created from outgassing, however, could have a wide range (Elkins-Tanton & Seager, 2008b). In contrast, the H/He composition of a gas layer captured from a nebula would reflect the composition of the nebula (modulated by ensuing atmospheric escape) and is presumably close to solar. It is conventional to accept that accretion of nebula gases is most important for massive protoplanetary cores; accretion of nebular gas is expected for rocky cores above 10 $M_{\oplus}$ while often neglected for planets below 6 $M_{\oplus}$ (e.g. Selsis et al., 2007b). We show the full quaternary diagram because planets in the intermediate-mass range $6-10$ $M_{\oplus}$ (such as GJ 581d) may still accrete a significant mass of H-rich gas (Alibert et al., 2006; Rafikov, 2006) and retain it under the right conditions.

A natural question in exploring the interior composition range of a hot super-Earth is whether or not a hot super-Earth can retain an interior water layer. We can set upper limits on the rate at which the low-mass exoplanet CoRoT-7b ($M_p = 4.8 \pm 0.8$ $M_{\oplus}$) would lose H_2O. CoRoT-7b is extremely close to its host star and suffering intense irradiation; the surface temperature is 1800-2600 K at the sub-stellar point depending on the planet Albedo and energy redistribution (Léger et al., 2009). Scaling the results of Selsis et al. (2007b) to CoRoT-7b's semimajor axis and host star luminosity, we find a minimum water content lifetime of 0.07-1.0 Gyr. Selsis et al. (2007b) set upper bounds on the water mass loss of ocean planets around Sun-like stars, considering both energy-limited thermal escape driven by extreme UV and X-ray irradiation heating the planet exospheres, and non-thermal escape driven by erosion from the stellar wind. Although we do not have an upper bound on the water content lifetime, we do not consider the presence of a water layer (or of H/He) on CoRoT-7b because of its extreme proximity to the host star. If CoRoT-7b does in fact have a significant water content, it would be in the form of a super-fluid H_2O envelope with no liquid-gas interface (see, e.g., Léger et al., 2004; Selsis et al., 2007b). Valencia et al. (2010) considered the possibility that CoRoT-7b might harbor a water vapor layer.

Atmospheric escape is another process that is difficult to model but could potentially be helpful in interpreting the composition of a planet by ruling out regions of the quaternary diagram. It is difficult to predict atmospheric escape as it depends on the detailed physical characteristics of the planet's atmosphere and its interaction with the stellar insolation. Examples of properties on which atmospheric escape rates depend are the composition of the atmosphere, the thermal structure of the atmosphere, the UV history of the host star, the density of the stellar wind, the speed of the stellar wind, and the planet's intrinsic magnetic moment. In order to understand whether or not a planet has retained any hydrogen, one would have to model a specific exoplanet, taking into consideration the range of possibilities for the factors controlling atmospheric escape. As an approximation, Lecavelier Des Etangs (2007) has considered energy-limited atmospheric escape to estimate atmosphere lifetimes. Following his approach, we estimate escape rates of 3×10^7 $\mathrm{kg\,s^{-1}}$ and 5×10^7 $\mathrm{kg\,s^{-1}}$ for GJ 436b and HAT-P-11b, respectively. As a second example, Selsis et al. (2007a) have found that at GJ 581A's current X-ray and EUV luminosity, GJ 581d should not currently be experiencing extreme atmospheric mass loss, although atmospheric erosion rates at earlier (and more active) stages in the GJ 581 system's lifetime are uncertain. It is fair to say that no published models conclusively detail the mass-loss history of a given Neptune or super-Earth exoplanet, and it is not clear for which cases this is even possible.

2.6.2 Chemical Composition of Interior Layers

The chemical make-up of a transiting planet's envelope, ices, mantle, and core is not known a priori. In this work, we have limited the chemical compositions that we consider for the interior layers of a planet to an H/He gas layer with solar composition, water ices, perovskite mantle, and a predominantly iron core. We have explored the effect of varying the mantle iron content and of including a light element in the planet core (see Section 2.4). We selected our fiducial choice for the chemical compounds comprising the interior planetary layers in our model to capture the dominant materials making up the solar system planets.

There are, however, several additional possibilities for the chemical make up of an exoplanet. For example, ammonia ices change the EOS of Neptunes interior (e.g. Podolak et al., 1995). Super-Earths that have outgassed an extended hydrogen envelope would lack helium (Elkins-Tanton & Seager, 2008b). A massive CO gas layer in a hydrogen-poor planet would have a different EOS than an H/He gas layer, but because of its density, likely would not contribute to an extended radius. Water-dominated "ocean" planets could have a vapor atmosphere or even a superfluid surface layer (e.g., Kuchner, 2003; Léger et al., 2004; Selsis et al., 2007b). Carbon planets will have different interior compositions entirely, as compared to silicate-based planets (Kuchner & Seager, 2005; Seager et al., 2007). When interpreting the mass and radius for a given exoplanet, these other compositions should be included in the future.

2.6.3 Planet Evolution

We have found that uncertainties in an H/He-laden planet's intrinsic luminosity significantly weaken the constraints that can be placed on the planet's interior composition. In the case of GJ 436b and HAT-P-11b, uncertainties in $T_{\rm eff}$ even dominate the observational uncertainties on the planet masses and radii. Developing models to better predict a low-mass planet's intrinsic luminosity is thus an important endeavor to further our ability to study the interior compositions of super-Earths and hot Neptunes.

Time-dependent simulations of planets as they age and cool could be employed to constrain the planets' intrinsic luminosities. Exoplanet evolution calculations have been performed in several previous studies (e.g. Baraffe et al., 2003; Burrows et al., 2003; Chabrier et al., 2004; Fortney & Hubbard, 2004; Baraffe et al., 2006; Fortney et al., 2007; Baraffe et al., 2008). Simulations of the solar system giants have illustrated how complicated the process of predicting a planet's intrinsic luminosity can be. While simple models of Jupiter's evolution and interior structure are in good agreement with the observed cooling rate (Hubbard, 1977), homogeneous contraction models predict intrinsic luminosities that are too low for Saturn (Guillot, 2005) and too high for Uranus and Neptune (Stevenson, 1982).

In this work, we have subsumed an evolution calculation by using a simple scaling relation to derive a plausible intrinsic luminosity range from a planet's mass, radius, and age. An evolution calculation coupled with our planet interior model may eventually offer a more self-consistent approach to constrain the intrinsic luminosities of low-mass exoplanets. The addition of a time-dependent cooling calculation would essentially shuffle our uncertainties in T_{eff} to uncertainties in temperature-dependent EOSs, the planet's chemical composition, and the planet's migration, geological, tidal evolution, and compositional histories. Poorly constrained planet ages further limit the improvements an evolution calculation could provide in the intrinsic luminosity constraints. These limitations and the added computational power demanded by time-dependent models motivate our use of an approximate phenomenological approach to constrain T_{eff}. In a future paper, we plan to perform an evolution calculation to verify that the range of T_{eff} values chosen in this work is representative of the uncertainties in a planet's age and history.

2.6.4 Beyond Mass and Radius - Further Observational Constraints on Compositions

In this paper, we have focused on the constraints that can be placed on a transiting exoplanet's interior composition using only knowledge about its mass, radius, and stellar insolation (all properties that can be measured by current spectroscopic or photometric techniques). Are there other observations that can further restrict the range of interior compositions of a low-mass exoplanet? Transmission spectra during primary transit can be used to discriminate between a planet with a significant hydrogen envelope and a hydrogen-poor super-Earth (Miller-Ricci et al., 2009). Observations will be extremely challenging, even with multiple transits (Kaltenegger & Traub, 2009; Deming et al., 2009). In the case of close-in transiting hot Jupiters, apsidal precession induced by tidal bulges on the planet could produce observable changes in the transit light-curve shape, revealing additional information about the interior density distribution of the planet (through the Love number; Ragozzine & Wolf, 2009). This idea is geared at hot Jupiters and it is unclear whether the effect will be significant for terrestrial or Neptune-size planets. The potential for an improved understanding of planetary interiors should provide strong motivation for the advancement of these observational techniques toward greater sensitivities.

2.7 Conclusions

We have quantified how observational uncertainties, model uncertainties, and inherent degeneracies all contribute to the range of plausible bulk compositions for transiting low-mass exoplanets. We have only considered the constraints imposed on the composition by the measured planetary mass, radius, and stellar insolation, and did not speculate on the formation history. Uncertainties in the formation, evolution, and age of the planets studied were encapsulated in the range of values chosen for the internal heat flux, albedo, γ, and mantle iron content. We summarize our main conclusions below.

1. The interior compositions of CoRoT-7b, GJ 436b, and HAT-P-11b (the three lowest mass transiting planets known to date) are constrained by our interior structure model.

    - CoRoT-7b: An Earth-like composition having 30% of its mass in an iron core and the remaining 70% of its mass in a silicate mantle is consistent with the measured mass and radius within 1 σ. Large core mass fractions ($x_{\mathrm{Fe}} \gtrsim 0.76 - 0.86$) are ruled out at the level of at least 3 σ, but all other combinations of core mass fraction and iron mantle content (in water-less, gas-less compositions) are allowed; the planet could have no core or could be composed of up to 86% pure iron by mass and still fall within the 3 σ error bars on M_p and R_p. If CoRoT-7b does not contain significant amounts of water or gas, some of the mass-radius pairs within $M_p \pm 1\sigma_M$ and $R_p \pm 1\sigma_R$ (specifically those that correspond to bulk densities lower than a pure silicate planet) can be ruled out.

- GJ 436b: GJ 436b must have between 2.3% and 15.5% H/He layer by mass to produce the observed transit depth. These lower and upper limits on the GJ 436b H/He layer depend on the intrinsic luminosity of the planet. The water content of GJ 436b is very poorly constrained by the mass and radius measurements alone: GJ 436b could be completely dry, or could alternatively consist of up to 96.4% water by mass.
- HAT-P-11b: Nominally, HAT-P-11b's measured density is lower than GJ 436b's. HAT-P-11b thus requires a higher minimum mass of gas (at least 7.1%) and can support a more massive gas envelope (up to 19.0% by mass). Comparisons between the range of plausible compositions for GJ 436b and HAT-P-11b are made difficult by the uncertain intrinsic luminosities of these planets and by the scatter in the observationally determined masses and radii for each planet.

2. Uncertainties in the intrinsic luminosities of low-mass exoplanets significantly weaken the compositional constraints that can be derived from a pair of mass and radius measurements. In the case of both GJ 436b and HAT-P-11b, the uncertainties on T_{eff} dominate the observational uncertainties. Better constraints on T_{eff} (possibly obtained through planetary evolution models) are required to improve our limits on the interior compositions of transiting hot Neptunes.

3. The degree to which we can constrain the composition of a super-Earth depends on the planet's density. Putative planets with extreme densities (especially those with very high densities) allow the tightest composition constraints (assuming similar observational uncertainties on M_p and R_p). Denser planets will have smaller radii, however, making it more difficult to measure their transit radii with high precision.

4. Quaternary diagrams provide a convenient way to illustrate the range of possible interior compositions for a transiting planet that harbors a significant gas layer. They allow one to display interior compositions consisting of four distinct components (in our case an iron core, silicate mantle, water ice layer, and H/He envelope).

5. When constraining the interior compositions of transiting exoplanets, modelers must include in their analysis many sources of uncertainty (model, observational, and inherent degeneracy). The Bayesian approach presented in Section 2.5 provides a framework with which one can combine all the sources of uncertainty contributing to ambiguities in a planet's interior composition in a formal way. Given explicitly stated assumptions and the measured planet parameters, the procedure described in Section 2.5 outlines how to calculate the relative likelihood that any interior composition on the ternary diagram is the true composition of the planet. The likelihoods obtained can be strongly dependent on the prior assumptions made. In the Bayesian framework, however, the prior assumptions are explicitly stated and so their effect can be explored and quantified.

6. Allowing for the possibility of a gas layer in future interpretations of the mass and radius measurements of transiting super-Earths will greatly increase the range of possible interior compositions of the planet. The presence of even a low-mass gas layer contributing to the transit radius can significantly alter the inferred characteristics of the underlying solid planet. Specifically, the higher the gas mass fraction the denser the solid planet interior must be to compensate.

Planetary science has come a long way toward understanding planetary interiors. With Jupiter, we know that its bulk composition is dominated by 50%-70% hydrogen by mass; that the helium abundance in its atmosphere is somewhat below the protosolar value; that it contains $1\ M_\oplus \lesssim M_Z \lesssim 39\ M_\oplus$ of heavy elements; and that between 0 and 11 $M_\oplus$ of the heavy elements could be concentrated in a core (Saumon & Guillot, 2004). For exoplanets, without recourse to in situ composition measurements and gravitational moment measurements from spacecraft flybys we will be permanently limited in what we can infer about the interior composition from the measured mass and radius. Not only are the measurement uncertainties relatively large (2% at best on R_p compared to $\sim 0.01\%$ for solar system planets), but models are also needed to map the planetary mass and radius into interior composition and the model uncertainties are high. We will have to be satisfied simply knowing that we can quantify the wide range of exoplanet plausible interior compositions.

Chapter 3

Three Possible Origins for the Gas Layer on GJ 1214b

Abstract

We present an analysis of the bulk composition of the MEarth transiting super Earth exoplanet GJ 1214b using planet interior structure models. We consider three possible origins for the gas layer on GJ 1214b: direct accretion of gas from the protoplanetary nebula, sublimation of ices, and outgassing from rocky material. Armed only with measurements of the planet mass ($M_p = 6.55 \pm 0.98\ M_\oplus$), radius ($R_p = 2.678 \pm 0.13\ R_\oplus$), and stellar irradiation level, our main conclusion is that we cannot infer a unique composition. A diverse range of planet interiors fits the measured planet properties. Nonetheless, GJ 1214b's relatively low average density ($\rho_p = 1870 \pm 400\ \mathrm{kg\,m^{-3}}$) means that it almost certainly has a significant gas component. Our second major conclusion is that under most conditions we consider GJ 1214b would not have liquid water. Even if the outer envelope is predominantly sublimated water ice, the envelope will likely consist of a super-fluid layer sandwiched between vapor above and plasma (electrically conductive fluid) below at greater depths. In our models, a low intrinsic planet luminosity ($\lesssim 2$ TW) is needed for a water envelope on GJ 1214b to pass through the liquid phase.

The contents of this chapter are also published in *Rogers, L. A., & Seager, S. 2010b, ApJ, 716, 1208.*

3.1 Introduction

The era of super Earths is upon us with the first two transiting sub-Neptune mass exoplanets recently discovered. The first such transiting planet, CoRoT-7b, is a $M = 4.8 \pm 0.8\ M_\oplus$ (Léger et al., 2009) and $R = 1.68 \pm 0.09\ R_\oplus$ (Queloz et al., 2009) hot relatively dense planet with an average density similar to Earth's. More recently, the MEarth project (Irwin et al., 2009) discovered transiting low-mass planet GJ 1214b (Charbonneau et al., 2009). GJ 1214b has a mass of $M_p = 6.55 \pm 0.98\ M_\oplus$ and a radius of $R_p = 2.678 \pm 0.13\ R_\oplus$. It is in a 1.5803952 ± 0.0000137 day period around an $L_* = 0.00328 \pm 0.00045\ L_\odot$ M dwarf of mass $M_* = 0.157 \pm 0.019\ M_\odot$ and radius $R_* = 0.2110 \pm 0.0097\ R_\odot$.

GJ 1214b has a low enough density ($\rho_p = 1870 \pm 400\ \mathrm{kg\,m^{-3}}$) that it cannot be composed of rocky and iron material alone. The planet almost certainly contains a gas component. Even a planet of pure water ice is still too dense to match the observed mass and radius. At 6.55 $M_\oplus$ a pure zero-temperature water ice planet would have a radius of 2.29 $R_\oplus$ while an Earth-like composition would have a radius of about 1.64 $R_\oplus$; these theoretical radii are 3 and 8σ lower than the value measured for GJ 1214b. While these simple arguments already reveal that GJ 1214b probably has a gaseous component, we are motivated to provide a more detailed analysis to quantify the range of possible planetary interior and gas layer compositions for GJ 1214b.

We use planet interior structure models to constrain the bulk composition of GJ 1214b. In this work, we focus on three possible sources for the GJ 1214b gas layer: direct accretion of gas from the protoplanetary nebula, sublimation of ices, and outgassing from rocky material. We examine end-member cases in which one of these three contributions dominates the gas layer. Based on GJ 1214b's mass and radius alone, we cannot infer a unique interior composition (see, e.g. Valencia et al., 2007a; Adams et al., 2008; Zeng & Seager, 2008). Instead, there is a range of compositions that are consistent with the transit and radial velocity observations. Despite the inherent degeneracies plaguing the under-constrained problem of inferring GJ 1214b's composition from its mass and radius, we can nonetheless place interesting bounds on the gas envelope mass and draw insights into GJ 1214b's prospects for harboring liquid water.

In Section 3.2 we explore the connection between the primordial material comprising a planet and the sources of a planet's gas envelope. In Section 3.3 we describe our model of low-mass planet interiors. In Section 3.4 we present constraints on the composition of GJ 1214b in each of three distinct scenarios for the origin of its gas layer. Discussion and conclusions follow in Sections 3.5 and 3.6.

3.2 Connecting Gas Layer Origins and Planet Interiors

There is a wide range of possible chemical compositions for GJ 1214b's interior and gas layer. To motivate the discrete representative scenarios considered in this work, we look to the broad phases of materials that can contribute to a planet's bulk and to its gas layer.

GJ 1214b may have formed from a variety of primordial material in its protoplanetary disk including gas (predominantly hydrogen and helium); ice-forming material (water, carbon monoxide, carbon dioxide, methane, and ammonia); and rocks or refractory material (iron, silicates, and sulfides). All three classes of primordial planet-building material (nebular gas, ices, and rocks) could have contributed to the gas layer observed on GJ 1214b today (Figure 3-1). Gas accreted directly from the nebula during planet formation, if retained, would contribute hydrogen and helium. Sublimation of ices (for example, due to the release of gravitational energy during initial planet formation, the increased stellar irradiation following inward planetary migration, or late delivery of ices by comets) would produce H_2O, CO, CO_2, CH_4, and NH_3 vapor. Finally, rocky material can release volatiles to the GJ 1214b gas layer via outgassing during formation (Elkins-Tanton & Seager, 2008b; Schaefer & Fegley, 2010) and tectonic activity after formation (Kite et al., 2009). Irrespective the origin of GJ 1214b's gas layer (be it from accreted nebular gas, sublimated ices, or outgassed rocky material), the gas envelope's mass and composition will have evolved over time under the influence of atmospheric escape.

In this work, we focus on direct accretion of nebular gas, sublimation of ices, and outgassing from rocky material as possible sources for the gas layer on GJ 1214b. There are, however, other atmosphere formation processes worth mentioning. Vaporization of rocky material can contribute to atmospheres surrounding highly irradiated super Earths like CoRoT-7b (Schaefer & Fegley, 2009), but GJ 1214b is not hot enough for this process to occur. Even at temperatures too low to sublimate ices or vaporize oceans, volatiles stored as clathrate hydrates in icy material can be outgassed into a planet's atmosphere. Sputtering by the stellar wind and micrometeorites, photolysis, radiolysis, and chemical reactions between stellar wind ions and planet surfaces all contribute to tenuous atmospheres surrounding solar system bodies. The contributions of these gas sources are negligible, however, compared to the gas volume needed to account for GJ 1214b's transit depth.

The actual bulk make-up of GJ 1214b is determined by its unknown formation, migration, and evolution history. For instance, if GJ 1214b initially formed beyond the snow line it would contain more icy material than if it formed closer to its star. The mass of nebular gas initially captured would depend upon the nascent GJ 1214b's accretion luminosity as well as the local conditions (density, temperature, opacity, and mean molecular weight) in the protoplanetary disk (Rafikov, 2006). In the solar system, there is a definite relationship between the relative abundances of rock-ice-gas and planet mass: small planets ($\leq 1\ M_{\oplus}$) are rocky, intermediate planets ($\sim 15 - 17\ M_{\oplus}$) are icy, and larger planets are predominantly composed of H and He. Rough constraints on solar system planet compositions from Guillot (2005) are plotted in Figure 3-2. We do not attempt to tighten the constraints on GJ 1214b's interior by directly incorporating planet formation theories into our analysis. Instead we allow for the full range of primordial gas-ice-rock ratios and explore the constraints imposed on these ratios by the measured mass and radius.

We consider a series of scenarios that encompasses all nebular gas-ice-rock mass fraction combinations for the primordial material making up GJ 1214b (Figure 3-

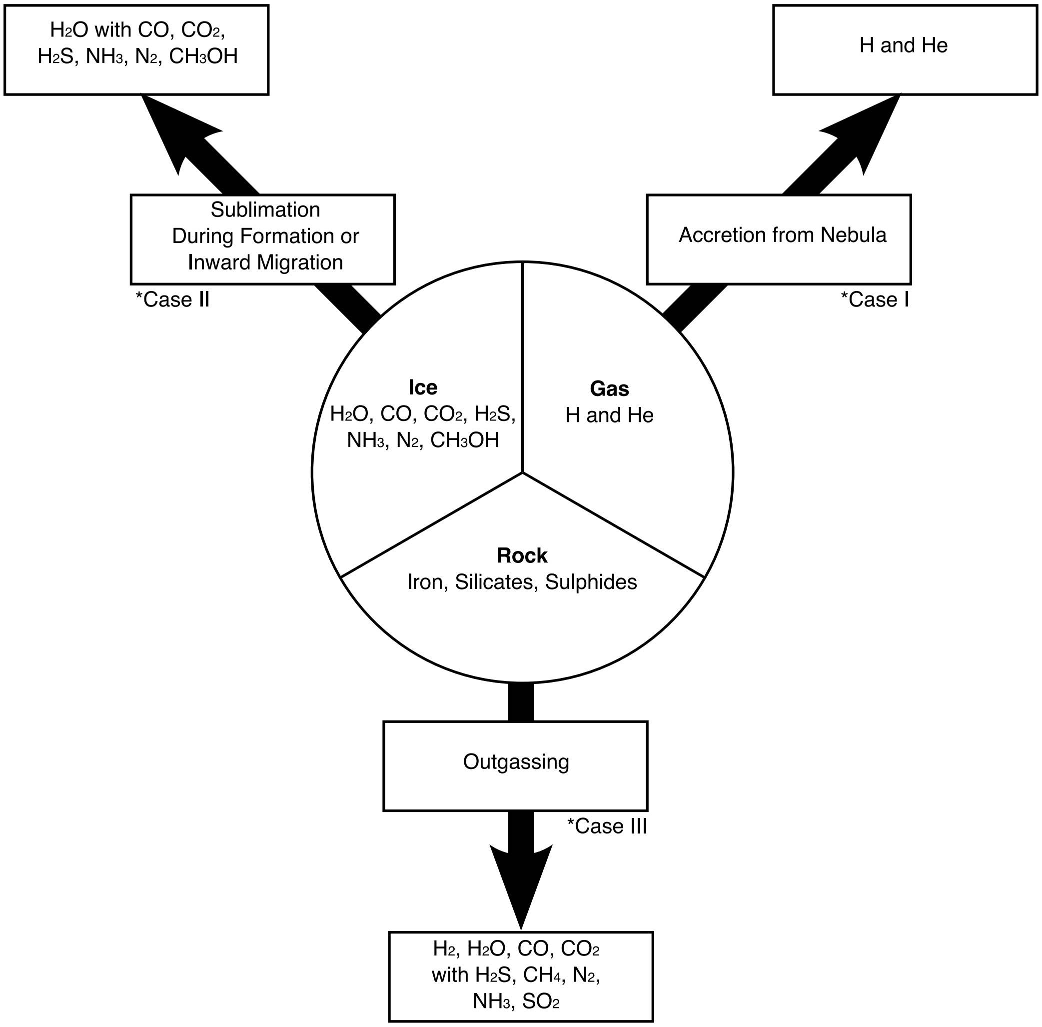

Figure 3-1: Diagram detailing possible sources considered in this work for GJ 1214b's gas layer. The segments of the circle represent the three categories of primordial material that could have contributed to forming GJ 1214b: refractory materials, ice-forming material, and nebular gas. All three categories of primordial material can contribute to an eventual planetary gas layer. The gas formation processes we consider for GJ 1214b are indicated by the black arrows. Each arrow points to a box describing possible initial chemical compositions for the gas contributed by each source. The ice compositions were taken from Marboeuf et al. (2008), and the outgassed atmosphere compositions reflect the chemical equilibrium results of Schaefer & Fegley (2010). The gas layer composition will evolve over time under the influence of atmospheric escape. While primordial gas, ice, and rocks are all given equal fractions of the circle in this diagram, the primordial gas-ice-rock ratios of planets can vary over a wide range and affect the relative importance of the three gas layer sources shown in the diagram. In this work, we consider three end-member cases (labeled as cases I, II, and III) in which a single gas layer source dominated on GJ 1214b; the case associated with each gas formation process is indicated in the diagram.

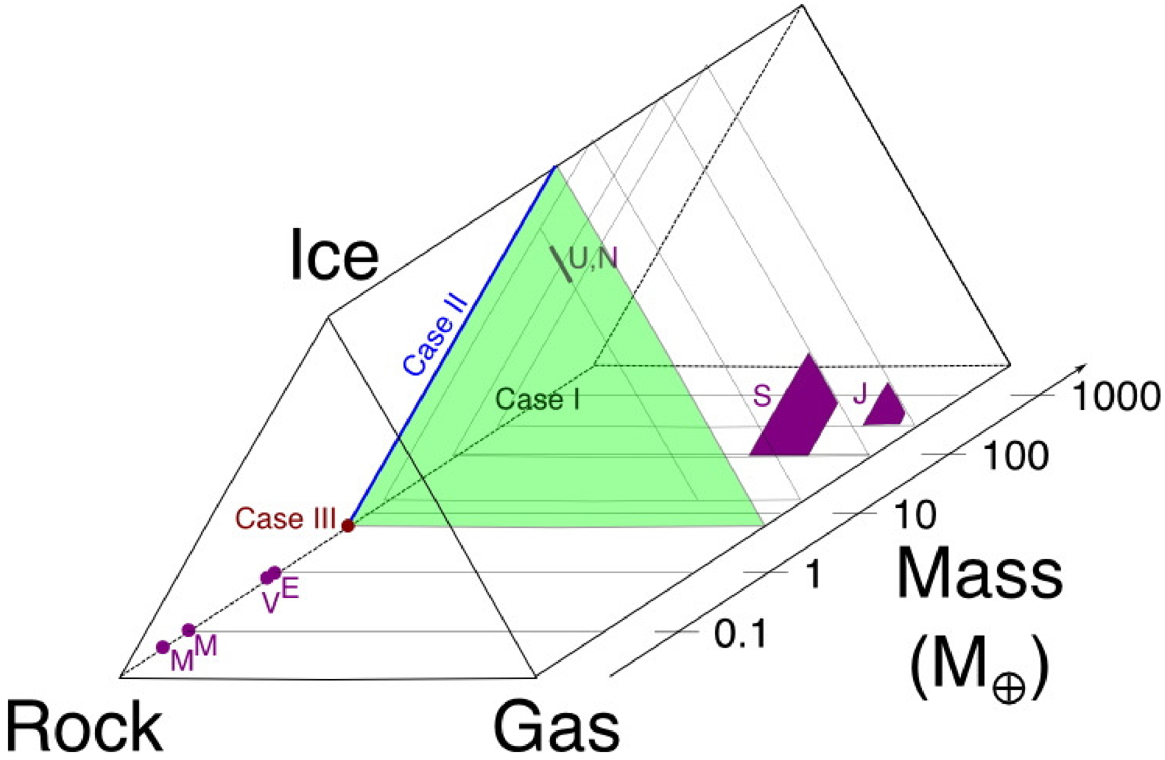

Figure 3-2: Schematic diagram illustrating the range of possible planet primordial bulk compositions. In this figure "gas" refers to primordial H and He accreted from the nebula, "ice" refers to ice-forming materials, and "rock" refers to refractory materials (e.g., iron and silicates). Constraints on the current compositions of the solar system planets are plotted in purple (planets are denoted by their first initial). For GJ 1214b, we consider the full possible range of primordial gas, ice and rock relative abundances. In case I (green), GJ 1214b accreted and retained primordial gas, ices and refractory material. In case II (blue), GJ 1214b did not retain any primordial gas, incorporating only icy and rocky materials. Finally in case III (red), GJ 1214b formed from purely rocky material. Planets in cases II and III, which do not contain any primordial gas, may still harbor a gas layer produced by sublimated ices or by outgassing. This diagram was inspired by Chambers (2010) and Stevenson (2004).

2). In each case, we assume that a single contributor (nebular gas, ice, and rock) dominated as the source for the gas envelope observed today on GJ 1214b. We are thus considering end-member scenarios within the continuum of possible gas envelope compositions. In case I, GJ 1214b managed to accrete and retain H and He gases from the nebula, and includes primordial gas, ice, and rock in its bulk make-up. In this scenario, we neglect any contributions to the gas envelope from the ices or rock, and take the current gas envelope on GJ 1214b to be composed of H and He. In case II, GJ 1214b has an interior formed from icy material and rock and did not retain any nebular gas (either having never accreted any in the first place or having lost any nebular gas that it once had). Here, we assume that vapors from the icy material dominate the gas layer (neglecting any contributions from the rocky material). Finally, in case III, GJ 1214b formed from purely rocky material and did not acquire any ices or gas from the protoplanetary disk. In the absence of accreted ices and gas, the planetary gas envelope must originate by outgassing during formation or tectonic activity.

3.3 Structure Model

Our model for the interior structure of low-mass exoplanets is described in detail in Rogers & Seager (2010a). Here, we give a brief summary.

We assume spherically symmetric and differentiated planets consisting of a core, mantle, ice layer, and gas envelope. The equation for the mass of a spherical shell and the equation describing hydrostatic equilibrium form a coupled set of differential equations for the radius $r(m)$ and pressure $P(m)$, viewed as functions of the interior mass m,

$$\frac{dr}{dm} = \frac{1}{4\pi r^2 \rho} \tag{3.1}$$

$$\frac{dP}{dm} = -\frac{Gm}{4\pi r^4}, \tag{3.2}$$

where ρ is the density and G is the gravitational constant. The equations of state

(EOS)

$$\rho_i = f_i\left(P, T\right) \tag{3.3}$$

relates the density $\rho\left(m\right)$ to the pressure $P\left(m\right)$ and temperature $T\left(m\right)$ within each distinct chemical layer i. We integrate Equations 3.1 and 3.2 imposing that both P and r are continuous across layer boundaries. The outer boundary conditions on the pressure and optical depth are calculated following the procedure described in Rogers & Seager (2010a) so as to take into account the 'transit radius effect' (Baraffe et al., 2003). We then solve iteratively for the core-mantle mass ratio that yields a consistent solution (for a given distribution of mass in the outer layers, set of atmospheric parameters, total planet mass and radius). This is the common general approach for modeling planet interiors (e.g. Valencia et al., 2006; Fortney et al., 2007; Adams et al., 2008; Zeng & Seager, 2008; Baraffe et al., 2008; Figueira et al., 2009; Grasset et al., 2009). The model we use in this work is improved over Rogers & Seager (2010a) by including a temperature-dependent water EOS and is different from most previous planet interior models by providing quantitative constraints on the range of plausible gas envelope masses for a given planet mass and radius.

The thermal profile of our model planets is divided into three regimes: an outer radiative regime in the gas/fluid envelope, an inner convective regime in the gas/fluid envelope, and a solid interior in which thermal effects are neglected. We assume that in the outermost region the planets' gas/fluid envelopes are in radiative equilibrium, and use a temperature profile derived from an analytic "two-stream" solution to the gray equations of radiative transfer for a plane-parallel irradiated atmosphere (Equation (45) in Hansen, 2008). The Hansen (2008) temperature profile describes the temperature $T\left(\tau\right)$ as a function of the optical depth, τ, and depends upon the degree of stellar insolation, internal luminosity of the planet, and the ratio of the thermal to visible opacities (parameterized by T_0, T_{eff}, and γ, respectively). The onset of convective instabilities ($0 < \left(\partial\rho/\partial s\right)_P ds/dm$) delimits the transition to the convective layer of the fluid envelope. In the convective regime, we adopt an adiabatic temperature profile. Finally, within the solid ice, mantle, and core of the planets we neglect the temperature dependence of the EOSs, employing an isothermal temperature profile. At the high pressures found in the solid interior layers, thermal corrections have only a small effect on the mass-density (Seager et al., 2007).

We choose both the fiducial values and uncertainty ranges for the atmospheric parameters in our model (T_0, $T_{\rm eff}$, and γ) following the prescription described in Rogers & Seager (2010a). As our fiducial value of T_0, we take 558 K, the equilibrium temperature of GJ 1214b assuming full redistribution and neglecting reflection. We also consider a range of T_0 values from 789 to 501 K, reflecting uncertainties in the planet's albedo and in the degree to which energy is redistributed within the planet's gas envelope. Planetary bond albedo values up to 0.35 are considered. The parameter $T_{\rm eff}$ describes the intrinsic luminosity of the planet. GJ 1214's old-disk kinematics and lack of chromospheric activity suggest that it has a stellar age between 3 and 10 Gyr (Charbonneau et al., 2009). We employ a simple approximate scaling relation, derived from a power-law fit to cooling calculations from Baraffe et al. (2008), to relate the planets intrinsic luminosity to its mass, radius, and age. For a planetary age of 3-10 Gyr, we estimate a plausible range for the intrinsic luminosity of the planet $T_{\rm eff} = 44 - 69$ K, while adopting a fiducial value of $T_{\rm eff} = 61$ K corresponding to 4.5 Gyr. For gas envelopes composed of some mixture of H and He, we adopt a fiducial value of $\gamma = 1$ and consider a range from $\gamma = 0.1$ to 10. Because the opacity of water is far higher in thermal wavelengths than in the visible, we expect that $\gamma < 1$ in a water envelope. For our water vapor atmospheres we thus adopt a fiducial value $\gamma = 0.1$ and consider an uncertainty range from $\gamma = 0.01$ to 1.

In the solid (uniform temperature) layers of the planet we employ EOS data sets from Seager et al. (2007) which were derived by combining experimental data at $P \lesssim 200$ GPa with the theoretical Thomas-Fermi-Dirac equation of state at high pressures, $P \gtrsim 10^4$ GPa. We consider Fe (ϵ) (Anderson et al., 2001), $Mg_{1-\chi}Fe_{\chi}SiO_3$ perovskite (Elkins-Tanton, 2008), and H_2O ice (Hemley et al., 1987). To describe hydrogen and helium envelopes we use EOSs for H/He mixtures from Saumon et al. (1995) and opacity tables from Freedman et al. (2008) and Ferguson et al. (2005). We have compiled a temperature-dependent EOS for water up to 32 GPa spanning liquid, vapor, super-fluid, and plasma phases. Our water EOS combines data from the "The IAPWS Formulation 1995 for the Thermodynamic Properties of Ordinary Water Substance for General and Scientific Use" (IAPWS-95; Wagner & Pruß, 2002) retrieved from the NIST Chemistry WebBook (Lemmon et al., 2009), extrapolations of the IAPWS-95 formulation calculated using FLUIDCAL software (Wagner, 2009), and the Thomas-Fermi-Dirac EOS (Salpeter & Zapolsky, 1967). For the opacity in the water vapor layer we use Planck means calculated with molecular line data from Freedman et al. (2008).

3.4 Results

3.4.1 Background

We consider three cases for the interior makeup of GJ 1214b: I) a planet that formed from nebular gas, ice, and rock and still harbors a primordial H/He envelope; II) an ice-rock planet that failed to accrete H/He gas from the protoplanetary disk but now has a vapor envelope; III) a rocky planet with an outgassed atmosphere (Figures 3-1 and 3-2). These scenarios determine what distinct chemical layers we consider in our differentiated planet model described in Section 3.3. We assume $Y = 0.28$ H/He for the nebular gas, and pure H_2O ice for the icy material. We model the rocky material by a combination of metallic iron and $Mg_{0.9}Fe_{0.1}SiO_3$ silicates without imposing any a priori constraints on the iron-to-silicates ratio. We assume that, during GJ 1214b's formation, the primordial rocky material differentiated to form an iron core and silicate mantle in the planet. In this way, the rocky material contributes two layers in our planet interior structure model. The effect of choosing other chemical compositions to represent the primordial gas, ice, and rock is discussed in Section 3.5.5.

We say that an interior composition is consistent with the measured planetary mass and radius within their $n\sigma$ observational uncertainties if there is some choice of planet mass within $\left(M_p - n\sigma_{M_p}, M_p + n\sigma_{M_p}\right)$, planet radius within $\left(R_p - n\sigma_{R_p}, R_p + n\sigma_{R_p}\right)$, and atmospheric parameters (T_{eff}, T_0, and γ) within the ranges given in Section 3.3

that yields a consistent solution for the interior composition. A more sophisticated error analysis (such as that described in Rogers & Seager, 2010a) is not yet warranted given the current error bars on GJ 1214b's mass and radius.

We employ ternary diagrams to graphically present our composition constraints for each scenario (Figures 3-3 and 3-4). Ternary diagrams are useful tools to graphically represent three component data (x, y, z) for which the components are constrained to be positive $(x, y, z \geq 0)$ and to have a constant sum $(x + y + z = 1)$. Since such data have only 2 degrees of freedom, it could easily be displayed with a x-y Cartesian plot, wherein the axes and the $z = 0$ line would form a right triangle. To show all three components (x, y, z) on an equal footing, the x-y Cartesian plot can be squished (via a linear transformation) so that the x and y axes meet at a 60° angle and form an equilateral triangle with the $z = 0$ line. The resulting equilateral triangle diagram is a ternary diagram. The three vertices of the diagram represent points where $x = 1$, $y = 1$, and $z = 1$, while $x = 0$, $y = 0$, and $z = 0$ along the respective opposing edge. At each interior point, the value of x is given by the perpendicular distance from the $x = 0$ edge, with the values of y and z defined analogously. More detailed descriptions of how to read ternary diagrams can be found in Valencia et al. (2007a) and Zeng & Seager (2008).

3.4.2 Case I: Gas-Ice-Rock Planet with Primordial Gas Envelope

We first consider the case in which GJ 1214b managed to acquire and retain H/He gas from the protoplanetary disk. In this scenario GJ 1214b incorporated primordial iron, silicates, ice, and gas into its bulk make-up. We thus allow for four chemically distinct layers in the planet interior: an iron core, silicate mantle, water-ice layer, and H/He envelope (with $Y = 0.28$).

Despite the range of allowed compositions, the mass of GJ 1214b's H/He gas envelope is tightly constrained (Figure 3-3). A gas mass fraction of 0% is not allowed within the 1σ observational error bars on M_p and R_p. The maximum and minimum gas envelope masses in this scenario occur for end-member mass distributions where the gas envelope surrounds a pure iron interior and a pure water ice interior, respectively. For $M_p = 6.55\ M_\oplus$, $R_p = 2.678\ R_\oplus$, the mass in the gas layer could be at most 3.6%-5.2% of the planet mass depending on the atmospheric thermal profile (hotter atmospheres require less mass of H and He to occupy a similar volume). When M_p and R_p are varied within their 1σ observational uncertainties, the range of maximum H/He mass fractions widens to 3.2%-6.8%. The minimum gas mass fraction is more sensitive than the maximum to the atmospheric energy budget and composition (e.g., metallicity and opacities) and could be in the range 9×10^{-5} and 2×10^{-3} at the fiducial planetary mass and radius.

In this scenario, GJ 1214b has a less massive H/He envelope than our solar system Neptune, whose composition is roughly 5%-15% H and He, 60%-70% ices, and 25% rocks by mass (Podolak et al., 1991; Hubbard et al., 1995). GJ 1214b could, nonetheless, support a gas envelope that is large as compared to the terrestrial solar system planets. For a Ganymede-like interior with iron:silicates:water ice in the ratio 3:22:75 by mass, GJ 1214b requires an H/He envelope accounting for between 0.01% and 0.6% of the planetary mass depending on the atmospheric temperature. This is up to 60 times larger than the atmosphere mass fraction on Venus ($\sim 10^{-4}$).

3.4.3 Case II: Ice-Rock planet with Sublimated Vapor Envelope

A planet interior dominated by ice and a concomitant gas envelope dominated by vapors from ice-forming materials is an intriguing possibility for GJ 1214b. This scenario is substantially different from any of the solar system planets, but could be thought of as a class of bigger, hotter versions of Jupiter's icy moons. Kuchner (2003) and Léger et al. (2004) first proposed that water-rich planets might be prevalent on orbits accessible to transit and radial velocity detections, although no such planets have been conclusively discovered so far. The formation pathway for these planets involves inward migration of proto-planets that formed from volatile ice-rich material beyond

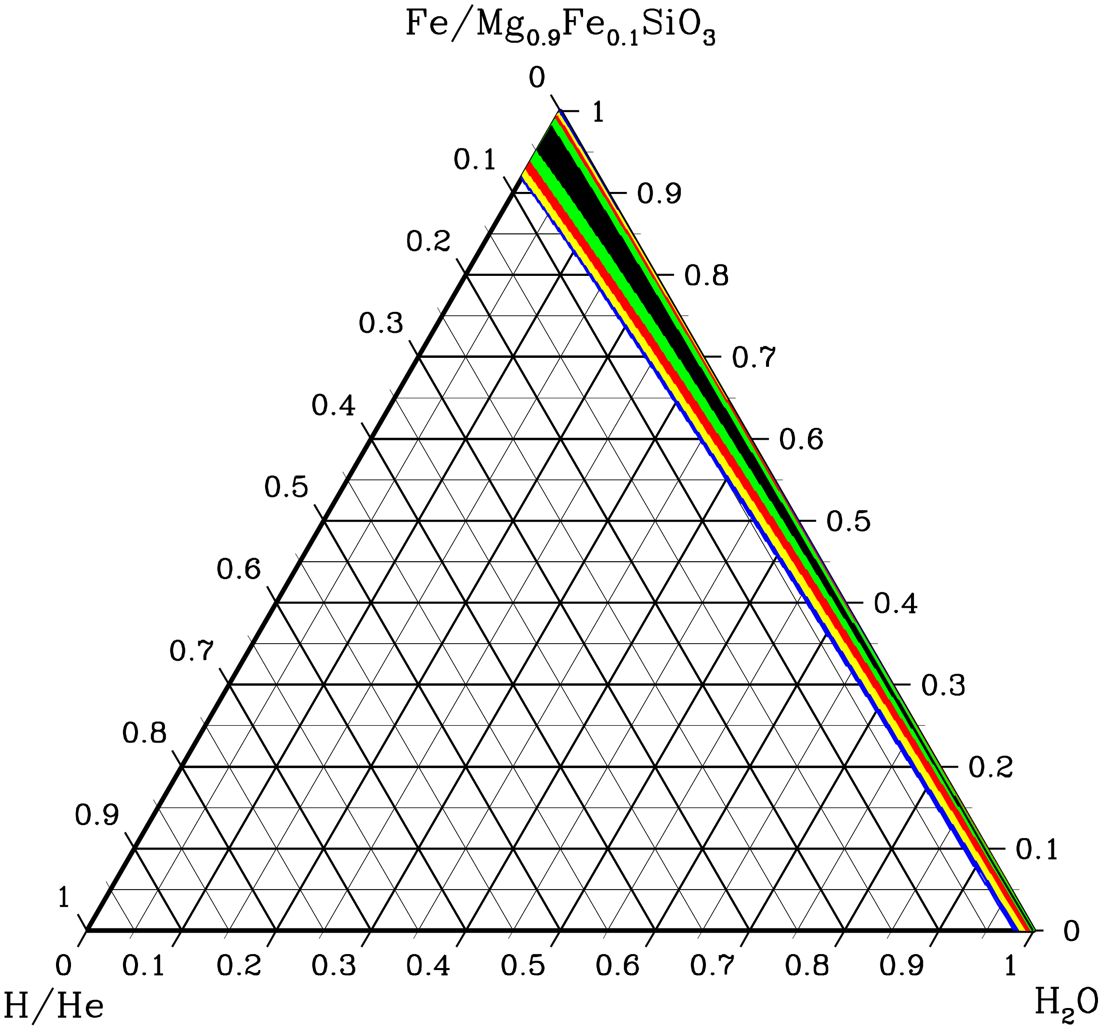

Figure 3-3: Ternary diagram for case I in which GJ 1214b retained a primordial H/He envelope, having formed from primordial gas, ice, and rock. The relative contributions of the iron core, $Mg_{0.9}Fe_{0.1}SiO_3$ mantle, H_2O ices, and H/He envelope to the mass of the planet are plotted. The core and mantle are combined together on a single axis, with the vertical distance from the upper vertex determined by the fraction of the planet's mass in the two innermost planet layers. The black shaded region denotes the interior compositions that are consistent with the nominal planet mass and radius ($M_p = 6.55\ M_{\oplus}$, $R_p = 2.678\ R_{\oplus}$) for our fiducial choice of atmospheric parameters ($\gamma = 1$, $T_0 = 558$ K, $T_{\text{eff}} = 61$ K). The H/He mass fraction has a spread in this case due to the range of possible core-to-mantle mass ratios. The span of plausible interior compositions widens to the green shaded area when the range of atmospheric parameter values delimited in Section 3.3 is considered. The red, yellow, and blue shaded regions denote compositions that are consistent with M_p and R_p to within 1, 2, and 3σ of their observational uncertainties, respectively, when uncertainties in the atmospheric parameters are also included.

the snow line but that never attained masses sufficient to accrete large amounts of H/He nebular gas. If GJ 1214b falls into this category, it could be the first discovered member of a whole new population of exoplanets.

For this scenario, in which GJ 1214b did not accrete or retain any H or He from the protoplanetary disk, we adopt an interior planet structure consisting of an iron core, silicate mantle, and water envelope. The pressure-temperature (PT) profile determines the phase of water in the envelope; vapor, liquid, super-fluid, high pressure ices, and plasma phases are all included in our H_2O EOS. We model the thermal profile of the water envelope following the same prescription as for the H/He layers (described in Section 3.3). To allow for the presence of a greenhouse effect, we take $\gamma = 0.01 - 1$ for H_2O (compared to $\gamma = 0.1 - 1.0$ for H and He).

We show in Figure 3-4 the possible distributions of mass between the core, mantle, and water envelope that are consistent with the measured mass and radius of GJ 1214b. A sublimated vapor dominated envelope on GJ 1214b is possible if water accounts for a large fraction of planet mass. At the fiducial measured planet mass and radius ($M_p = 6.55\ M_\oplus$, $R_p = 2.678\ R_\oplus$) at least 88% H_2O by mass is required. To account for the observed planet mass and radius within their 1, 2, and 3σ observational uncertainties, at least 47%, 24%, and 6% water by mass are required, respectively. Léger et al. (2004) and Selsis et al. (2007b) have put forward that ice-rock planets formed beyond the snow line may have a comet-like bulk composition with 50% H_2O and 50% silicates and iron by mass. This composition is consistent with the measured GJ 1214b radius within 1σ. Interior structure considerations do not preclude the possibility that GJ 1214b is water rich.

GJ 1214b does not contain liquid water in any of our model interiors displayed in Figure 3-4. The PT profiles that result from the range of equilibrium temperature and internal heat flux (T_0 and T_{eff}) values we considered are too hot to allow liquid water, even at high pressures. Our putative GJ 1214b water envelopes begin in the vapor phase at low pressures, then continuously transition to a super-fluid at $P = 22.1$ MPa (the critical pressure of water), before eventually becoming an electronically conductive dense fluid plasma at greater depths ($T \gtrsim 4000$ K).

To obtain liquid water in our model interior, we must decrease GJ 1214b's assumed intrinsic energy flux below 5×10^{-4} W m^{-2} or $T_{\rm eff} \lesssim 10$ K; for comparison, Earth's internal heat flux is 0.087 W m^{-2} (Turcotte & Schubert, 2002). The intrinsic luminosity of GJ 1214b is very uncertain, and a detailed evolution calculation to better constrain its magnitude is out of the scope of this work. Nonetheless, we predict that, in this scenario, GJ 1214b would need a cold interior in order to harbor liquid water.

Our conclusions regarding the possibility of liquid water in an extended vapor atmosphere on GJ 1214b are contingent upon our parameterized PT profile adequately describing the water envelope. It is important to note that our model thermal profile assumes GJ 1214b is in radiative equilibrium with the incident stellar irradiation it receives at its current orbital location. If GJ 1214b has recently migrated and is undergoing active vaporization (as in the scenarios considered by Kuchner (2003) and Valencia et al. (2010)) it could have temperature and H_2O-phase profiles within its envelope that are very different from those available within the framework of our models (e.g., atmospheres with a temperature inversion or those out of radiative-convective equilibrium).

3.4.4 Case III: Rocky Planet with Outgassed Atmosphere

We turn to the possibility that GJ 1214b formed from purely rocky material without retaining any H/He gas or icy material from the protoplanetary disk. We reiterate that GJ 1214b must still have a substantial gas layer in this case, because a rocky planet is too dense to account for the measured mass and radius (e.g., a gasless Earth-like composition yields a planet radius that is 8σ lower than that measured for GJ 1214b). In this rocky planet scenario, an outgassed atmosphere contributes to the GJ 1214b transit radius. We focus here on an atmosphere produced by outgassing during planet formation; outgassing from post-formation geological activity is another possibility, which is discussed in Section 3.5.3.

It is difficult to predict a priori the composition of the gas layer that would be produced by outgassing on GJ 1214b. The initial composition of the outgassed atmosphere is strongly dependent on the composition of planetesimals comprising GJ 1214b.

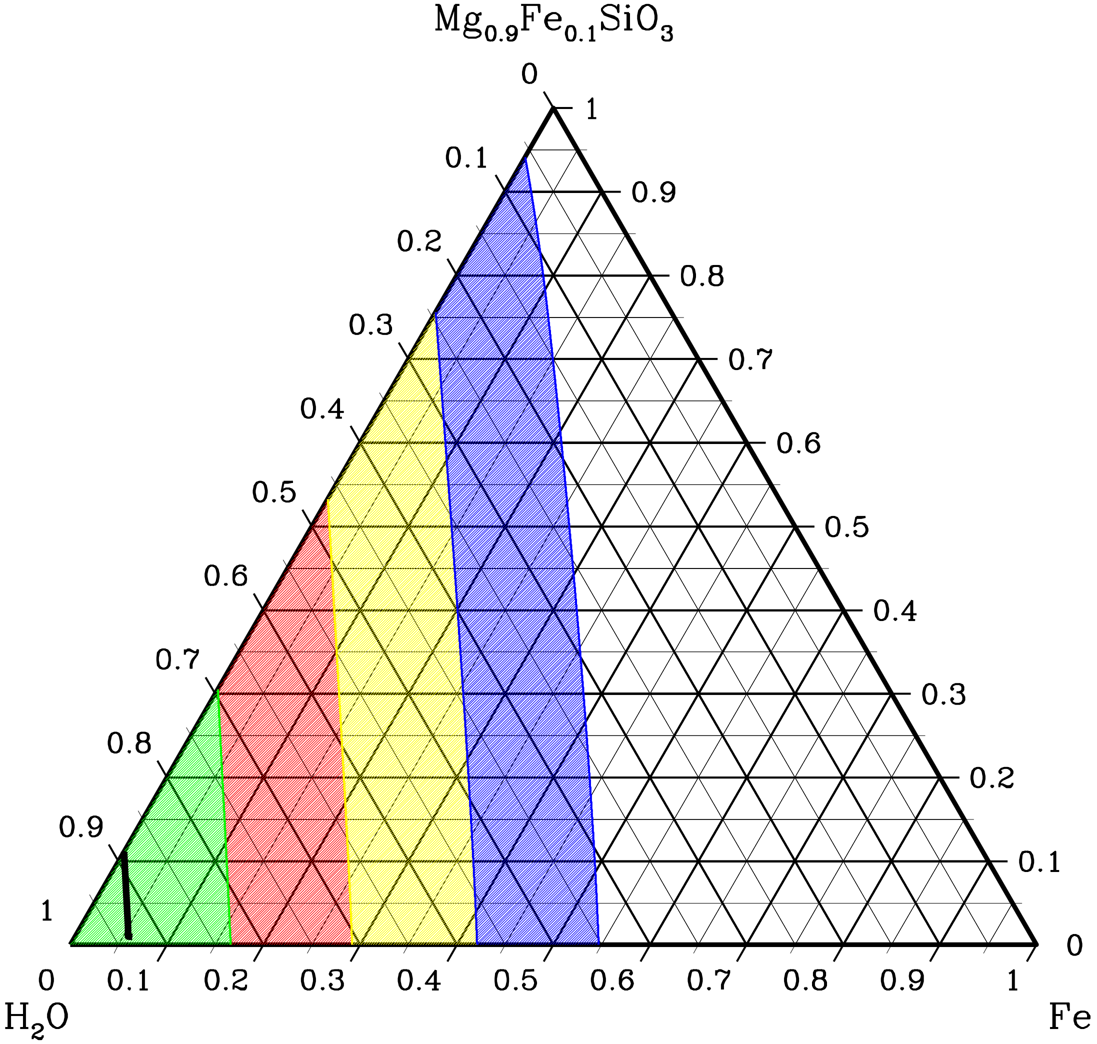

Figure 3-4: Ternary diagram for case II in which GJ 1214b formed from refractory material and ices and has an envelope dominated by vapor from sublimated ice. The fractions of the planet's mass in the Fe core, the $Mg_{0.9}Fe_{0.1}SiO_3$ silicate mantle, and the water vapor envelope are plotted on the three axes. The solid black curve represents the locus of interior compositions that are consistent with the nominal planetary mass and radius ($M_p = 6.55\ M_\oplus$, $R_p = 2.678\ R_\oplus$) for our fiducial choice of atmospheric parameters ($\gamma = 1$, $T_0 = 558$ K, $T_{\rm eff} = 61$ K). The colors in this figure have the same designations as in Figure 3-3.

Even among solar system chondrites, the outgassed atmosphere compositions would range from H_2-dominated, to H_2O-dominated, to CO-dominated, to CO_2-dominated (Schaefer & Fegley, 2010). In addition, the conditions during magma solidification and outgassing affect the gas layer outcome (Elkins-Tanton & Seager, 2008b; Schaefer & Fegley, 2010). Further complicating the rocky planet gas layer, is the subsequent atmospheric escape (Charbonneau et al., 2009) and photochemistry. Despite this uncertainty in composition, we can nevertheless make some concrete statements about a putative outgassed envelope on GJ 1214b.

If GJ 1214b's gas layer was produced by outgassing, a substantial fraction of it must be in a component that is less dense than water vapor. The light component is needed for GJ 1214b's envelope to have both a mass low enough to be produced by outgassing and a volume large enough to account for the transit radius. From our study of case II, we found that if water is the least dense component of GJ 1214b, at least 47% H_2O by mass is required within 1σ (Figure 3-4). This is more water than a terrestrial planet formed from chondritic planetesimals can degas (up to 23% by mass) (Elkins-Tanton & Seager, 2008b). Volatile molecules heavier than water (such as CO, CO_2, and N_2) have even smaller upper bounds (in % planet mass) on the amounts they can be outgassed. The requirement for substantial quantities of a light species is interesting because it limits the outgassed atmosphere compositions that can be relevant to GJ 1214b from among the wide range of a priori possibilities. In particular, an Earth-like N_2-dominated outgassed atmospheric composition and a Venus-like CO_2 outgassed atmosphere are both ruled out for GJ 1214b.

Molecular hydrogen, H_2, is the most likely candidate for an atmospheric species that is both light enough and plausibly outgassed in sufficient quantities to account for GJ 1214b's transit radius. In fact, H_2 is predicted to dominate the atmospheres outgassed by ordinary H, L, LL, and high iron enstatite EH chondrite-composition planetesimals (Elkins-Tanton & Seager, 2008b; Schaefer & Fegley, 2010). Although He has a low molecular weight, it does not bind to minerals the way H does, and consequently it cannot be accreted with the rocky primordial material and later released through outgassing (Elkins-Tanton & Seager, 2008b). The other possible species, CH_4 and NH_3, have molecular weights only slightly lower than water and are not typically outgassed in large quantities.

We emphasize that only a relatively small “out-gassable” amount of H_2 is required to account for GJ 1214b’s transit radius. We show this quantitatively by considering a pure hydrogen gas layer surrounding a rocky interior in Figure 3-5. Just 5×10^{-4} of the planet mass in H_2 surrounding a rocky core is sufficient to account for the transit radius to within 1σ. This is 2 orders of magnitude below the maximal amount of hydrogen that might be outgassed by a rocky planet (6% of the planet mass), which corresponds to the extreme where the planet formed from planetesimals similar to EH chondrites and fully oxidized during formation (Elkins-Tanton & Seager, 2008b). For an iron core mass fraction similar to Earth’s (30%), GJ 1214b needs 0.3%-1.2% of its mass in a pure H_2 gas layer at the nominal mass and radius. This H_2 gas layer is small compared to the H_2O envelopes in the water planet scenario, but is still large compared to Earth’s atmosphere (which accounts for roughly 0.0001% of Earth’s mass).

A pure H_2 envelope as we have assumed above is somewhat artificial; realistically H_2 will not be outgassed on its own but in combination with heavier molecules. At a given Fe core mass fraction, including H_2O, CO, CO_2, and other additional species in the outgassed envelope would in general tend to decrease the mass fraction of H_2 required to reproduce the planet radius (Figure 3-5), while increasing the total gas mass fraction of all volatile species combined. This is because *i)* the heavier outgassed volatiles are still less dense than silicates and *ii)* the additional atmospheric species would increase the opacity of the atmosphere. This strengthens the result that an outgassed hydrogen-rich envelope surrounding a rocky solid interior is not ruled out by the measured mass and radius of GJ 1214b. We consider how this interpretation is influenced when atmospheric escape is taken into account in Section 3.5.2.

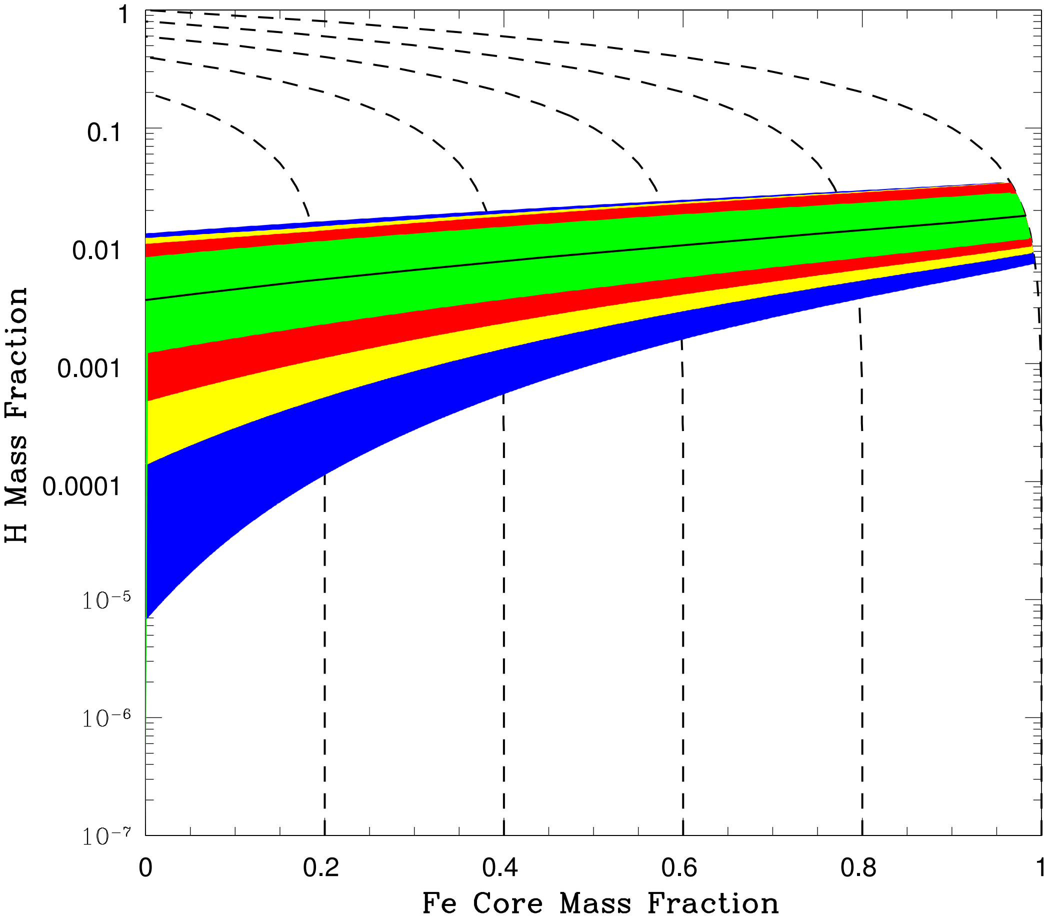

Figure 3-5: GJ 1214b as a rocky planet with an outgassed atmosphere. A three-layered planet structure composed of an iron core, silicate mantle, and pure hydrogen envelope is assumed. The fraction of the planet's mass in the hydrogen gas envelope is plotted as a function of the fraction of the planet's mass in the iron core. Any mass not in the hydrogen envelope or iron core is contained in the silicate mantle; the dashed black lines represent contours of constant mantle mass fraction. The colored shaded regions have the same designations as in Figure 3-3.

3.5 Discussion

3.5.1 Atmosphere Observations

What further observations can discriminate among the gas layer origin possibilities? A promising possibility is spectral observations of the planetary atmosphere. Here, we summarize some ideas for how atmospheric spectra might help to distinguish between a gas envelope dominated by nebular gas, sublimated ices, or outgassing.

Atmospheric He is the discriminator between captured H/He envelopes or outgassed envelopes (Elkins-Tanton & Seager, 2008b). He is difficult to observe spectroscopically at planetary temperatures, however. Recent outgassing by geological activity could be revealed through the detection of spectral features from species with short photochemical lifetimes such as SO_2 (Kite et al., 2009). A water vapor dominated atmosphere would have saturated water vapor features (e.g., absorption bands at $\lambda \sim 5 - 8\mu$m and $\lambda \sim 16 - 18\mu$m Léger et al. (2004)), but these may not be unique identifiers. Discriminating between a hydrogen-rich envelope and a water vapor atmosphere on the basis of the atmospheric scale height (Miller-Ricci et al., 2009) might be more promising than discriminating on the basis of the presence or absence of spectral lines. The scale height is accessible via the depth of strong (or saturated) transit transmission spectral features. Although it will be tricky to constrain interior compositions from atmospheric spectra, the prospect of greater insights into the composition and formation of GJ 1214b and its envelope is compelling.

3.5.2 Atmospheric Escape

We cannot definitely rule out any of our three composition scenarios on the basis of atmospheric escape calculations. The water vapor envelope in case II is most resilient against atmospheric escape. While mass loss is a more important consideration for the hydrogen-rich primordial and outgassed envelopes in cases I and III, uncertainties in the mass-loss rate and planet age leave room for the possibility that GJ 1214b retained sufficient H/He or H_2 to account for its transit depth. Further observations are warranted to tighten the constraints on the origin and character of GJ 1214b's gas layer.

Atmospheric escape may have an important influence on mass and composition evolution of the GJ 1214b gas envelope. We calculate 2×10^6 kg s^{-1} for an energy-limited upper bound on the current mass-loss rate of GJ 1214b following the approximate approach of Lecavelier Des Etangs (2007). This is on the same order as the 9×10^5 kg s^{-1} escape rate Charbonneau et al. (2009) predicted for a hydrogen-rich atmosphere escaping hydrodynamically from GJ 1214b. At 2×10^6 kg s^{-1}, 0.03 $M_\oplus$ would be lost over 3 Gyr and 0.1 $M_\oplus$ would be lost over 10 Gyr. The actual cumulative mass lost over GJ 1214b's lifetime may be much higher than these values because the host star was probably brighter in UV at earlier times.

Out of the three cases we considered for GJ 1214b's composition, case II, the ice-rock scenario having a water vapor envelope, is most robust against atmospheric escape. First, water has a higher molecular weight than H or He which makes it easier to retain (although photodissociation of H_2O may be important). Second, with H_2O comprising upward of 50% of GJ 1214b's current mass in this scenario, a cumulative water loss on the order of 0.1 $M_\oplus$ will not have significantly changed the overall character of the planet. In contrast, losses of this magnitude are far more significant for the hydrogen-rich envelopes considered in cases I (primordial gas dominated) and III (outgassing dominated), since these envelopes can account for at most a few percent of GJ 1214b's current mass.

In case I, atmospheric escape increases the amount of gas GJ 1214b would have needed to accrete from the protoplanetary nebula. Protoplanetary cores between 1 and 10 $M_\oplus$ can acquire substantial primordial atmospheres even if the cores are too small for the nucleated instability and runaway gas accretion to commence (Mizuno, 1980). For instance, Rafikov (2006) found that a 6.5 $M_\oplus$ core in a minimum mass solar nebula could develop an atmosphere of up to several tenths of an Earth mass of nebular gas (depending on the core's semimajor axis and accretion luminosity). Whether GJ 1214b could accrete and retain enough nebular gas to account for its transit radius is ambiguous.

Atmospheric mass loss creates the most tension with case III, because there is an upper bound on the cumulative amount of gas GJ 1214b can outgas over its lifetime. Based on solar system meteorites, a rocky planet can outgas at most 6% of its mass as hydrogen (Elkins-Tanton & Seager, 2008b) and less will be outgassed if the iron content of the rocky material is not fully oxidized. It is likely that GJ 1214b has lost most of any H-atmosphere outgassed during formation. However, only $\sim 0.1\%$ of the planet mass in H_2 surrounding a rocky core could be needed to account for the transit radius to within 1σ. Due to the large uncertainties on the planet age and time averaged mass-loss rate, the outgassing cannot be fully ruled out as the source of GJ 1214b's gas layer.

3.5.3 Ongoing Outgassing

If GJ 1214b is a rocky planet with an outgassed atmosphere as in case III, ongoing outgassing by geological activity could be contributing to its gas envelope. However, the rate of ongoing outgassing is expected to be smaller than the atmospheric escape rate. Kite et al. (2009) predict that a $\sim 6.5\ M_\oplus$ super Earth experiencing plate tectonics would have rates of volcanism per unit planet mass 6 times Earth's current rate at planet age of 3 Gyr and 0.2-0.3 times Earth's current rate at a planet age of 10 Gyr. Lower rates of volcanism are predicted for planets 3-10 Gyr old that are not tectonically active. If we consider the most optimistic case for the rate of volcanism of GJ 1214b and assume a magma volatile content similar to volatile-rich terrestrial magmas at mid-ocean ridges (1.5% H_2O and 400 ppm CO_2 by mass Oppenheimer (2003)), we obtain an upper limit on the volcanic outgassing rate of $1 \times 10^6\ \mathrm{kg\,s^{-1}}$ H_2O and $4 \times 10^4\ \mathrm{kg\,s^{-1}}$ CO_2. Although outgassing by geological activity may help to replenish the GJ 1214b envelope, it probably cannot completely offset the effect of atmospheric escape if the planet is older than 3 Gyr.

3.5.4 Necessity of a Gas Layer

GJ 1214b's low average density implies that it has a low density gas envelope. This statement is valid as long as the true planet mass and radius lie within the 2σ measurement uncertainties. If GJ 1214b's mass and radius both differ from their measured values by more than $\sim 2\sigma$, a solid, ice-dominated interior composition with no gas envelope is barely allowed. A pure ice planet seems physically implausible, however, because silicates (i.e., higher density material) are expected to be accreted along with ices during planet formation. Charbonneau et al. (2009) point out, however, that the stellar radius they derived for GJ 1214 from observations is 15% larger than that predicted by the theoretical models Baraffe et al. (1998). If systematics have led to an overestimation of the planet radius, the evidence for a gas layer on GJ 1214b would be reduced.

3.5.5 Model Uncertainties

Despite our quantitative constraints on the range of interior compositions, we are faced with some uncertainties. One uncertainty is the atmospheric temperature, controlled by the unknown interior energy and unknown albedo. A hotter atmosphere fills a larger volume than a cooler atmosphere, requiring less atmospheric mass to fit the planet radius. We have chosen a range of reasonable values for the parameters governing the atmospheric PT profile (Section 3.3) and found that the model uncertainty is roughly comparable to the observational uncertainties. Although we adopted nearly identical atmospheric parameter ranges for all three interior structure cases we considered, in reality GJ 1214b's albedo, atmospheric absorption, and interior luminosity are coupled to its interior composition.

The precise chemical make-up of GJ 1214b's interior layers is another source of uncertainty. We have adopted artificially clean single-chemical materials to represent GJ 1214b's core (pure Fe), mantle ($Mg_{0.9}Fe_{0.1}SiO_3$ perovskite), and ice layer (pure H_2O). In reality, we expect a mixture of chemical compounds to contribute to each layer. The presence of a light element (such as sulfur) in the iron core would decrease the mass required in the low-density outer envelope. In contrast, a higher iron content in the mantle would increase the density of the planet interior, requiring a higher mass fraction of gas. While H_2O should dominate any primordial ices forming GJ 1214b (contributing more than $\gtrsim 60\%$ by mass), substantial quantities (more than 1% by mass) of CO, CO_2, H_2S, NH_3, N_2, and CH_3OH are also expected in ices formed from a protoplanetary disk of roughly solar composition (Marboeuf et al., 2008). The presence of significant quantities of CO_2 could have dramatic effects on the evolution and thermal structure of a water planet, maintaining the steam atmosphere in a hot state (Léger et al., 2004). It is important to note that the range of possibilities for the chemical materials comprising GJ 1214b's interior is constrained by the cosmic abundance of the elements. We have focused on possible silicate-based interior composition scenarios for GJ 1214b. Alternatively, SiC, graphite, and other carbon compounds could dominate the interiors of planets formed under conditions where $C/O > 1$ by number (Kuchner & Seager, 2005), but we have not considered this possibility here.

We find that the choice of opacities used to model the GJ 1214b envelope has a considerable effect on the H/He mass fraction constraints in case I. Freedman et al. (2008) opacities were used to generate the composition constraints shown in Figure 3-3. The Ferguson et al. (2005) opacities, which include condensate and grain opacity sources, tend to be higher overall than the Freedman et al. (2008) opacities, which do not include grain opacity sources. Consequently, gas envelopes modeled with the Ferguson et al. (2005) opacities systematically require less H/He mass to reproduce the observed transit radius than those modeled with the Freedman et al. (2008) opacities. This illustrates that the relationship between the radial thickness of an H/He envelope and its mass is sensitive to the precise metallicity and composition assumed. Despite the added uncertainty introduced by the metallicity of the H/He layer our inferences regarding the plausibility of a primordial gas envelope on GJ 1214b remain unchanged.

3.6 Summary and Conclusions

The MEarth transiting planet, GJ 1214b, is exciting because it lies in a mass and density regime for which there are no solar system analogs; GJ 1214b is smaller than the ice giants Neptune and Uranus, while larger than the terrestrial Earth, Venus, and Mars. We emphasize that, based on its measured planetary mass and radius alone, we can constrain GJ 1214b's composition but we cannot infer its unique true composition.

GJ 1214b requires a gas envelope to account for its low average density so long as the true planet mass and radius lie within 2σ of their measured values. With interior structure models, we explored three possible scenarios for the gas layer and concomitant interior of GJ 1214b. An important conclusion from this investigation is that, under most of the conditions we considered, GJ 1214b would not have liquid water. We summarize more detailed results for each of the three cases below.

If GJ 1214b's gas layer was accreted directly from the protoplanetary nebula, the primordial H/He layer surrounding an interior of iron, silicates, and ice would need to contain between 0.01% and 5% of the planet mass in order to account for the transit radius. This is interesting because the gas envelope would be less massive than Uranus' and Neptune's envelopes (which account for 5%-15% of the planet mass), yet greater than Earth's or Venus' atmospheres (which contribute 0.0001% and 0.01% of the planet mass, respectively).

If, instead, sublimated ices dominate the gas layer, a massive water envelope comprising at least 47% of the planet mass could account for GJ 1214b's observed parameters to within 1 σ. We thus do not require an H/He layer to explain the measured mass and radius. In this sublimated ice-dominated case, for our assumptions about the planet albedo ($A \leq 0.35$) and internal heat flux, we find that GJ 1214b's water envelope would generically be too hot to allow liquid water, even at high pressures. Instead of a liquid water layer the planet would have a super-fluid water layer sandwiched between plasma below and vapor above. To obtain liquid water in our model interior, we must decrease GJ 1214b's assumed intrinsic energy flux to $\lesssim 0.01$ of Earth's intrinsic energy flux.

Third, if the nascent GJ 1214b did not manage to retain any primordial gas or ices, outgassing from rocky material could produce a gas layer surrounding a terrestrial interior. In order for sufficient gas to be released in this scenario to account for the transit radius, the outgassed atmosphere would need to be hydrogen rich. This in turn constrains the mineralogy of the primordial rocky material from which GJ 1214b would need to have formed in this case. Based on models of outgassing of chondritic material found in the solar system, even if hydrogen is the dominant outgassed species other heavier volatiles would be present as well. It is also expected that atmospheric escape would have eroded a substantial amount of the H atmosphere (Charbonneau et al., 2009), which provides added tension with this scenario. Although outgassing is not ruled out as the primary contributor of GJ 1214b's gas layer, more modeling is required to verify its viability.

The ideal hope is that we may gain insights into planet migration and formation if future observations succeed in constraining the composition of GJ 1214b's atmosphere and then by extension the planet's interior. Despite the link between atmospheres and interiors, we caution that the solar system planet atmospheres, especially terrestrial atmospheres that have undergone substantial evolution, are divorced from their interiors. Progress toward constraining GJ 1214b's interior might thus be challenging. Additional complications arise from the fact that multiple processes may have contributed to the gas layer on GJ 1214b. Nevertheless, here are some hopeful possible outcomes. If GJ 1214b's gas layer is found to have close to solar abundance of He, then it is likely composed of nebular gases, and together with atmospheric escape estimates may yield bounds on the accretion of gas from protoplanetary disks by small planetesimals. If instead sublimated ices dominate with no observable H and He, it would indicate that GJ 1214b formed beyond its star's snow line and migrated inward to its current orbital distance. Finally, if GJ 1214b's envelope has no He but a substantial amount of H and other volatiles, it would likely be the result of outgassing, and may help to constrain its atmospheric mass-loss rate and the broad-brush oxidation properties of the rocky material from which GJ 1214b formed. No matter which atmospheric sources turn out to be dominant on GJ 1214b (be it nebular gas, sublimated vapors, or outgassing) we will learn something interesting, and perhaps achieve our first glimpse of a planetary atmosphere on a whole new class of low-mass exoplanets.

Chapter 4

Formation and Structure of Low-Density Exo-Neptunes

Abstract

Kepler has found hundreds of Neptune-size (2–6 $R_\oplus$) planet candidates within 0.5 AU of their stars. The nature of the vast majority of these planets is not known because their masses have not been measured. Using theoretical models of planet formation, evolution, and structure, we explore the range of minimum plausible masses for low-density exo-Neptunes. We focus on highly irradiated planets with $T_{\rm eq} \geq 500$ K. We consider two separate formation pathways for low-mass planets with voluminous atmospheres of light gases: core-nucleated accretion and outgassing of hydrogen from dissociated ices. We show that Neptune-size planets at $T_{\rm eq} = 500$ K with masses as small as a few times that of Earth can plausibly be formed core-nucleated accretion coupled with subsequent inward migration. We also derive a limiting low-density mass–radius relation for rocky planets with outgassed hydrogen envelopes but no surface water. Rocky planets with outgassed hydrogen envelopes typically have computed radii well below 3 $R_\oplus$. For both planets with H/He envelopes from core-nucleated accretion and planets with outgassed hydrogen envelopes, we employ planet interior models to map the range of planet mass–envelope mass–equilibrium temperature parameter space that is consistent with Neptune-size planet radii. Atmospheric mass loss mediates which corners of this parameter space are populated by actual planets and ultimately governs the minimum plausible mass at a specified transit radius. We find that *Kepler*'s 2–6 $R_\oplus$ planet candidates at $T_{\rm eq} = 500$–1000 K could potentially have masses $\lesssim 4$ $M_\oplus$. Although our quantitative results depend on several assumptions, our qualitative finding that warm Neptune-size planets can have masses substantially smaller than those given by interpolating the masses and radii of planets within our Solar System is robust.

The contents of this chapter are also published in *Rogers, L. A., Bodenheimer,* *P., Lissauer, J. J., & Seager, S. 2011, ApJ, 738, 59.*

4.1 Introduction

The first 4.5 months of *Kepler* data provide evidence for hundreds of "Neptune-size" (2 – 6 $R_\oplus$, where $R_\oplus$ is Earth's radius) planets orbiting within 0.5 AU of their stars (Borucki et al., 2011a,a). The prevalence of planet candidates within this size range raises questions about both planetary growth and migration of Neptune-size planets. Assuming that many of these candidates are true planets, what are they, how did they form, and why are they so numerous?

Kepler measures planetary sizes and orbital periods. In some cases, planet masses can be estimated from dynamical interactions between the planet and its star (Doppler method) or among planets in a multi-planet system (transit timing variations, TTVs; Holman et al., 2010). However, the masses of most of *Kepler*'s Neptune-size planet candidates will be difficult to measure.

We model herein the growth, physical evolution, and interior structure of Neptune-size planets that possess voluminous atmospheres of light gases. Our focus is on obtaining estimates of the minimum plausible masses of *Kepler*'s planet candidates. The maximum plausible mass of a planet of radius $R_p \lesssim 3R_\oplus$ can be estimated from the mass–radius relationship for rocky (Earth-like composition) planets (e.g., Valencia et al., 2006; Seager et al., 2007; Fortney et al., 2007; Marcus et al., 2010). In contrast, estimation of minimum plausible masses requires more detailed modeling of planetary growth, because formation of low-mass planets of solar composition demands complicated and contrived scenarios involving large amounts of mass loss. We consider formation of low-density planets both through core-nucleated accretion and through outgassing of low-molecular weight atmospheres. This work does not consider planet formation via gravitational instability (Boss, 1997) or tidal downsizing (Nayakshin, 2010a,b, 2011).

We present new core-nucleated planet accretion calculations following the approach of Pollack et al. (1996) and Movshovitz et al. (2010). Whereas all previous papers with this code emphasize the formation of Uranus mass and larger planets, here we present a new application of the code to a lower mass regime ($M_p < 10\ M_\oplus$). We push to lower planet masses by modeling formation scenarios where the gas disk dissipates well before rapid gas accretion. We also consider lower solid planetesimal surface densities (4 $\mathrm{g\,cm^{-2}}$ at 5.2 AU and 6 $\mathrm{g\,cm^{-2}}$ at 4 AU) than most previous calculations (10 $\mathrm{g\,cm^{-2}}$ at 5.2 AU) to attain lower heavy-element core masses. Until recently, high planetesimal surface densities (about three times the minimum mass solar nebula at 5.2 AU) were needed to model Jupiter formation on a reasonable timescale. Advances in the modeling of grain physics (Movshovitz et al., 2010) now allow for a reasonable formation time for Jupiter, even with $\sigma = 4\ \mathrm{g\,cm^{-2}}$ considered here.

We supplement the detailed core-nucleated accretion calculations with equilibrium models of Neptune-size planets having H/He envelopes calculated following the approach of Rogers & Seager (2010a,b). The equilibrium model is less computationally time consuming and allows us to more comprehensively sample the parameter space (heavy-element core masses, envelope masses, irradiation levels, and intrinsic planet luminosities) of interest. We focus on low-density planets having equilibrium temperatures of 500–1000 K, since these temperatures are relevant to the planet candidates found in *Kepler's* first quarter data (Borucki et al., 2011a).

We also explore outgassing during planet formation as a possible origin pathway for low-density Neptune-size planets, and derive a limiting mass–radius (M_p–R_p) relation bounding the maximum radius/minimum density for planets with primary de-gassed envelopes. Following Elkins-Tanton & Seager (2008b), we consider outgassing of hydrogen gas produced when water reacts with metallic Fe in accreting materials during planet formation. Our outgassed exoplanet models self-consistently treat the connection between the planets' interior structure (iron core mass and mantle composition) and the mass of H_2 degassed. We thereby provide the first exoplanet M_p–R_p relations that include the effect of an outgassed H_2 gas layer. To derive the limiting M_p–R_p relation, we study planets that accreted from a mixture of water and material with chemical composition characteristic of the high-iron enstatite (EH) chondrite meteorite class, corresponding to end-member scenarios yielding maximum outgassed H_2.

We begin by describing our equilibrium model for low-mass planets with gas layers in Section 4.2. This model is applied in later sections to explore the mass–radius (M_p–R_p) relationships for low-mass planets with voluminous atmospheres of light gases acquired by core-nucleated accretion and outgassing of hydrogen. Section 4.3 describes the formation and properties of Neptune-size planets that assembled through core accretion, and Section 4.4 describes the formation and properties of planets that outgassed hydrogen from dissociated ices. We consider mass loss from the envelope in Section 4.5. We discuss our results and conclusions in Section 4.6.

4.2 Models of Planets in Equilibrium: Methods

We use equilibrium models–spherically symmetric planets in hydrostatic equilibrium–for two applications. The first (Section 4.3) is to explore the mass–radius relationships for low-mass planets formed via core-nucleated accretion. The second application is to again study mass–radius relationships for planets that acquired an envelope of light gases through outgassing (Section 4.4).

Our equilibrium model is based upon the planet interior model from Rogers & Seager (2010a,b). We have, however, included updates to the temperature profile in the radiative regime of the envelope and to the outer boundary conditions of the planet. We use equilibrium models to study instantaneous states of evolving planets assuming that the planets are undergoing quasi-static evolution. Our work does not focus on cases where the envelope dynamics or variations in the interior luminosity profile have an important effect.

We assume spherically symmetric and differentiated planets consisting of up to four layers. From the inside out, these layers are an iron core, a silicate mixture, H_2O, and a gas envelope. The coupled differential equations describing the mass of a spherical shell in hydrostatic equilibrium:

$$\frac{dr}{dm} = \frac{1}{4\pi r^2 \rho} \tag{4.1}$$

$$\frac{dP}{dm} = -\frac{Gm}{4\pi r^4}, \tag{4.2}$$

and the differential equation describing the radial optical depth, τ, in the gas layer

$$\frac{d\tau}{dm} = -\frac{\kappa}{4\pi r^2}. \tag{4.3}$$

are integrated inward from the top of the planet's envelope. Above, m is the interior mass coordinate, r is the distance from the planet center, P is the pressure, ρ is the mass density, κ is the mean opacity at thermal wavelengths, and G is the gravitational constant.

Within each chemical layer, the equation of state (EOS) relates the density $\rho(m)$ to the pressure $P(m)$ and temperature $T(m)$. In analogy to the models in Section 4.3, we define the exterior boundary condition on the planet envelope ($r = R_p$, $m = M_p$, $\tau = \tau_R$, $P = P_R$) at radial optical depth $\tau_R = 2/3$. We then determine the corresponding pressure P_R by imposing

$$P_R = \frac{g\tau_R}{\kappa_R}, \tag{4.4}$$

where κ_R is the Rosseland mean opacity at the photosphere boundary, and $g = GM_p/R_p^2$ is the gravitational acceleration. While the density ρ varies abruptly between the chemical layers, both P and T are continuous across layer boundaries. For a specified planet composition, energy budget, and mass, M_p, the planet radius, R_p, is iterated until a self-consistent solution satisfying the inner boundary condition ($r = 0$, $m = 0$) is achieved.

We assume that the gas envelope is in radiative–convective equilibrium, with an outer radiative zone surrounding a convective layer at greater depths. Within the thin outer edge of the envelope, we adopt the isotropic average temperature profile from

Equation (29) in Guillot (2010),

$$T^4(\tau) = \frac{3T_{\mathrm{int}}^4}{4}\left[\frac{2}{3} + \tau\right] + \frac{3T_{\mathrm{irr}}^4}{4} f \left[\frac{2}{3} + \frac{1}{\gamma\sqrt{3}} + \left(\frac{\gamma}{\sqrt{3}} - \frac{1}{\gamma\sqrt{3}}\right) e^{-\gamma\tau\sqrt{3}}\right], \tag{4.5}$$

an analytic solution to the "two-stream" gray equations of radiative transfer for a plane-parallel irradiated atmosphere. The irradiation temperature, T_{irr}, characterizes the short wave energy flux received by the planet from the star and relates through the redistribution factor, f, to the equilibrium temperature of the planet in the radiation field of the star $T_{\mathrm{eq}} = f^{1/4} T_{\mathrm{irr}}$ ($f = 1/4$ for full redistribution). The intrinsic temperature $T_{\mathrm{int}} = \left(L_p/4\pi R_p^2 \sigma_B\right)^{1/4}$ parameterizes the total intrinsic luminosity of the planet, L_p (σ_B denotes the Stefan–Boltzmann constant). The total intrinsic planet luminosity, L_p, is the sum total of contributions from envelope contraction, radioactive decay, and secular cooling of the core. The ratio of the short-wave and long-wave optical depths is represented by γ. We take $\gamma = 0.6\sqrt{T_{\mathrm{irr}}/2000\ \mathrm{K}}$, which Guillot (2010) found provided a good match to detailed calculations of hot Jupiter atmospheres from Fortney et al. (2008).

In highly irradiated planet atmospheres, the radiative regime of the envelope may extend to depths beyond where the plane-parallel approximation (assumed when deriving Equation (4.5)) is valid. In these cases, once all of the incoming stellar radiation is absorbed at optical depths $\tau \gg 1/\sqrt{3}\gamma$, we transition smoothly to the radiative diffusion equation,

$$\frac{dT}{dr} = -\frac{3\kappa\rho}{16\sigma_B T^3}\frac{L_p}{4\pi r^2}. \tag{4.6}$$

The onset of convective instabilities $(0 < (\partial\rho/\partial s)_P\, ds/dm)$ determines the depth of the transition to the convective layer of the gas envelope. In the convective regime, we adopt an adiabatic temperature profile.

We use the EOS from Saumon et al. (1995). The effect of uncertainties in the H/He EOS (see, e.g., Militzer et al., 2008; Nettelmann et al., 2008) will be small compared to the effect of uncertainties in the heavy-element composition and distribution, for the low-mass planets we are considering. While the major uncertainties in the EOS are at Mbar pressures or above, the pressures at the base of our H/He envelopes are typically less than a few tenths of a Mbar. As in the formation and evolution models of Section 4.3, we use Rosseland mean molecular opacities from Freedman et al. (2008). We neglect grain opacities in our equilibrium models, however, since we are interested in the planet radii at late times, after all the grains have settled.

Under the H/He envelope, the rock–ice interior is modeled with differentiated layers of iron, $Fe_{0.1}Mg_{0.9}SiO_3$ silicates, and H_2O. For these materials, we employ EOS data sets from Seager et al. (2007), which were derived by combining experimental data at $P \lesssim 200$ GPa with the theoretical Thomas–Fermi–Dirac (TFD) equation of state at high pressures, $P \gtrsim 10^4$ GPa. The equation of state at intermediate pressures between ~ 200 and 10,000 GPa is not well known, since this pressure range is neither easily accessible by experiments nor by TFD theory. For H_2O, Seager et al. (2007) used density functional theory calculations to fill in the EOS in this pressure regime, while for all other materials, they bridged the pressure gap by extrapolating the empirical Birch–Murnagham EOS and the theoretical TFD EOS to higher and lower pressures, respectively. Thermal effects are neglected in the Seager et al. (2007) EOSs—at the high pressures found in the interior layers, thermal corrections have only a small effect on the density, ρ. An improvement over our previous models is that we now more consistently take into account the Si/Mg/Fe ratios in the mantle by calculating EOSs for mixtures of MgO, FeO, and SiO_2. Core mass–radius relations calculated following this scheme (but neglecting the small contribution to pressure from the gaseous envelope) were also employed in the planet evolution calculations of Section 4.3.

A major uncertainty in the validity of the models comes from the assumption that the layers of water and H (or H/He) are not mixed. For the $T_{\rm eq} = 500 - 1000$ K planets considered in this work, H_2 and H_2O are miscible at the pressures and temperatures in the model envelopes. So they could, in principle, be homogeneously mixed. By considering the extreme where the H and H_2O are fully separated, we set an upper bound on the planet radius; typically if hydrogen is mixed into the water layer one expects the planet's radius to be smaller (e.g., Nettelmann et al., 2010). Although our aim is to model H/He envelope planets, some of our models do have significant water content, and future work should include the miscibility of H_2 and H_2O.

The planet radii in both our equilibrium and evolution models underestimate the planet radii measured during transit in a predictable way. This "transit radius effect" (Baraffe et al., 2003; Burrows et al., 2003) is a consequence of our exterior boundary condition (Equation (4.4)), which pegs our model planet radii, R_p, at a radial optical depth $\tau_R = 2/3$. In contrast, it is the transverse optical depth for transmission through the planet limb that determines the transit radius. Hansen (2008) derived a correction for the transit radius effect,

$$\Delta R = H_R \ln \left[\gamma \tau_R \left(\frac{2\pi R_T}{H_R} \right)^{1/2} \right], \tag{4.7}$$

where the transit radius $R_T = R_p + \Delta R$ is defined at a transverse optical depth of unity, and H_R represents the atmospheric scale height at the planet limb. Equation (4.7) applies when $H_R \ll R_p$, and assumes that the outer limb of the planet atmosphere is well described by an ideal gas. For the low-mass ($M_p < 30\ M_\oplus$) planets with hydrogen-rich envelopes we are considering, the transit radius correction is typically between 1% and 10%. Equation (4.7) assumes a clear cloud-free planet atmosphere; high-level clouds or hazes could further enhance the transit radius effect.

4.3 Planet Formation by Core-nucleated Accretion

4.3.1 Methods

Models for the formation and evolution of a planet consisting of a core of heavy-elements and a gaseous envelope of solar composition are calculated according to the procedures described by Pollack et al. (1996) and Movshovitz et al. (2010). The formation calculation consists of three major parts, (2) the accretion rate of planetesimals onto the planet; (1) the interaction of the infalling planetesimals with the gaseous envelope, and (3) the evolution of the gaseous envelope and the determination of the gas accretion rate.

The planetesimal accretion rate onto the planetary embryo is based on the equation originated by Safronov (1969). If $M_{\rm core}$ is the mass of the embryo, then the fundamental equation for its growth is

$$\frac{dM_{\rm core}}{dt} = \pi R_{\rm capt}^2 \sigma \Omega F_g, \tag{4.8}$$

where $\pi R_{\rm capt}^2$ is the effective geometrical capture cross-section, σ is the surface density of solid material (planetesimals), Ω is the orbital frequency, and the value of the gravitational enhancement factor, F_g, is obtained from Greenzweig & Lissauer (1992), assuming a planetesimal radius of 100 km. If no gaseous envelope is present, then $R_{\rm capt} = R_{\rm core}$, the heavy-element core radius. As in our previous publications, we take the feeding zone from which the embryo can accrete planetesimals to extend 4 Hill sphere radii on either side of the orbit (Kary & Lissauer, 1994), and assume that the solid surface density σ is constant within that zone. The value of σ in the feeding zone is adjusted at each time step to take into account depletion of planetesimals by accretion onto the embryo and expansion of the feeding zone into undepleted regions, as the embryo's mass increases.

The second element of the code calculates the interactions between planetesimals and the gaseous envelope of the protoplanet as they fall through it (Podolak et al., 1988). The details of how this calculation is performed are described in Pollack et al. (1996), Hubickyj et al. (2005), and Movshovitz et al. (2010). These calculations provide the effective capture radius $R_{\rm capt}$ to be used in Equation (4.8), as well as the deposition of mass and energy as a function of radius in the gaseous envelope. The effective capture radius can be several times larger than the actual solid heavy-element core radius because of the effects of the gas on slowing down, ablating, and fragmenting the planetesimals. It is assumed that the material from the planetesimals that is deposited in the envelope later sinks to the heavy-element core, releasing gravitational energy in the process (Pollack et al., 1996). This assumption is not entirely accurate: Iaroslavitz & Podolak (2007) show that some of the heavy-element material should actually dissolve in the envelope. Thus, the 'core masses' that we calculate actually represent the total heavy-element abundance in the planet in excess of the solar metal abundance; most of these heavy-elements (including all of the rock and organic compounds) would be expected to reside in the actual core of the planet.

The third element of the simulation is the solution of the four differential equations of stellar structure for the gaseous envelope, with energy sources from accreting planetesimals, from gravitational contraction, and from cooling. The adiabatic temperature gradient is assumed in convection zones. At the heavy-element core boundary, the luminosity L_r is set to the energy deposition rate for the planetesimals that hit the heavy-element core. Outside the heavy-element core, the energy supplied by ablated and fragmented planetesimals is included as a source term in the energy equation.

At the core–envelope interface, the radius is set to that of the outer edge of the heavy-element core. The heavy-element core mass–radius relation is calculated using the equilibrium model described in Section 4.2, assuming 10% Fe, 23% $\mathrm{Fe_{0.1}Mg_{0.9}SiO_3}$, and 67% $\mathrm{H_2O}$, by mass. The heavy-element core composition we adopt is motivated by comet compositions, and represents rock with an Fe/Si ratio near solar mixed with ice in a ratio of 1:2 by mass.

At the surface, gaseous mass of solar composition is added at a sufficient rate to maintain an outer radius $R_p = R_{\mathrm{eff}}$, which is given by Bodenheimer et al. (2000) as

$$R_{\mathrm{eff}} = \frac{GM_p}{c_s^2 + \frac{GM_p}{KR_H}}, \tag{4.9}$$

where R_H is the Hill sphere radius, c_s is the sound speed in the disk outside the planet, M_p is the total planet mass, and, nominally, $K = 1$. Note that when R_H is large compared with the Bondi accretion radius, GM_p/c_s^2, the expression reduces to the Bondi radius, while in the case of the opposite limit, $R_{\mathrm{eff}} \to R_H$. In developments after the above expression was formulated, it turned out that K had to be modified. Three-dimensional (3D) calculations of disk–planet interaction (Lissauer et al., 2009) gave the result that not all the gas passing through the Hill sphere is actually accreted by the planet; some of it simply flows through and rejoins the disk's azimuthal motion. The 3D simulations provided an estimate of the effective planetary radius, which corresponds to $K = 0.25$, the value used in this paper.

The density and temperature at the planet's surface are set to assumed nebular values $\rho_{\rm neb}$, $T_{\rm neb}$, respectively. The value of $T_{\rm neb}$ is constant in time, while $\rho_{\rm neb}$ decreases linearly to zero with time, over a timescale $T_d \approx$ 2–3 Myr. In a variation of this boundary condition, $\rho_{\rm neb}$ is constant in time up to a time comparable to T_d, then it is linearly reduced to zero on a timescale of 10^5 yr. These assumptions roughly characterize the dissipation of the gaseous disk. $T_{\rm neb}$ is held constant while the planet is accreting; our model incorporates migration only through temperature increases subsequent to the conclusion of the planet's growth. Modeling simultaneous migration and accretion is beyond the scope of this work.

When $\rho_{\rm neb}$ approaches zero, the accretion of gas is halted and the evolution is calculated at constant mass over timescales up to 3–4 Gyr. The envelope mass at cutoff in these simulations is always small enough that rapid runaway gas accretion does not occur, and Equation (4.9) is always valid for the determination of the gas accretion rate. The accretion rate required to keep $R_p = R_{\rm eff}$ remains much lower than the limit imposed by disk physics in supplying material to the Hill sphere of the planet (Lissauer et al., 2009). Once gas accretion is shut off, R_p rapidly falls below $R_{\rm eff}$, and the planet becomes isolated from the disk. The surface boundary condition changes to that of a hydrostatic atmosphere that radiates from the photosphere:

$$L = 4\pi R_p^2 \sigma_B T_{\rm eff}^4, \tag{4.10a}$$

$$\kappa P = \frac{2}{3} g, \tag{4.10b}$$

where σ_B is the Stefan–Boltzmann constant, $T_{\rm eff}$ is the surface temperature, L is the total luminosity (energy radiated per second) of the planet, and κ, P, and g are, respectively, the Rosseland mean opacity, the pressure, and the acceleration of gravity at the photosphere. There are two contributions to $T_{\rm eff}$: one from the internal luminosity provided by the planet, and the other from the energy absorbed from the central star and re-radiated by the planet. Thus,

$$T_{\rm eff}^4 = T_{\rm int}^4 + T_{\rm eq}^4, \tag{4.11}$$

where $T_{\rm int}$ is the internal contribution (generally small), and $T_{\rm eq}$ is the equilibrium temperature of the planet in the radiation field of the star. The former quantity is determined from the evolutionary calculation, while the latter is a parameter that depends on the assumed distance of the planet from the star and the stellar luminosity.

The equation of state of the gas is taken from Saumon et al. (1995), interpolated to our assumed composition of hydrogen mass fraction $X = 0.74$, helium mass fraction $Y = 0.243$, and metal mass fraction $Z = 1 - X - Y = 0.017$. Although the equation of state in the outer, low-density layers is essentially that of an ideal gas, the inner regions near the heavy-element core can be significantly non-ideal once the envelope has become sufficiently compressed.

The Rosseland mean opacity calculation has three components. At temperatures above 3000 K, the molecular/atomic opacities of Alexander & Ferguson (1994) are used. In practice, the details of the opacities in this region are unimportant because the energy transport is almost always by convection. In the temperature range 100–3000 K, the molecular opacities, without grains, of Freedman et al. (2008) are used. Grain opacities are then added in the temperature range 100–1800 K. Two sources of grains are taken into account; first, those provided by the ablating planetesimals as they interact with the envelope, and, second, those that accrete along with the gas at the surface of the planet. At each time step of the evolutionary calculation, and at each depth in the envelope, the grain size distribution is recalculated, taking into account the coagulation and settling of grains. The size distribution is represented by 34 bins, covering the size range 1.26 μm to 2.58 mm. The effective cross-sections for absorption and scattering are calculated as a function of grain size and frequency; then an integration over grain size and frequency gives the Rosseland mean opacity as a function of depth. The details of the grain physics are given in Movshovitz & Podolak (2008) and Movshovitz et al. (2010). The grains are composed purely of silicates, with a dust-to-gas ratio of about 0.01 by mass; little error results from this assumption compared to the uncertainties in grain shape, sticking probability, and radiative properties (Movshovitz et al., 2010). Grains are assumed to be completely evaporated above 1800 K. The grains are important during the gas accretion phase. Once accretion is shut off, the grains rapidly settle toward the center and are evaporated. This effect is included in the calculations and indicates that any grains remaining in the atmosphere have a negligible effect upon the evolution. Thus, in the final constant-mass evolution phase, the molecular opacities completely dominate.

4.3.2 Evolution Input Parameters and Results

The planet initially consists of a heavy-element core of 1 $M_\oplus$ and a light element envelope of about 10^{-5} $M_\oplus$. The protoplanet is located at either 5.2 AU or 4.0 AU in a protoplanetary disk, with the solid surface density $\sigma = 4$ g cm^{-2} at 5.2 AU and 6 g cm^{-2} at 4 AU. The initial evolutionary time is set to 7.3×10^5 yr and 4.8×10^5 yr, respectively, for $\sigma = 4$ and 6 g cm^{-2}, approximately the time needed to assemble a heavy-element core of mass $M_{\rm core} = 1$ $M_\oplus$.

The quantity $T_{\rm neb}$ is set to 115 K at 5.2 AU and 125 K at 4 AU. Then $\rho_{\rm neb} = \sigma_{XY}/(2H)$, where $\sigma_{XY} = 70\sigma$ is the surface density of the gas component. As mentioned above, $\rho_{\rm neb}$ in general declines with time. The scale height of the gas in the disk $H = 0.05a$, where a is the orbital distance from the star. Once started, the evolution consists of three main phases. The first phase primarily involves accretion of solids onto the heavy-element core, with a relatively low-mass envelope and a low gas accretion rate. The solids accretion rate slows down significantly near the point where the isolation mass ($M_{\rm iso}$) for the core is reached; for $\sigma = 4$ g cm^{-2} at 5.2 AU this mass is about 2.9 $M_\oplus$ and for $\sigma = 6$ g cm^{-2} at 4 AU, about 2.4 $M_\oplus$. During the second phase, the gas accretion rate is about three times as high as the core accretion rate, $\dot{M}_{\rm env} \approx 3\dot{M}_{\rm core}$, and both are nearly constant in time (Pollack et al., 1996). The envelope mass builds up relative to the heavy-element core mass, which grows slowly. The phase of rapid gas accretion, which for giant planets begins once the envelope mass $M_{\rm env}$ becomes about equal to $M_{\rm core}$, does not occur in these calculations. Instead, gas accretion is cut off and the planet evolves through a third phase at constant mass with boundary conditions provided by Equation (4.10). During the early part of this phase, the planet is assumed to migrate to a position within 1 AU from the star. Representative cases with $T_{\rm eq} = 500$ K and 1000 K are presented.

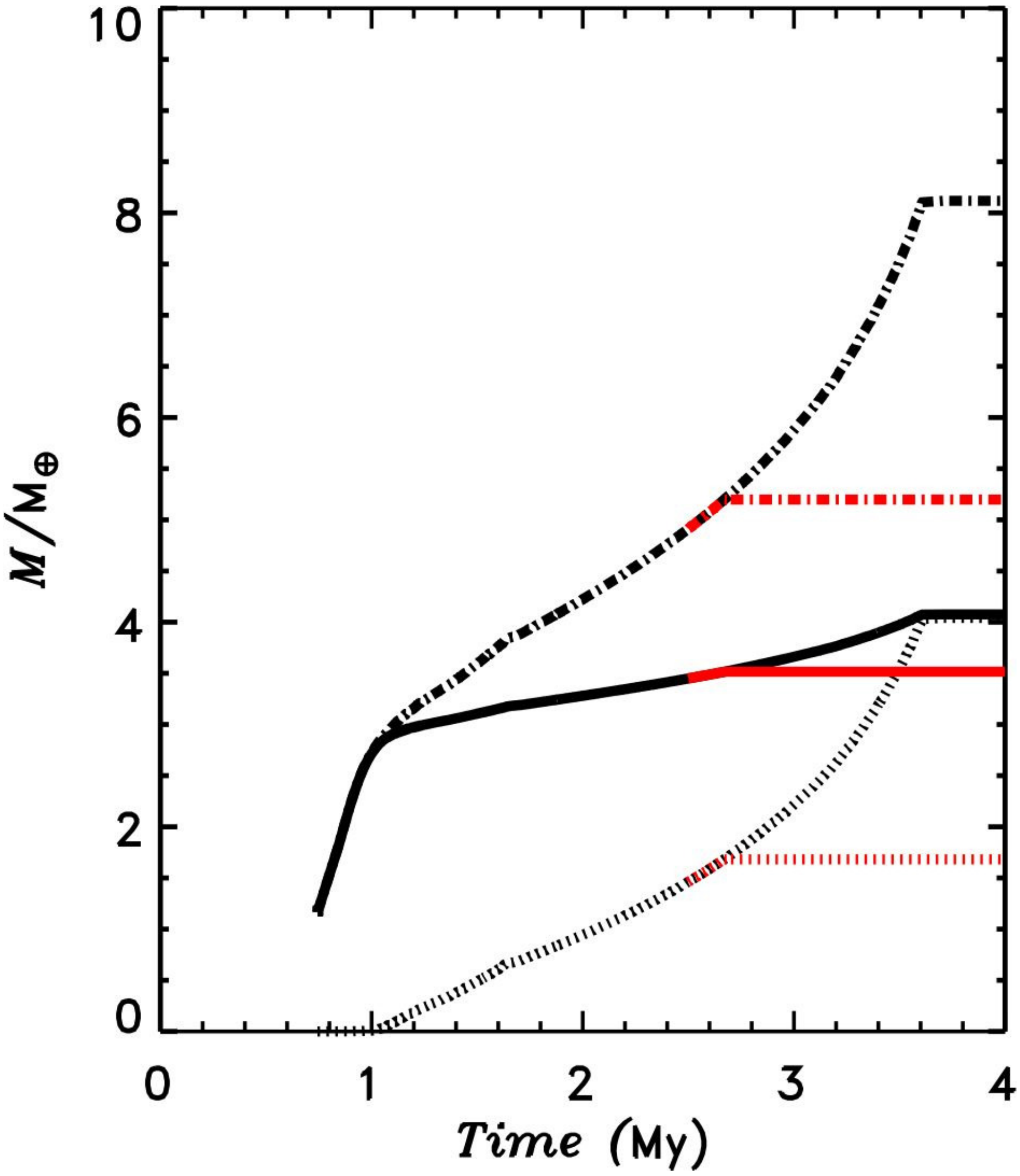

Figure 4-1: Mass of the protoplanet as a function of time for Runs I. For Run Ia (black curves) the solid line denotes the mass of the heavy-element core, the dotted line the mass of the H/He envelope, and the short-dash-dot line the total mass. For Run Ib, the same line types are shown in red.

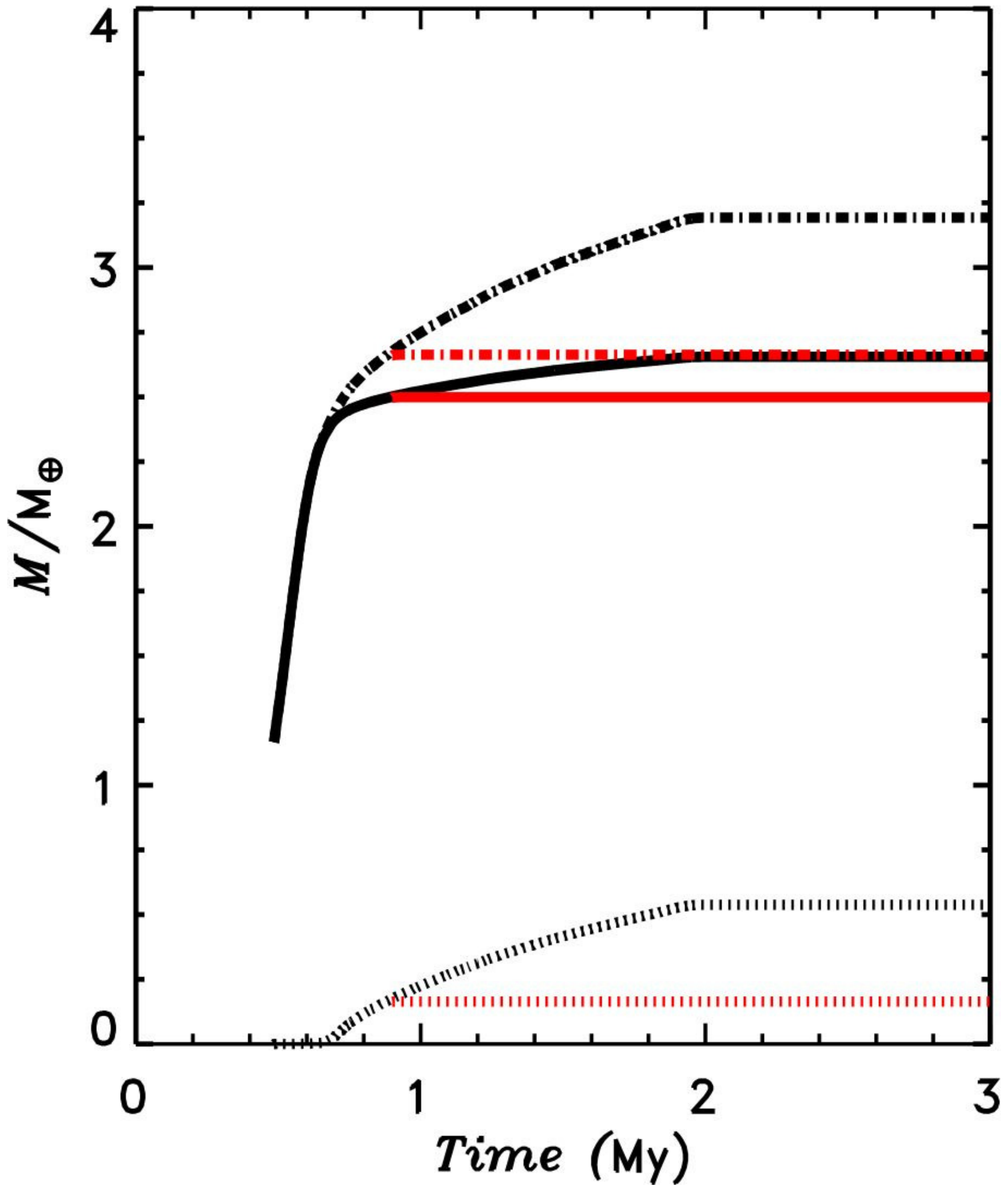

Figure 4-2: Mass of the protoplanet as a function of time for Runs II. For Run IIa (black curves) the solid line denotes the mass of the heavy-element core, the dotted line the mass of the H/He envelope, and the short-dash-dot line the total mass. For Run IIb, the same line types are shown in red.

Table 4.1: Input Parameters for Evolutionary Runs

Run	a (AU)	σ (g cm^{-2})	σ_{XY} (g cm^{-2})	$T_{\rm neb}$ (K)	T_d (Myr)	$M_{\rm iso}$ ($M_\oplus$)
Ia	5.2	4	280	115	3.5	2.92
Ib	5.2	4	280	115	2.5	2.92
IIa	4.0	6	420	125	2.0	2.42
IIb	4.0	6	420	125	0.9	2.42

Table 4.2: Results from Evolutionary Runs: Masses and Radii

Run	M_p ($M_\oplus$)	$M_{\rm core}$ ($M_\oplus$)	$M_{\rm env}$ ($M_\oplus$)	$R_{1;500}$ ($R_\oplus$)	$R_{4;500}$ ($R_\oplus$)	$R_{1;1000}$ ($R_\oplus$)	$R_{4;1000}$ ($R_\oplus$)
Ia	8.13	4.08	4.05	9.8	8.1	14.8	11.6
Ib	5.20	3.52	1.68	8.0	6.6	15.7	11.5
IIa	3.19	2.65	0.54	6.0	5.0	17.9	11.7
IIb	2.66	2.50	0.16	3.6	3.3	6.7	6.2

Notes. The first subscript on the radius gives the evolutionary time in gigayears. The second subscript gives the assumed equilibrium temperature of the planet.

The input parameters of the four runs are shown in Table 1, which includes σ, the gas surface density σ_{XY}, the surface boundary temperature $T_{\rm neb}$, and the isolation mass $M_{\rm iso}$.

The results of our calculations for Runs Ia, Ib, IIa, and IIb are shown in Figures 4-1–4-3. The masses and radii that are derived for the four runs are listed in Table 2.

Run Ia is based on a disk with $\sigma = 4$ g cm^{-2} at 5.2 AU. This value is only slightly greater than that of the minimum mass solar nebula. But note that our calculation of F_g (Equation (4.8)) neglects transport of solids into or away from the planet's accretion zone. Moreover, our planetesimals are all assumed to have the same radius, 100 km. In fact there must be a range of planetesimal sizes, and the effective planetesimal size is not well known. Smaller planetesimals would result in more rapid accretion (see footnote 3 of Lissauer et al., 2009). The accretion rate that is actually calculated may thus correspond to a value of σ slightly different from 4 g cm^{-2}.

The details of the calculation with the parameters of Run Ia are presented in Run σ4 of Movshovitz et al. (2010). In that paper, the run is continued well into the phase of rapid gas accretion, and is terminated with $M_{\rm core} = 4.74\ M_\oplus$ and $M_{\rm env} = 34\ M_\oplus$. The formation time for a giant planet is found to be 4 Myr. In the present run, the accretion of gas and solids is cut off at a time of 3.5 Myr, consistent with estimated lifetimes of protoplanetary disks (Hillenbrand, 2008). At that time, the value of $\rho_{\rm neb}$ is assumed to decrease to zero on a timescale of 10^5 yr. The calculation is then continued up to Gyr times with constant values of $M_{\rm core} = 4.08\ M_\oplus$ and $M_{\rm env} = 4.05\ M_\oplus$. At the beginning of this phase, the equilibrium temperature is gradually increased, on a timescale of 4 Myr, to an assumed final value of 500 K. A gradual increase in $T_{\rm eq}$ to 1000 K was accomplished in a total time of 6×10^7 yr. The final values of R_p for these two temperatures and for times of 1 and 4 Gyr are given in Table 2; they are close to Jupiter's radius $R_J \approx 11\ R_\oplus$, even though the planet's mass is only $8.13\ M_\oplus$.

Run Ib also is based on the run σ4 from Movshovitz et al. (2010). In this case the accretion of gas and solids was cut off at 2.5 Myr, at which point $M_{\rm core} = 3.52\ M_\oplus$ and $M_{\rm env} = 1.68\ M_\oplus$. The evolution was again continued into the phase of cooling and contraction at constant mass, with assumed values of $T_{\rm eq}$ of 500 and 1000 K. In

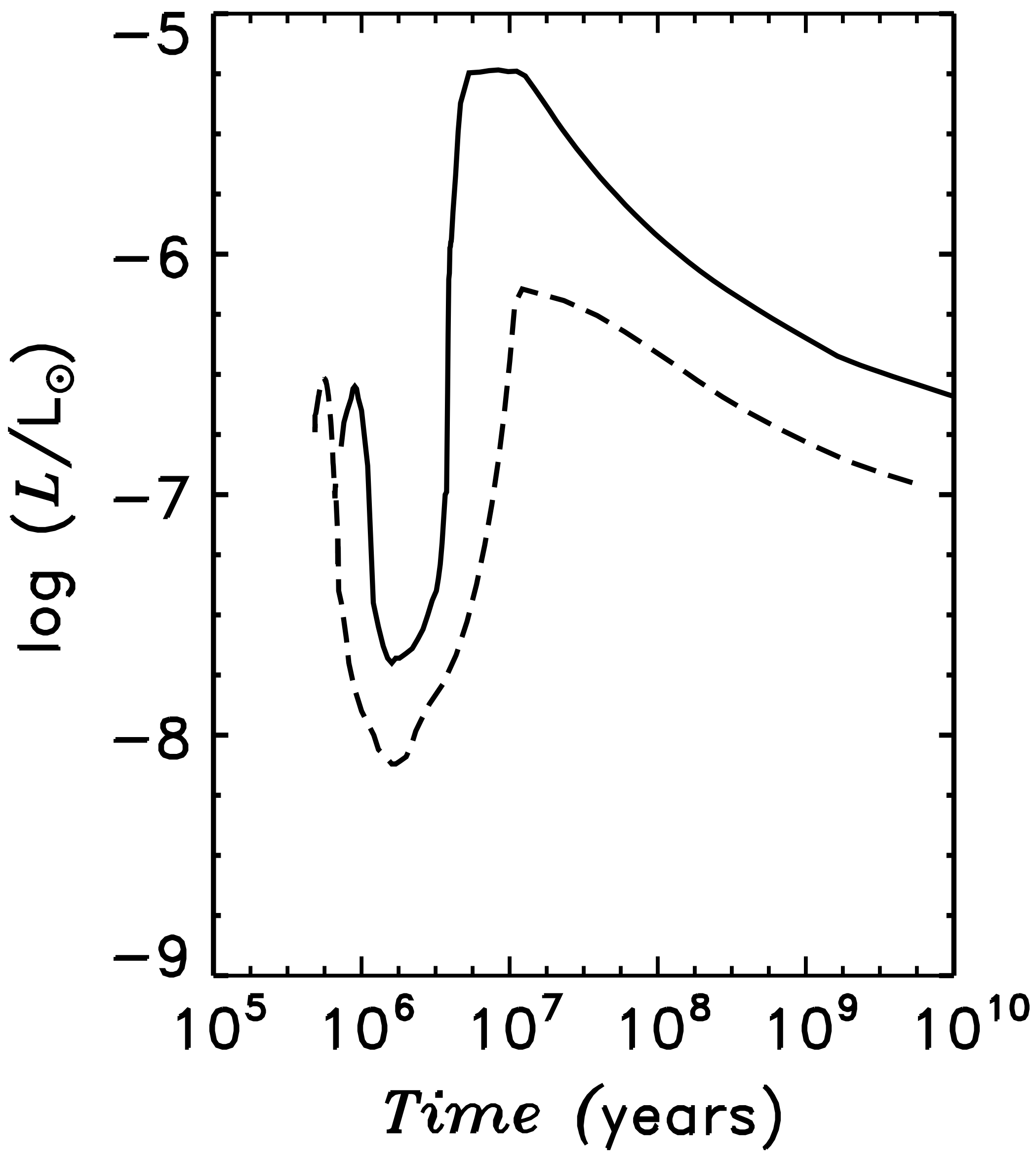

Figure 4-3: Protoplanet's total luminosity, including internal and irradiation contributions, as a function of time during the formation phase and the contraction/cooling phase for Run Ia (solid curve) and Run IIa (dashed curve). The equilibrium temperature is increased to 500 K, after the formation phase, during these runs.

the case with $T_{\rm eq} = 1000$ K, the final radii are again comparable to or larger than R_J. In the case with $T_{\rm eq} = 500$ K, the minimum radius is 6.6 $R_\oplus$, only slightly smaller than the corresponding value in Run Ia.

Run IIa is an entirely new calculation, with the planet forming at 4 AU in a disk with $\sigma = 6$ g cm^{-2}. During the initial phase of rapid core accretion, the luminosity reaches a maximum of 3.1×10^{-7} $L_\odot$ at a time of 6.2×10^5 yr. The heavy-element core mass is 2.2 $M_\oplus$ and the core accretion rate $\dot{M}_{\rm core} = 5 \times 10^{-6}$ $M_\oplus$ yr^{-1} at this time. Later, at 1 Myr, $\dot{M}_{\rm core}$ has decreased to 2×10^{-7} $M_\oplus$ yr^{-1} and $\dot{M}_{\rm env}$ has increased to 5×10^{-7} $M_\oplus$ yr^{-1}. The luminosity has decreased to 10^{-8} $L_\odot$. Because of computational time limitations, and to obtain a lower envelope mass than that found for Run Ib, the accretion in this run was cut off at 2 Myr, with $M_{\rm core} = 2.65$ $M_\oplus$ and $M_{\rm env} = 0.54$ $M_\oplus$. If the evolution had been continued up to 2.5 Myr, the heavy-element core mass would have been practically unchanged, and $M_{\rm env}$ would have increased by about 0.25 $M_\oplus$. At the end of the contraction/cooling phase, the radii are in the range 5–6 $R_\oplus$ for the case of $T_{\rm eq} = 500$ K, and for $T_{\rm eq} = 1000$ K they are larger than R_J, close to the values obtained in Runs I for that temperature.

To investigate the effect of an even smaller value of $M_{\rm env}$, Run IIb was calculated with the same parameters as Run IIa, but with an arbitrary accretion cutoff at 9.1×10^5 yr. At that point, $M_{\rm core} = 2.5$ $M_\oplus$ and $M_{\rm env} = 0.16$ $M_\oplus$. Final radii turned out to be in the range 3–4 $R_\oplus$ for $T_{\rm eq} = 500$ K and in the range 6–7 $R_\oplus$ for $T_{\rm eq} = 1000$ K. The significant reduction in envelope mass resulted in final radii that are about half the values obtained for Run IIa.

We neglect heating from radioactive decay in the core-nucleated accretion calculations. Including this additional energy source would delay envelope contraction and planet cooling. Consequently, the planet radii at 1 Gyr and 4 Gyr in Table 2 may be systematically underestimated by a small amount. We estimate that, for the cases in Table 2, the planet luminosity from radioactive decay would be roughly one order of magnitude smaller than the luminosity from envelope contraction, assuming bulk Earth abundances of K, U, and Th in the heavy-element cores (Van Schmus, 1995). The fractional contribution to the planet energy budget from radioactive heating will be higher for older planets (4 Gyr) and cases where the heavy-element core contributes a larger fraction of the planet mass (Run II).

4.3.3 Equilibrium Model Results

In this section we explore planet radii over a wide range of heavy-element core masses, envelope masses, irradiation levels, and intrinsic planet luminosities. The planet formation and evolution model described in Section 4.3.1 is computationally intensive. Since it is not feasible to simulate planets under all conditions of interest following that approach alone, we enlist an equilibrium planet structure model (Section 4.2) to cover a wider range of parameter space.

Our equilibrium model shows good agreement with the planet evolution models in Section 4.3.2 despite the differences in their treatment of the outer radiative regime, the intrinsic planet luminosity, and the effects of stellar insolation. For each entry in Table 4.2, we applied the equilibrium model to simulate the same combination of M_{core}, M_{env}, T_{eq}, and T_{int}. The radii at $T_{\mathrm{eq}} = 500$ K in the two models agree to better than 0.2 $R_{\oplus}$ in every case. The planet radii at $T_{\mathrm{eq}} = 1000$ K are more sensitive to model assumptions and exhibit larger discrepancies (up to 14%, with the equilibrium model radii systematically below those in Table 4.2).

We explored the parameter space of M_{core}, M_{env}, T_{eq}, and T_{int} with our equilibrium model. Figures 4-4 and 4-5 present a selection of mass–radius (M_p–R_p) curves at (a) $T_{\mathrm{eq}} = 500$ K and (b) $T_{\mathrm{eq}} = 1000$ K. Figure 4-4 displays the effect on the radius of varying the envelope mass fraction, while Figure 4-5 shows the effect of varying the planet's intrinsic luminosity, $L_p = 4\pi R_p^2 \sigma T_{\mathrm{int}}^4$. The thick solid line is common between Figures 4-4 and 4-5, representing $M_{\mathrm{env}} = 0.2 M_p$ and $L_p/M_p = 10^{-10.5}$ W kg^{-1}. Here, $L_p/M_p = 10^{-10.5}$ W kg^{-1} corresponds to both the 8.3 $M_{\oplus}$ evolution model (Run Ia) at 4 Gyr and the 3.19 $M_{\oplus}$ evolution model (Run IIa) at 1 Gyr (independent of T_{eq}).

The M_p–R_p curves for low-mass planets with voluminous gas layers show several notable features. First, the planet radii (at constant envelope mass fraction, T_{eq}, and L_p/M_p) increase dramatically toward low planet masses. This is due to the low surface gravities, and thus large atmospheric scale heights found at low masses.

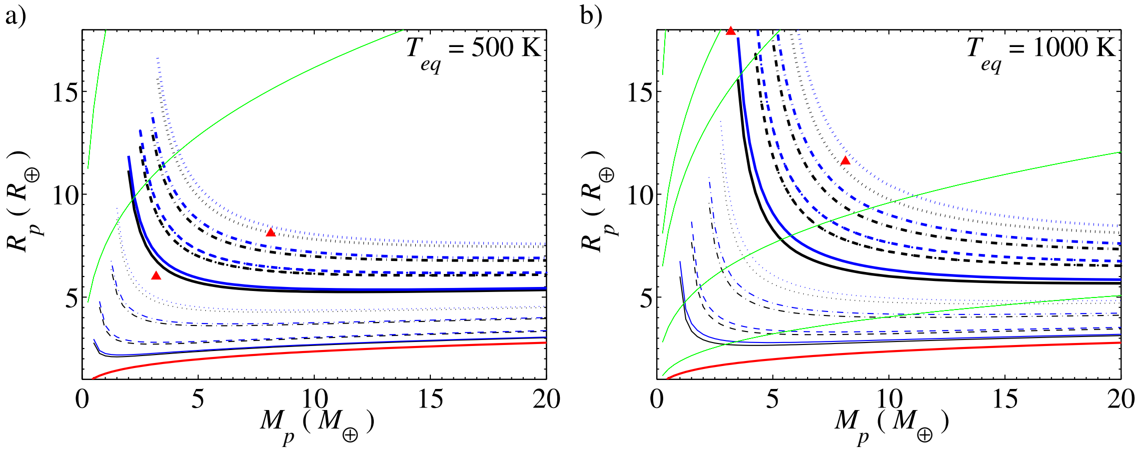

Figure 4-4: Equilibrium mass–radius relations for various choices of envelope mass fraction, $M_{\rm env}/M_p$. All data in this plot have $L_p/M_p = 10^{-10.5}$ W kg^{-1}, and (a) $T_{\rm eq} = 500$ K or (b) $T_{\rm eq} = 1000$ K. Each curve corresponds to a different value of $M_{\rm env}/M_p$: 0.001 (thin solid), 0.01 (thin dashed), 0.05 (thin dot-dashed), 0.1 (thin dotted), 0.2 (thick solid), 0.3 (thick dashed), 0.4 (thick dot-dashed), and 0.5 (thick dotted). Black lines denote our model radii (defined at a radial optical depth $\tau = 2/3$), while the corresponding blue lines represent radii corrected for the transit radius effect. The thick red line is the mass–radius relation for icy heavy-element cores having no envelope ($M_{\rm env} = 0$). Red triangles present the subset of Table 4.2 evolutionary run results that have $L_p/M_p \approx 10^{-10.5}$ W kg^{-1}: Run Ia ($M_p = 8.3\ M_\oplus$) at 4 Gyr and Run IIa ($M_p = 3.19\ M_\oplus$) at 1 Gyr. The green curves show the effective planet Roche-lobe radius for four different choices of host-star properties representative of spectral classes M5 V, M0 5V, K0 V, and G2 V (in order of increasing Roche-lobe radii). The K0 V and G2 V Roche-lobe radii are beyond the scale of the $T_{\rm eq} = 500$ K plot.

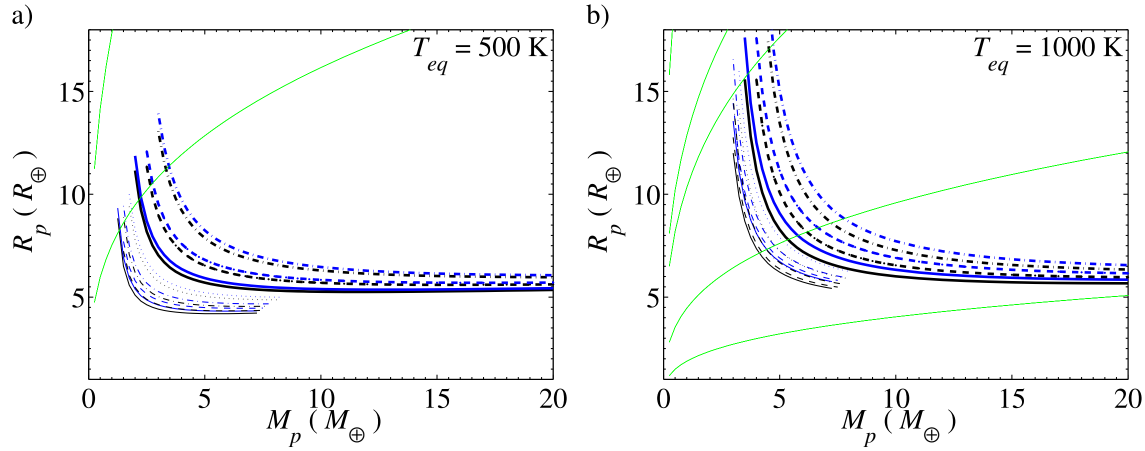

Figure 4-5: Equilibrium mass–radius relations for various choices of intrinsic planet luminosity L_p/M_p. All data in this plot have $M_{\rm env}/M_p = 0.2$, and (a) $T_{\rm eq} = 500$ K or (b) $T_{\rm eq} = 1000$ K. Each curve corresponds to a different value of L_p/M_p: $10^{-12.5}$ W kg^{-1} (thin solid), $10^{-12.0}$ W kg^{-1} (thin dashed), $10^{-11.5}$ W kg^{-1} (thin dot-dashed), $10^{-11.0}$ W kg^{-1} (thin dotted), $10^{-10.5}$ W kg^{-1} (thick solid), $10^{-10.0}$ W kg^{-1} (thick dashed), and $10^{-9.5}$ W kg^{-1} (thick dot-dashed). Black lines denote our model radii (defined at a radial optical depth $\tau = 2/3$), while the corresponding blue lines represent radii corrected for the transit radius effect. The green curves show the effective planet Roche-lobe radius for four different choices of host-star properties representative of spectral classes M5 V, M0 5V, K0 V, and G2 V (in order of increasing Roche-lobe radii). The K0 V and G2 V Roche-lobe radii are beyond the scale of the $T_{\rm eq} = 500$ K plot.

Second, the radius of planets having identical envelope mass fractions, $M_{\rm env}/M_p$, is remarkably insensitive to the planet mass when $M_p \gtrsim 15\ M_\oplus$. At these masses, increased compression of the envelope offsets the effect of increasing the planet mass. Third, for planets of identical total mass (within the mass range plotted), the planet radius increases monotonically with the envelope mass fraction. Fourth, $T_{\rm int}$ and $T_{\rm eq}$ both have a stronger effect on the radius of low-mass planets compared to their more massive counterparts. This is understandable, because, given the same envelope mass fraction, in lower mass planets the envelope accounts for a larger fraction of the planet radius.

Planet radii between 2 and 6 $R_\oplus$ are of special interest, because *Kepler* is finding a large number of planet candidates within this size range (Borucki et al., 2011a,a). We plot in Figure 4-6 combinations of $M_{\rm env}$ and M_p that yield planet radii within this range. Planets at 2 $R_\oplus$ can contain at most 0.08% of their mass in H/He at $T_{\rm eq} = 500$ K, and at most 0.0015% at $T_{\rm eq} = 1000$ K. Larger planets can support more massive envelopes. A 6 $R_\oplus$ planet at $T_{\rm eq} = 500$ K requires an envelope accounting for at least a few percent of the planet mass. At $T_{\rm eq} = 1000$ K and 6 $R_\oplus$, between 0.1% and 23% H/He by mass is possible, depending on the planet mass and intrinsic luminosity.

It is important to note that the M_p–R_p relations in Figures 4-4–4-6 are not isochrons, but correspond instead to constant total intrinsic luminosity per unit mass, L_p/M_p. The total intrinsic luminosity, L_p, is the sum total of heating from radioactive decay, cooling of the planet core, and contraction of the planet envelope. In the evolution calculations from Table 4.2, the planet luminosity contribution from envelope contraction alone ranges from $10^{-9.8}$ to $10^{-11.2}$ W kg^{-1} at 1 Gyr and from $10^{-10.5}$ to $10^{-12.4}$ W kg^{-1} at 4 Gyr. Some of the low-L_p curves in Figures 4-5 and 4-6 do not extend to higher masses because they encounter unphysically low planet interior entropies. Although L_p is a proxy for the age of the planet, the relationship between L_p and planet age depends on the planet's mass, composition, abundance of radioactive isotopes, insolation history, and dynamical history. Since our equilibrium models are presented at a specified L_p, we have side-stepped the issue of relating L_p

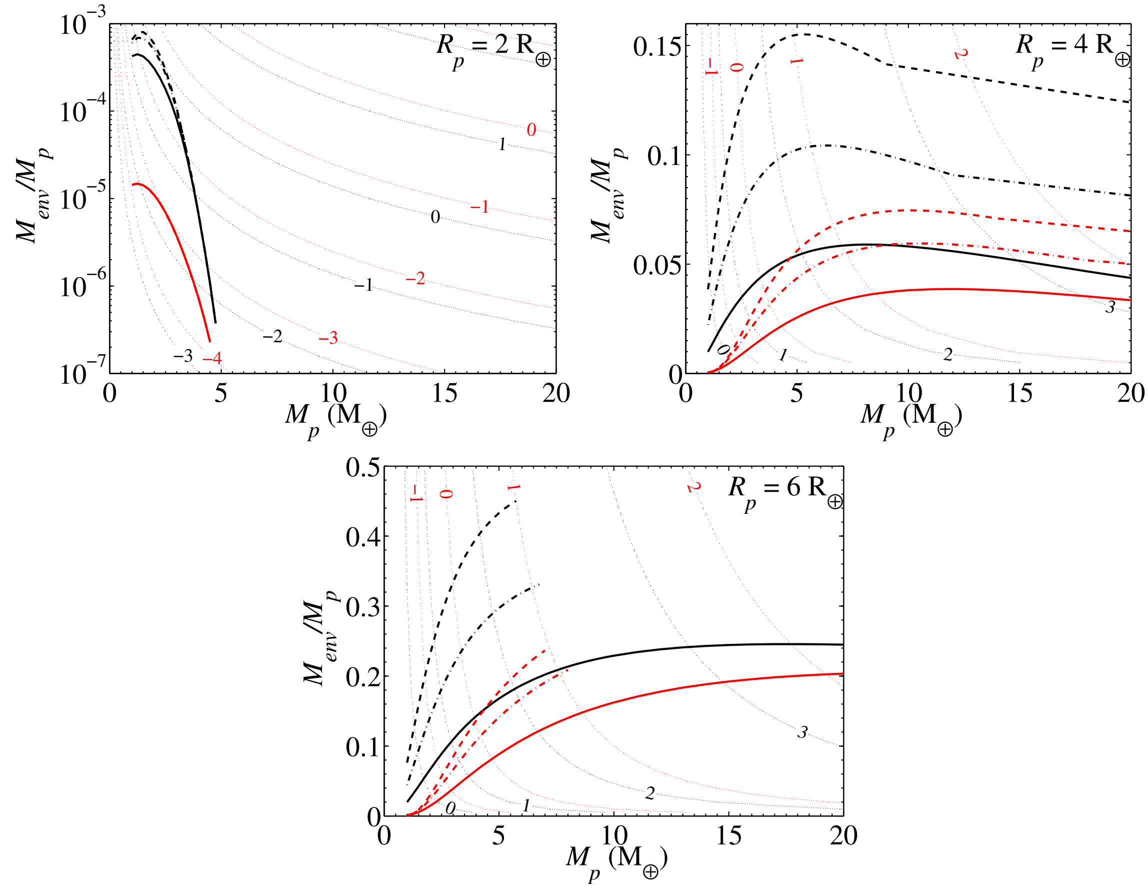

Figure 4-6: Planet mass and envelope mass that are consistent with a particular planet radius, for planets comprised of ice–rock interiors surrounded by H_2 and He in protosolar proportions. These models represent planets that formed beyond the snow line by core-nucleated accretion. We plot the envelope mass fraction as a function of total planet mass for planets with radii (a) $R_p = 2\ R_\oplus$, (b) 4 $R_\oplus$, and (c) 6 $R_\oplus$. Black curves represent planets at $T_{\rm eq} = 500$ K, while red curves correspond to $T_{\rm eq} = 1000$ K. The line style indicates the planet luminosity: $L_p/M_p = 10^{-11}\ {\rm W\,kg^{-1}}$ (dashed), $L_p/M_p = 10^{-10}\ {\rm W\,kg^{-1}}$ (dot-dashed), and $L_p/M_p = 10^{-9}\ {\rm W\,kg^{-1}}$ (solid). The thin dotted lines are contours of constant envelope mass-loss timescale, $t_{\dot{M}} \equiv M_{\rm env}/\dot{M}$. Each contour is labeled with $\log(t_{\dot{M}}/{\rm Gyr})$ for $\epsilon L_{\rm XUV}/L_{\rm BOL} = 10^{-6}$, and can easily be scaled for other choices of $\epsilon L_{\rm XUV}/L_{\rm BOL}$ using Equation (4.15).

to planet age and present the model radii in a way such that they can be applied to many different evolution scenarios. Our aim with the equilibrium models is to broadly explore parameter space; it is beyond the scope of this work to relate L_p and age directly by simulating all possible planet evolution histories.

Simulated planet radii for planets at $T_{\rm eq} = 1000$ K may be in error by up to 20%. The problem is in extrapolating the opacity tables at the high pressure end. This in turn makes the radiative–convective boundary uncertain (a deeper radiative–convective boundary makes for a smaller planet). Planets at $T_{\rm eq} = 500$ K are less affected by this opacity-caused radius problem ($\lesssim 10\%$ radius uncertainty for $M_p \geq 3\ M_\oplus$). This issue affects both our equilibrium and evolution models.

4.4 Planet Formation by Outgassing of Hydrogen

4.4.1 Model

Outgassing provides a mechanism for low-mass terrestrial planets to acquire an atmosphere even if they fail to accrete H and He from the protoplanetary nebula. In this section we explore the optimum conditions for a planet to acquire a voluminous gas envelope through outgassing. We base our model approach on Elkins-Tanton & Seager (2008b,a), with the improvements of a more detailed interior structure model and a calculation of the planet radius.

We focus on outgassing of H_2 produced when water reacts with metallic Fe in accreting materials during planet formation (Ringwood, 1979; Wanke & Dreibus, 1994; Elkins-Tanton & Seager, 2008b). Hydrogen gas has the potential to yield the most voluminous outgassed atmospheres, being both of low-molecular weight and (for some planetesimal compositions) degassed in substantial quantities. Although we do not consider these processes in detail here, in general, outgassing may also proceed during accretion as impinging planetesimals are heated and vaporized upon impact, during magma ocean solidification as volatiles are partitioned between the atmosphere and melt, and during volcanic/tectonic activity after the planet has formed.

The reaction between water and metals during planetary accretion and differentiation intrinsically links the planet's interior structure to its initial atmosphere's mass and composition. Metallic iron forming the planet will either differentiate to contribute to the planet iron core, or become oxidized and incorporate into the planet mantle. Given an initial composition for the primordial material forming a planet, there are two extremes to the eventual planet outcomes. If none of the available water and metals in the accreting materials react (reducing conditions), the planet will have a maximally massive metallic core, relatively iron-poor mantle, minimal outgassed H_2, and maximal leftover H_2O. In contrast, if the water and metals react to the maximal extent possible (oxidizing conditions), the planet will have a minimal iron core mass, iron-rich mantle, maximal outgassed H_2, and minimal leftover H_2O. When Fe is the limiting reagent, this extreme will correspond to a coreless planet (Elkins-Tanton & Seager, 2008a).

To bound the radii of outgassed rocky planets, we consider the end-member case of a planet formed purely from high iron enstatite (EH) primordial material. The motivation for this choice is three-fold. First, out of all meteoritic compositions, EH material has the potential to degas the most H_2 per unit mass (up to 3.6%, Elkins-Tanton & Seager, 2008b). Second, the oxygen isotope mixing model (Lodders, 2000) predicts that the Earth accreted from material that was 70% EH chondritic matter by mass. Third, heating of EH material releases a low mean molecular weight atmosphere; Schaefer & Fegley (2010) calculated 44% H_2, 31% CO, 17% H_2O, 5% CO_2, and 3% other molecules by volume under their nominal conditions (1500 K, 100 bars). Thus, complete oxidation of an EH planet should achieve effectively the maximum radius plausible for planets with outgassed atmospheres.

For the EH material we adopt the chemical composition of meteorite ALHA77295 from Jarosewich (1990). We distill the mineralogy in our model to include only the most plentiful and important constituents: metallic Fe, FeS, FeO, Fe_2O_3, MgO, SiO_2, H_2O, and H_2. Following an approach similar to Sotin et al. (2007), less abundant elements are represented by their most similar neighbors in the periodic table: metallic Ni is added to metallic Fe, Ca is added to Mg, and Al is divided equally (by number) between Si and Mg to preserve charge conservation. Other trace constituents (TiO_2, Cr_2O_3, MnO, Na_2O, K_2O, P_2O_5, Co, which together account for less than 2.2% by mass) are neglected. The resulting simplified composition adopted for the primordial rocky EH planetesimals consists of (by mass) 38.2% SiO_2, 25.2% metallic Fe, 14.3% FeS, 20.6% MgO, and 1.7% H_2O. Note that H_2O included in the EH material is adsorbed to the surface or chemically bound to the minerals.

We consider planets initially formed from a mixture of EH material and H_2O ice. The H_2O ice is in addition to the 1.7% H_2O by mass included in the EH minerals. We compute the planet bulk composition after outgassing from stoichiometry (Table 4.3), assuming some fraction of the accreted iron reacted with water ($Fe + H_2O \rightarrow FeO + H_2$) before sinking to form the planet's metallic core. We note that although we consider only Fe in our reduced EH chemical composition, Ni can also form oxides and be incorporated in silicates. Nickel accounts for 8% of the generalized metallic Fe in our distilled EH chemical composition — the Ni abundance in ALHA77295 is 1.83% by mass. We do not vary the S mass fraction of the iron core in our models, effectively assuming metallic Fe and FeS oxidize in equal proportions. We do not follow any S released in the conversion of FeS to FeO.

Our interior models of outgassed planets comprise up to four chemically distinct layers: an Fe/FeS core, silicate mantle, water layer, and hydrogen atmosphere. The bulk chemical composition of the planet after outgassing determines the relative masses of the planet layers and the composition of the silicate mantle. All of the degassed H_2 is included in a gas layer surrounding the planet. We place all of the FeS and metallic iron in the planet core. We model the H_2O in a differentiated water layer surrounding the mantle, although in practice some water may be sequestered into the silicates (e.g., Elkins-Tanton, 2008, and references therein). All of the remaining species (SiO_2, MgO, FeO, Fe_2O_3) make up the mantle. The ratio of MgO/FeO sets the Mg # of the silicates (Mg # = Mg/(Mg+Fe) by number). We adjust the mantle equation of state to reflect the relative abundances of SiO_2, MgO, FeO, and Fe_2O_3, modeling the silicates as a mixture of (Mg,Fe)O magnesiowustite (Elkins-Tanton, 2008), Fe_2O_3 hematite (Wilburn & Bassett, 1978), and stishovite SiO_2 (Andrault et al., 1998). Outgassed bulk compositions and the corresponding planet properties are reported in Table 4.3.

4.4.2 Results

We find that planets accreted from solid bodies that were abundant in our solar nebula can degas at most 1.7% of their mass in H_2. This limit obtains for a fully degassed coreless EH composition planet that accreted just enough additional water (13.0% by mass) to fully oxidize all available iron to Fe_2O_3. EH material alone does not contain sufficient H_2O on its own to oxidize all the metallic Fe within its bulk (only up to 15.2% of the Fe). The accreted material must include an additional 8.6% H_2O by mass in order to convert all the metallic Fe into FeO, or an additional 13.0% H_2O by mass to convert all the metallic Fe into Fe_2O_3. With any more water than this, the metallic Fe becomes the limiting reagent. The maximal outgassed H_2 atmosphere that we derive here is slightly lower than the value 3.6 wt % H_2 found by Elkins-Tanton & Seager (2008b). Differences in the representative EH chemical compositions assumed account for this disparity.

Mass–radius relations for planets harboring H_2 envelopes from outgassing are shown in Figure 4-7 at both $T_{\rm eq} = 500$ K (Figure 4-7(a)) and $T_{\rm eq} = 1000$ K (Figure 4-7(b)). The blue dot-dashed curve provides an upper limit on the radius of planets accreted from primordial chondritic material alone (without additional water ice), corresponding to the extreme where the oxidizing reaction proceeds until all of the H_2O bound to the minerals is expended and 0.2% of the planet mass is released in H_2. After accreting enough additional water (13% by mass) to convert all available Fe to Fe_2O_3, the magenta solid line represents planets having the maximal fraction of their mass (1.7%) in a degassed H_2 envelope. This curve may be taken to bound the maximum radius/minimum density relation for planets with degassed H_2 envelopes, but no free H_2O.

Planets that accreted more than 13.0% by mass water with the EH chondrite material would have water left over even if all the metals in the planet iron core were expended in the outgassing reaction. In Figure 4-7 we show M_p–R_p relations of an

Table 4.3: Bulk Compositions of EH-composition Planets with Outgassed H_2 Envelopes

% Fe oxidized	Core wt%	Silicate wt%	H_2O wt% excess	H_2 wt%	Silicate Composition				
					MgO wt%	FeO wt%	Fe_2O_3 wt%	SiO_2 wt%	Mg #
0.0	39.5	58.8	1.7	0.0	35.1	0.0	0.0	64.9	1.00
15.2	33.8	66.0	0.0	0.2	31.5	10.3	0.0	58.3	0.85
50.0	19.5	79.9	–3.7	0.6	25.5	27.3	0.0	47.2	0.62
100.0	0.0	98.8	–8.6	1.2	20.0	42.9	0.0	37.1	0.45
100.0	0.0	98.3	–13.0	1.7	19.1	0.0	45.5	35.4	0.45

Notes. The first column represents the fraction of accreted iron that is oxidized and incorporated in the planet's mantle. The next four columns give the composition of the EH planet after outgassing, assuming all outgassed H_2 is retained. Negative entries in the H_2O column indicate a water deficit and represent the proportion of additional water (beyond what is included in the EH material) that needs to be accreted in order to oxidize the specified fraction of iron. The last five columns represent the chemical make-up of the silicate mantle, and determine the mantle equation of state. In rows 2–4 we neglect Fe_2O_3 and assume only FeO is produced when iron is oxidized. Row 5 lists the extreme end-member case where all iron is oxidized to Fe_2O_3.

example with initially 20% by mass water ice in the primordial composition (dotted curves). The fully degassed planets with excess water have, in fact, a lower average density compared to the planets with the highest mass fraction of degassed H_2 — the effect of the lower density ice-rock interior offsets the decreased proportion of H_2. In Figure 4-7, we model the H_2O layer as a distinct chemical layer below the outgassed H_2 envelope, but mixing of H_2O and H_2 is another possibility. If H_2O and H_2 are mixed in the envelope, the planet radii would be smaller than the model radii in Figure 4-7 due to the decreased atmospheric scale height compared to the differentiated case.

The radii of the outgassed planets depend on the intrinsic luminosity of the planet. In Figure 4-7, we show mass–radius relations for planets with $L_p/M_p = 10^{-10.5}\,\mathrm{W\,kg^{-1}}$. Increasing (decreasing) the planet's intrinsic luminosity by a factor of 10 affects the planet radii in Figure 4-7 by at most +16% (–9.5%) at 5 $M_\oplus$ and +4.5% (–3.2%) at 30 $M_\oplus$. Small planet masses and high H_2 contents both increase the radius dependence on L_p.

We explore in Figure 4-8 the mass of H_2 required by EH composition planets to reach radii of 2 to 3 $R_\oplus$. Figure 4-8 is the outgassing analog to Figure 4-6 for core-nucleated accretion. In Figure 4-8, we restrict our attention to planets without significant amounts of H_2O on their surface or in their envelopes. The envelope mass fractions, M_{env}/M_p, at a specified radius are not strongly sensitive to the distribution of Fe within the planet interior (i.e., whether the Fe is differentiated in the metallic core or included in the mantle as oxides) — we show the case where all Fe is oxidized to FeO. Upper bounds on the H_2 wt% for several of the limiting cases in Table 4.3 are indicated by colored horizontal lines.

Our main conclusion from this section is that planets of mass $M_p < 30\ M_\oplus$ with outgassed H atmospheres typically have radii less than 3 $R_\oplus$ (Figures 4-7 and 4-8). Larger radii are found at the low-mass extreme of the M_p–R_p relations in Figure 4-7, but correspond to planets with very tenuous, loosely bound, envelopes. Outgassing of H_2 from planets accreted from rocky material alone most likely cannot account for the *Kepler* planet candidates with radii between 3 and 6 $R_\oplus$.

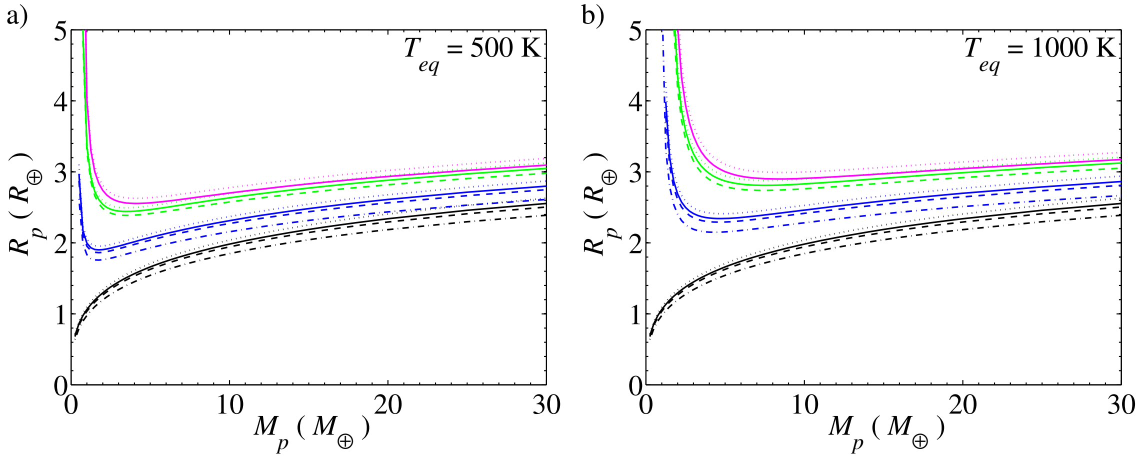

Figure 4-7: Mass–radius relations for exoplanets with outgassed H_2 envelopes. The planets are assumed to have formed purely from a combination of EH chondrite material and water ice. Accreting material with 20% water ice by mass (dotted lines), 13% water ice by mass (solid lines), 8.6% water ice by mass (dashed lines), and no additional water ice (dot-dashed lines) are considered. The line color indicates the fraction of accreted iron that reacted with water. Black corresponds to planets with no outgassed H_2 and a maximally massive iron core (0% Fe reacted). Blue corresponds to planets where 15.2% of the Fe reacted—the maximum amount possible for pure EH material without added water. Green represents an end-member case wherein all the metallic Fe that accreted to the planet is converted to FeO. Finally, magenta lines correspond to planets that outgassed the maximum possible H_2 for their initial chemical makeup—100% of their accreted iron is oxidized to Fe_2O_3. Both the green and magenta M_p–R_p relations represent core-less planets, but they differ in the oxidation state of iron inside the planet (FeO vs. Fe_2O_3) and in the overall proportion of H_2 released. Planet equilibrium temperatures of (a) $T_{\rm eq} = 500$ K and (b) $T_{\rm eq} = 1000$ K are shown. A fiducial intrinsic luminosity $L_p/M_p = 10^{-10.5}$ W kg^{-1} is assumed in all cases. These curves do not include atmospheric escape of H_2.

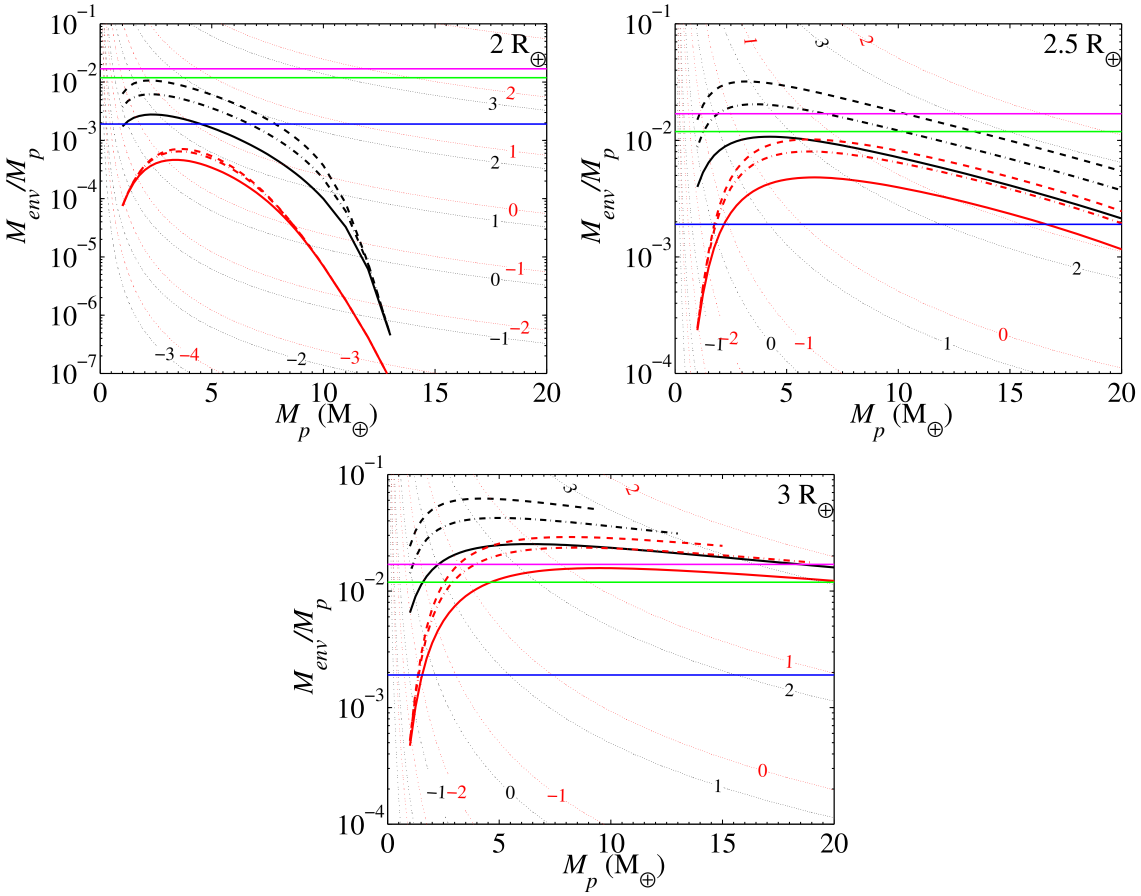

Figure 4-8: Planet mass and outgassed H_2 envelope mass that are consistent with a particular planet radius, for EH composition planets without H_2O on their surface or in their envelopes. We plot the envelope mass fraction as a function of the total mass of the planet for planets with radii (a) $R_p = 2\ R_\oplus$, (b) 2.5 $R_\oplus$, and (c) 3 $R_\oplus$. Horizontal lines indicate the maximal H_2 wt% degassed in three limiting cases: if all H_2O adsorbed in the EH material reacts with metals (0.2%, blue), if all Fe in the EH material is converted to FeO (1.2%, green), and if all Fe in the EH material is converted to Fe_2O_3 (1.7%, magenta). This figure is the outgassing analog to Figure 4-6 for core-nucleated accretion, and all the red and black lines follow the same naming conventions. Black curves represent planets at $T_{\rm eq} = 500$ K, while red curves correspond to $T_{\rm eq} = 1000$ K. The line style indicates the planet luminosity: $L_p/M_p = 10^{-11}\ {\rm W\,kg^{-1}}$ (dashed), $L_p/M_p = 10^{-10}\ {\rm W\,kg^{-1}}$ (dot-dashed), and $L_p/M_p = 10^{-9}\ {\rm W\,kg^{-1}}$ (solid). The thin dotted lines are contours of constant envelope mass-loss timescale, $t_{\dot{M}} \equiv M_{\rm env}/\dot{M}$. Each contour is labeled with $\log(t_{\dot{M}}/{\rm Gyr})$ given $\epsilon L_{\rm XUV}/L_{\rm BOL} = 10^{-6}$.

4.5 Mass Loss from Low-Density Envelopes

A major question is whether the high $T_{\rm eq}$, light element, low gravitational binding energy envelopes modeled above are stable and could be retained over gigayear timescales. It is precisely in the low-mass, low-molecular weight, high $T_{\rm eq}$ regime we are considering in which planets are expected to be most susceptible to mass loss. Below we consider, in turn, the importance of Roche-lobe overflow and X-ray and ultraviolet (XUV)-driven atmospheric escape.

Roche-lobe overflow can limit the radii of low-density planets at close orbital separations from their host stars. Our planet interior model assumes spherical symmetry and neglects tidal forces, but this approximation starts to break down for planets near their star. The effective radius of a planet's Roche lobe is approximated by

$$\frac{r_L}{a} = \frac{0.49q^{2/3}}{0.6q^{2/3} + \ln\left(1 + q^{1/3}\right)} \approx 0.49q^{1/3} - 0.049q^{2/3}, \tag{4.12}$$

where $q \equiv M_p/M_\star$ (Eggleton, 1983). The Roche-lobe radius sets a firm upper limit on the planet radius; any material outside the planet's Roche lobe is not gravitationally bound to the planet and can escape. We plot planet Roche-lobe radii in Figures 4-4 and 4-5 for a sampling of representative host star properties: G2 (1 $M_\odot$, 1 $L_\odot$), K0 (0.79 $M_\odot$, 0.552 $L_\odot$), M0 (0.51 $M_\odot$, 0.077 $L_\odot$), and M5 (0.21 $M_\odot$, 0.0076 $L_\odot$) (Carroll & Ostlie, 2007). In computing the Roche-lobe radii, we have assumed a planetary albedo $A = 0$ when relating $T_{\rm eq}$ to the semi-major axis, a; taking reflection into account with $A \neq 0$ will result in smaller semi-major axes and smaller r_L. Roche-lobe overflow is not an issue for $T_{\rm eq} = 500$–1000 K planets surrounding a solar analog star. In contrast, when orbiting an M star, many of our low-density low-mass planets do fill their Roche lobes. Our equilibrium planet models are not a priori pegged to a given star spectral type. Tidal effects and the Roche-lobe radius set a lower bound on $M_\star$ for which the low-M_p tail of our equilibrium models is applicable.

XUV-driven mass loss is expected to be very important for low-mass, low-density planets. This results from the combined effect of large cross-sections to stellar irradiation, low surface gravities, and low envelope binding energies. Predictions for the exoplanet mass-loss rates suffer from unknowns in the stellar XUV fluxes, the conditions at the planet exosphere, and the mass-loss efficiency. We consider energy-limited mass loss (e.g., Lammer et al., 2003; Lecavelier Des Etangs, 2007; Valencia et al., 2010)

$$\dot{M} = -\frac{\epsilon \pi F_{\rm XUV} R_{\rm XUV}^2 R_p}{G M_p K_{\rm tide}}. \tag{4.13}$$

The efficiency ϵ represents the fraction of the energy in XUV photons incident on the planet that goes into unbinding particles in the planet atmosphere; we take $\epsilon = 0.1$, but $\dot{M}$ can easily be rescaled to another choice of ϵ. $F_{\rm XUV}$ represents the flux of photoionizing radiation impinging on the planet. $K_{\rm tide}$ is a correction factor that accounts for tidal effects in the Roche potential of planets in close proximity to their star (given by Equation (17) in Erkaev et al., 2007). Finally, $R_{\rm XUV}$ reflects the planet radius at which XUV photons are absorbed. We estimate $R_{\rm XUV}$ following order-of-magnitude arguments gleaned from Section 2 of Murray-Clay et al. (2009),

$$R_{\rm XUV} \approx R_p + H_R \ln\left(\frac{P_R R_{\rm XUV}^2}{N_{\rm H} m_{\rm H} G M_p}\right), \tag{4.14}$$

where $N_{\rm H} \sim 5 \times 10^{21}~\rm m^{-2}$ is roughly the column of neutral hydrogen needed to reach $\tau_{\rm XUV} \sim 1$, P_R is the pressure at R_p, and H_R is the pressure scale height at R_p (where $\tau \sim 1$ for visible light).

We take an illustrative example of planets orbiting a solar analog star to explore the order of magnitude of mass-loss rates. Figure 4-9 shows estimated mass-loss rates for the planet models presented in Figure 4-4. For our assumed solar-twin host star, we compute $F_{\rm XUV}$ for $T_{\rm eq}$ by scaling the integrated solar XUV flux measured by Ribas et al. (2005) ($F_{\rm XUV\odot} = 4.6 \times 10^{-3}~\rm W\,m^{-2}$ at 1 AU). We find that, for $L_{\rm XUV}/L_{\rm BOL} = 3.4 \times 10^{-6} = L_{\rm XUV\odot}/L_{\rm BOL\odot}$ and $\epsilon = 0.1$, planets at the low-mass extreme of our M_p–R_p relations have implausibly short envelope mass-loss timescales $t_{\dot{M}} \equiv M_{\rm env}/\dot{M} \lesssim 1$ Gyr.

We use energy-limited mass loss (Equation (4.13)) to include contours of constant $\log(t_{\dot{M}}/\rm Gyr)$ in Figures 4-6 and 4-8. The contour values represent $\log(t_{\dot{M}}/\rm Gyr)$ corresponding to ($\epsilon L_{\rm XUV}/L_{\rm BOL} = 10^{-6}$), but can easily be scaled to reflect other parameter choices:

$$t_{\dot{M}} = \frac{M_{\rm env}}{\dot{M}_p} \propto (\epsilon L_{\rm XUV}/L_{\rm BOL})^{-1}\,. \tag{4.15}$$

At a specified $T_{\rm eq}$, the $t_{\dot{M}}$ contours are independent of the host star mass so long as tidal effects can be neglected ($K_{\rm tide} \approx 1$). For the ($T_{\rm eq}$, R_p) combinations sampled in Figures 4-6 and 4-8, this approximation holds for main-sequence host stars that are K0 V or earlier, but breaks down for M stars. We emphasize that $t_{\dot{M}}$ gives an instantaneous measure of the time that the planet would take to lose its envelope at the calculated current mass-loss rate. $\dot{M}$ is expected to vary over a planet's lifetime. Stars that are more active (e.g., younger) than our Sun would have higher photoionizing fluxes.

We find that planets at the low-mass extremes of Figures 4-6 and 4-8 have short envelope mass-loss timescales $t_{\dot{M}} \equiv M_{\rm env}/\dot{M} \lesssim 1$ Gyr (assuming $\epsilon L_{\rm XUV}/L_{\rm BOL} = 10^{-6}$). One could conceivably choose a threshold envelope loss timescale $t_{\dot{M}0}$ and then derive a lower bound on the planet mass at a given radius based on that assumption. We elaborate this possibility further in Section 4.6.3.

4.6 Discussion

4.6.1 Formation of Low-density Neptune-size Planets

Core-nucleated Accretion

Can core-nucleated accretion form low-density planets in the size range of 2–6 $R_\oplus$? The answer is yes, given appropriate conditions. The solids surface density in the protoplanetary disk must be appropriate for the accretion of heavy-element cores a few times as massive as Earth. These cores must grow early enough to accrete significant gaseous envelopes, but gas accretion must end early enough to avoid runaway gas accretion. Our evolution calculations in Section 4.3 demonstrate that $M_p < 10\ M_\oplus$ H/He-rich planets can form for plausible choices of σ and disk lifetimes. The values we choose for σ are only slightly above that in the minimum-mass solar nebula, but high enough so that Jupiter at 5 AU can form in 4 Myr.

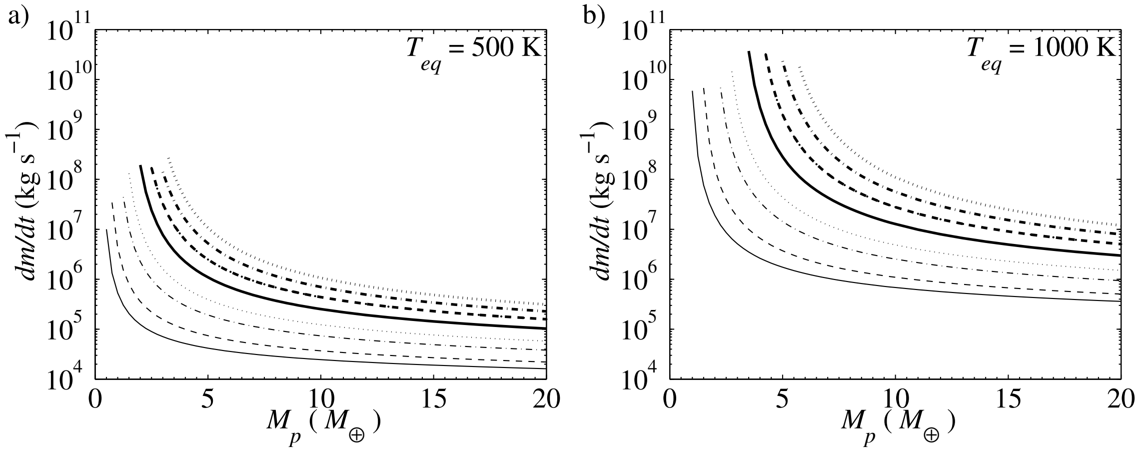

Figure 4-9: Energy-limited mass-loss rates for the planet models in Figure 4-4. Mass-loss rates are estimated for the case where the planets orbit a star with similar properties to our Sun ($M_\star = 1\ M_\odot$, $L_\star = 1\ L_\odot$, and $L_{\rm XUV} = 3.4 \times 10^{-6}\ L_\odot$). A mass-loss efficiency of $\epsilon = 0.1$ is assumed. The line styles have the same meanings and correspond to the same model planets as in Figure 4-4. Each curve corresponds to a different value of $M_{\rm env}/M_p$: 0.001 (thin solid), 0.01 (thin dashed), 0.05 (thin dot-dashed), 0.1 (thin dotted), 0.2 (thick solid), 0.3 (thick dashed), 0.4 (thick dot-dashed), and 0.5 (thick dotted). All data in this plot have $L_p/M_p = 10^{-10.5}$ W kg^{-1}, and (a) $T_{\rm eq} = 500$ K or (b) $T_{\rm eq} = 1000$ K.

A second related question is whether core-nucleated accretion with subsequent migration can lead to Neptune-size planets at high irradiation temperatures $T_{\rm eq} \geq 500$ K. Our evolution calculations uncover two factors that complicate achieving 2–6 $R_\oplus$ planets following inward migration. First, high irradiation temperatures lead to very large fluffy planets with radii $R_p > 6\ R_\oplus$. Second, very long migration timescales are required to heat a planet to $T_{\rm eq} = 1000$ K while keeping its envelope intact. We elaborate both of these points below.

The salient feature of our evolution calculations is that, despite $M_p < 10\ M_\oplus$, the irradiated planet radii at 1 and 4 Gyr are, in many cases, larger than 6 $R_\oplus$. Specifically, all cases in Table 4.2 with $T_{\rm eq} = 1000$ K or $M_p > 5\ M_\oplus$ have radii in excess of 6 $R_\oplus$. Lower mass envelopes are required to yield Neptune-size planets at these high irradiation levels (Figure 4-6). Truncating gas accretion earlier (shorter disk lifetime) and subsequent envelope mass loss are two potential avenues toward $R_p < 6\ R_\oplus$. While the model radii at 1000 K are very uncertain due to uncertainties in the opacities near the radiative–convective boundary, for the cases in Table 4.2 the conclusion that $R_p > 6\ R_\oplus$ is, nonetheless, robust.

We found that slow planetary migration is needed for the low-mass envelopes to stay bound as the temperature at the planetary surface increases. In our evolution calculations, the planets initially assemble at $T_{\rm neb} = 115$ K or 125 K and then migrate inward to $T_{\rm eq} = 500$ K or 1000 K. The long migration timescale (~ 40 Myr) taken to reach $T_{\rm eq} = 1000$ K with the envelope intact is in tension with typical disk lifetimes (1–10 Myr). The migration timescale to reach 500 K (~ 5 Myr) is more plausible. It is possible that evaporative cooling or increases in the envelope mean molecular weight from preferential loss of hydrogen could help the envelope remain bound. The planet evolution tracks presented do not include mass loss.

There do exist Neptune-size equilibrium configurations at $T_{\rm eq} \geq 500$ K for planets with H/He envelopes from core-nucleated accretion. Our equilibrium planet structure models in Section 4.2 explore and map out the ($M_{\rm env}$, M_c, $T_{\rm eq}$, $T_{\rm int}$) parameter space that yields radii within the range 2–6 $R_\oplus$ (Figure 4-6). It is important to note, however, that the equilibrium models provide "snap shots" of possible equilibrium configurations of planets undergoing quasi-static evolution. The models do not address how a planet could reach a given state, nor the timescale for the planet to evolve out of the state.

Outgassing of H_2

The second formation pathway to low-density Neptune-size planets we considered was outgassing of H_2 from rocky planets. Outgassed low-mass planets ($M_p < 30\ M_\oplus$) without substantial H_2O envelopes, however, can only account for radii up to $\sim 3\ R_\oplus$. Even achieving $3\ R_\oplus$ with an outgassed envelope is a stretch, requiring (concurrently) a near-optimal initial planetesimal composition, full oxidization of accreted metals, and retention of most H_2 released. Realistically, the majority of outgassed planets will be smaller than this radius limit, as we elaborate below.

The metal and H_2O content of the primordial material forming a planet set a strict limit on the amount of H_2 that can be released via the outgassing reaction, $2Fe + 3H_2O \rightarrow Fe_2O_3 + 3H_2$. In this work, we have adopted a primordial chemical composition representative of EH chondrites mixed with just enough additional H_2O ice to fully oxidize all the metals. Out of the Solar System chondrites, this composition should be near optimum for outgassing of H_2 due to the high proportion of unoxidized iron (in metal or sulfide form) (Elkins-Tanton & Seager, 2008b). Typically, planets forming from a mixture of Solar System chondrite-like material (Jarosewich, 1990, within which the proportion of metallic iron varies from 0.1 to 22 wt%) would have a lower capacity to outgas H_2.

Even given a high initial amount of reduced metals, a planet's eventual outgassed envelope mass is contingent upon the fraction of metals that oxidizes. To bound the radii of outgassed planets, we considered the end-member case of complete oxidation of all Fe to Fe_2O_3. In this limiting case, the planet is core-less with all its iron incorporated in the mantle as oxides (Elkins-Tanton & Seager, 2008a). Planets retaining a metallic core would degas less H_2. Ultimately, the overall fraction of Fe that reacts with water is determined by the competition between the rate of oxidation and the rate of sinking of metallic Fe to form the planet iron core. For a more detailed discussion, see

Elkins-Tanton & Seager (2008a).

Finally, the mass–radius relations for outgassed planets in Section 4.4 considered 100% retention of all outgassed H_2. Atmospheric escape leads to less massive H_2 envelopes and smaller planets overall (Section 4.5). Indeed, while the primary outgassed atmospheres surrounding Earth and Mars during their accretion were likely H_2-dominated (Schaefer & Fegley, 2010), both planets today harbor secondary atmospheres with higher mean molecular weights.

How close can outgassed-planet radii plausibly get to the limiting outgassing M_p–R_p relation? Relaxing our assumptions of optimum outgassing conditions, we investigate an intermediate, incomplete-oxidation case in which 50% of the accreted Fe is converted to FeO. This scenario leads to planets with 19.5% of their (initial) mass in an iron core, 0.6% by mass degassed in H_2, and a mantle Mg# of 0.62 (Table 4.3). With no loss of H_2, these planets could have radii up to 2.7 $R_\oplus$ (again considering $M_p \leq 30\ M_\oplus$), whereas, with atmospheric mass loss, planets that retain only 1%–10% of the degassed H_2 would have radii up to at most 2.4–2.5 $R_\oplus$ for $T_{\rm eq} = 500$–1000 K. Thus, radii up to $\sim 2.5\ R_\oplus$ are more realistically achieved by rocky planets with outgassed H_2 envelopes but no free water. Planets with a water layer between the rocky interior and H_2 envelope could be slightly larger, but only if little or no H_2 was mixed in with the H_2O.

4.6.2 Maximum Planet Radius at Specified Mass

We have modeled the internal structure of low-mass, large-radius planets with hydrogen-dominated atmospheres. For planets with outgassed H envelopes, we derived a limiting low-density M_p–R_p relation by leveraging an upper bound on the amount of H_2 that can be degassed from rocky planetesimals. The limiting low-density M_p–R_p relation is less clear-cut for planets formed from core-nucleated accretion, because the initial reservoir of H/He accreted from the nebula need not be a constraining factor. Our detailed planet formation calculations provide discrete examples of planets at $T_{\rm eq} = 1000$ K with only a few Earth masses yet radii larger than Jupiter.

The low-density limit for planets formed from core-nucleated accretion depends on the heavy-element core and envelope masses achievable at a given equilibrium temperature. The plausible combinations of (M_{env}, M_c, T_{eq}) in turn rely on the protoplanetary disk properties and the migration history of the planet. The heavy-element core mass is determined by the isolation mass, given the solid surface density and the distance from the star where the planet forms. The isolation mass (and thus M_c) can have a wide range of values, from less than 0.1 $M_\oplus$ to more than 20 $M_\oplus$. The initial mass of H/He accreted by the planet is determined by the availability of a gas supply from the disk as governed by disk lifetime relative to the time taken for the heavy-element core to reach isolation mass. Disk lifetimes range over an order of magnitude—from 1 to 10 Myr, with a characteristic value of a few megayears (Hillenbrand, 2008)—leading to some freedom in the initial M_{env} expected from core-nucleated accretion. Mass loss over the planet's history would serve to decrease M_{env} over time. Finally, the current equilibrium temperature T_{eq} depends on the migration history of the planet, and can, in principle, be anywhere from 100 K to 2000 K. Thus, due to the large spread in observed disk properties, a wide range of (M_{env}, M_c, T_{eq}) from core-nucleated accretion are plausible. We have shown detailed planet formation calculations for four reasonable choices of disk planetesimal densities and lifetimes.

We have succeeded in placing a tighter constraint on the low-density M_p–R_p relation for outgassed planets than we have for planets from core-nucleated accretion. This is due to the inherent limits on outgassed envelope masses; at very most, only a few percent of the mass of a planet can be outgassed in H_2. The end-member case of a planet that accreted from an optimum mixture of EH material and H_2O ice, where all the water and iron reacted, and where all released H_2 was retained, sets an upper bound on the transit radius possible at a given mass for a rocky planet with out-gassed H_2 atmosphere (Figure 4-7). Typically, rocky planets with outgassed H_2 atmospheres would have mean densities above this limiting M_p–R_p relation. It should be noted that our limiting M_p–R_p relation applies to planets formed from material similar to Solar System chondrites. Planets formed from material with higher metallic Fe content would have the potential to outgas more H_2.

We have so far considered either core-nucleated accretion or outgassing due to water–

iron reactions as separate pathways for planets to acquire hydrogen-rich envelopes. Core-nucleated accretion contributes near solar composition material to the envelope ($Y \sim 0.25$), while water–iron reactions contribute hydrogen but not helium ($Y = 0$). If both processes occur on the same exoplanet, an envelope with intermediate, sub-solar, non-zero Helium content ($0 < Y < 0.25$) may result.

The assumed chemical make-up of the planet envelope and heavy-element core affect the planet M_p–R_p relations for planets formed by core-nucleated accretion and by outgassing. H/He envelopes in which He is depleted relative to solar will be more voluminous, for the same envelope masses, temperatures, and heavy-element core properties. This is largely due to the influence of the mean molecular weight on the atmospheric scale height. For instance, decreasing $Y = 0.25$ to $Y = 0.0$ in the equilibrium planet models of Section 4.3.3, increases the radial extent of the envelopes by $\sim$ 15%–20% for $M_p > 20\ M_\oplus$. For lower mass planets, the change in the gravitational acceleration between the top and bottom of the envelope can be substantial and Y can have a larger effect on the envelope thickness. Pure H envelopes can be up to twice as thick as the corresponding H/He envelope, near the low-mass extreme of the M_p–R_p relations in Section 4.3.3. In our planet structure models, however, the effect of the envelope He abundance is largely offset by the higher density heavy-element core composition in our outgassing models (EH chondrite cores) as compared to our core-nucleated accretion models (ice–rock cores).

We have mapped out the contribution of low-mass planets with hydrogen-dominated atmospheres to the limiting low-density $M_p\,(R_p)$ relation. Although we have not considered them in detail here, planets may also form with high molecular weight envelopes, for instance, after having accreted large amounts of ices beyond the snow line (e.g., Kuchner, 2003; Léger et al., 2004). Higher molecular weight envelopes are more dense (with smaller atmospheric scale heights) than their hydrogen-dominated counterparts, but may be less affected by atmospheric escape. It is possible that planets with high molecular weight atmospheres could also contribute to the limiting low-density $M_p\,(R_p)$ relation for Neptune-size planets.

4.6.3 Minimum Planet Mass at Specified Radius

Our ideal goal was to determine a lower bound on the plausible planet mass given a planet radius in the range 2–6 $R_\oplus$ and equilibrium temperature $T \geq 500$ K. We note that the relation defining the maximum radius for a given planet mass does not necessarily translate into a relation for the minimum planet mass at a given radius. Indeed, at low masses, $dR_p/dM_p < 0$ in the iso-composition M_p–R_p relations for planets with gas envelopes (e.g., Figures 4-4, 4-5 and 4-7). Thus, in order to bracket the minimum planet mass of a transiting planet candidate, we must assess the survivability of low-mass planets for a range of interior compositions.

Mass loss is a major limiting factor that constrains the minimum $M_p\,(R_p)$ for strongly irradiated ($T \geq 500$ K) Neptune-size planets harboring hydrogen-dominated envelopes (Section 4.5). This is true whether the planet acquired its envelope through core-nucleated accretion or through outgassing. If the heavy-element core mass is small ($\lesssim 2\ M_\oplus$) and $T_{\rm eq}$ is high (1000 K) then the planet will not be able to hold on to very much gas. With the energy-limited mass-loss rates from Equation (4.13), we may roughly assess the survivability of potential planet configurations. By choosing a threshold envelope loss timescale $t_{\dot{M}0}$, we can derive a lower bound on the planet mass at a given radius based on the requirement $t_{\dot{M}} \geq t_{\dot{M}0}$. To illustrate this approach, we adopt $t_{\dot{M}0} = 1$ Gyr and explore what this implies for planets with low mean molecular weight envelopes from core-nucleated accretion (Figure 4-6) and from outgassing (Figure 4-8).

We estimate, using Figure 4-6, the minimum masses of $R_p = 2$–$6\ R_\oplus$ planets with H/He envelopes formed by core-nucleated accretion beyond the snow line. For $R_p = 6\ R_\oplus$ planets, the least massive planet models that satisfy $t_{\dot{M}} \geq 1$ Gyr are 1.3 to 1.7 $M_\oplus$ at $T_{\rm eq} = 500$ K, and 4.0 to 4.7 $M_\oplus$ at $T_{\rm eq} = 1000$ K (for L_p/M_p between 10^{-9} and 10^{-11} W kg^{-1}). Analogously, at $R_p = 4\ R_\oplus$, the $t_{\dot{M}} \geq 1$ Gyr survivability constraint requires that $M_p \gtrsim 1.1$ to 1.4 $M_\oplus$ at $T_{\rm eq} = 500$ K, and $M_p \gtrsim 3.6$ to 4.3 $M_\oplus$ at $T_{\rm eq} = 1000$ K. At $R_p = 2\ R_\oplus$, almost all possible (M_p, $M_{\rm env}$, L_p, $T_{\rm eq}$) configurations in Figure 4-6 have sub-gigayear envelope loss timescales, due to the small planet and envelope masses ($M_p < 5\ M_\oplus$, $0 \leq M_{\rm env} < 0.1\%\ M_p$). An ice/rock core surrounded by an H/He envelope from core-nucleated accretion may not be a plausible interior composition scenario for 2 $R_\oplus$ planets at these equilibrium temperatures. Instead, other possibilities not considered here (e.g., high molecular weight envelopes or envelope-less planets) may account for the minimum plausible planet mass at 2 $R_\oplus$.

We turn now to planets with outgassed hydrogen envelopes but no surface water, and apply the envelope mass-loss threshold to Figure 4-8. In addition to atmospheric escape, hydrogen-rich envelopes acquired by outgassing are also constrained by the limited H_2 reservoir (magenta line in Figure 4-8). We find that, at $T_{\rm eq} = 500$ K, there exist potential planet configurations that satisfy $t_{\dot{M}} \geq 1$ Gyr with masses as low as 1 $M_\oplus$ for planet radii ranging from 2 to 3 $R_\oplus$. Granted, these minimum-mass outgassing scenarios necessitate near-maximal release and retention of H_2. In contrast, at $T_{\rm eq} = 1000$ K, all possible H_2 envelopes leading to $R_p = 2\ R_\oplus$ have sub-gigayear envelope loss timescales. For larger radii (2.5, and 3 $R_\oplus$), planets with masses as low as 3.5 – 4 $M_\oplus$ (depending on L_p) may pass the $t_{\dot{M}} \geq 1$ Gyr survivability criterion.

We emphasize that minimum masses estimated following the approach above are contingent upon the chosen $t_{\dot{M}}$ threshold, the energy-limited mass-loss parameter values assumed (here we took $\epsilon L_{\rm XUV}/L_{\rm BOL} = 10^{-6}$), and the range of planet ages/intrinsic luminosities under consideration. High (lower) $t_{\dot{M}0}$ would lead to higher (lower) minimum $M_p(R_p)$. Although quantitatively very assumption-dependent, minimum masses derived from $t_{\dot{M}0}$ may nonetheless yield important qualitative insights.

4.6.4 Implications for *Kepler* Planet Candidates

We conclude with a discussion of the implications of our results for the Neptune-size planet candidates discovered by *Kepler*. Candidates in the 2–6 $R_\oplus$ size range account for a large fraction of the current candidates detected by *Kepler* (Borucki et al., 2011a,a). This raises the question of why Neptune-size planet candidates are so common. One possible contributing factor revealed by this study is that not very much mass is needed in a hydrogen-dominated envelope for a rocky heavy-element core to reach radii within 2–6 $R_\oplus$.

Our main conclusion is that the Neptune-size planet candidates could have low mass ($M_p < 4\ M_\oplus$). This deduction is supported by our calculations of the formation, structure, and survival of planets with voluminous envelopes of light gasses.

1. *Formation.* We demonstrated that planets 3–8 $M_\oplus$ with substantial H/He envelopes can plausibly form by core-nucleated accretion beyond the snow line and migrate to $T_{\mathrm{eq}} \sim 500$ K given reasonable disk surface densities and disk dissipation timescales. Migration to $T_{\mathrm{eq}} \sim 1000$ K with the envelope intact in timescales of a few megayears is more challenging.
2. *Structure.* We mapped the regions of (M_p, M_{env}, T_{eq}, L_p) parameter space that yield radii between 2 and 6 $R_\oplus$ for planets with H/He envelopes from core-nucleated accretion and for planets with outgassed H_2 envelopes (Figures 4-6 and 4-8, respectively). Since at most a few percent of a planet's mass can be degassed as H_2, rocky super-Earths ($M_p < 30\ M_\oplus$) with outgassed hydrogen atmospheres but without substantial H_2O typically will not account for *Kepler* planet candidates larger than $\sim 3\ R_\oplus$.
3. *Survival.* Envelope mass loss plays a major role governing the minimum plausible $M_p\,(R_p)$ for strongly irradiated ($T \geq 500$ K) Neptune-size planets with hydrogen-dominated envelopes. At $R_p = 2\ R_\oplus$, H/He envelopes surrounding ice–rock cores would likely be lost in short order. At larger radii (2.5–6 $R_\oplus$), planet configurations with envelope mass-loss timescales longer than a gigayear (assuming $\epsilon L_{\mathrm{XUV}}/L_{\mathrm{BOL}} = 10^{-6}$) exist down to masses $\sim 1\ M_\oplus$ at $T_{\mathrm{eq}} = 500$ K and down to $\sim 4\ M_\oplus$ at $T_{\mathrm{eq}} = 1000$ K.

Neptune-size planets with masses $M_p < 4\ M_\oplus$ could prove a challenge for radial velocity (RV) follow-up due to their low RV semi-amplitudes, but confirmation and mass measurements through transit timing variations may be possible in some cases (e.g., Kepler-11, Lissauer et al., 2011). Figures 4-6 and 4-8 may be useful tools for assessing minimum masses for *Kepler* planet candidates.

Chapter 5

Which Super-Earths and Mini-Neptunes Can Have Liquid Water Oceans?

Abstract

The presence of liquid water has been hypothesized as an important ingredient for planet habitability. A sub-Neptune mass planet with a liquid water ocean below a hydrogen-rich envelope is an intriguing prospect. If the planet transits, its atmosphere could be amenable to characterization with transmission spectroscopy. A practical method to assess whether a planet with measured mass and radius could potentially harbor a liquid water ocean is needed. Equilibrium temperature alone is insufficient to determine whether a planet could have a liquid water ocean; the planet intrinsic luminosity, envelope mass, and greenhouse effect also influence the surface pressure and temperature. Using a one-dimensional radiative-convective model of energy transport through water-saturated hydrogen-rich envelopes, we constrain the combinations of planet properties (mass, radius, equilibrium temperature, intrinsic luminosity) that are conducive to liquid water oceans. We find that sub-Neptune-mass planets with radii exceeding $\sim 3.25\ R_\oplus$, or equilibrium temperature $T_{\mathrm{eq}} > 370$ K cannot have liquid water oceans. For hydrogen-rich super-Earths, a surface pressure on the order of $\sim 10^7$ Pa of H_2 is optimum to allow liquid water oceans over the widest range of planet energy budgets. Kepler-22b need not be rock-dominated, but must have a mass of at least 7.0 $M_\oplus$ to support a liquid water ocean. In contrast, GJ 1214b is too strongly irradiated to have a liquid water ocean.

5.1 Introduction

The quest for habitable environments beyond the confines of the Earth inspires professional and citizen scientists alike. The presence of liquid water has been hypothesized as an important ingredient for habitability, driving intense interest in the search for liquid water on planets both within the Solar System, and beyond. Habitability is not the sole motivation for exploring scenarios for liquid water oceans on exoplanets, however. The presence of liquid water oceans on planetary bodies also has important implications for the planets' mineralogical, geochemical, and thermal evolution.

In the Solar System, there is evidence for liquid water oceans on Earth's surface, in Titan's subsurface (Lorenz et al., 2008), in Europa's subsurface, and on ancient Mars. Despite potentially large reserves of water, Uranus and Neptune are too warm (interior entropy too high) and too dry (interior molar abundance of water too low) to have liquid water oceans (Wiktorowicz & Ingersoll, 2007). Among the transiting super-Earth planets discovered to date, most are too hot to harbor water in the liquid phase. Indeed, CoRoT-7b, Kepler-10b, and 55 Cnc e all have equilibrium temperatures ($T_{\rm eq} \sim 2000$ K), far exceeding the critical temperature of water ($T_c = 647.096$ K). The equilibrium temperature of GJ 1214b is sub-critical (~ 500 K, depending on the planet albedo), but GJ 1214b's surface temperature at the base of its voluminous envelope will still be too hot for liquid water unless the planet has a low intrinsic luminosity (Rogers & Seager, 2010b). Gl 581 may host planets in the habitable zone (Selsis et al., 2007a; Wordsworth et al., 2011), but they are so far only detected by radial velocity observations. A practical and useful approach to assess the potential for a transiting planet to harbor liquid water, given the observable properties (planet M_p, R_p, atmospheric scale height, orbital period and stellar spectral type) is needed.

Traditionally, the circumstellar habitable zone is defined as the range of orbits on which an Earth-like planet could harbor a surface liquid water ocean. Most habitable zone studies focus on planets with CO_2–H_2O–N_2 atmospheres (e.g., Huang, 1960; Hart, 1979; Kasting et al., 1993; Selsis et al., 2007b), since this composition class encompasses Venus, Earth, and Mars. The inner edge of the habitable zone is delimited by the onset of runaway greenhouse states and vaporization of planet oceans (e.g., Komabayashi, 1967; Ingersoll, 1969; Kasting, 1988), while the outer edge is delimited by the condensation of CO_2 (which cools the planet surface by increasing the albedo and decreasing the convective lapse rate). For the Solar System, Kasting et al. (1993) estimate that the circumstellar habitable zone around the current sun ranges from 0.95 to 1.37 AU.

The discovery and characterization of a habitable Earth-twin is a driving impetus in the field of exoplanets. With current technology, however, super-Earth and mini-Neptune planets are the state of the art. Super-Earths with hydrogen-dominated envelopes are especially amenable to discovery and characterization. A hydrogen gas layer, with its low mean molecular weight and large scale height, can contribute to the transit radius and exhibit detectable variations in the transit depth as a function of wavelength. As transit surveys are uncovering sub-Neptune planets with bulk densities that betray massive gas envelopes (e.g., GJ 1214b, Kepler-11c, d, e, f, and 55 Cnc e), a study of the possibility for high pressure water oceans surrounded by massive hydrogen-rich envelopes is especially timely.

There are several important differences between the habitable zone for H_2-rich planets and the "traditional" habitable zone for planets with CO_2–H_2O atmosphere. First, due to collision induced absorption (CIA), H_2 can serve as a non-condensing green-house gas allowing planets to support liquid water oceans at orbital separations far exceeding the CO_2-condensation outer limit (Stevenson, 1999; Pierrehumbert & Gaidos, 2011). Second, super-Earth and sub-Neptune planets with massive gas layers may have more entries in their energy budgets than the Solar System terrestrial planets. On Earth, incoming starlight is the primary driver of the atmosphere energy budget, but on more massive planets the intrinsic luminosity (from radioactive decay, core cooling, and envelope contraction) can be of comparable (or at least of non-negligible) importance. Third, gas layers that are massive enough may be optically thick. Absorption of visible light can affect the envelope temperature profile and the inner edge of the habitable zone. Finally, hydrogen gas layers can contribute significantly to the radius of super-Earth planets (Rogers et al., 2011), so the planet radius should be important when delimiting the habitable zone for hydrogen-rich planets.

The goal of this paper is to explore the range of scenarios in which sub-Neptune mass planets with hydrogen-dominated envelopes may harbor a liquid water ocean. To accomplish this goal, we bridge the gap between basic climate models of terrestrial planets and interior structure models of Neptunes. We construct a one-dimensional semi-grey radiative-convective model of energy transport through water-saturated hydrogen-rich super-Earth and mini-Neptune envelopes. With our model, we explore the range of planet interior pressure–temperature (P–T) profiles that lead to surface conditions conducive to liquid water. We delimit the "habitable zone" or "liquid water ocean parameter space" for planets with H_2-H_2O envelopes in terms of exoplanet observables (mass, radius, orbital period). It is our aim to provide a useful diagnostic tool for observers and theorist alike to quickly assess the potential scenarios in which a hydrogen-rich exoplanet could harbor liquid water.

In Section 5.2, we review the physical concepts relevant to modeling the interior and atmospheres of planet with oceans. We describe our model in Section 5.3. In Section 5.4, we constrain the radii and global energy budgets of planets with liquid water oceans below H_2-H_2O envelopes. We consider the Solar System Planets, GJ 1214b, and Kepler-22b as case studies in Section 5.5. We discuss the implications of our results and conclude in Sections 5.6 and 5.7.

5.2 Theory

The planet interior temperature profiles that encounter conditions allowing liquid water are constrained by *i)* the water phase diagram, which sets the pressure–temperature–composition conditions for liquid water, *ii)* the planet energy budget, *iii)* the physics of energy transport through planet envelopes, which mediates the possible (long-lived/persistent) P–T profiles of a planet and *iv)* the thermophysical and radiative properties of the envelope gases. We discuss each of these concepts below.

5.2.1 Water phase diagram

The water phase diagram (Figure 5-1) is key to understanding which planetary environments may have liquid water. Pure water is liquid over a limited range of pressures-temperature conditions. The low-pressure limit for liquid water is set by the liquid-vapor coexistence curve, which extends from the ice I–liquid–vapor triple point (273.15 K, 611.655 Pa) to the critical point (T_c = 647.096 K, P_c = 22.0640 MPa). The critical temperature, T_c, is the maximum temperature for liquid water. At temperatures exceeding T_c there is no first order liquid–vapor phase transition—water instead transitions continuously from vapor to super-critical fluid. The low-temperature boundary for liquid water is delimited by the melting curve for ice Ih. The ice Ih melting curve is nearly isothermal, changing by only 22 K over more than 5 orders of magnitude in pressure (from 273.15 K at 611.655 Pa to 251.165 K at 209.9MPa). At high pressures (0.2 to $\sim$ 10 GPa) liquid water freezes to form high pressure ices III, V, VI, and VII. For a planet to sustain a liquid water ocean, its surface pressure and surface temperature must lie within the liquid regime in Figure 5-1.

The pressures and temperatures relevant to liquid water oceans on planets are readily accessible to experiments. For water in the liquid, vapor, or super-fluid phases we adopt thermodynamic properties (e.g., molar volume v, entropy s, latent heat L, heat capacity at constant pressure c_P, heat capacity at constant volume c_v) from the IAPWS-95 formulation Wagner & Pruß (2002), which is based on a compilation of experimental studies. For water phase boundaries, we use the saturated liquid-vapor properties from Wagner & Pruss (1993), ice I sublimation pressure equation from Wagner et al. (1994), and high-pressure ice melting curves from Dunaeva et al. (2010). These phase boundaries are all analytic fits to experimental data.

5.2.2 Equation of State for Mixtures

To model the atmospheres of planets with surface liquid water oceans, we need to know the thermophysical properties of water vapor mixed with other gases. In this work, we adopt the notational convention that all specific variables (v, s, L, c_P,

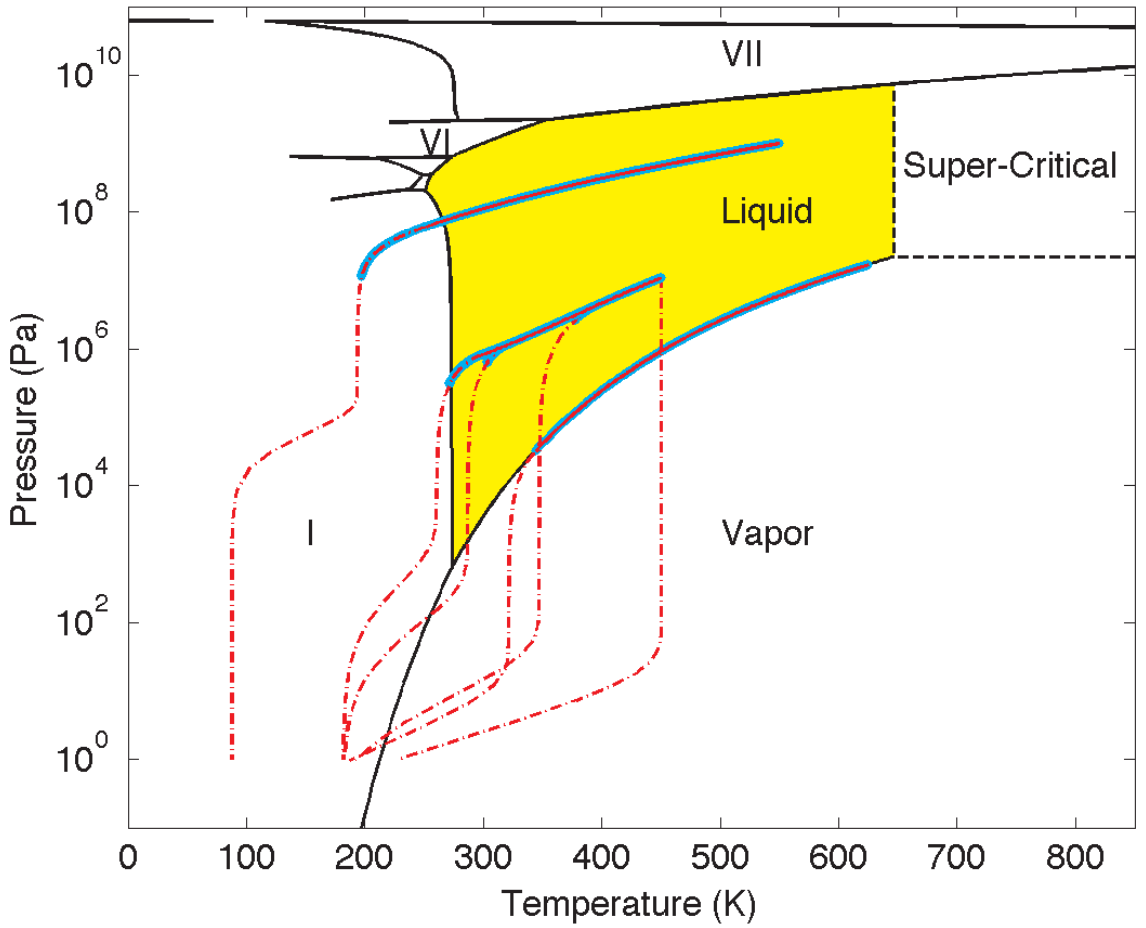

Figure 5-1: Pure H_2O phase diagram with envelope P–T profiles for ocean-bearing hydrogen-rich super-Earth exoplanets. The conditions under which water is in the liquid phase are shaded in yellow. Black lines demarcate phase transitions of pure water. Sample P–T profiles for saturated H_2–H_2O envelopes are plotted in red. Solid lines denote convective regions of the planet envelope, while dot-dashed lines indicate radiative regions. Saturated (condensing) regimes of the planet envelope are highlighted in cyan. From top to bottom, the profiles shown correspond to: *i)* $P_{\rm ns} = 10^9$ Pa, $T_{\rm s} = 550$ K, $T_{\rm int} = 5$ K, $T_{\rm eq} = 103$ K; *ii)* $P_{\rm ns} = 10^7$ Pa, $T_{\rm s} = 450$ K, $T_{\rm int} = 30$ K, $T_{\rm eq} = 207$ K; *iii)* $P_{\rm ns} = 10^7$ Pa, $T_{\rm s} = 450$ K, $T_{\rm int} = 20$ K, $T_{\rm eq} = 210$ K; *iv)* $P_{\rm ns} = 10^7$ Pa, $T_{\rm s} = 450$ K, $T_{\rm eq} = 10$ K, $T_{\rm eq} = 225$ K; *iv)* $P_{\rm ns} = 10^7$ Pa, $T_{\rm s} = 450$ K, $T_{\rm eq} = 0$ K, $T_{\rm eq} = 268$ K; *v)* $P_{\rm ns} = 0$ Pa, $T_{\rm s} = 625$ K, $T_{\rm int} = 20$ K, $T_{\rm eq} = 217$ K. At high pressures, each P–T profile line terminates at an ocean surface. Fiducial values are assumed for the separation between the planet center and ocean surface, $r_{\rm s} = 2.2\ R_\oplus$, and for the mass interior to the ocean surface, $m_{\rm s} = 5.0\ M_\oplus$ (surface gravity $g_{\rm s} = 10\ {\rm m\,s^{-2}}$).

c_v) describe quantities per unit mol. We describe here a composition interpolation approach (following Ingersoll, 1969; Kasting, 1988) to compute the equation of state (EOS) of a mixture from the EOSs of the pure component gases, neglecting non-ideal mixing effects.

We adopt Dalton's Law to construct an EOS for gas mixtures from the EOSs of the pure component gases. Dalton's law states that the pressure, P, of a gas mixture is equal to the sum of the pressures of the pure component gases separately occupying the same volume at the same temperature.

$$P\left(v, T, \{x_i\}\right) = \sum_i P_i\left(v_i, T\right) \tag{5.1}$$

Above, $P_i\left(v_i, T\right)$ is the equation of state of the pure ith component gas contributing a fraction x_i by number of the molecules in the mixture. Although another composition interpolation scheme called Amagat's law (the "additive volume" rule) is favored for hydrogen, helium, and water mixtures in the super-critical regime (Saumon et al., 1995; Nettelmann et al., 2008, e.g.,), Amagat's law breaks down for mixtures near saturation. Both Dalton's law and Amagat's law are exact and equivalent for ideal mixtures of ideal gases in the low density limit.

The entropy of the gas mixture is assumed to be given by the sum of the entropy of the individual pure components,

$$s\left(v, T, \{x_i\}\right) = \sum_i x_i s_i\left(v_i, T\right) \tag{5.2}$$

It follows that the molar heat capacity at constant volume of the gas mixture is given by the sum of the component heat capacities.

$$c_v\left(v, T, \{x_i\}\right) = T\left.\frac{\partial s}{\partial T}\right|_v = \sum_i x_i T\left.\frac{\partial s_i}{\partial T}\right|_v = \sum_i x_i c_{vi} \tag{5.3}$$

For molecular hydrogen, we interpolate the $c_{P\mathrm{H}_2}\left(T\right)$ data from Woolley (1948), assuming a normal mixture of 25% parahydrogen and 75% orthohydrogen. We treat the heat capacity of saturated H_2O vapor following the same approach as Feistel & Wagner (2007). For $T > 130$ K, we use the formula for $c_{P\mathrm{H_2O}}(T)$ from Cooper (1982), while below 130 K we interpolate $c_{P\mathrm{H_2O}}(T)$ data from Woolley (1980).

5.2.3 Planet Energy Budgets

The flow of energy within a planet's interior governs the evolution and eventual steady/equilibrium state of a planet's interior temperature profile. In this section we describe the sources that may contribute to the energy budget of a planet, and introduce parameters to describe them. We treat the envelope with a semi-grey model, so the parameters below describe wavelength integrated quantities.

A planet is irradiated by its star. This is the dominant energy source driving the climate of the Solar System terrestrial planets. The energy flux from the star, F_{irr}, at the orbital distance of the planet, a, is related to the radius, $R_\star$, and effective temperature, $T_{\mathrm{eff}\star}$, of the host star,

$$F_{\mathrm{irr}} = \sigma T_{\mathrm{irr}}^4 = \left(\frac{R_\star}{a}\right)^2 T_{\mathrm{eff}\star}^4. \tag{5.4}$$

The irradiation temperature, T_{irr}, parameterizes the stellar irradiation flux incident on the dayside of a planet. Some fraction of the irradiation incident on the planet will be reflected back to space; the fraction reflected is known as the Bond albedo, A. Further, the incidence angle of the collimated stellar irradiation varies with latitude and longitude on the planet. The equilibrium temperature T_{eq} of the planet in the radiation field of the star is given by,

$$T_{\mathrm{eq}} = (1 - A)^{1/4} f^{1/4} T_{\mathrm{irr}}. \tag{5.5}$$

The factor f accounts for the redistribution of energy between the day and night side ($f = 1/4$ for full redistribution). The equilibrium temperature, T_{eq}, parameterizes the planet-average energy absorbed from the central star.

In addition to the heating from above by stellar irradiation, a planet's envelope may also be heated from below by sources intrinsic to the planet interior. Luminosity sources in the planet itself include radioactive decay, cooling of the planet "core"/rocky interior, envelope contraction, tidal heating, and ohmic dissipation. We denote the total intrinsic luminosity of the planet by L_{int}. We also parameterize the planet interior luminosity by the interior temperature, T_{int},

$$L_{\text{int}} = 4\pi R_p^2 \sigma_B T_{\text{int}}^4. \tag{5.6}$$

The interior luminosity of the planet must be processed through the planet envelope (if present) before being radiated away.

The planet will radiate away energy to space from an effective photosphere. The total (bolometric) planet luminosity is given by,

$$L_p = 4\pi R_p^2 \sigma_B T_{\text{eff}}^4, \tag{5.7}$$

where T_{eff} is the effective temperature of the planet. If the planet envelope is in equilibrium with the rate of heating it receives from the star above and planet interior below, then

$$T_{\text{eff}}^4 = T_{\text{int}}^4 + T_{\text{eq}}^4. \tag{5.8}$$

If the transport of energy within the planet is slow enough, the timescale to reach equilibrium may be long and the planet may never actually attain equilibrium throughout its entire envelope. In this work, however, we focus on equilibrium scenarios in which Equation 5.8 is satisfied.

5.2.4 Energy Transport in Planetary Envelopes

Transport of energy through a planet's envelope couples the planet's energy budget to the temperature gradients inside the planet. Within the envelope, radiation and convection are the dominant energy transport mechanisms.

Radiation

Electromagnetic radiation is one of the most important modes of energy transfer is planet atmospheres. In the Rosseland approximation to the radiative diffusion temperature gradient,

$$F_{\rm rad}(r) = -\frac{16\sigma_B T^3}{3\bar{\kappa}\rho}\frac{\partial T}{\partial r}. \tag{5.9}$$

Above, r is the distance from the planet center, $F_{\rm rad}(r)$ is the outgoing energy flux carried by radiative diffusion, σ_B is the Stefan-Boltzmann constant, $\bar{\kappa}$ is the Rosseland mean opacity, ρ is the mass density of the envelope, and T is the local temperature. Radiative transport of large energy fluxes (high $F_{\rm rad}(r)$) through regions with high opacities (high $\bar{\kappa}$) require steep temperature gradients (large $|\partial T/\partial r|$).

The Rosseland approximation to the energy flux (Equations 5.9) truly only applies deep in the atmosphere where the radiation field is nearly isotropic. When envelope properties change significantly over a photon mean free path—such as in the outer reaches of the planet envelope ($\tau \sim 1$)—Equation 5.9 is no longer valid. A separate approach is needed to model the radiative transfer in the optically thin free-streaming regime and to set the outer boundary conditions on the planet temperature.

We model the planet photosphere with a temperature profile that generalizes the well known Eddington atmosphere to account for irradiation effects (Hansen, 2008; Guillot, 2010; Heng et al., 2011). Guillot (2010) derived an analytic solution to the "two-stream" semi-grey equations of radiative transfer for a plane-parallel irradiated atmosphere, obtaining the following expression for the isotropic average temperature, T, at long-wave optical depth τ,

$$T^4(\tau) = \frac{3T_{\rm int}^4}{4}\left[\frac{2}{3} + \tau\right] + \frac{3T_{\rm eq}^4}{4}\left[\frac{2}{3} + \frac{1}{\gamma\sqrt{3}} + \left(\frac{\gamma}{\sqrt{3}} - \frac{1}{\gamma\sqrt{3}}\right)e^{-\gamma\tau\sqrt{3}}\right]. \tag{5.10}$$

The ratio of the short-wave and long-wave opacities, $\gamma = \bar{\kappa}_S/\bar{\kappa}_L$ (assumed constant in Equation 5.10), determines the magnitude of the greenhouse effect. In general, γ will depend on the composition and temperature of the photosphere. The long-wave absorption opacity in Equation 5.10 is averaged over the thermal outgoing radiation field of the planet. This is effectively a Planck mean,

$$\bar{\kappa}_L\left(P, T\right) = \frac{\int \kappa\left(P, T\right) B_\lambda\left(T\right) d\lambda}{\int B_\lambda\left(T\right) d\lambda}, \tag{5.11}$$

where, $B_\lambda\left(T\right)$ denotes the Planck function at the local temperature T in the planet envelope. The shortwave opacity is an absorption mean integrated over the spectrum of incoming stellar irradiation.

$$\bar{\kappa}_S\left(P, T\right) = \frac{\int \kappa\left(P, T\right) J_{\lambda\star} d\lambda}{\int J_{\lambda\star}\left(T\right) d\lambda} \tag{5.12}$$

At depths where the envelope is optically thick to the incoming short wave radiation, ($\gamma\tau \gg 1$), the Guillot (2010) temperature profile reduces to

$$T^4\left(\tau\right) \to \frac{3T_{\mathrm{int}}^4}{4}\left\{\tau + \frac{2}{3}\right\} + \frac{3T_{\mathrm{eq}}^4}{4}\left\{\frac{2}{3} + \frac{1}{\sqrt{3}\gamma}\right\}. \tag{5.13}$$

This is effectively the Eddington atmosphere P–T profiles with an equilibrium temperature dependent offset.

Dry Convection

The outgoing energy flux through the planet envelope will, in general, be transported by the most efficient mechanism. If the radiative temperature gradient is too large, the envelope will become convectively unstable. Convective instabilities arise in a homogeneous-composition fluid when

$$0 < \left.\frac{\partial\rho}{\partial s}\right|_P \frac{ds}{dm} \tag{5.14}$$

This is the Schwarzschild criterion for convection. In practice, for an ideal gas, this criterion is equivalent to comparing temperature gradients: when the radiative temperature gradient dT/dP exceeds the adiabatic gradient, convection will ensue.

In a convective regime of a planet envelope, the P–T profile is very nearly adiabatic (constant entropy). The convection is expected to be very efficient, requiring a negligible super-adiabaticity to drive the bulk fluid motions. The adiabatic temperature gradient is given by

$$\left(\frac{\partial T}{\partial P}\right)_s = \frac{\alpha v T}{c_P} = \frac{\gamma_A - 1}{\gamma_A}\frac{T}{P}, \tag{5.15}$$

where the last equality holds for an ideal gas. The adiabatic temperature gradient depends on the thermodynamic properties of the fluid: $c_P = T\ \partial s/\partial T|_P$ is the specific heat at constant pressure, $\alpha = \partial v/\partial T|_P$ is the thermal expansivity, and γ_A is the adiabatic index ($\gamma_A = c_P/c_v$).

The adiabatic index is always greater than unity because thermodynamics requires $c_P > c_v$. Adiabatic indices range from 1.66 for a mono-atomic ideal gas, to 1.4 for an ideal diatomic gas, and lower for gas molecules with more degrees of freedom. At low pressures, water vapor has $\gamma_A = 1.33$ at 273.16 K decreasing with temperature to 1.23 at 1273 K. Near the critical point, c_P of water vapor diverges, and non-ideal behavior is especially important.

Saturation, Condensation and Moist Convection

The dry adiabat temperature gradient applies to convective atmospheres with constant uniform composition. The water mixing ratio of in a planet envelope can vary with pressure due to condensation. This is a familiar effect on Earth, where air is dryer on cold mountain-tops and in the frigid conditions of Antarctica. Condensation can have an important effect on planet envelope compositions and temperature profiles. In this section we describe the effect saturation, condensation, and moist convection, assuming the mixing rules described in Section 5.2.2. Quantities with subscript "v" refer to water vapor, while quantities with subscript "n" refer to the non-condensing gas (H_2).

The water mixing ratio at the base of the envelope is set by the requirement of saturation. For a liquid water ocean to persist on the surface of a planet, the water vapor in the envelope and liquid on the surface must be in phase equilibrium. If the envelope is too dry the ocean will evaporate, while if the envelope is super-saturated it will precipitate or collapse. When a gas mixture is saturated in H_2O, the partial pressure of water equals the saturated vapor pressure at the specified temperature.

$$P_{\mathrm{v}} = P_{\mathrm{v,sat}}(T) \tag{5.16}$$

The saturation vapor pressure, $P_{\mathrm{v,sat}}(T)$, is defined either by the liquid-vapor coexistence curve ($T > 273.15$ K) or by the Ice I sublimation curve ($T < 273.15$ K).

Condensation is possible when the envelope P–T profile passes through conditions where water is liquid or ice I ($P\left(T\right) \geq P_{\mathrm{v,sat}}\left(T\right)$, see Figure 5-1). Condensation will ensue if *i)* the envelope is saturated and *ii)* the gradient of temperature as a function of water partial pressure is steeper than the water saturation curve ($dP_{\mathrm{v}}/dT \leq dP_{\mathrm{v,sat}}/dT$). In regimes where the both these conditions are obtained, the water mixing ratio will decrease with altitude. We neglect the possibility of super-saturation ($P_{\mathrm{v}} = P_{\mathrm{v,sat}}(T)$), instead assuming 100% humidity (Equation 5.16). When condensation is not occurring, we assume the composition of the planet envelope is constant (x_{v} constant).

Latent heat released by condensation decreases the adiabatic temperature gradient. Consequently, moist envelopes are more prone to convective instabilities than dry envelopes. Following Ingersoll (1969) and Kasting (1988) we denote the ratio of water-vapor mass density, ρ_{v}, to noncondensable gas mass density, ρ_{n}, by

$$\alpha_{\mathrm{v}} = \frac{\rho_{\mathrm{v}}}{\rho_{\mathrm{n}}} = \frac{m_{\mathrm{v}}}{m_{\mathrm{n}}} \frac{x_{\mathrm{v}}}{1 - x_{\mathrm{v}}} \tag{5.17}$$

In convective regions where water is condensing, α_{v} varies with temperature according to,

$$\frac{d \ln \alpha_{\mathrm{v}}}{d \ln T} = \frac{\left(R/m_{\mathrm{n}}\right)\left(d \ln \rho_{\mathrm{v}}/d \ln T\right) - c_{v\mathrm{n}}/m_{\mathrm{n}} - \left(\alpha_{\mathrm{v}}/m_{\mathrm{v}}\right)\left(ds_{\mathrm{v}}/d \ln T\right)}{\alpha_{\mathrm{v}}\left(s_{\mathrm{v}} - s_{\mathrm{v}}\right)/m_{\mathrm{v}} + R/m_{\mathrm{v}}} \tag{5.18}$$

Equation (5.18) treats the condensing liquid as pure water (assuming negligible solubility of the noncondensable gas) that is instantaneously rained-out/removed from the upwelling parcel of gas (pseudo-adiabat). The non-condensing gas (H_2) is modeled as an ideal gas. Non-ideal effects in the water EOS are taken into account, as these are important near the critical point. Combining Equation (5.18) with Dalton's law of partial pressures,

$$P = P_{\mathrm{v}} + P_{\mathrm{n}}, \tag{5.19}$$

the saturated moist pseudo-adiabatic temperature gradient is given by,

$$\left(\frac{d\ln P}{d\ln T}\right)_{s,\mathrm{moist}} = \frac{P_{\mathrm{v}}}{P}\frac{d\ln P_{\mathrm{v}}}{d\ln T} + \frac{P_{\mathrm{n}}}{P}\left(1 + \frac{d\ln \rho_{\mathrm{v}}}{d\ln T} - \frac{d\ln \alpha_{\mathrm{v}}}{d\ln T}\right). \tag{5.20}$$

In condensation regions, $d\ln\alpha_{\mathrm{v}}/d\ln T > 0$ and the last term on the right hand side serves to decrease the adiabatic gradient, $d\ln P/d\ln T|_s$. Coupled integration of Equations (5.20) and (5.18) yields the moist pseudo-adiabatic temperature profile. In regimes where condensation is not occurring, we assume a constant water mixing ratio ($d\ln\alpha_{\mathrm{v}}/d\ln T = 0$) and take the dry adiabatic gradient (Equation (5.15)).

5.2.5 Opacities

The opacities in a planet envelope have an important influence on the planet P–T profile and thermal evolution. The opacities govern the radiative transfer through the planet atmosphere, the rate of planet cooling, the location of the tropopause (radiative-convection transition), and the level of the greenhouse effect.

In our model of grain-free H_2–H_2O atmospheres, we consider bound-bound absorption from H_2O, H_2–H_2 collision induced absorption (CIA), and Rayleigh scattering by both H_2O and H_2 molecules. We employ wavelength-dependent H_2O bound-bound cross-sections from HITRAN. Without a permanent dipole moment, isolated H_2 molecules are not spectrally active in the IR or visible. During inter-molecular collisions, however, transient dipole moments are induced in H_2 and weak dipole absorption becomes possible. This collision induced absorption is a continuum opacity source that can dominate at high pressures. We take continuum H_2-H_2 CIA cross-sections from Borysow (2002) (temperatures below 1000 K) and Borysow U. G. Jorgensen & Fu (2001) (temperatures exceeding 1000 K). At short wavelengths, Rayleigh scattering is a dominant source of extinction. We take Rayleigh scattering cross-sections for H_2

and H_2O molecules from Dalgarno & Williams (1965) and Schiebener et al. (1990), respectively.

For our semi-grey atmosphere model, we compute wavelength-integrated mean long-wave and shortwave opacities (Equations 5.11 and 5.12) from the wavelength-dependent cross-sections described above. We choose a sun-like G2 spectral type for the host star, and approximate the stellar irradiation as a black-body at temperature $T_{\mathrm{eff}\star} = 5770$ K ($J_{\lambda\star} \approx B_\lambda\left(T_{\mathrm{eff}\star}\right)$). Water absorption dominates the H_2-H_2 CIA in both the short and long wave at pressures up to $\sim 10^7$ Pa. The ratio of shortwave to long-wave absorption in H_2–H_2O ranges from $\gamma \sim 0.04$ to 0.24 (decreasing with temperature) at low-pressures ($\lesssim 100$ Pa).

5.3 Method

We use equilibrium hydrostatic models to study instantaneous states of planets assuming the planets are undergoing quasistatic evolution. Our planet interior model is based on that from Rogers & Seager (2010a,b); Rogers et al. (2011), but includes several updates. We have extended the model to allow changes in the gas layer composition with depth. We can now treat a wider variety of envelope compositions, including the effects of moist convection, and condensation. We do not consider cases where the envelope dynamics or variations in the interior luminosity profile have an important effect, and instead take the planet intrinsic luminosity L_{int} (or analogously T_{int}^4/r^2) to be constant through out the planet envelope. We further focus on planets in thermal equilibrium at their current orbital distance, deferring a discussion of non-equilibrium cases until Section 5.6. We summarize our model below.

We assume spherically symmetric and differentiated planets in hydrostatic equilibrium. We model the planet with four layers: an iron core, a silicate mantle, a water mantle, and an H/H_2O gas–vapor envelope. We focus in this work on planets that harbor liquid water oceans at their "surface"—the interface between the gas–vapor envelope and the water mantle. At greater depths, the water mantle may pass through other phases including high-pressure ices, super-critical fluid, plasma, and/or super-ionic solid. We model the planet envelope and interior separately. The ocean surface serves as the boundary conditions for both segments of our planet model.

The structure of a planet in hydrostatic equilibrium is described by the coupled differential equations for the mass of a spherical shell, hydrostatic equilibrium, and optical depth

$$\frac{dr}{dm} = \frac{1}{4\pi r^2 \rho} \tag{5.21}$$

$$\frac{dP}{dm} = -\frac{Gm}{4\pi r^4} \tag{5.22}$$

$$\frac{d\tau}{dm} = -\frac{\kappa}{4\pi r^2}, \tag{5.23}$$

Above, m is the interior mass coordinate, r is the distance from the planet center, P is the pressure, ρ is the mass density, τ is the radial long-wave optical depth, and G is the gravitational constant. Within each chemical layer, the equation of state (EOS) relates the density $\rho(m)$ to the pressure $P(m)$ and temperature $T(m)$. In addition to Equations (5.21), (5.22), and (5.23), a solution for the interior structure also requires a model for the temperature and composition of the planet as a function of depth. We divide the thermal and chemical profile of the planet into four distinct regimes: *(i)* the gas-vapor envelope at low optical depths, *(ii)* the gas-vapor envelope at higher optical depths, *(iii)* the water layer, and *(iv)* the iron-silicate interior. We describe our model for each regime below.

The optically thin atmosphere of the planet at low pressures sets the outer boundary condition on the planet envelope. At low optical depths ($\gamma\tau \lesssim 1$), we adopt the Guillot (2010) temperature profile for irradiated planet atmospheres . We define the exterior boundary condition on the planet envelope ($r = R_p$, $m = M_p$) at optical depth $\tau_R = 2/3$, imposing

$$\kappa P_R = \frac{2}{3} g \tag{5.24}$$

to determine the corresponding pressure P_R at the boundary. We take the composition of the planet envelope to be homogeneous ($x_{\rm v}$ constant at its last saturated value) within this thin layer.

At greater depths in the gas-vapor envelope, we calculate the pressure–temperature–composition profile assuming radiative-convective equilibrium, and phase-equilibrium with the underlying liquid ocean. The water mixing ratio is allowed to vary with depth, yielding an inhomogeneous envelope composition. In addition to Equations (5.21), (5.22), and (5.23), we also simultaneously solve for the temperature and water mixing ratio. At each radial step, we evaluate whether water is condensing (see Section 5.2.4) and whether the envelope is convectively unstable (see Section 5.2.4). The temperature gradient is set by the dry adiabat (Equation (5.15)) in the non-condensing convective regime, the saturated moist-adiabat (Equation (5.20)) in the condensing convective regime, and the radiative diffusion temperature gradient (Equation (5.9)) in the radiative regime. We assume saturation of H_2O wherever condensation is occurring, effectively imposing a relative humidity of 100%. In non-condensing regions of the planet envelope, the mixing ratio of water is fixed at its last saturated value.

The third regime of the our thermal model is the water layer. We consider a convective ocean and adopt an adiabatic interior temperature profile. In this case, the planet ocean must be heated from below by some intrinsic luminosity source originating in the rocky interior. Although the ocean begins in the liquid phase at its surface, it may transition to a super-critical fluid, plasma, super-ionic solid, or high pressure ices at greater depths.

Finally, the innermost regime of our model temperature-composition profile is the rocky interior. We model the rocky interior with differentiated layers of iron, and $Fe_{0.1}Mg_{0.9}SiO_3$ silicates. For these materials, we employ EOS data sets from Seager et al. (2007), which were derived by combining experimental data at $P \lesssim 200$ GPa with the theoretical Thomas-Fermi-Dirac equation of state at high pressures, $P \gtrsim 10^4$ GPa. Thermal effects are neglected in these EOSs—at the high pressures found in the interior layers, thermal corrections have only a small effect on the density (Seager et al., 2007).

The ocean surface provides the boundary conditions at which the envelope and interior solutions are connected. The presence of a liquid water ocean imposes important constraints on the conditions at the ocean surface. In particular, the surface pressure P_s and temperature T_s must fall within the liquid regime of the water phase diagram, and the envelope just above the ocean must be saturated ($P_\mathrm{vs} = P_\mathrm{v,sat}(T)$). We use subscript "s" to denote all surface properties (e.g., m_s, r_s, τ_s, P_s, T_s, and x_vs).

Models of the planet interior (rock and water layers) constrain the mass–radius relation at the ocean surface. For a given choice of P_s, T_s, m_s and interior composition (iron–silicate–water ratios), we integrate Equations (5.21) and (5.22) from the surface toward the planet center. We then iterate r_s until a self-consistent solution satisfying the inner boundary condition ($r = 0$, $m = 0$) is achieved.

The surface conditions provide a lower boundary conditions our model of the envelope structure. To model the envelope structure for a given choice of m_s, r_s, P_s, T_s, and L_int, we start at the ocean surface and integrate Equations (5.21), (5.22), (5.23), (5.9), (5.15), and (5.20) upwards to the outer boundary on the planet. We then use the limiting low-pressure behavior of the integrated radiative-convective temperature profile to find the value of T_eq that provides a consistent match with the Guillot (2010) atmosphere (Equation (5.10)).

5.4 Results

We combine radiative-convective climate models and planet interior structure models to constrain the range of scenarios in which hydrogen-rich super-Earths can have liquid water oceans. The relevant parameters are M_p, R_p, T_eq, T_int, composition (both interior and atmosphere), and the conditions at the ocean surface (P_s, T_s, m_s, r_s).

The envelope and interior structure models each constrain different dimensions of the liquid water ocean parameter space. Given P_s, T_s, m_s, r_s and T_int as inputs, our model for saturated H_2-H_2O envelopes determines the associated T_eq, the envelope composition, M_p, and R_p (provided a solution exists). The requirements that the envelope is in radiative-convective equilibrium and is saturated at its base together constrain the range of scenarios for liquid water oceans. Given P_s, T_s and the interior composition, our interior structure model constrains r_s as a function of m_s. These constraints ultimately stem from the densities and compression properties of materials at high pressure.

The parameter space describing planets with liquid water oceans is many-dimensional. In the ensuing sections we explore the parameter space from a variety of different perspectives (taking slices and projections to focus on constraining a few parameters at a time). We explore constraints on the P–T profiles linking the ocean surface to the top of the atmosphere, the planet energy budget, envelope composition, envelope thickness, and mass-radius relations for planets with saturated H_2-H_2O envelopes. In Sections 5.4.1 to 5.4.3 we focus on a fiducial mass and radius for the planet interior. Specifically, we take $r_{\mathrm{s}} = 2.2\ R_{\oplus}$ for the separation between the planet center and ocean surface, and $m_{\mathrm{s}} = 5.0\ M_{\oplus}$ for the mass interior to the ocean surface (surface gravity $g_{\mathrm{s}} = 10\ \mathrm{m\,s^{-2}}$). In Section 5.4.4 we broaden our perspective to consider a wider range of planet M_p and R_p.

The major new results we present are *i)* upper limits to the radii of planets with liquid water oceans, and *ii)* constraints on the energy budgets (T_{int} and T_{eq}) of planets with liquid water oceans below hydrogen envelopes.

5.4.1 Connecting the Planet Surface to the Top of the Atmosphere

Exoplanet transit observations probe the outer boundary of a planet's atmosphere (near $\gamma\tau \lesssim 1$). To discern whether a planet has a water ocean, we must relate the surface conditions to the outer atmosphere. We do this by computing planet envelope P–T profiles following the procedure described in Section 5.3. We show in Figure 5-1 a few sample saturated P–T profiles for H_2–H_2O envelopes (assuming a planet with $m_{\mathrm{s}} = 5.0\ M_{\oplus}$ and gravity $g_{\mathrm{s}} = 10\ \mathrm{m\,s^{-2}}$ at the ocean surface). At high pressures, each P–T profile line terminates at an ocean surface.

At high pressures and optical depths, the sample envelopes in Figure 5-1 are saturated in water vapor and are experiencing moist convection. Only the extreme low-luminosity ($T_{\mathrm{int}} = 0$ K) case shown does not have sufficient internal heat flux to drive convection. In the saturation regions, the partial pressure of water vapor traces the liquid-vapor coexistence curve. For water-dominated envelopes, the moist adiabat P–T profiles approach the saturation curve for water vapor (i.e., as $x_\mathrm{v} \to 1$, $dP/dT|_{s,\mathrm{moist}} \to dP_\mathrm{v,sat}/dT$). At the other extreme, when water is a trace component (x_v small) the moist P–T profiles are not very different from dry P–T profiles. For trace amounts of water vapor, the main effect of condensation is to decrease the pressure of the radiative-convective transition (the tropopause) by decreasing the adiabatic temperature gradient. Planets with cold tropopauses (low temperatures at the radiative-convective transition) tend to have the driest (lowest x_v) envelopes due to the steep decrease in $P_\mathrm{v,sat}(T)$ along the ice Ih sublimation curve.

At low pressures, radiation begins to dominate the energy transport in the planet envelopes. The radiative regions of the planet envelopes can be very isothermal. The radiative diffusion temperature gradient driven by outgoing thermal radiation becomes significant at $\tau \sim \left(\frac{T_\mathrm{eq}}{T_\mathrm{int}}\right)^4$. Absorption of short-wave stellar radiation heats the planet envelopes near $\gamma\tau \sim 1$ (seen as a temperature increase at $P < 10^5$ Pa in the P–T profiles in Figure 5-1). When $T_\mathrm{int}^4 \ll T_\mathrm{eq}^4$, the depth of short-wave absorption and the onset of radiative diffusion are well separated by an isothermal segment at $T^4 \approx \frac{T_\mathrm{int}^4}{2} + \frac{3T_\mathrm{eq}^4}{4}\left\{\frac{2}{3} + \frac{1}{\sqrt{3}\gamma}\right\}$.

Planets with the same conditions at the ocean surface can have a range of different energy budgets and conditions at the top of the atmosphere. At fixed P_s and T_s, increasing T_int increases the radiative diffusion gradient making the envelope more convectively unstable. As a result, the tropopause is pushed to lower temperatures that correspond to lower T_eq in the Guillot (2010) boundary condition. The limit $T_\mathrm{int} \to 0$ sets an upper bound of on the equilibrium temperature,

$$T_\mathrm{eq,max}^4 \approx \frac{4T_\mathrm{s}^4}{3\left\{\frac{2}{3} + \frac{1}{\sqrt{3}\gamma}\right\}}. \tag{5.25}$$

5.4.2 Constraints on Ocean Planet Energy Budgets

We now turn to exploring the "goldilocks" range of planet energy budgets that allow for surface liquid water oceans. Traditionally, studies of the habitable zone have focussed on constraining the level of stellar irradiation ($T_{\rm eq}$) that is "just right" for liquid water oceans, avoiding ocean vaporization on the one hand and freezing conditions on the other. In this work, we generalize this approach to take into account the intrinsic luminosity of the planet ($T_{\rm int}$) in addition to the stellar irradiation.

We compute P–T profiles following the approach described in Section 5.3 for the full range of surface conditions ($T_{\rm s}$, $P_{\rm s}$, and $x_{\rm vs}$) that are amenable to stable liquid-phase water. We again take our fiducial choice $m_{\rm s} = 5.0\ M_{\oplus}$ and $r_{\rm s} = 2.2\ R_{\oplus}$ at the base of the envelope (in Section 5.4.4 we will explore a range of planet masses and radii). Figure 5-2 shows the planet energy budgets (parameterized by $T_{\rm int}$ and $T_{\rm eq}$) for which water-saturated radiative-convective equilibrium envelope solutions exist. Each panel corresponds to a different surface pressure of H_2, $P_{\rm ns}$. At fixed H_2 surface pressure, the surface temperature increases with increasing $T_{\rm eq}$ and $T_{\rm int}$ (moving toward the upper right in Figure 5-2). The mixing ratio of H_2O increases in concert with the surface temperature (as the saturation vapor pressure increases), approaching pure water-envelopes ($x_{\rm vs} \rightarrow 1$) at the upper $T_{\rm int}$ boundary when $P_{\rm ns} \ll P_{\rm v,sat}\,(T_s)$.

The outer boundary of the circumstellar habitable zone corresponds to the edge of the liquid water parameter space at low $T_{\rm int}$ and $T_{\rm eq}$. The planets at this limiting boundary have surface conditions on water ice melting curves. Combinations of $T_{\rm int}$ and $T_{\rm eq}$ outside the liquid water parameter space in the lower-left corner of Figure 5-2 represent cases where any water on the planet surface is frozen—the greenhouse effect and thermal blanketing of the intrinsic luminosity are insufficient to maintain a surface temperature warm enough for liquid water.

Planets with $T_{\rm int}$ and $T_{\rm eq}$ exceeding the upper boundary to the liquid water parameter space (upper right of Figure 5-2) will be too hot at their surface to sustain an ocean. Planets in this regime are in "runaway greenhouse" states, where surface water oceans cannot exist in equilibrium regardless of the total planet water mass. The envelope P–T profiles transition directly from the water vapor phase to super-critical fluid. The maximum $T_{\rm int}$-$T_{\rm eq}$ locus of the liquid water parameter space defines a strict lower limit on the orbital separations at which a planet with a hydrogen-dominated atmosphere might retain a liquid water ocean (constraining the inner edge of the

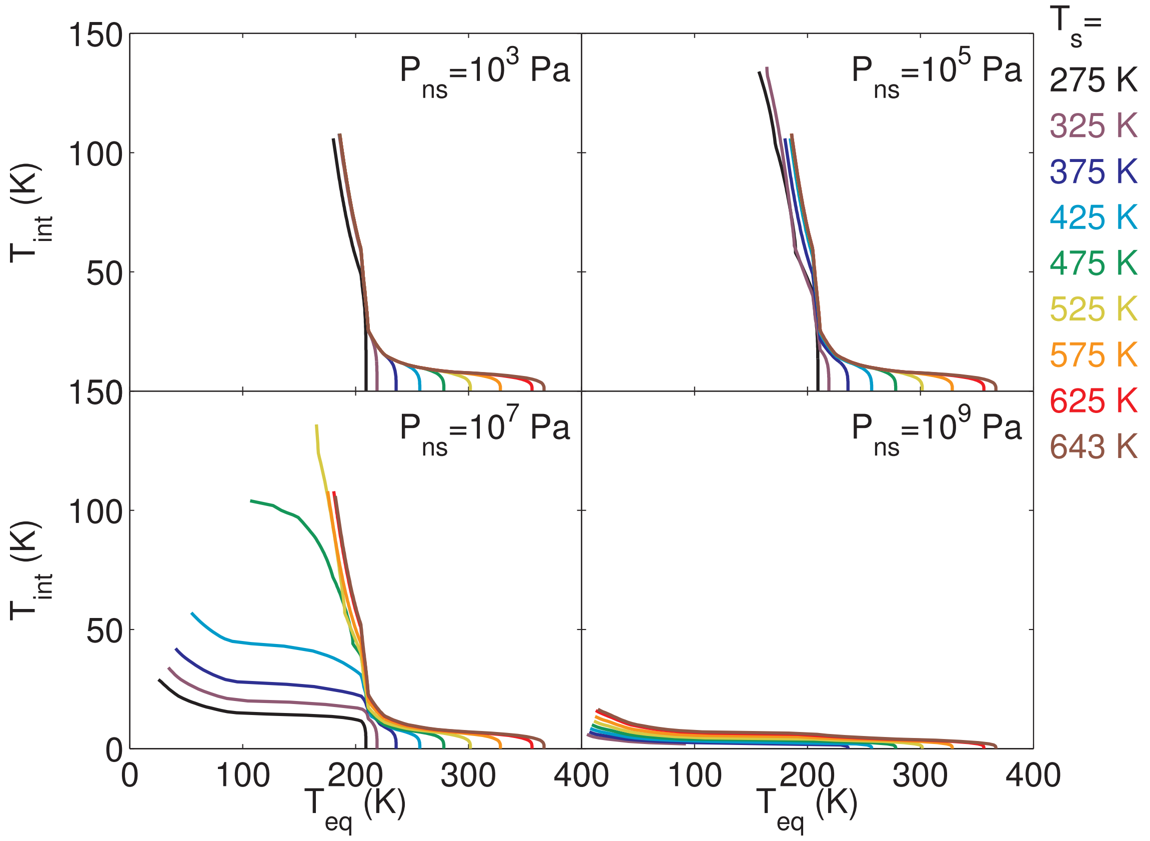

Figure 5-2: Energy Budgets for super-Earths with hydrogen-rich envelopes. A planet mass of $m_{\mathrm{s}} = 5.0\ M_{\oplus}$ and surface-gravity of $g = 10\ \mathrm{m\,s^{-2}}$ are assumed. Each panel corresponds to a different surface pressure of H_2: 10^3 Pa, 10^5 Pa, 10^7 Pa, and 10^9 Pa. Each line represents a contour of constant surface temperature (from 275 K to 625K in increments of 50 K, and a high temperature contour at 645K near the critical temperature). The curves terminate at high T_{int} where the envelopes start to become optically thin and our treatment of the our treatment P–T profile breaks down.

habitable zone).

There is a trade-off between $T_{\rm eq}$ and $T_{\rm int}$ in the liquid water parameter space. The higher the level of irradiation incident on the planet envelope from above, the lower the planet's intrinsic luminosity must be to still allow a surface liquid water ocean. This is intuitively understandable: if the outer boundary temperature of the planet envelope is higher (higher $T_{\rm eq}$) then the temperature gradient throughout the planet envelope must be shallower (smaller dT/dP and lower $T_{\rm int}$) to avoid exceeding T_c at the planet surface.

Increasing the surface pressure of H_2 at a given $T_{\rm eq}$ tends to decrease both the maximum $T_{\rm int}$ possible before a runaway greenhouse state is reached, and the minimum $T_{\rm int}$ needed to prevent the oceans from freezing. This effect can be attributed to both the increase in the surface pressure (necessitating a smaller mean dT/dP between the outer atmosphere and surface) and to the strong pressure dependence of the H_2 CIA opacity. An envelope with $\sim 10^7$ Pa of H_2 allows liquid water oceans over the widest range of planet energy budgets. This H_2 surface pressure is high enough such that H_2–H_2 CIA is comparable to water bound-bound absorption for planets with cool surface temperatures, yet still low enough such that the planet envelopes are water dominated at high surface temperatures (i.e., 10^7 Pa $\lesssim$ $\mathrm{P_c}$).

5.4.3 Maximum H_2 and Minimum H_2O Content of Ocean Planets

The composition of the planet envelope, in addition to planet energy budget, plays an important role in determining whether liquid water oceans are possible.

To support a liquid water ocean, a planet must have sufficient water to saturate the envelope. Otherwise, all the free water (i.e., water not locked in the planet interior) will be found in vapor form in the planet envelope. The boundaries of the traditional habitable zone are typically calculated assuming that the abundance of H_2O on the planet surface is not a limiting factor. For our fiducial $m_{\rm s}$ and $r_{\rm s}$, up to $7 \times 10^{-5}\ M_\oplus$ of water is needed to saturate the envelope at $T_{\rm s} = 300$ K, while up to $0.1\ M_\oplus$ of water is needed at $T_\mathrm{s} = 645$ K. Any water in excess of these limits will contribute to a surface ocean. Planets with smaller H_2O reservoirs, have a more restricted span of orbits on which they can harbor liquid water oceans.

The mass of hydrogen surrounding a planet must also fall within a limited range to permit surface liquid water oceans. If the surface pressure of H_2 exceeds ~ 10 GPa, any condensed water on the surface would form high pressure water ices (ice V, VI, VII). For our fiducial $m_\mathrm{s} = 5.0\ M_\oplus$ and $r_\mathrm{s} = 2.2\ R_\oplus$, we find that no more than 11 % of the planet's mass can reside in an H_2 envelope if there is to be a liquid water ocean.

5.4.4 Upper Limit to Ocean Planet Radii

We now turn to constraining the transit radii of hydrogen-rich planets with liquid water oceans based on the coupled constraints we have derived on the planet energy budgets and envelope compositions. At a specified equilibrium temperature (or orbital distance), the scenarios that maximize z_env have massive hydrogen-dominated envelopes overlying an ocean surface on the threshold of the liquid–ice VI or liquid–ice VII phase transition ($P_\mathrm{s} \lesssim 10$ GPa). We present in Figure 5-3, upper limits on z_env as a function of both planet equilibrium temperature and surface temperature. We find that a saturated H_2–H_2O will add no more than $0.94\ R_\oplus$ to the transit radius of our fiducial $r_\mathrm{s} = 2.2\ R_\oplus$, $m_\mathrm{s} = 5.0\ M_\oplus$ planet. The maximum z_env increases with both increasing T_s and increasing T_eq; cooler ocean-bearing planets have tighter constraints on their radii.

How do planet mass and surface gravity affect the liquid water parameter space? We have so far focussed on a single choice for the radius and interior mass at the ocean-envelope interface. In the constant surface gravity and plane-parallel atmosphere approximations, a simple mapping exists between the P–T solutions at different surface gravities. A planet with surface gravity g_0, intrinsic luminosity T_int0, equilibrium temperature T_eq0, envelope thickness z_env0, and total envelope surface mass density σ_env0 will have a radiative-convective P–T profile that is nearly identical to the P–T

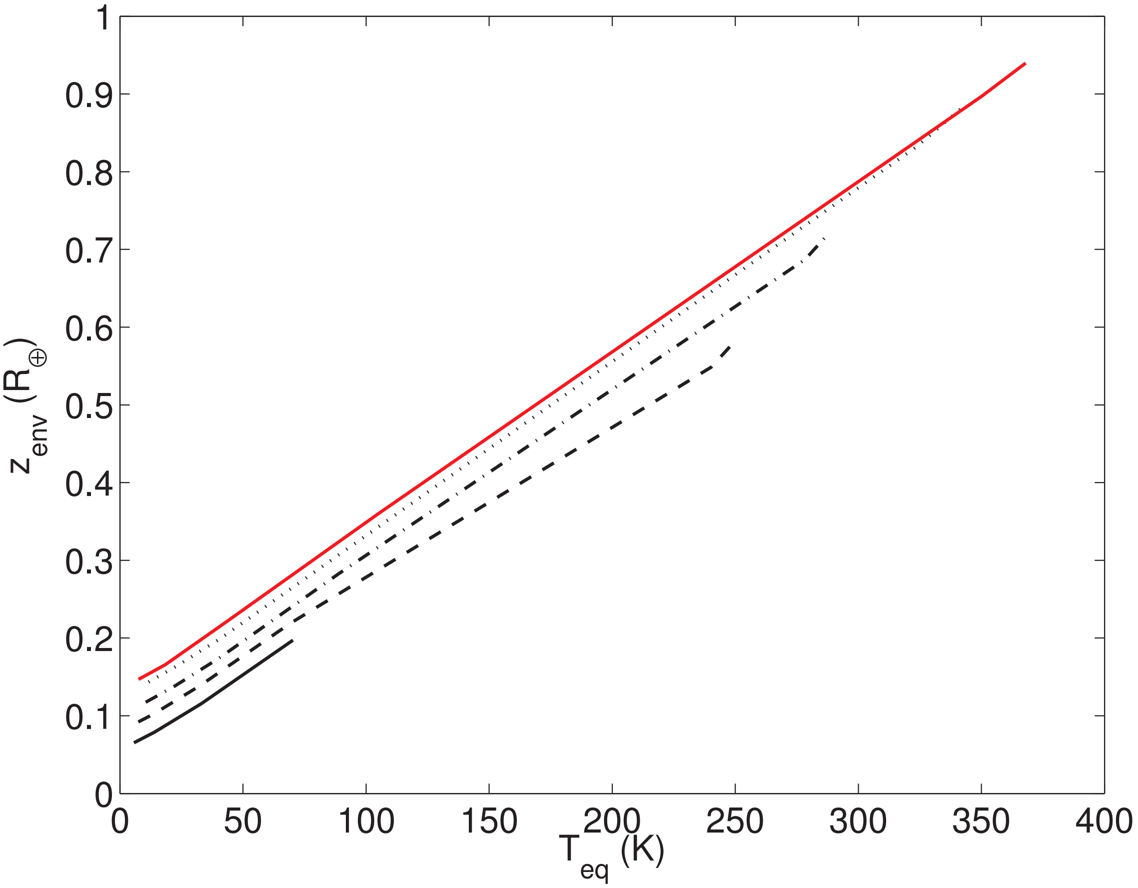

Figure 5-3: Maximum radial thicknesses, z_{env}, as a function of equilibrium temperature for saturated H_2–H_2O envelopes surrounding super-Earths with liquid water oceans. The mass and radius at the ocean surface are fixed at $m_{\mathrm{s}} = 5.0\ M_\oplus$ and $r_{\mathrm{s}} = 2.2\ R_\oplus$, respectively. Each line corresponds to a different ocean surface temperature: $T_{\mathrm{s}} = 300$ K (black solid), $T_s = 400$ K (black dashed), $T_s = 500$ K (black dot-dashed), $T_s = 600$ K (black dotted), and $T_s = 645$ K (red solid).

profile of a planet with surface gravity g and,

$$\begin{aligned}
T_{\text{int}}^4 &= T_{\text{int0}}^4 \left(\frac{g}{g_0}\right) && (5.26)\\
T_{\text{eq}}^4 &= T_{\text{eq0}}^4 + T_{\text{int0}}^4 \left(\frac{1-\frac{g}{g_0}}{1+\frac{\sqrt{3}}{2\gamma}}\right) && (5.27)\\
z_{\text{env}} &= z_{\text{env0}} \left(\frac{g_0}{g}\right) - \frac{kT_0}{\bar{m}g} \ln \frac{g}{g_0} && (5.28)\\
\sigma_{\text{env}} &= \sigma_{\text{env0}} \left(\frac{g_0}{g}\right). && (5.29)
\end{aligned}$$

At the top of the atmosphere, the envelope is treated as an ideal gas with mean molecular weight $\bar{m}$ and temperature $T_0 = \lim_{P\to 0} T$. The scaling of $T_{\text{int}} \propto g^{1/4}$ stems from the gravity dependence of the radiative diffusion gradient $\frac{dT}{dP}\big|_{\text{rad}} = \frac{3\kappa T_{\text{int}}^4}{16gT^3}$, while the scaling of $\sigma_{\text{env}} \propto g^{-1}$ stems from its pressure gradient $\left(\frac{d\sigma}{dP} = -\frac{1}{g}\right)$. Analogously, the first term of the g-mapping for z_{env} is due to its pressure gradient $\left(\frac{dz}{dP} = -\frac{1}{\rho g}\right)$, while the second term corrects for the g-dependence of P_R (the outer pressure boundary condition specified at $\tau = 2/3$). The liquid water parameter space for lower surface-gravity planets has lower intrinsic energy fluxes and puffier envelopes. This basic intuition holds, even when the plane-parallel and constant g approximations break down.

We now couple models of water-saturated envelopes to planet interior structure models to constrain the possible masses and radii of hydrogen-rich planets with liquid water oceans. We choose three nominal compositions for the planet interior (in order of decreasing density): Mercury-like (70% Fe core, 30% silicate mantle), Earth-like (32% Fe core, 68% silicate mantle), and ice (100% water). In Figure 5-4 we present upper limits on the transit radii of planets with liquid water oceans for various choices of the equilibrium temperature T_{eq}. Cooler ocean-bearing planets with lower T_{eq} have tighter constraints on their radii. The transiting super-Earths known to date are also included in Figure 5-4. All confirmed transiting exoplanets (with both M_p and R_p measured) are either too hot, or too low density to harbor a liquid water ocean. We consider individual planets in greater detail in Section 5.5.

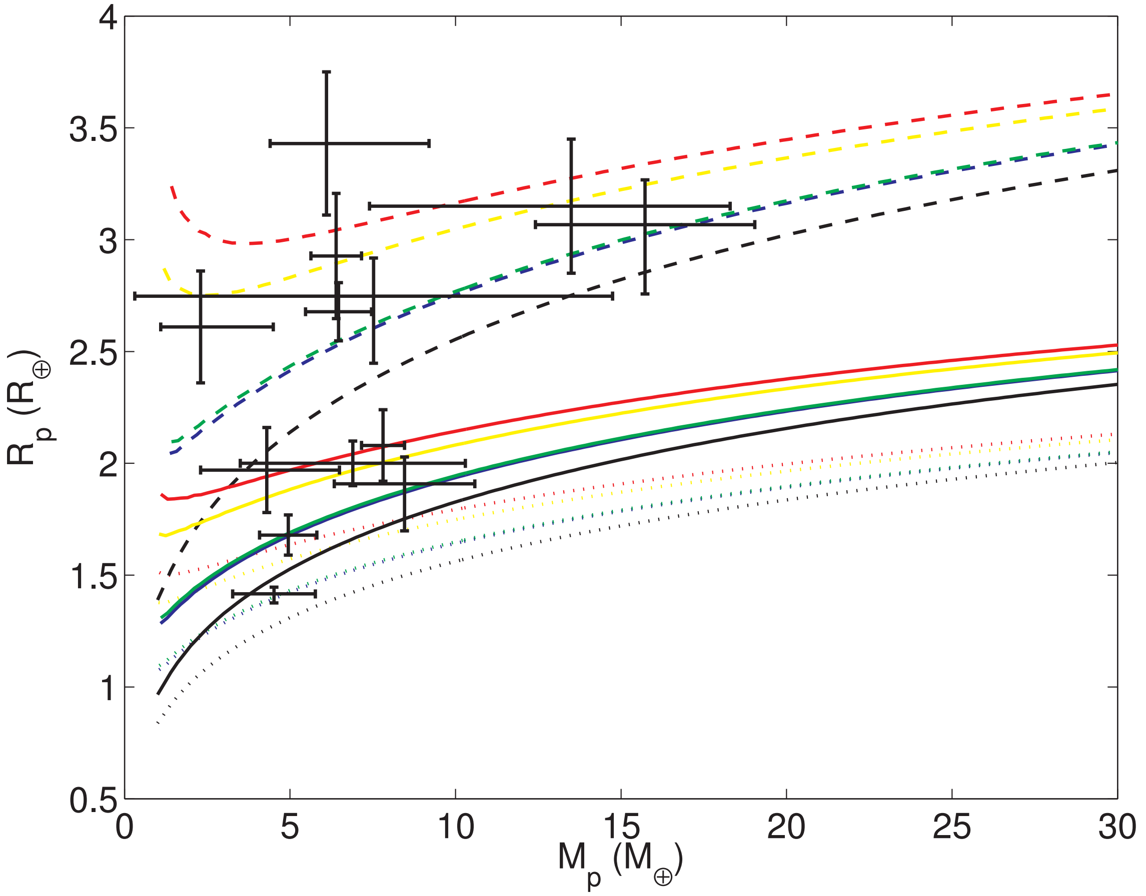

Figure 5-4: Upper bounds on the radii of hydrogen-rich super-Earth exoplanets with surface liquid water oceans. The mass-radius relations for the planet interior (without an ocean or an envelope) are plotted in black. We sample three compositions for the planet interior: Mercury-like with 70% Fe core and 30% silicate mantle (dotted), Earth-like with 32% Fe core 68% silicate mantle (solid), and 100% water ice (dashed). Color indicates the equilibrium temperature: $T_{\text{eq}} \leq 100$ K (blue), $T_{\text{eq}} \leq 200$ K (green), $T_{\text{eq}} \leq 300$ K (yellow), and $T_{\text{eq}} \leq 400$ K (red).

The M_p–R_p–T_{eq} liquid water parameter space we have derived sets a strict lower limit to the densities of mini-Neptune planets with liquid water oceans. Liquid water oceans are definitely ruled out for planets with radii exceeding the limiting mass-radius relations in Figure 5-4. We have taken a very inclusive approach to the liquid water parameter space, considering every saturated radiative-convective equilibrium solution for the H_2–H_2O envelope to be viable. The radius limits in Figure 5-4 encompass the full range of surface temperatures, surface pressures, and intrinsic luminosities. Planet formation and evolution considerations may further constrain (but likely not expand) the range of scenarios for liquid water oceans. We defer until Section 5.6.1 a discussion assessing which corners of the liquid water parameter space may be plausibly realized by planets in nature.

5.5 Case Studies

5.5.1 Solar System Planets

Where do the Solar System planets fall in the habitable zone for H_2-rich planets that we have derived? The energy budgets of the Solar System planet are summarized in Table 5.1 (see, Kandel & Viollier, 2005, and references therein.). To compare the Solar System planets to the liquid water parameter space energy budget constraints in Figure 5-2 (which is nominally for $g = 10\ \mathrm{m\,s^{-2}}$), we scaled the Solar System T_{int} values with surface gravity $g^{1/4}$ (Equation (5.26)). We also took into account the measured Bond albedos of the Solar System planets when computing their equilibrium temperatures.

The Solar System giant planets are all too hot and/or too dry to harbor liquid water oceans in their interior. These planets find themselves with intrinsic luminosities and equilibrium temperatures exceeding the liquid water ocean parameter space for H_2 surface pressures of 1 GPa or more. High total pressures of H_2 are needed in the interiors of Jupiter, Saturn, Neptune and Uranus to account for the planet masses, radii, and gravitational moments. Even though these planets have low equilibrium

Table 5.1: Energy budgets of the Solar System planets. Data is taken from Kandel & Viollier (2005) and references therein.

Planet	a (AU)	A	g ($\mathrm{m\,s^{-2}}$)	T_{eq} (K)	T_{int} (K)	$T_{\mathrm{int}}\left(10\,\mathrm{m\,s^{-2}}/\mathrm{g}\right)^{1/4}$ (K)
Earth	1.000	0.306	9.8	255	36	36
Jupiter	5.203	0.343	25.9	110	98	76
Saturn	9.546	0.342	11.2	82	76	74
Uranus	19.20	0.300	9.0	58	26	26
Neptune	30.05	0.290	11.23	47	52	52

temperatures ($T_{\mathrm{eq}} \lesssim 100$ K), the temperature within the envelope increases with depth and exceeds the critical temperature of water before reaching the base of the envelope. Neptune, Uranus, Jupiter, and Saturn may have regions in their atmosphere where water clouds condense and liquid water coexists with a vapor phase. These regimes will end in a cloud base, however, instead of an ocean surface. Wiktorowicz & Ingersoll (2007) came to a similar conclusion regarding the absence of a liquid water ocean on Neptune.

Figure 5-2 formally does not apply to the terrestrial Solar System planets because their envelopes are optically thin. The energy budgets of the Solar System terrestrial planets are dominated by thermal radiation from their sun-heated surfaces—the true intrinsic luminosities of the terrestrial planets are insignificant. Figure 5-2 does not account for the radiative properties of the planet surface. The curves terminate at high T_{int} where the envelopes start to become optically thin and our treatment of the radiative transfer breaks down (i.e., when $\gamma\tau \lesssim 1$ at the radiative-convective transition).

5.5.2 GJ 1214b

We explore now the possibility for liquid water oceans on GJ 1214b, a transiting super-Earth orbiting a neaby M-dwarf star (Charbonneau et al., 2009). Based on its mass and radius ($M_p = 6.55 \pm 0.98\ M_{\oplus}$, $R_p = 2.678 \pm 0.13\ R_{\oplus}$), GJ 1214b needs a gas layer to account for its low bulk density. However, there are a range of possible scenarios for the envelope and interior compositions (Rogers & Seager, 2010b). In most interior structure models for GJ 1214b, the pressure at the base of the envelope ranges from 3 GPa to 40 GPa. Given the planet's equilibrium temperature of $T_{\rm eq}$ of 400-550 K (depending on the albedo), Figure 5-2 reveals that GJ 1214b is too strongly irradiated to have a liquid water ocean on its surface. This conclusion still holds when we repeat our calculations with mean shortwave opacities (Equatiion (5.12)) tailored to GJ 1214's M4.5 spectral type.

Previously, Rogers & Seager (2010b) found that GJ 1214b would be too hot for liquid water unless the planet has a low intrinsic luminosity ($L_{\rm int}/M_p$ more than two orders of magnitude smaller than the Earth). We have strengthened and improved these constraints with a better treatment of the radiative properties of the planet envelope (especially the green house heating factor γ) and a more rigorous model of condensation in the planet envelope.

5.5.3 Kepler-22b

The primary goal of the *Kepler Mission* is to discover habitable Earth-size planets. Kepler-22b (Borucki et al., 2012) is the first confirmed sub-Neptune-size transiting planet orbiting in the habitable zone of its star (a G5 dwarf). Kepler-22b has an equilibrium temperature of $T_{\rm eq} = 262$ K (assuming an Earth-like Bond albedo of $A = 0.29$ and full-redistribution). The planetary radius is measured to be $R_p = 2.38 \pm 0.13\ R_\oplus$, but the planet mass is unknown; Keck-HIRES radial velocity measurements place a 3σ upper limit of $M_p \leq 124\ M_\oplus$. If Kepler-22b had a rocky-composition similar to the Earth, its mass would be $M_p = 34\ M_\oplus$, in excess of the critical core mass at which runaway gas accretion is expected to ensue (Rafikov, 2006; Alibert et al., 2006). With a radius similar to GJ 1214b, it is very plausible that Kepler-22b harbors a significant volatile reservoir (consisting of ice-forming material and/or nebular gas).

Kepler-22b need not be rock-dominated to harbor a liquid water ocean; it may have a liquid water ocean persisting below a voluminous water-hydrogen envelope. Our model sets a lower limit on the mean planet density that is consistent with the presence of an ocean on the $R_p = 2.4\ R_\oplus$, $T_{\rm eq} = 262$ K planet. We find that Kepler-22b must have a mass of at least $7.0\ M_\oplus$ to harbor a liquid water ocean, assuming an interior composition that is 33 % rock and 66 % water. For masses below this, a water-saturated envelope would not be puffy enough to account for Kepler-22b's low mean density—an un-saturated hydrogen-rich composition would be required.

5.6 Discussion

5.6.1 Further Restrictions on Liquid Water Parameter Space

The mere existence of a solution satisfying both radiative-convective and phase equilibrium constraints is a necessary but not sufficient criterion to identify planets with the potential for liquid water oceans. Not all of the liquid water ocean parameter space in Figures 5-2 and 5-4 may be physically plausible or attainable by planets in nature. We turn now to a discussion of which regimes of our liquid water parameter space are most plausible. We explore how climate stability, atmospheric escape, planet luminosity evolution may all further restrict the habitable zone for hydrogen-rich planets.

Climate Stability

A planet will be most likely to retain a liquid water ocean if its climate is stable against perturbations in the surface temperature and the level of incident irradiation. The radiative feedback between water vapor content and opacity in a planet atmosphere can have a destabilizing influence and potentially lead to a runaway greenhouse (e.g., Komabayashi, 1967; Ingersoll, 1969; Abe & Matsui, 1988; Kasting, 1988; Nakajima et al., 1992). An increase in the planet surface temperature leads to a dramatic increase in the envelope water vapor content, which increases the opacity, which leads to a decrease in T_{eff}, which finally engenders a further increase in T_{s}. More generally, any scenarios where the flux radiated by the planet (T_{eff}) decreases with increasing T_{s} at fixed T_{eq} could be subject to a destabilizing climate feedback leading to runaway greenhouse instabilities.

The planets near the limiting high-T_{int} high-T_{eq} locus at $P_{\mathrm{ns}} < P_c$ in Figure 5-2 are potentially subject to the runaway greenhouse instability. These potentially unstable radiative-convective equilibrium solutions correspond to envelopes with high water mixing ratios for which the moist-adiabat P–T profiles pile up along the water saturation curve. As a result, the planet radiative properties (T_{eq} and T_{eff}) are largely insensitive to the surface temperature T_{s}. We qualify these P–T profiles as "potentially" unstable because the above description of the runaway greenhouse instability implicitly assumes that the equilibrium T_{s}–T_{eff} relation also holds when the planet is perturbed from equilibrium. Dynamical models of the planet envelope response to perturbation are necessary to assess whether the instability actually occurs (Nakajima et al., 1992), but are out of the scope of this work.

Planet Mass Loss

Atmospheric mass loss could play an important role sculpting the inner edge of the habitable zone for H_2-rich planets. Escape sets a lower bound on the planet mass that can retain H_2 at a given level of irradiation. Considering H_2 escape would have the effect of ruling out liquid ocean scenarios for low mass planets at high equilibrium temperatures, effectively chopping off the low-M_p high-T_{eq} corner of Figure 5-4.

Atmospheric escape is imperfectly understood, and predictions for exoplanet mass-loss rates suffer from unknowns in the stellar X/EUV fluxes, the conditions at the planet exosphere, and the mass-loss efficiency. An upper limit on the escape rate is determined by the rate at which X/EUV heating of the planet's upper atmosphere can supply the energy needed overcome the gravitational binding energy of the planet's outer layers (energy-limited mass loss, e.g., Lammer et al., 2003; Lecavelier Des Etangs, 2007; Valencia et al., 2010; Rogers et al., 2011),

$$\dot{M} = -\frac{\epsilon \pi F_{\mathrm{XUV}} R_{\mathrm{XUV}}^2 R_p}{G M_p K_{\mathrm{tide}}}. \tag{5.30}$$

F_{XUV} represents the flux of photoionizing radiation impinging on the planet. K_{tide} is a correction factor that accounts for tidal effects for planets in close proximity to their star (given by Equation (17) in Erkaev et al., 2007). Finally, $R_{\mathrm{X/EUV}}$ reflects the planet radius at which X/EUV photons are absorbed. Much of the poorly-understood physics is encapsulated in the mass loss efficiency, ϵ, representing fraction of the energy in X/EUV photons incident on the planet that goes into unbinding particles in the planet atmosphere. The envelope mass loss timescale, $t_{\dot{M}} \equiv M_{\rm env}/\dot{M}$ provides a rough measure of envelope survival plausibility.

Observations suggest that planets a few times the mass of the Earth can, in some cases, retain hydrogen atmospheres at the equilibrium temperatures of interest to the liquid water parameter space ($T_{\rm eq} \lesssim 400$ K). *Kepler* has found, at equilibrium temperatures $T_{\rm eq} \gtrsim 500$ K, super-Earths with densities so low they demand atmospheres of light gases (e.g., Kepler-11c, d, e, f). These discoveries provide empirical motivation for considering the range of scenarios for liquid water oceans on strongly irradiated hydrogen-rich planets. As *Kepler* continues to search for transits in its extended mission, the accumulating distribution of close-in planet mean densities will hopefully shed light on planet mass loss processes.

Planet Luminosity Evolution

An exoplanet's intrinsic luminosity is not directly measurable. Many sources can contribute to the intrinsic luminosity of a planet, including envelope contraction, radioactive heating, secular cooling of the "core"/rocky interior, tidal heating, and ohmic dissipation. In this section we discuss bounding the planet luminosity to diagnose planet configurations that may be implausible for a planet to evolve into, and to identify planet configurations that may be very short lived.

The decay of radioactive isotopes sets a rough lower floor on the intrinsic planet luminosity of low-mass planets. The rate of radioactive heating is set by the initial (uncertain) abundances of long-lived radio-nuclides in the planet, and does not depend on the thermal or dynamical evolution of the planet. On Earth, radioactive heating is estimated to contribute about 50% of the heat flux from the interior (Van Schmus, 1995). Currently the decay chains from ^{40}K, ^{232}Th, ^{235}U and ^{238}U dominate the radioactive heating of Solar System bodies. Using the elemental abundances for CI material from Wasson & Kallemeyn (1988); nuclide rest masses, isotopic abundances, and half lives from National Nuclear Data Center (2011); and estimated mean neutrino energy losses from Van Schmus (1995), we find that radioactive heating would contributes roughly 3.4×10^{-12} W kg^{-1} per mass of mantle material at the current Solar System age (4.55 Gyr). Extrapolating to 1 and 10 Gyr, we find heating rates of 1.7×10^{-11} W kg^{-1} and 9.6×10^{-13} W kg^{-1}, respectively. Lower intrinsic luminosities are possible if the planet is deficient in radioactive nuclei relative to the Earth, or if the transport of energy from the planet interior to the envelope is a limiting factor (e.g., if the mantle is heating up).

An order of magnitude upper limit on the intrinsic luminosity of a planet may be estimated based on the energy available for the planet to radiate away. The luminosity released by the planet's cooling and contraction is intrinsically linked to the rate of evolution of a planet. Very high luminosity states would be short-lived (without another sustaining energy source). At the other extreme, very low luminosity states may correspond to planets older than a Hubble time (assuming a hot-start). The timescale, t_{evolve}, for passive evolution through a particular configuration is,

$$t_{\mathrm{evolve}} = \frac{\Delta E}{L_{\mathrm{int}}}, \tag{5.31}$$

where ΔE is the energy available to the planet to radiate away.

In future work, we will calculate the passive evolution timescale t_{evolve} as a function of L_{int} along iso-mass and iso-composition models. We will estimate the available energy ΔE by comparing planet models with the same T_{eq} and $\mathrm{H_2}$ envelope mass, accounting for cooling of the planet core, ocean and envelope as well as latent heat released as the ocean grows by condensation. In this way, we will approximate the timespan over which passive evolution of the planet could maintain a given contraction luminosity. High luminosity, apparently short-lived, planet configurations will not be completely ruled out, but would require additional energy sources such as tidal heating (Bodenheimer et al., 2001; Goldreich & Soter, 1966), kinetic heating (Guillot & Showman, 2002), ohmic dissipation (Batygin & Stevenson, 2010), and ongoing chemical differentiation (Fortney & Hubbard, 2004) to slow their cooling.

5.6.2 Comparison to Previous Work

Our constraints on the inner edge of the habitable zone for H_2-rich planets (the maximum $T_{\rm int}$-$T_{\rm eq}$ curves in Figure 5-2) corresponds to a generalization of the Komabayashi-Ingersoll flux limit. In the late 1960's, Komabayashi (1967) and Ingersoll (1969) noted that there is an upper limit to the outgoing IR flux that a planet with a saturated envelope above a water ocean can radiate away. This limit results from the interplay between vapor-liquid phase equilibrium and radiative equilibrium with a water vapor-mediated opacity. Derivations of the "traditional" K–I flux limit (e.g., Komabayashi, 1967; Ingersoll, 1969) assume the incoming stellar radiation is absorbed and reprocessed by the planet surface, and neglect any short-wave absorption in the envelope. Generalizing to the Guillot (2010) photosphere, we find that the total outgoing IR flux ($T_{\rm eff}^4 = T_{\rm int}^4 + T_{\rm eq}^4$) can be higher if the interior heat flow is reduced and the incoming stellar irradiation is absorbed in the planet atmosphere before reaching the planet surface. The region of liquid water parameter space with $T_{\rm eff}$ exceeding the traditional K–I limit correspond to planets with very isothermal envelope P–T profiles.

Our exploration of the outer boundary of the habitable zone unifies several previous studies of H_2-rich planets. Stevenson (1999) pointed out that an interstellar planet (scattered from its star during the late stages of formation) may sustain liquid water oceans on its surface even in the absence of stellar irradiation if it retains an H_2 atmosphere that blankets its intrinsic luminosity from long-lived radionuclides. This scenario corresponds to the $T_{\rm eq} = 0$ limit (y-intercept) of the liquid water parameter space in Figure 5-2. More recently, Pierrehumbert & Gaidos (2011) modeled the climate of hydrogen greenhouse planets and found that 4×10^6 Pa of pure H_2 could maintain a surface temperature of 280 K out to 10 AU ($T_{\rm eq} \approx 90$ K) from a G-type star. Our results show good qualitative agreement to these previous studies.

5.6.3 Habitability of high pressure liquid water

Liquid water may neither be a necessary nor sufficient criterion for habitability. Temperature, water activity, nutrients, pore space, and free energy availability also limit the environments in which extremophiles can survive (Baross et al., 2007; Jakosky et al., 2007). Although only 12% of the volume of Earth where liquid water exits is known to host life (Jones & Lineweaver, 2010), Earth-based extremophiles are nonetheless amazingly versatile. The current high-temperature limit for known life is 395 K, but hydrothermal vent environments at higher temperatures have not yet been fully explored. Complex molecules necessary for life break down at temperatures approaching ~ 500 K, so this may set a thermodynamically-motivated temperature upper limit. Life has been found at the maximum depths/pressures for which it has been searched (155 MPa, Szewzyk et al., 1994), while dormant bacterial spores at altitudes of 77 km (2 Pa) in the atmosphere have been shown to retain their viability (Imshenetsky et al., 1978). Our approach to constraining the parameter space for planets with liquid water oceans could be generalized to consider only planets that may harbor liquid water at pressures and temperatures where Earth-based extremophiles are known to survive (e.g., $T \leq 395$ K, $P \leq 155$ MPa Jones & Lineweaver, 2010) instead of the full stability field of pure liquid water.

A hydrogen-rich envelope presents a challenge for detecting biosignatures. Though the scale-height and spectral features in the transmission spectrum are large, if the envelope is very massive, large rates of biological production may be necessary to reach a detectable concentration of biomarker (Seager et al. in prep). Ecosystems on hydrogen-rich planets may also be short-lived and/or self-limiting. Pierrehumbert & Gaidos (2011) described a scenario where methanogens in a H_2-rich atmosphere could “nurture the seeds of their own destruction” by consuming the envelope H_2 to form CH_4 from outgassed CO_2.

5.6.4 Caveats

In this section we review the approximations that we have made in our models of H_2-rich planets with liquid water oceans, and discuss the limits of their applicability.

Radiative Transfer Approximations

To broadly explore the parameter space for liquid water oceans, we have made several simplifying approximations in our model of the radiative transfer through planet envelopes. We have taken a one-dimensional treatment. In this way, we do not attempt to accurately capture seasonal or latitudinal variations in the planet irradiation and temperature. We have also used a semi-grey model. By constraining γ directly from the wavelength-dependent absorption cross-sections of H_2 and H_2O we account for the dominant wavelength dependent effect: green-house warming due to the enhanced absorption of long-wave thermal radiation compared to the shortwave incident irradiation ($\gamma \sim 0.1$). However, our grey model will not resolve higher order wavelength-dependent effects.

We have focused on planet envelopes in full radiative-convective equilibrium at their current level of irradiation. A planet may never actually attain equilibrium throughout its entire envelope. If the distribution of energy within the planet is slow enough, the timescale to reach equilibrium may be long, and the planet may reach a non-equilibrium steady-state instead. In those cases, the planet envelope (and any liquid water ocean beneath) could be slowly heating or cooling (Equation (5.8) would not be fully satisfied). The self-limiting water ocean vaporization scenario described by Kuchner (2003) is one example of a non-equilibrium, steady state configuration.

In this work we have emphasized planets with massive, optically thick envelopes. This complements the vast literature on the "traditional" habitable zone for planets with optically thin Earth-like envelopes. Our treatment of the radiative regime of the planet envelope breaks down for optically thin envelopes. If $\gamma\tau \gg 1$ is not satisfied at the tropopause (radiative-convective boundary), the ongoing absorption of shortwave radiation deep in the envelope could affect the location of the radiative convective transition. If the incoming stellar radiation penetrates all the way to the solid/ocean surface, the radiative properties of the surface can also have an important influence on the P–T profile of the envelope. These surface effects are not accounted for in the Guillot (2010) temperature profile. In our investigation of the habitable zone we have already eliminated all the optically thin scenarios (e.g. ocurring at high $T_{\rm int}$, low $T_{\rm eq}$ in Figure 5-2) that do not satisfy $\gamma\tau \lesssim 1$.

By pursuing a one-dimensional, semi-grey model for optically thick hydrogen-rich super-Earths in radiative-convective equilibrium, we have proceeded in the same spirit as the pioneering grey climate models studying the habitable zone for Earth-like planets (Ingersoll, 1969; Nakajima et al., 1992). Our aim is capture the leading order physics with sufficient fidelity to identify the major factors that limit the scenarios for liquid water oceans on planets with hydrogen envelopes.

Effect of Other Envelope Gases

We have considered H_2–H_2O planet envelopes in detail since both these molecules are expected to be major constituents of the material from which planets form. Binary mixtures of just H_2 and H_2O are an idealization, however; planet envelopes will contain a wide range of species that will affect the atmosphere mean molecular weight, opacity, heat capacity and latent heat.

The presence of He will shrink the habitable zone for hydrogen-rich planets (decreasing the maximum planet radii and increasing the minimum stellar irradiation). Any hydrogen that a planet accretes from the protoplanetary disk will be accompanied by approximately one in four parts He (by mass). Replacing some H_2 molecules by He will reduce the overall opacity (and greenhouse heating) of the envelope; He is not spectrally active, and H_2-He CIA is typically weaker than H_2-H_2 (Borysow et al., 1988). The physical thickness of the envelope will also decrease due to the higher mean molecular weight and correspondingly smaller scale height. Finally, the smaller specific heat of He (as a monoatomic gas) will steepen the adiabat.

The dominant effect of polluting the H_2–H_2O envelope with other ice-forming molecules (e.g. CO_2, CH_4, NH_3) is to shift both the inner and outer boundaries of the habitable zone to greater distances. The addition of CO_2, CH_4, and NH_3 increases the greenhouse warming of the atmosphere and surface. Condensation of these species and the associated release of latent heat will make the adiabat more shallow, effectively decreasing the temperature contrast between the planet surface and photosphere.

Effect of Solutes in the Ocean

Reality is more complex than the pure water oceans we have considered in our models. The Earth's oceans contain salts and dissolved gases. The "ice" layers on Neptune are thought to be water mixed with NH_3, CH_4, and CO_2. Super-Earths with hydrogen-rich gas layers will likely have hydrogen dissolved in the ocean. When modeling planets, pure water is an idealization, and the presence of contaminants can have important effects on the water EOS and phase boundaries.

The phase diagram of mixtures with more than one chemical component are more complicated than those for a single "pure" chemical species. The potential complexity of a phase diagram is encapsulated by the Gibbs phase rule, which describes the number of variables, $\mathcal{F}$, needed to describe the state of a system with $\mathcal{C}$ chemical components and $\mathcal{P}$ coexisting phases,

$$\mathcal{F} = \mathcal{C} - \mathcal{P} + 2. \tag{5.32}$$

The pure water phase diagram in Figure 5-1 is a one-component ($\mathcal{C} = 1$) system. If one phase of pure water is present ($\mathcal{P} = 1$) there are $\mathcal{F} = 2$ degree of freedom and P and T can be varied independently (e.g., the liquid water regime spans an area in P–T space). If $\mathcal{P} = 2$ phases coexist there is a a single degree of freedom (e.g., the liquid-vapor coexistence curve is a line $P_{\mathrm{v,sat}}(T)$ in Figure 5-1), while $\mathcal{P} = 3$ phases can only coexist in equilibrium at isolated P–T points ($\mathcal{F} = 0$). In contrast, for a binary mixture (e.g., H_2-H_2O), single phase regions are described by 3 variables (P, T, and mixing ratio x_{H_2}), and the vapor-liquid coexistence region forms a composition-dependent surface ($P(T, x_{\mathrm{H_2}})$). The phase boundaries, critical points, and triple points of a multi-component mixture are, in general, composition dependent. At fixed composition and pressure, a mixture may boil and condense at different temperatures. Further, at fixed P and T two phases of different composition may coexist.

Binary mixtures of H_2 and H_2O are of particular interest for the exploration of liquid water oceans on hydrogen-rich super-Earths and mini-Neptunes. Seward & Franck (1981) studied the H_2-H_2O system experimentally up to 713 K and 2.5 kbar, measuring the phase boundaries and critical curve for H_2 concentrations ranging from 0.5 to 90 mol–% H_2. The critical-curve of the H_2-H_2O mixture generalizes the concept of the water critical point to include dependence on the mixing ratio of H_2. Adding H_2 to water substantially increases the critical pressure of the mixture, but has a lesser effect on the critical temperature (e.g., $P_c = 252.0$ MPa and $T_c = 654.5$ K for 38 mol–% H_2). At temperatures exceeding the critical curve, the H_2-H_2O mixture is completely miscible, while at lower temperatures the system will, for a range of H_2 mixing ratios, exhibit phase separation (where a H_2O-rich fluid phase coexists in equilibrium with a H_2-rich gas phase). The higher the H_2 mixing ratio dissolved in a H_2O ocean, the higher the pressure must be at the ocean surface to keep the ocean in a liquid condensed phase.

Future work will include the effect of H_2 solubility on the liquid water parameter space. H_2 solubility will not only affect the conditions at the ocean-envelope interface, it will also influence the moist adiabat (H_2 will be raining out along with H_2O). Including H_2 solubility will likely increase the maximum radii for planets with a liquid water oceans (or more precisely, planets with a first order phase transition between a water-rich condensed phase and a hydrogen-rich gas phase). The radius increase is expected on two fronts: *i)* the possibility of saturated H_2 envelopes extending to higher pressures, and *ii)* the dissolved H_2 decreasing the density of the liquid water ocean.

5.7 Summary and Conclusions

How Neptune-like can a planet be and still support a liquid water ocean on its surface below a hydrogen-rich envelope? We investigated this question by combining planet interior structure models and semi-grey atmosphere structure models for saturated radiative-convective envelopes. We summarize our main results and conclusions below.

- There is an upper limit to the radius of planets with liquid water oceans. The precise radius limit depends on the planet mass, the equilibrium temperature, and the assumed interior composition (Figure 5-4). Sub-Neptune-mass planets with radii exceeding $\sim 3.25\ R_\oplus$ cannot have liquid water oceans, even if they have an extreme low density pure-ice interior composition.

- A surface pressure on the order of $\sim 10^7$ Pa of H_2 is optimum for hydrogen rich planets in the habitable zone because it allows liquid water oceans over the widest range of planet energy budgets. H_2–H_2 CIA starts to become comparable to water bound-bound absorption at this pressure. Planets with surface pressures in excess of 10^7 Pa of H_2 need very low intrinsic luminosities (cold interiors) to avoid a surface that is too hot (super-critical) due to strong CIA. Planets with lower surface pressures of H_2 have less green house heating from CIA and must be closer to their star to avoid freezing.

- We demonstrated how a sub-Neptune planet's interior luminosity can affect the range of orbits (range of $T_{\rm eq}$) on which it could have a liquid water ocean. We set limits on the equilibrium temperatures and intrinsic luminosities of planets with surface water oceans (Figure 5-2).

- In our model, planets with $T_{\rm eq} > 370$ K in orbit around G-dwarf stars will not have liquid water oceans. This inner edge of the habitable zone for massive optically thick H_2 envelopes is closer to the star than traditionally found for optically thin envelopes. Planets with liquid water oceans this close to their star correspond to cases with very low intrinsic luminosities and very isothermal envelopes that absorb all the incoming stellar irradiation before it reaches the planet surface. Detailed non-grey radiative transfer calculations should be performed to verify whether this class of solutions persists.

- We applied our models to study specific planets.
  - The Solar System jovian planets do not have liquid water oceans because their interior entropy and H_2 mixing ratio are too high.
  - GJ 1214b does not have a liquid water ocean because it is too strongly irradiated ($T_{\rm eq}$ too high).

  - Kepler-22b need not be rock-dominated to harbor a liquid water ocean. Assuming an interior composition that is 33 % rock and 66 % water, we find that Kepler-22b must have a mass of at least 7.0 $M_\oplus$ to have a liquid water ocean.

- The liquid water parameter space we have derived is conservative. Our model strongly disfavors liquid oceans on planets falling outside the liquid water parameter space delimited in this work. Planets falling within the parameter space may or may not have liquid water oceans on their surface and require further study. Climate stability, atmospheric escape, and planet evolution considerations may eventually help to rule out some ocean–planet scenarios.

Although there are currently no known confirmed transiting exoplanets (with both M_p and R_p measured) falling within the liquid water parameter space that we have defined, the habitable zone for hydrogen-rich planets will not remain unpopulated for long. *Kepler*, in its extended mission, will continue to find smaller planet candidates on longer and longer orbital periods. This models will provide a useful tool to identify (based on observable planet properties) the best habitable zone candidates for further observational follow-up and detailed climate modeling.

Bibliography

Abe, Y., & Matsui, T. 1988, Journal of Atmospheric Sciences, 45, 3081

Adams, E. R., Seager, S., & Elkins-Tanton, L. 2008, ApJ, 673, 1160

Alexander, D. R., & Ferguson, J. W. 1994, ApJ, 437, 879

Alibert, Y., Baraffe, I., Benz, W., et al. 2006, A&A, 455, L25

Anderson, O. L., Dubrovinsky, L., Saxena, S. K., & LeBihan, T. 2001, Geophys. Res. Lett., 28, 399

Andrault, D., Fiquet, G., Guyot, F., & Hanfland, M. 1998, Science, 282, 720

Baglin, A., Auvergne, M., Barge, P., et al. 2009, in IAU Symposium, Vol. 253, IAU Symposium, 71–81

Bakos, G. Á., Torres, G., Pál, A., et al. 2010, ApJ, 710, 1724

Baraffe, I., Alibert, Y., Chabrier, G., & Benz, W. 2006, A&A, 450, 1221

Baraffe, I., Chabrier, G., Allard, F., & Hauschildt, P. H. 1998, A&A, 337, 403

Baraffe, I., Chabrier, G., & Barman, T. 2008, A&A, 482, 315

Baraffe, I., Chabrier, G., Barman, T. S., Allard, F., & Hauschildt, P. H. 2003, A&A, 402, 701

Baross, J., Benner, S., Cody, G., et al. 2007, The Limits of Organic Life in Planetary Systems (Washington DC: National Research Council, National Academies Press)

Basri, G., & Brown, M. E. 2006, Annual Review of Earth and Planetary Sciences, 34, 193

Batalha, N. M., Rowe, J. F., Bryson, S. T., et al. 2012, ArXiv e-prints

Batygin, K., & Stevenson, D. J. 2010, ApJ, 714, L238

Bean, J. L., Benedict, G. F., Charbonneau, D., et al. 2008, A&A, 486, 1039

Birch, F. 1947, Physical Review, 71, 809

Bodenheimer, P., Hubickyj, O., & Lissauer, J. J. 2000, Icarus, 143, 2

Bodenheimer, P., Lin, D. N. C., & Mardling, R. A. 2001, ApJ, 548, 466

Borucki, W., Koch, D., Basri, G., et al. 2008, in IAU Symposium, Vol. 249, IAU Symposium, ed. Y.-S. Sun, S. Ferraz-Mello, & J.-L. Zhou, 17–24

Borucki, W. J., Koch, D. G., Basri, G., et al. 2011a, ApJ, 728, 117

—. 2011b, ApJ, 736, 19

Borucki, W. J., Koch, D. G., Batalha, N., et al. 2012, ApJ, 745, 120

Borysow, A. 2002, A&A, 390, 779

Borysow, J., Frommhold, L., & Birnbaum, G. 1988, ApJ, 326, 509

Borysow U. G. Jorgensen, A., & Fu, Y. 2001, Journal of Quantitative Spectroscopy and Radiative Transfer, 68, 235

Boss, A. P. 1997, Science, 276, 1836

Burrows, A., Sudarsky, D., & Hubbard, W. B. 2003, ApJ, 594, 545

Butler, R. P., Vogt, S. S., Marcy, G. W., et al. 2004, ApJ, 617, 580

Carroll, B. W., & Ostlie, D. A. 2007, An Introduction to Modern Astrophysics, 2nd edn. (Boston: Pearson Addison-Wesley)

Chabrier, G., Barman, T., Baraffe, I., Allard, F., & Hauschildt, P. H. 2004, ApJ, 603, L53

Chambers, J. 2010, Terrestrial Planet Formation, ed. S. Seager (Tucson, AZ: University of Arizona Press)

Charbonneau, D., Brown, T. M., Latham, D. W., & Mayor, M. 2000, ApJ, 529, L45

Charbonneau, D., Berta, Z. K., Irwin, J., et al. 2009, Nature, 462, 891

Cooper, J. 1982, International Journal of Thermophysics, 3, 35, 10.1007/BF00503957

Dalgarno, A., & Williams, D. A. 1965, Proceedings of the Physical Society, 85, 685

Deming, D., Harrington, J., Laughlin, G., et al. 2007, ApJ, 667, L199

Deming, D., Seager, S., Winn, J., et al. 2009, PASP, 121, 952

Dittmann, J. A., Close, L. M., Green, E. M., Scuderi, L. J., & Males, J. R. 2009, ApJ, 699, L48

Dodson-Robinson, S. E., & Bodenheimer, P. 2010, Icarus, 207, 491

Driver, K. P., & Militzer, B. 2012, Physical Review Letters, 108, 115502

Dunaeva, A. N., Antsyshkin, D. V., & Kuskov, O. L. 2010, Solar System Research, 44, 202

Eggert, J., Brygoo, S., Loubeyre, P., et al. 2008, Physical Review Letters, 100, 124503

Eggleton, P. P. 1983, ApJ, 268, 368

Elkins-Tanton, L. T. 2008, Earth and Planetary Science Letters, 271, 181

Elkins-Tanton, L. T., & Seager, S. 2008a, ApJ, 688, 628

—. 2008b, ApJ, 685, 1237

Erkaev, N. V., Kulikov, Y. N., Lammer, H., et al. 2007, A&A, 472, 329

Feistel, R., & Wagner, W. 2007, Geochim. Cosmochim. Acta, 71, 36

Ferguson, J. W., Alexander, D. R., Allard, F., et al. 2005, ApJ, 623, 585

Figueira, P., Pont, F., Mordasini, C., et al. 2009, A&A, 493, 671

Fischer, D. A., Marcy, G. W., Butler, R. P., et al. 2008, ApJ, 675, 790

Fortney, J. J., Glenzer, S. H., Koenig, M., et al. 2009, Physics of Plasmas, 16, 041003

Fortney, J. J., & Hubbard, W. B. 2004, ApJ, 608, 1039

Fortney, J. J., Lodders, K., Marley, M. S., & Freedman, R. S. 2008, ApJ, 678, 1419

Fortney, J. J., Marley, M. S., & Barnes, J. W. 2007, ApJ, 659, 1661

Freedman, R. S., Marley, M. S., & Lodders, K. 2008, ApJS, 174, 504

Fujiwara, A., Kawaguchi, J., Yeomans, D. K., et al. 2006, Science, 312, 1330

Gillon, M., Demory, B.-O., Barman, T., et al. 2007a, A&A, 471, L51

Gillon, M., Pont, F., Demory, B.-O., et al. 2007b, A&A, 472, L13

Goldreich, P., & Soter, S. 1966, Icarus, 5, 375

Grasset, O., Schneider, J., & Sotin, C. 2009, ApJ, 693, 722

Greenzweig, Y., & Lissauer, J. J. 1992, Icarus, 100, 440

Guillot, T. 2005, Annual Review of Earth and Planetary Sciences, 33, 493

—. 2010, A&A, 520, A27

Guillot, T., & Showman, A. P. 2002, A&A, 385, 156

Hansen, B. M. S. 2008, ApJS, 179, 484

Harris, A. W. 1978, in Lunar and Planetary Institute Science Conference Abstracts, Vol. 9, Lunar and Planetary Institute Science Conference Abstracts, 459–461

Hart, M. H. 1979, Icarus, 37, 351

Heber, V. S., Brooker, R. A., Kelley, S. P., & Wood, B. J. 2007, Geochim. Cosmochim. Acta, 71, 1041

Hemley, R. J., Jephcoat, A. P., Mao, H. K., et al. 1987, Nature, 330, 737

Heng, K., Hayek, W., Pont, F., & Sing, D. K. 2011, ArXiv e-prints

Henry, G. W., Marcy, G. W., Butler, R. P., & Vogt, S. S. 2000, ApJ, 529, L41

Hillenbrand, L. A. 2008, Physica Scripta Volume T, 130, 014024

Holman, M. J., Fabrycky, D. C., Ragozzine, D., et al. 2010, Science, 330, 51

Howard, A. W., Marcy, G. W., Johnson, J. A., et al. 2010, Science, 330, 653

Howard, A. W., Marcy, G. W., Bryson, S. T., et al. 2011, ArXiv e-prints

Huang, S.-S. 1960, Sci. Am., 202, 55

Hubbard, W. B. 1977, Icarus, 30, 305

Hubbard, W. B., & Macfarlane, J. J. 1980, J. Geophys. Res., 85, 225

Hubbard, W. B., Podolak, M., & Stevenson, D. J. 1995, in Neptune and Triton, ed. D. P. Cruikshank, M. S. Matthews, & A. M. Schumann (Tucson, AZ: University of Arizona Press), 109–138

Hubickyj, O., Bodenheimer, P., & Lissauer, J. J. 2005, Icarus, 179, 415

Iaroslavitz, E., & Podolak, M. 2007, Icarus, 187, 600

Ida, S., & Lin, D. N. C. 2004, ApJ, 604, 388

Imshenetsky, A., Lysenko, S., & Kazakov, G. 1978, Appl. Environ. Microbiol., 35, 1

Ingersoll, A. P. 1969, Journal of Atmospheric Sciences, 26, 1191

Irwin, J., Charbonneau, D., Nutzman, P., & Falco, E. 2009, in IAU Symposium, Vol. 253, IAU Symposium, 37–43

Jakosky, B., Amend, J., Berelson, W., et al. 2007, An Astrobiology Strategy for the Exploration of Mars (Washington DC: National Research Council, National Academies Press)

Jarosewich, E. 1990, Meteoritics, 25, 323

Jones, E. G., & Lineweaver, C. H. 2010, Astrobiology, 10, 349

Kaltenegger, L., & Traub, W. A. 2009, ApJ, 698, 519

Kandel, R., & Viollier, M. 2005, Space Science Reviews, 120, 1

Kary, D. M., & Lissauer, J. J. 1994, in Numerical Simulations in Astrophysics, ed. J. Franco, S. Lizano, L. Aguilar, & E. Daltabuit (Cambridge: Cambridge University Press), 364

Kasting, J. F. 1988, Icarus, 74, 472

Kasting, J. F., Whitmire, D. P., & Reynolds, R. T. 1993, Icarus, 101, 108

Kite, E. S., Manga, M., & Gaidos, E. 2009, ApJ, 700, 1732

Komabayashi, M. 1967, J. Meteor. Soc. Japan, 45, 137

Kuchner, M. J. 2003, ApJ, 596, L105

Kuchner, M. J., & Seager, S. 2005, ArXiv Astrophysics e-prints

Lammer, H., Selsis, F., Ribas, I., et al. 2003, ApJ, 598, L121

Lecavelier Des Etangs, A. 2007, A&A, 461, 1185

Léger, A., Selsis, F., Sotin, C., et al. 2004, Icarus, 169, 499

Léger, A., Rouan, D., Schneider, J., et al. 2009, A&A, 506, 287

Lemmon, E. W., McLinden, M. O., & Friend, D. G. 2009, Thermophysical Properties of Fluid Systems, NIST Chemistry WebBook, `http://webbook.nist.gov`

Lissauer, J. J., Hubickyj, O., D'Angelo, G., & Bodenheimer, P. 2009, Icarus, 199, 338

Lissauer, J. J., Fabrycky, D. C., Ford, E. B., et al. 2011, Nature, 470, 53

Lodders, K. 2000, Space Sci. Rev., 92, 341

—. 2003, ApJ, 591, 1220

Lorenz, R. D., Stiles, B. W., Kirk, R. L., et al. 2008, Science, 319, 1649

Lovis, C., Mayor, M., Bouchy, F., et al. 2009, in IAU Symposium, Vol. 253, IAU Symposium, 502–505

Maness, H. L., Marcy, G. W., Ford, E. B., et al. 2007, PASP, 119, 90

Marboeuf, U., Mousis, O., Ehrenreich, D., et al. 2008, ApJ, 681, 1624

Marcus, R. A., Sasselov, D., Hernquist, L., & Stewart, S. T. 2010, ApJ, 712, L73

Mayor, M., & Queloz, D. 1995, Nature, 378, 355

Mayor, M., Udry, S., Lovis, C., et al. 2009a, A&A, 493, 639

Mayor, M., Bonfils, X., Forveille, T., et al. 2009b, A&A, 507, 487

Militzer, B., Hubbard, W. B., Vorberger, J., Tamblyn, I., & Bonev, S. A. 2008, ApJ, 688, L45

Miller-Ricci, E., Seager, S., & Sasselov, D. 2009, ApJ, 690, 1056

Mizuno, H. 1980, Progress of Theoretical Physics, 64, 544

Movshovitz, N., Bodenheimer, P., Podolak, M., & Lissauer, J. J. 2010, Icarus, 209, 616

Movshovitz, N., & Podolak, M. 2008, Icarus, 194, 368

Murray-Clay, R. A., Chiang, E. I., & Murray, N. 2009, ApJ, 693, 23

Nakajima, S., Hayashi, Y.-Y., & Abe, Y. 1992, Journal of Atmospheric Sciences, 49, 2256

National Nuclear Data Center. 2011, Chart of Nuclides, `http://www.nndc.bnl.gov/chart/`

Nayakshin, S. 2010a, MNRAS, 408, L36

—. 2010b, MNRAS, 408, 2381

—. 2011, MNRAS, 413, 1462

Nettelmann, N., Becker, A., Holst, B., & Redmer, R. 2012, ApJ, 750, 52

Nettelmann, N., Fortney, J. J., Kramm, U., & Redmer, R. 2010, arXiv:1010.0277

Nettelmann, N., Holst, B., Kietzmann, A., et al. 2008, ApJ, 683, 1217

Oppenheimer, C. 2003, Treatise on Geochemistry, 3, 123

Pierrehumbert, R., & Gaidos, E. 2011, ApJ, 734, L13+

Podolak, M., Hubbard, W. B., & Stevenson, D. J. 1991, Model of Uranus' interior and magnetic field, ed. J. T. Bergstralh, E. D. Miner, & M. S. Matthews (Tucson, AZ: University of Arizona Press), 29–61

Podolak, M., Pollack, J. B., & Reynolds, R. T. 1988, Icarus, 73, 163

Podolak, M., Weizman, A., & Marley, M. 1995, Planet. Space Sci., 43, 1517

Pollack, J. B., Hubickyj, O., Bodenheimer, P., et al. 1996, Icarus, 124, 62

Queloz, D., Bouchy, F., Moutou, C., et al. 2009, A&A, 506, 303

Rafikov, R. R. 2006, ApJ, 648, 666

Ragozzine, D., & Wolf, A. S. 2009, ApJ, 698, 1778

Ribas, I., Guinan, E. F., Güdel, M., & Audard, M. 2005, ApJ, 622, 680

Ringwood, A. E. 1979, Origin of the earth and moon (New York: Springer-Verlag)

Rogers, L. A., Bodenheimer, P., Lissauer, J. J., & Seager, S. 2011, ApJ, 738, 59

Rogers, L. A., & Schechter, P. L. 2011, in IAU Symposium, Vol. 276, IAU Symposium, ed. A. Sozzetti, M. G. Lattanzi, & A. P. Boss, 457–458

Rogers, L. A., & Seager, S. 2010a, ApJ, 712, 974

—. 2010b, ApJ, 716, 1208

Safronov, V. S. 1969, Evoliutsiia doplanetnogo oblaka. (Moscow: Nauka)

Salpeter, E. E., & Zapolsky, H. S. 1967, Physical Review, 158, 876

Saumon, D., Chabrier, G., & van Horn, H. M. 1995, ApJS, 99, 713

Saumon, D., & Guillot, T. 2004, ApJ, 609, 1170

Schaefer, L., & Fegley, B. 2009, ApJ, 703, L113

—. 2010, Icarus, 208, 438

Schiebener, P., Straub, J., Levelt Sengers, J. M. H., & Gallagher, J. S. 1990, Journal of Physical and Chemical Reference Data, 19, 677

Seager, S., Kuchner, M., Hier-Majumder, C. A., & Militzer, B. 2007, ApJ, 669, 1279

Selsis, F., Kasting, J. F., Levrard, B., et al. 2007a, A&A, 476, 1373

Selsis, F., Chazelas, B., Bordé, P., et al. 2007b, Icarus, 191, 453

Seward, T. M., & Franck, E. U. 1981, Ber. Bunsenges. Phys. Chem., 85, 2

Shporer, A., Mazeh, T., Pont, F., et al. 2009, ApJ, 694, 1559

Sotin, C., Grasset, O., & Mocquet, A. 2007, Icarus, 191, 337

Spiegel, D. S., Burrows, A., & Milsom, J. A. 2011, The Astrophysical Journal, 727, 57

Stevenson, D. J. 1982, Planet. Space Sci., 30, 755

—. 1999, Nature, 400, 32

—. 2004, Physics Today, 57, 040000

Sumi, T., Bennett, D. P., Bond, I. A., et al. 2010, ApJ, 710, 1641

Szewzyk, U., Szewzyk, R., & Stenstrom, T.-A. 1994, Proceedings of the National Academy of Science, 91, 1810

Torres, G. 2007, ApJ, 671, L65

Torres, G., Winn, J. N., & Holman, M. J. 2008, ApJ, 677, 1324

Turcotte, D. L., & Schubert, G. 2002, Geodynamics (Cambridge, UK: Cambridge University Press)

Udry, S., Bonfils, X., Delfosse, X., et al. 2007, A&A, 469, L43

Valencia, D., Ikoma, M., Guillot, T., & Nettelmann, N. 2010, A&A, 516, A20+

Valencia, D., O'Connell, R. J., & Sasselov, D. 2006, Icarus, 181, 545

Valencia, D., Sasselov, D. D., & O'Connell, R. J. 2007a, ApJ, 665, 1413

—. 2007b, ApJ, 656, 545

Van Schmus, W. R. 1995, in Global Earth Physics: A Handbook of Physical Constants, ed. T. J. Ahrens, 283–291

Vinet, P., Ferrante, J., Rose, J. H., & Smith, J. R. 1987, J. Geophys. Res., 92, 9319

Vinet, P., Rose, J. H., Ferrante, J., & Smith, J. R. 1989, Journal of Physics Condensed Matter, 1, 1941

Wagner, W. 2009, Software for the Calculation of Thermodynamic Properties for a Great Number of Substances, FLUIDCAL, `http://www.ruhr-uni-bochum.de/thermo/Software/Seiten/Fluidcal-eng.htm`

Wagner, W., & Pruss, A. 1993, Journal of Physical and Chemical Reference Data, 22, 783

Wagner, W., & Pruß, A. 2002, Journal of Physical and Chemical Reference Data, 31, 387

Wagner, W., Saul, A., & Pruss, A. 1994, Journal of Physical and Chemical Reference Data, 23, 515

Wanke, H., & Dreibus, G. 1994, Royal Society of London Philosophical Transactions Series A, 349, 285

Wasson, J. T., & Kallemeyn, G. W. 1988, Royal Society of London Philosophical Transactions Series A, 325, 535

Wiktorowicz, S. J., & Ingersoll, A. P. 2007, Icarus, 186, 436

Wilburn, D. R., & Bassett, W. A. 1978, American Mineralogist, 63, 591

Woolley, H. W. 1948, Compilation of thermal properties of hydrogen in its various isotopic and ortho-para modifications (Washington: National Bureau of Standards)

Woolley, H. W. 1980, in Water and Steam Proceedings of the 9th International Conference on the Properties of Steam, ed. J. Straub, K. Scheffler (New York: Pergamon Press), 166–175

Wordsworth, R. D., Forget, F., Selsis, F., et al. 2011, ApJ, 733, L48

Yi, S., Demarque, P., Kim, Y.-C., et al. 2001, ApJS, 136, 417

Zeng, L., & Seager, S. 2008, PASP, 120, 983